Journal of Applied Mathematics

Applied Mathematics in Biomedical Sciences and Engineering 2014

Guest Editors: Chang-Hwan Im, Kiwoon Kwon, Hang Joon Jo, and Pedro Serranho

Applied Mathematics in Biomedical Sciences and Engineering 2014

Journal of Applied Mathematics

Applied Mathematics in Biomedical Sciences and Engineering 2014

Guest Editors: Chang-Hwan Im, Kiwoon Kwon, Hang Joon Jo, and Pedro Serranho

Copyright © 2014 Hindawi Publishing Corporation. All rights reserved.

This is a special issue published in "Journal of Applied Mathematics." All articles are open access articles distributed under the Creative Commons Attribution License, which permits unrestricted use, distribution, and reproduction in any medium, provided the original work is properly cited.

Editorial Board

Saeid Abbasbandy, Iran
Mina B. Abd-El-Malek, Egypt
Mohamed A. Abdou, Egypt
Subhas Abel, India
Janos Abonyi, Hungary
Sergei Alexandrov, Russia
M. Montaz Ali, South Africa
Mohammad R, Aliha, Iran
Carlos J. S. Alves, Portugal
Mohamad Alwash, USA
Gholam R. Amin, Oman
Saiied Aminossadati, Australia
Igor Andrianov, Germany
Boris Andrievsky, Russia
Whye-Teong Ang, Singapore
Abul-Fazal M. Arif, Saudi Arabia
Sabri Arik, Turkey
Ali R. Ashrafi, Iran
Allaberen Ashyralyev, Turkey
Francis T. K. Au, Hong Kong
Francesco Aymerich, Italy
Jalel Azaiez, Canada
Seungik Baek, USA
Hamid Bahai, UK
Olivier Bahn, Canada
Antonio Bandera, Spain
Jean-Pierre Barbot, France
Mostafa Barigou, UK
Roberto Barrio, Spain
Henri Baudrand, Brazil
Alfredo Bellen, Italy
Vasile Berinde, Romania
Jafar Biazar, Iran
Anjan Biswas, Saudi Arabia
Abdellah Bnouhachem, Morocco
Gabriele Bonanno, Italy
Walter Briec, France
James Robert Buchanan, USA
Humberto Bustince, Spain
Xiao Chuan Cai, USA
Piermarco Cannarsa, Italy
Jinde Cao, China
Yijia Cao, China
Zhenfu Cao, China
B. Carpentieri, The Netherlands
Ana Carpio, Spain
Alexandre Carvalho, Brazil
Song Cen, China
Tai-Ping Chang, Taiwan
Shih-sen Chang, China
Wei-Der Chang, Taiwan
Shuenn-Yih Chang, Taiwan
Kripasindhu Chaudhuri, India
Ru-Dong Chen, China
Zhang Chen, China
Zhi-Zhong Chen, Japan
Jianbing Chen, China
Yuming Chen, Canada
Xinkai Chen, Japan
Rushan Chen, China
Ke Chen, UK
Eric Cheng, Hong Kong
Ching-Hsue Cheng, Taiwan
Qi Cheng, USA
Jin Cheng, China
Chin-Hsiang Cheng, Taiwan
Hui Cheng, China
Francisco Chiclana, UK
Jen-Tzung Chien, Taiwan
Chongdu Cho, Korea
Han H. Choi, Republic of Korea
Md S. H. Chowdhury, Malaysia
Yu-Ming Chu, China
Hung-Yuan Chung, Taiwan
Angelo Ciaramella, Italy
Pedro J. Coelho, Portugal
Carlos Conca, Chile
Vitor Costa, Portugal
Lirong Cui, China
Jie Cui, USA
Livija Cveticanin, Serbia
Hua Dai, China
Gaoliang Dai, Germany
Binxiang Dai, China
Michael Defoort, France
Hilmi Demiray, Turkey
Ming-Cong Deng, Japan
Youjun Deng, France
Orazio Descalzi, Chile
Raffaele Di Gregorio, Italy
Kai Diethelm, Germany
Daniele Dini, UK
Urmila Diwekar, USA
Vit Dolejsi, Czech Republic
BoQing Dong, China
Rodrigo W. dos Santos, Brazil
Wenbin Dou, China
Rafael Escarela-Perez, Mexico
Magdy A. Ezzat, Egypt
Meng Fan, China
Ya Ping Fang, China
István Faragó, Hungary
Didier Felbacq, France
Ricardo Femat, Mexico
Antonio J. M. Ferreira, Portugal
George Fikioris, Greece
Michel Fliess, France
Marco A. Fontelos, Spain
Dimitris Fotakis, Serbia
Tomonari Furukawa, USA
Maria Gandarias, Spain
Naiping Gao, China
Xiao-wei Gao, China
Huijun Gao, China
Xin-Lin Gao, USA
Laura Gardini, Italy
Winston Garira, South Africa
Leonidas N. Gergidis, Greece
Bernard J. Geurts, The Netherlands
Sandip Ghosal, USA
Dibakar Ghosh, India
Pablo Gonzlez-Vera, Spain
Alexander N. Gorban, UK
Keshlan S. Govinder, South Africa
Said R. Grace, Egypt
Jose L. Gracia, Spain
Maurizio Grasselli, Italy
Zhi-Hong Guan, China
Nicola Guglielmi, Italy
Frédéric Guichard, Canada
Kerim Guney, Turkey
Shu-Xiang Guo, China
Vijay Gupta, India
Saman K. Halgamuge, Australia
Ridha Hambli, France

Abdelmagid S. Hamouda, Qatar
Bo Han, China
Maoan Han, China
Pierre Hansen, Canada
Ferenc Hartung, Hungary
Xiao-Qiao He, China
Yuqing He, China
Nicolae Herisanu, Romania
O. Hernandez-Lerma, Mexico
Luis J. Herrera, Spain
J. Hoenderkamp, The Netherlands
Thomas Höhne, Germany
Wei-Chiang Hong, Taiwan
Sun-Yuan Hsieh, Taiwan
Ning Hu, Japan
Ying Hu, France
Zhilong L. Huang, China
Jianguo Huang, China
Dan Huang, China
Ting-Zhu Huang, China
Zhenkun Huang, China
Asier Ibeas, Spain
Mustafa Inc, Turkey
Gerardo Iovane, Italy
Anuar Ishak, Malaysia
Takeshi Iwamoto, Japan
George Jaiani, Georgia
GunHee Jang, Korea
Zhongxiao Jia, China
Daqing Jiang, China
Haijun Jiang, China
Jianjun Jiao, China
Xing Jin, China
Zhen Jin, China
Lucas Jódar, Spain
Zlatko Jovanoski, Australia
Tadeusz Kaczorek, Poland
Dongsheng Kang, China
Sangmo Kang, USA
Ido Kanter, Israel
Abdul Hamid Kara, South Africa
Dimitrios A. Karras, Greece
Ihsan Kaya, Turkey
Dogan Kaya, Turkey
C. M. Khalique, South Africa
Waqar A. Khan, Pakistan
Khalil Khanafer, USA
Adem Kılıçman, Malaysia
Hyunsung Kim, Korea
Younjea Kim, Republic of Korea
Jong Hae Kim, Republic of Korea
Svein Kleiven, Sweden
Kazutake Komori, Japan
Vassilis Kostopoulos, Greece
Jisheng Kou, China
Roberto A. Kraenkel, Brazil
Kannan Krithivasan, India
Vadim . Krysko, Russia
Jin L. Kuang, Singapore
Gennady M. Kulikov, Russia
Venugopal Kumaran, India
Miroslaw Lachowicz, Poland
Hak-Keung Lam, UK
Tak-Wah Lam, Hong Kong
Heung-Fai Lam, Hong Kong
Luciano Lamberti, Italy
Peter G L Leach, Cyprus
Jaehong Lee, Republic of Korea
Myung-Gyu Lee, Korea
Wen-Chuan Lee, Taiwan
Usik Lee, Republic of Korea
Jinsong Leng, China
Xiang Li, China
Qingdu Li, China
Yongkun Li, China
Wan-Tong Li, China
Wenlong Li, Hong Kong
Shuai Li, Hong Kong
Shiyong Li, China
Hua Li, Singapore
Lixiang Li, China
Qin Li, China
Yan Liang, China
Jin Liang, China
Dongfang Liang, UK
Ching-Jong Liao, Taiwan
Teh-Lu Liao, Taiwan
Yiping Lin, China
Gao Lin, China
Yong-Cheng Lin, China
Chong Lin, China
Ignacio Lira, Chile
Peide Liu, China
Meiqin Liu, China
Sheng Liu, Australia
Pengfei Liu, China
Zhengrong Liu, China
Zhuangjian Liu, Singapore
Yansheng Liu, China
Zhijun Liu, China
Kang Liu, USA
Chein-Shan Liu, Taiwan
Peter Liu, Taiwan
Tao Liu, China
Weiqing Liu, China
Shutian Liu, China
Fei Liu, China
Chongxin Liu, China
Jose L. Lpez, Spain
Shiping Lu, China
Hongbing Lu, China
Benzhuo Lu, China
Henry Horng-Shing Lu, Taiwan
Yuan Lu, China
Hao Lu, USA
Gilles Lubineau, Saudi Arabia
Zhen Luo, China
Shuping Ma, China
Changfeng Ma, China
Ruyun Ma, China
Li Ma, China
Lifeng Ma, China
Krzysztof Magnucki, Poland
Nazim I. Mahmudov, Turkey
Oluwole Daniel Makinde, South Africa
Flavio Manenti, Italy
Francisco J. Marcellán, Spain
Vasile Marinca, Romania
Giuseppe Marino, Italy
Guiomar Martín-Herrán, Spain
Carlos Martín-Vide, Spain
Alessandro Marzani, Italy
Nikos E. Mastorakis, Bulgaria
Nicola Mastronardi, Italy
P. Takis Mathiopouloss, Greece
Gianluca Mazzini, Italy
Michael McAleer, The Netherlands
Stephane Metens, France
Michael Meylan, Australia
Efrén Mezura-Montes, Mexico
Fan Min, China
Alain Miranville, France
Ram N. Mohapatra, USA
Syed Abdul Mohiuddine, Saudi Arabia

Gisele Mophou, France
José Morais, Portugal
Cristinel Mortici, Romania
Emmanuel Moulay, France
Jaime E. Munoz Rivera, Brazil
Javier Murillo, Spain
Roberto Natalini, Italy
Srinivasan Natesan, India
Tatsushi Nishi, Japan
Mustapha Nourelfath, Canada
Andreas Öchsner, Australia
Wlodzimierz Ogryczak, Poland
Roger Ohayon, France
Javier Oliver, Spain
Soontorn Oraintara, USA
Donal O'Regan, Ireland
Martin Ostoja-Starzewski, USA
Turgut Öziş, Turkey
Claudio Padra, Argentina
Vincent Pagneux, France
Reinaldo Martinez Palhares, Brazil
Quanke Pan, China
Endre Pap, Serbia
Sehie Park, Korea
Manuel Pastor, Spain
Giuseppe Pellicane, South Africa
Francesco Pellicano, Italy
Juan Manuel Peña, Spain
Jian-Wen Peng, China
Ricardo Perera, Spain
Malgorzata Peszynska, USA
Allan C. Peterson, USA
Andrew Pickering, Spain
Somyot Plubtieng, Thailand
Hector Pomares, Spain
Roland Potthast, UK
Kerehalli V. Prasad, India
Radu-Emil Precup, Romania
Mario Primicerio, Italy
Morteza Rafei, The Netherlands
P. Rattanadecho, Thailand
Laura Rebollo-Neira, UK
Mahmoud M. Reda Taha, USA
Roberto Renò, Italy
Bruno G. M. Robert, France
J. Rodriguez-Velázquez, Spain
Ignacio Rojas, Spain
Carla Roque, Portugal
Debasish Roy, India
Imre J. Rudas, Hungary
Abbas Saadatmandi, Iran
Kunihiko Sadakane, Japan
Samir Saker, Egypt
R. Sakthivel, Republic of Korea
Juan José Salazar González, Spain
Miguel A. F. Sanjuan, Spain
Bogdan Sasu, Romania
Richard Saurel, France
Wolfgang Schmidt, Germany
Mehmet Sezer, Turkey
Naseer Shahzad, Saudi Arabia
Pengjian Shang, China
M. Shariyat, Iran
Hui-Shen Shen, China
Jian Hua Shen, China
Yong Shi, China
Yasuhide Shindo, Japan
Patrick Siarry, France
Fernando Simes, Portugal
Theodore E. Simos, Greece
Georgios Sirakoulis, Greece
Robert J. Smith?, Canada
Francesco Soldovieri, Italy
Abdel-Maksoud Soliman, Egypt
Qiankun Song, China
Xinyu Song, China
Yuri N. Sotskov, Belarus
Ivanka Stamova, USA
Niclas Strömberg, Sweden
Ray K.L. Su, Hong Kong
Housheng Su, China
Jitao Sun, China
Wenyu Sun, China
Chengjun Sun, Hong Kong
Wai Yuen Szeto, Hong Kong
Toshio Tagawa, Japan
Ying Tan, China
San-Yi Tang, China
XianHua Tang, China
Nasser-Eddine Tatar, Saudi Arabia
Zhidong Teng, China
Engang Tian, China
Alexander Timokha, Norway
Aydin Tiryaki, Turkey
Yiying Tong, USA
Hossein Torkaman, Iran
Mariano Torrisi, Italy
Juan J. Trujillo, Spain
Jung-Fa Tsai, Taiwan
George Tsiatas, Greece
Charalampos Tsitouras, Greece
Antonia Tulino, USA
Stefano Ubertini, Italy
Jeong S. Ume, Korea
Alexandrina Untaroiu, USA
Sergey Utyuzhnikov, UK
Kuppalapalle Vajravelu, USA
Alvaro Valencia, Chile
Olaf van der Sluis, The Netherlands
Erik Van Vleck, USA
Ezio Venturino, Italy
Jesus Vigo-Aguiar, Spain
Michael N. Vrahatis, Greece
Michael Vynnycky, Sweden
Youqing Wang, China
Dongqing Wang, China
Yuh-Rau Wang, Taiwan
Peiguang Wang, China
Shuming Wang, Singapore
Xiang Wang, China
Yaonan Wang, China
Heng Wang, Singapore
Baolin Wang, China
Mingxin Wang, China
Qing-Wen Wang, China
Guangchen Wang, China
Junzo Watada, Japan
Jinjia Wei, China
Wei Wei, China
Guoliang Wei, China
Junjie Wei, China
Li Weili, China
Martin Weiser, Germany
Frank Werner, Germany
Man Leung Wong, Hong Kong
Min-Hsien Wu, Taiwan
Wei Wu, China
Yuqiang Wu, China
Xiangjun Wu, China
Qingbiao Wu, China
Xian Wu, China
Shi-Liang Wu, China
Cheng Wu, China
Shanhe Wu, China

Yonghui Xia, China
Tiecheng Xia, China
Xian Xian-Yong, China
Xuejun Xie, China
Gongnan Xie, China
Daoyi Xu, China
Zhiqiang Xu, China
Yuesheng Xu, USA
Wei Xu, China
Fuzhen Xuan, China
Gregory S. Yablonsky, USA
Chao Yan, USA
Chao Yang, China
Suh-Yuh Yang, Taiwan
Chao-Tung Yang, Taiwan
Bin Yang, China
Guowei Yang, China
Na Yang, China
Zhichun Yang, China
Chunyu Yang, China
Dar-Li Yang, Taiwan
Xiao-Jun Yang, China
Her-Terng Yau, Taiwan
Wei-Chang Yeh, Taiwan
Guan H. Yeoh, Australia
Chih-Wei Yi, Taiwan
Simin Yu, China
Bo Yu, China
Xiaohui Yuan, China
Jinyun Yuan, Brazil
Gonglin Yuan, China
Rafal Zdunek, Poland
Ashraf Zenkour, Egypt
Guisheng Zhai, Japan
Jianming Zhan, China
Meng Zhan, China
Ke Zhang, China
Zhengqiu Zhang, China
Sheng Zhang, China
Heping Zhang, China
Jifeng Zhang, China
Long Zhang, China
Liang Zhang, China
Jiangang Zhang, China
Henggui Zhang, UK
Zhihua Zhang, China
Jingxin Zhang, Australia
Shan Zhao, USA
Chongbin Zhao, Australia
Yun-Bo Zhao, UK
Baosheng Zhao, China
Renat Zhdanov, USA
Dong Zheng, USA
Huaichun Zhou, China
Shangbo Zhou, China
Huamin Zhou, China
Bin Zhou, China
Xinqun Zhu, Australia
William Zhu, China
Quanxin Zhu, China
Goangseup Zi, Korea
Zhiqiang Zuo, China

Contents

Hindawi Publishing Corporation
Journal of Applied Mathematics
Volume 2014, Article ID 470483, 2 pages
http://dx.doi.org/10.1155/2014/470483

Editorial

Applied Mathematics in Biomedical Sciences and Engineering 2014

Chang-Hwan Im,[1] Kiwoon Kwon,[2] Hang Joon Jo,[3] and Pedro Serranho[4]

[1]*Department of Biomedical Engineering, Hanyang University, 222 Wangsimni-ro, Seongdong-gu, Seoul 133-791, Republic of Korea*
[2]*Department of Mathematics, Dongguk University, Seoul 100-715, Republic of Korea*
[3]*National Institute of Mental Health, National Institutes of Health (NIH), Bethesda, MD 20892, USA*
[4]*Department of Sciences and Technology, Universidade Aberta, 1269-001 Lisboa, Portugal*

Correspondence should be addressed to Chang-Hwan Im; ich@hanyang.ac.kr

Received 9 November 2014; Accepted 9 November 2014; Published 24 December 2014

Copyright © 2014 Chang-Hwan Im et al. This is an open access article distributed under the Creative Commons Attribution License, which permits unrestricted use, distribution, and reproduction in any medium, provided the original work is properly cited.

The interdisciplinary approach is becoming an increasing need in scientific and industrial communities. The most evident example of such a need is the strong interconnection between applied mathematics and biomedical sciences/engineering. Indeed, biomedical sciences and engineering have become one of the most important application areas of applied mathematics.

This annual issue includes seven high-quality, peer-reviewed articles that might provide researchers in the field of applied mathematics with the current state-of-the-art knowledge of this emerging interdisciplinary research field. With this annual issue, we hope to stimulate the continuing efforts to solve real-world biomedical problems with advanced theories and technologies of applied mathematics.

The paper "*Continuous nondestructive monitoring method using the reconstructed three-dimensional conductivity images via GREIT for tissue engineering*" by S. Ahn et al. presents a data collection strategy for microscale electrical impedance tomography (EIT). The authors modified Graz consensus reconstruction (GREIT) algorithm that has advantages to be applied to the microscale EIT structure and applied it to the micro-EIT cuboid container with the specific current driving method.

The paper "*Neuronal ensemble decoding using a dynamical maximum entropy model*" by D. Sin et al. proposes a new decoder for extracting the dynamical neuronal information, which is based on the conventional maximum entropy decoding that can consider correlations between neurons and firing rates of individual neurons. Two simulation studies well demonstrate that the proposed dynamic maximum entropy decoder is capable of capturing the time-varying feature of neuronal ensemble activity.

The paper "*Modeling TB-HIV syndemic and treatment*" by C. J. Silva and D. F. M. Torres describes the formulation of a model for tuberculosis and HIV transmission dynamics, considering individuals that pass from HIV to AIDS and giving simulations for the evolution of infection, considering treatments of both or each of the diseases separately.

The paper "*Regularization of DT-MRI using 3D median filtering methods*" by S. Kwon et al. proposes a new regularization strategy for diffusion tensor magnetic resonance imaging (DT-MRI) tractography. The authors extended two-dimensional median filters to three-dimensional medial filters and compared their performances with real human MRI data.

The paper "*A constitutive model for the annulus of human intervertebral disc: implications for developing a degeneration model and its influence on lumbar spine functioning*" by J. Cegonino et al. proposes a mathematical model for the annulus of human intervertebral disc containing porous matrix, water, proteoglycan, and collagen fibres network. Finite element analysis, numerical characterization, and the validation based on experimental results were carried out for the proposed model.

The paper "*Removal of muscle artifacts from single-channel EEG based on ensemble empirical mode decomposition and multiset canonical correlation analysis*" by X. Chen et al. proposes an effective method to remove muscle artifacts contaminating EEG signals based on ensemble empirical mode decomposition (EEMD) and multiset canonical correlation analysis (MCCA). The performance of the proposed method was validated using numerical simulations and real EEG data analyses.

The paper "*Enhanced template matching using dynamic positional warping for identification of specific patterns in electroencephalogram*" by W.-D. Chang and C.-H. Im treats an improved template matching approach for signal pattern recognition for EEG. In the approach, they adopted dynamic positional warping technique developed recently for handwriting pattern analysis.

Acknowledgments

We would like to express our deepest gratitude to many reviewers, whose professional comments guaranteed the high quality of the selected papers. In addition, we would also like to express our appreciation to editorial board members for their help and support throughout the preparation of this special issue.

Chang-Hwan Im
Kiwoon Kwon
Hang Joon Jo
Pedro Serranho

Hindawi Publishing Corporation
Journal of Applied Mathematics
Volume 2014, Article ID 562176, 11 pages
http://dx.doi.org/10.1155/2014/562176

Research Article

Continuous Nondestructive Monitoring Method Using the Reconstructed Three-Dimensional Conductivity Images via GREIT for Tissue Engineering

Sujin Ahn,[1] Hun Wi,[2] Tong In Oh,[2] Alistair Lee McEwan,[2,3] Sung Chan Jun,[1] and Eung Je Woo[2]

[1] *School of Information & Communications, Gwangju Institute of Science and Technology, Gwangju 500-712, Republic of Korea*
[2] *Impedance Imaging Research Center and Department of Biomedical Engineering, Kyung Hee University, Yongin 446-701, Republic of Korea*
[3] *School of Electrical and Information Engineering, The University of Sydney, Sydney, NSW 2006, Australia*

Correspondence should be addressed to Tong In Oh; tioh@khu.ac.kr

Received 27 February 2014; Accepted 19 June 2014; Published 26 August 2014

Academic Editor: Hang Joon Jo

Copyright © 2014 Sujin Ahn et al. This is an open access article distributed under the Creative Commons Attribution License, which permits unrestricted use, distribution, and reproduction in any medium, provided the original work is properly cited.

A continuous Nondestructive monitoring method is required to apply proper feedback controls during tissue regeneration. Conductivity is one of valuable information to assess the physiological function and structural formation of regenerated tissues or cultured cells. However, conductivity imaging methods suffered from inherited ill-posed characteristics in image reconstruction, unknown boundary geometry, uncertainty in electrode position, and systematic artifacts. In order to overcome the limitation of microscopic electrical impedance tomography (micro-EIT), we applied a 3D-specific container with a fixed boundary geometry and electrode configuration to maximize the performance of Graz consensus reconstruction algorithm for EIT (GREIT). The separation of driving and sensing electrodes allows us to simplify the hardware complexity and obtain higher measurement accuracy from a large number of small sensing electrodes. We investigated the applicability of the GREIT to 3D micro-EIT images via numerical simulations and large-scale phantom experiments. We could reconstruct multiple objects regardless of the location. The resolution was 5 mm^3 with 30 dB SNR and the position error was less than 2.54 mm. This shows that the new micro-EIT system integrated with GREIT is robust with the intended resolution. With further refinement and scaling down to a microscale container, it may be a continuous nondestructive monitoring tool for tissue engineering applications.

1. Introduction

There are many reports that nerve or tissue regeneration is a successful treatment modality in skin, muscle, nerve, and periodontal reconstruction [1–5]. In order to implant a regenerated tissue, there must be a systematic and stable method to cultivate. For efficient cytothesis, they extract potentially autologous regenerative cells and expand cells *in vitro* before replacing degenerated tissue. However, current monitoring methods such as histological analysis and quantification of various components using a microscope and chemical dye are invasive and the examined tissue sample may be not reused for implanting. Considering the shortage of donor tissues, it requires the real-time, continuous nondestructive monitoring methods for proper feedback controls inside a bioreactor to enhance the quality of the final implant. When we consider the monitoring of three-dimensional (3D) tissue growth inside a 3D scaffold for bone or tissue formation, conventional molecular imaging methods using optical fluorescent and bioluminescent markers are difficult to represent the functionality deep inside regenerative tissues [6]. The micro-CT provides high-throughput images with high spatial resolution to describe the appearance of bone regeneration and structural changes; however, it has limitations of continuous monitoring and functional imaging of regenerative tissues [7, 8]. Simultaneous PET-MRI is a new

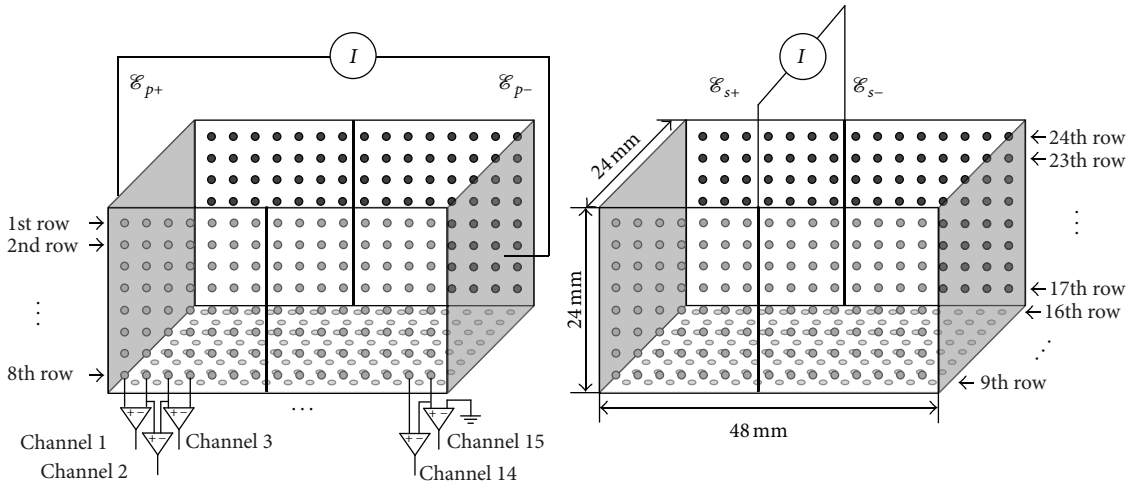

FIGURE 1: The structure of sample container and the method used for the primary ($\mathscr{E}_{p\pm}$) and secondary injection currents ($\mathscr{E}_{s\pm}$).

approach with synergizing for functional and morphological imaging [9]. However, it is too expensive and cannot be installed inside the bioreactor.

Bioelectromagnetic phenomena are fairly correlated with physiological functions and structural formation of cells and tissues directly. Therefore, the distribution of electric field generated by induced currents inside biological tissue can be used for monitoring tissue growth and its functions noninvasively [10, 11]. We would like to develop the continuous monitoring method to find the functionality of the ingrowth neotissue in the scaffold using bioelectric properties. Electrical impedance tomography (EIT) can produce cross-sectional images of conductivity and permittivity distributions inside a tissue using pairs of injection currents and induced boundary voltages [12]. There have been several attempts to develop EIT systems on the microscopic scale (micro-EIT systems) with high spatial resolution using conventional EIT approaches [13–17]. They inherited some technical difficulties, suffering from the ill-posed problem with limited electrode measurements, and were affected by unknown boundary geometry, uncertainty in electrode position, and systematic artifacts, even though EIT is uniquely able to show conductivity time variations with high temporal resolution, nondestructive, label-free, and multidimensional in space, time, and frequency.

To solve the difficulties in developing micro-EIT, Lee et al. [18] and Liu et al. [19] suggested a mathematical framework and system for a new micro-EIT method with a rectangular cuboid container that included two pairs of current injection electrodes and numerous voltage sensing electrodes, as shown in Figure 1. They applied a projected image reconstruction algorithm to produce conductivity images from the front, bottom, and back sides; they were combined to make a 3D conductivity image using a back-projection algorithm. Although this method showed better resolution than that found from the conventional micro-EIT methods, it required an automatic estimation of the position and volume of a regenerated tissue and a fast detection for physiological changes. In this study, we used the Graz consensus reconstruction algorithm for EIT (GREIT) to reconstruct the 3D conductivity images representing the tissue status or morphological changes [20]. Since a specific container has a fixed boundary geometry and electrode configurations, electrode movement or the deformation of the boundary shape does not need to be considered. The modified GREIT algorithm based on the concept of the equivalent homogeneous complex conductivity may be able to provide real-time 3D reconstructed images without significant artifacts [21, 22]. This can be achieved through a matrix-vector multiplication after precomputation of the reconstruction matrix **R**. We investigated the applicability of the GREIT to 3D micro-EIT images via numerical simulations and large-scale phantom experiments using five figures of merit.

2. Methods

2.1. The Mathematical Framework. We chose the rectangular cuboid container of Ω to maximize the performance of GREIT. Two pairs of driving electrodes $\mathscr{E}_{p\pm}$ and $\mathscr{E}_{s\pm}$ are assigned to the primary and secondary current injections, respectively. Each pair of electrodes takes turns in injecting current. After applying a low-frequency current of amplitude I, the electrical potential, u_j $(j = p, s)$, satisfies the following:

$$\begin{gathered}
\nabla \cdot \left(\sigma \nabla u_j\right) = 0 \quad \text{in } \Omega \\
\int_{\mathscr{E}_{j\pm}} \sigma \frac{\partial u_j}{\partial \mathbf{n}} = \pm I, \quad \int_{\mathscr{E}_{k\pm}} \sigma \frac{\partial u_j}{\partial \mathbf{n}} = 0 \quad \text{for } k \neq j \ (k = p, s) \\
\mathbf{n} \times \nabla u_j = 0 \quad \text{on } \mathscr{E}_{p\pm} \bigcup \mathscr{E}_{s\pm} \\
\sigma \frac{\partial u_j}{\partial \mathbf{n}} = 0 \quad \text{on } \partial\Omega \setminus \left(\mathscr{E}_{p\pm} \bigcup \mathscr{E}_{s\pm}\right),
\end{gathered} \tag{1}$$

where σ is the conductivity and $\mathbf{n}$ is the outer unit normal vector on the boundary [18]. The container is designed for separated current driving electrodes from voltage sensing

electrodes, which means that the contact impedance of the sensing electrodes can be ignored. Since we adopt the tetrapolar measurement, we exclude the electrode properties and reduce the channel dependent characteristics. One therefore can use the simple electrode model instead of the complete electrode model to minimize the error induced by inappropriate modeling and differences between channels. The separation of the driving and sensing electrodes allows us to simplify the hardware complexity and obtain higher measurement accuracy from a large number of small electrodes. In addition, only two driving patterns are created, which makes for simple boundary conditions.

2.2. Image Reconstruction Algorithm. We adopted the GREIT in order to reconstruct the conductivity distribution [20]. This linear reconstruction algorithm was developed to overcome several issues regarding the reconstructed EIT images, which cause a poor spatial resolution: amplitude, position error, shape deformation, and ringing effect. Adler et al. [20] applied the GREIT to two-dimensional (2D) EIT of the lungs employing a single-ring electrode configuration using adjacent current injection and measurement. In their study, the 2D conductivity change could be obtained by the GREIT based on a 3D forward model. For the micro-EIT system, we use the "3D desired volume" instead of the 2D desired image to recover the 3D volume of conductivity change.

The linear EIT image reconstruction can be represented by computing the reconstruction matrix $\mathbf{R}$, which corresponds to measurement $\mathbf{y}$ in order to produce the reconstructed image $\widehat{\mathbf{x}}$, as follows:

$$\widehat{\mathbf{x}} = \mathbf{R}\mathbf{y}. \tag{2}$$

The GREIT procedure depends on the forward model, a noise model, and the desired performance metrics. When a kth anomaly is positioned in the domain, we can compute the EIT measurement data $\mathbf{y}^{(k)}$ from the change in the conductivity distribution $\mathbf{x}_t^{(k)} = \sigma^{(k)} - \sigma_r^{(k)}$, where σ, σ_r are the present and reference conductivity distributions, respectively. For a given anomaly position, a reconstructed object in the desired image, $\widetilde{\mathbf{x}}_t^{(k)}$, is located at the same center of the conductivity target in the model. However, its shape would be circular because of the blurring effect inherent in EIT. To tune the relative importance of the performance metrics, image weighting factor, $\mathbf{w}^{(k)}$, is used for each pixel in $\widetilde{\mathbf{x}}_t^{(k)}$. When the transition zone is defined as the pixels in which the conductivity change gradually converges to zero, the weighting $\mathbf{w}^{(k)}$ allows us to have a small error outside the transition zone and a large one inside. The reconstruction matrix $\mathbf{R}$ can be obtained by minimizing the total weighted sum of residual errors ϵ^2; one has

$$\epsilon^2 = \sum_k \left\| \widetilde{\mathbf{x}}^{(k)} - \mathbf{R}\mathbf{y}^{(k)} \right\|^2_{\mathbf{W}^{(k)}}, \tag{3}$$

where $\mathbf{W}^{(k)} = \left(\operatorname{diag} \mathbf{w}^{(k)}\right)^2$.

The existing GREIT algorithm was restricted to the cylinder model and mainly focused on the 2D imaging plane at the same level as the height of the single-ring electrodes. Therefore, a reconstruction matrix $\mathbf{R}$ was required for the imaging plane. If one would obtain another image at a different height from electrodes, the reconstruction matrix $\mathbf{R}$ needs to be recomputed, corresponding to the other imaging plane. Since we use the "3D desired volume" for the training data set in the micro-EIT system, we do not need to calculate $\mathbf{R}$ repeatedly; the $\mathbf{R}$ will allow us to obtain any volume inside the container or for several slice images at different positions. The EIT measurement data $\mathbf{y}^{(k)}$ is also calculated using the 3D forward model employing governing equation (1) when the change in conductivity $\mathbf{x}_t^{(k)} = \sigma^{(k)} - \sigma_r^{(k)}$ is given. Most of the noise is introduced from electronic noise, shape change, and electrode positioning error. However, we do not need to consider the shape of the imaging domain and electrode movement in the micro-EIT system due to the use of a container with fixed dimensions and shape. Therefore, the measurement data is only degraded by the electronic noise in the system. The 3D desired volume $\widetilde{\mathbf{z}}_t^{(k)}$ corresponding to $\mathbf{x}_t^{(k)}$ is created at the position with the same center as the center of gravity ($\mathbf{CoG}$) of $\mathbf{x}_t^{(k)}$. The shape of the volume is defined by the spherical volume due to the blurring effect inherent in EIT. We assume that the volume weighting factor, $\mathbf{w}^{(k)}$, is the same for each training data set in order to simplify the algorithm. Therefore, the reconstruction matrix $\mathbf{R}$ can be computed by minimizing $\left\| [\widetilde{\mathbf{Z}}_\mathbf{t} \mid \mathbf{0}] - \mathbf{R}[\mathbf{Y}_\mathbf{t} \mid \mathbf{Y}_\mathbf{n}] \right\|^2_\mathbf{W}$ as follows:

$$\mathbf{R} = \left[\widetilde{\mathbf{Z}}_\mathbf{t} \mid \mathbf{0}\right] \left[\mathbf{Y}_\mathbf{t} \mid \mathbf{Y}_\mathbf{n}\right]^\mathbf{T} \left(\left[\mathbf{Y}_\mathbf{t} \mid \mathbf{Y}_\mathbf{n}\right] \left[\mathbf{Y}_\mathbf{t} \mid \mathbf{Y}_\mathbf{n}\right]^\mathbf{T} \right)^{-1}, \tag{4}$$

where $[\cdot \mid \cdot]$ stands for the matrix concatenation, $\mathbf{Y_t} = (\mathbf{1/N})[\mathbf{y_t^{(1)}} \cdots \mathbf{y_t^{(N)}}]$, $\widetilde{\mathbf{Z}}_\mathbf{t} = (\mathbf{1/N})[\widetilde{\mathbf{z}}_\mathbf{t}^{(\mathbf{1})} \cdots \widetilde{\mathbf{z}}_\mathbf{t}^{(\mathbf{N})}]$, and $\mathbf{Y_n} = (\mathbf{1/N})[\mathbf{y_n^{(1)}} \cdots \mathbf{y_n^{(N)}}]$. The noise $\mathbf{y}_n^{(k)}$ is an estimate of the noise amplitude variance $\operatorname{var}(\mathbf{y}_n^{(k)}) = E[\|\mathbf{y}_n^{(k)}\|^2]$ with a mean of zero.

2.3. Performance Figures of Merit. In order to evaluate the performance of the reconstruction method and measurement configuration, we compute five figures of merit: amplitude response (**AR**), position error (**PE**), resolution (**RES**), shape deformation (**SD**), and ringing artifacts (**RNG**). They are described well in the reference paper [20]. Here, we summarized them with simple equations and the desired characteristics. $[\widehat{\mathbf{x}}_q]$ is defined by the voxels in which the absolute values of the conductivity change are bigger than one-fourth of the maximum change as follows:

$$\left[\widehat{\mathbf{x}}_q\right]_i = \begin{cases} 1, & \text{if } \left|[\widehat{\mathbf{x}}]_i\right| \geq \dfrac{1}{4} \cdot \max(\widehat{\mathbf{x}}) \\ 0, & \text{otherwise.} \end{cases} \tag{5}$$

(i) Amplitude response (**AR**): this parameter gives us a quantitative result related to the ratio of conductivity amplitude on pixels in the region of interest (ROI; $\widehat{\mathbf{x}}_k$) to the reference conductivity. Considering a spherical perturbation with conductivity of σ_t and volume of V_t

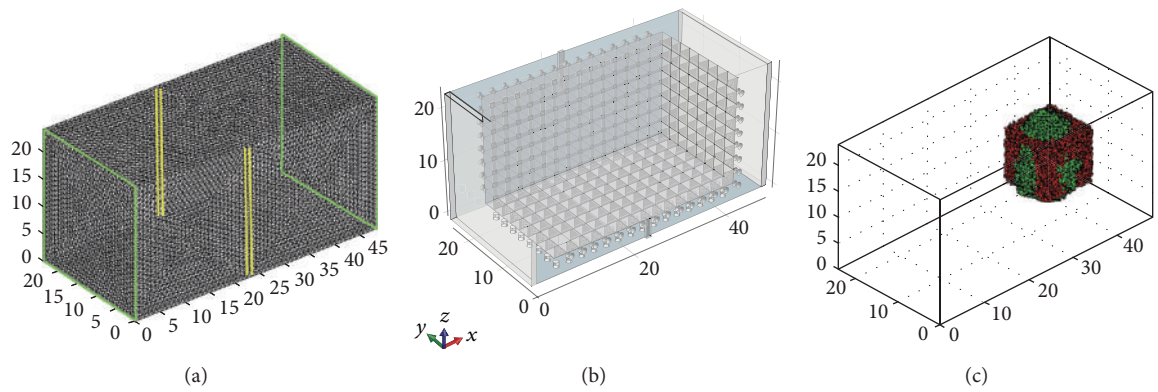

Figure 2: (a) Tetrahedral elements for numerical simulation within the domain, (b) grid voxels for image reconstruction, and (c) an example of simulation of sample target (red voxels) and reconstructed object (green voxels).

inside a homogenous medium with conductivity σ_r, the **AR** is

$$\mathbf{AR} = \frac{\sum_k [\hat{\mathbf{x}}]_k}{V_t \cdot ((\sigma_t - \sigma_r)/\sigma_r)}. \quad (6)$$

It should be uniform within the region of any homogenous target.

(ii) Position error (**PE**): this quantitative parameter represents the difference of **CoG** between the actual position of object, $\mathbf{r}_o$, and the estimated center position, $\mathbf{r}_q$, using pixels greater than one-fourth of the maximum amplitude, $[\hat{\mathbf{x}}_q]$. Consider

$$\mathbf{PE} = \left|\mathbf{r}_q - \mathbf{r}_o\right|. \quad (7)$$

Ideally, it should be zero. It provides accuracy regarding the positional information for a target object. The **PE** should be small and possess little variability within the 3D domain.

(iii) Resolution (**RES**): it means the relative volume of the reconstructed point target compared to the size of total medium which is equal to the value of the point spread function (PSF). Consider

$$\mathbf{RES} = \sqrt{\frac{V_q}{V_0}}, \quad (8)$$

where V_q is the volume of $\{[\hat{\mathbf{x}}_q]_k = 1\}$ and V_0 is the volume of the whole domain, Ω. It should be uniform and small.

(iv) Shape deformation (**SD**): when we consider the spherical object in the homogenous medium, we can define an index set **S** representing the indices of $[\hat{\mathbf{x}}_q]$ inside a sphere centered at the **CoG** of $[\hat{\mathbf{x}}_q]$ with the same volume as V_q. The **SD** measures the portion of $\{[\hat{\mathbf{x}}_q]_k \mid k \notin \mathbf{S}\}$ over the reconstructed target as follows:

$$\mathbf{SD} = \frac{\left(\sum_{k\notin\mathbf{S}} \left[\hat{\mathbf{x}}_q\right]_k\right)}{\left(\sum_k \left[\hat{\mathbf{x}}_q\right]_k\right)}. \quad (9)$$

(v) Ringing artifact (**RNG**): it measures the portion of voxels with the opposite sign of image amplitude which is called undershoot or overshoot surrounding the main reconstructed target. For an index set **OV** representing the voxels as follows:

$$\mathbf{RNG} = \frac{\left(\sum_{k\in\mathbf{OV}\&k\notin\mathbf{S}} \left[\hat{\mathbf{x}}_q\right]_k\right)}{\left(\sum_{k\in S} \left[\hat{\mathbf{x}}_q\right]_k\right)}. \quad (10)$$

3. Numerical Experiments

We constructed the large-scale computational model to be the same size as the container ($48 \times 24 \times 24\,\text{mm}^3$) for phantom experiments shown in Figure 1. The results for numerical simulation in a container of this size are the same as ones of microscopic container except of scaling effect, and phantom experiments are easily performed in that size. The whole domain was decomposed into 646,781 tetrahedral elements in Figure 2(a). We computed the boundary voltages and added white Gaussian noise at various levels from noise free to 15 dB signal-to-noise ratio (SNR). In order to obtain reconstructed images with a 1 mm spatial resolution, we defined the 27,648 (= $48 \times 24 \times 24$) grid voxels used for reconstruction as in Figure 2(b). When we considered the number of grid points with the spatial resolution of 0.7 mm for each direction, we could get 80,606 possible targets for training. 981 objects were removed because they were too close to injection electrodes or less sensitive to contribute to the reconstruction matrix **R**. We chose 79,625 training targets for the computation of matrix **R** in (4). There were a pair of electrodes fully covering the left and right sides of the container used for the primary current injection, a pair of thin vertical electrodes at the middle of the front and back sides for the secondary current injection, and 360 gold-coated voltage sensing electrodes with 1 mm diameter on the front, bottom, and back sides. A planar array of 8×15 electrodes was placed on each of the three sides. The voltage difference was measured between two horizontally adjacent electrodes for each current injection pattern; the last column of each row measured the voltage reference to the circuit ground [19]. There were 360 measured differential voltages

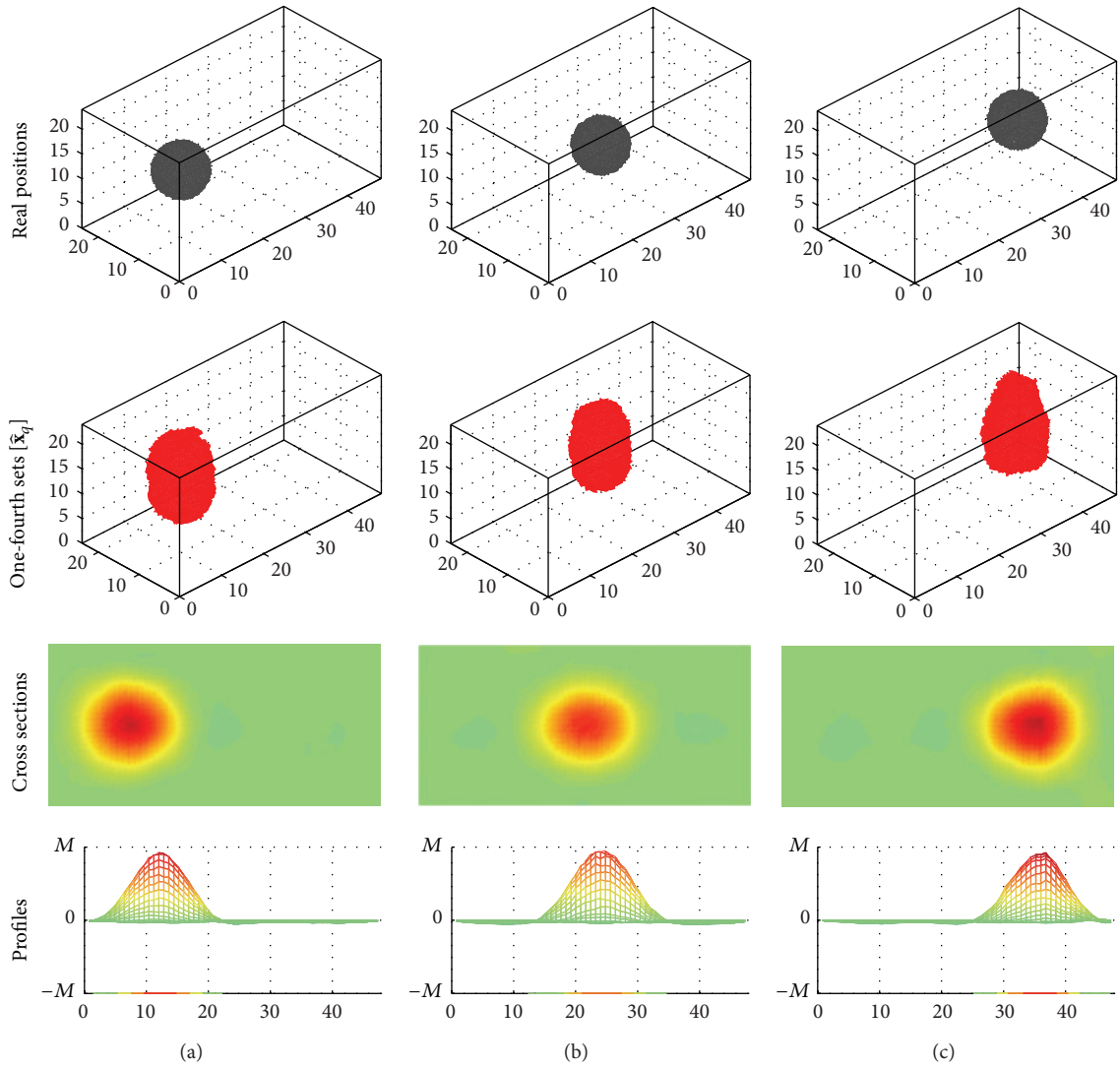

FIGURE 3: Single object placed at (a) (12, 12, 12), (b) (24, 12, 12), and (c) (36, 12, 12), respectively, with noise of 40 dB.

along the horizontal direction for each injection current. We generated the vertically measured voltage data using the last measurement channel in each row. The total number of measured voltages was 1,410 including 690 additional vertical measurements. Figure 2(c) shows an example of target object (red voxels) and reconstructed object (green voxels). For the numerical experiments, we considered the following cases: (1) a single object at different positions, (2) two objects to the left and right, and (3) multiple objects.

3.1. Case 1: Single Object. A single object was located at (12, 12, 12) (left), (24, 12, 12) (center), and (36, 12, 12) (right) (unit: mm) in the container, as shown in Figure 3. The conductivity of the object was ten times greater than that of the background. Figure 3 shows the real position of each object, the reconstructed volume above one-fourth amplitude ([$\hat{\mathbf{x}}_q$]), and the cross-sectional images at the height passing through the object. Here, we defined the reconstructed volume as where the absolute values of the conductivity change were greater than one-fourth of the maximum change. The center of the reconstructed anomaly ranged within 1 to 2 mm from the original center. The shape of the one-fourth amplitude set was ellipsoid with a longer radius along the z-axis. Since the primary and secondary currents were parallel to the x- and y-axes, information along the z-axis was lacking. Therefore, the shapes along the x- and y-directions were relatively exact; however, the shape along the z-direction was blurred.

We computed five figures of merit explained in Section 2.3 to evaluate the performance of the algorithm and measurement configuration. We moved a single 5 mm radius object from 6 to 42 mm with 3 mm intervals along the x-axis. Lee et al. [18] and Liu et al. [19] used horizontally measured boundary voltages (H-data) in their studies. However, we found that the method using H-data only did not yield an image with high quality when using the GREIT. We thus decided to use vertically measured boundary voltage data (V-data) as well as H-data since V-data was independent on H-data. The strategy using both H-data and V-data can

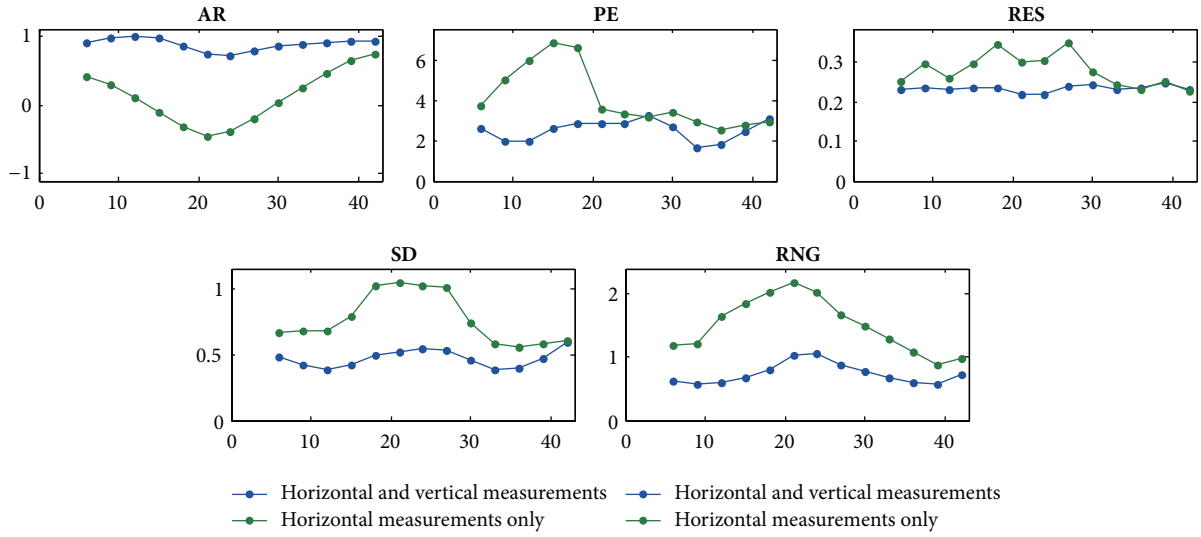

Figure 4: Five figures of merit (**AR**, **PE**, **RES**, **SD**, and **RNG**) for the results in the numerical experiment with SNR of 40 dB.

increase the rank of the reconstruction matrix **R**; therefore, the solution of matrix inversion was closer to the desired one. This method was compared with one using only H-data. When the additional V-data was used, we obtained a flatter **AR**, a smaller **PE** with slight variations, and a more uniform and smaller **RES**, **SD**, and **RNG** in Figure 4. We examined these figures of merit for SNR of 60 dB to 15 dB and found a significant deviation began to appear **PE**, **RES**, and **SD** when the SNR degraded to 30 dB. Further, with the SNR set at 40 dB we simulated the case where there was a 1% mismatch between the 360 channels and found that all figures of merit did not deviate more than 2.5%.

3.2. Case 2: Two Objects. Two objects that had ten times higher conductivity than the background conductivity and the same 5 mm radius were simultaneously located on the left and the right, as shown in Figure 5(a). The radius of the right object was altered to 3.75 and 2.5 mm in order to observe the distinguishability of two objects of different sizes in Figures 5(b)-5(c). We also assigned two different conductivity values to two objects having the same size: one was ten times greater than the background conductivity; the other was ten times less than the background conductivity, as shown in Figure 5(d).

As the right object became smaller, the amplitude of the reconstructed image also decreased. In the case of the smallest object of 2.5 mm radius, the reconstructed amplitude of the right object was so small that it was beneath the similar level of undershoot of large left object. However, we can make a distinction of small object in the profile. The GREIT reconstructed the two objects even for the case when the two objects had opposite conductivity values. Overall, the GREIT was able to distinguish two separated objects and reconstruct them, but it had difficulties in reconstructing an object with a 2.5 mm radius, which was roughly 1/20 of the largest edge length of the container.

3.3. Case 3: Multiple Objects. We used the modified Shepp-Logan model to implement more than eight objects. All of the objects had the same conductivity, which was ten times higher than the background conductivity. Figure 6 shows that the different sized multiple objects were reasonably reconstructed by the GREIT. However, it was not possible to reconstruct three small objects with diameters less than 5 mm, and this was a similar result found in Figure 5(c). According to the profile along line (b) in Figure 6 for the middle cross section of the container, three small objects were detected; however, their amplitudes were as lower than the undershoot threshold level. They were not visible directly in the images due to high amplitude contrast of the larger objects.

4. Phantom Experiments

We used a container with the same size as that laid out in the numerical experiments. The container was filled with saline having 0.2 S/m conductivity. We tested the new method in two different configurations.

(i) A biological object of 0.02 S/m size $10 \times 10 \times 10\,\text{mm}^3$ was placed at (12, 12, 12) (left), (24, 12, 12) (center), and (36, 12, 12) (right), respectively (unit: mm), as shown in Figure 7.

(ii) One biological object was positioned on the left side and another biological object was simultaneously placed on the right side. The object on the left side was $6 \times 6 \times 6\,\text{mm}^3$ and the object on the right was $10 \times 10 \times 10\,\text{mm}^3$, as shown in Figure 8.

We measured the voltages from the container without any object in it subjected to the primary and secondary current, separately, as a baseline. We compared the measurements of voltage data to the simulated data with different gains in each

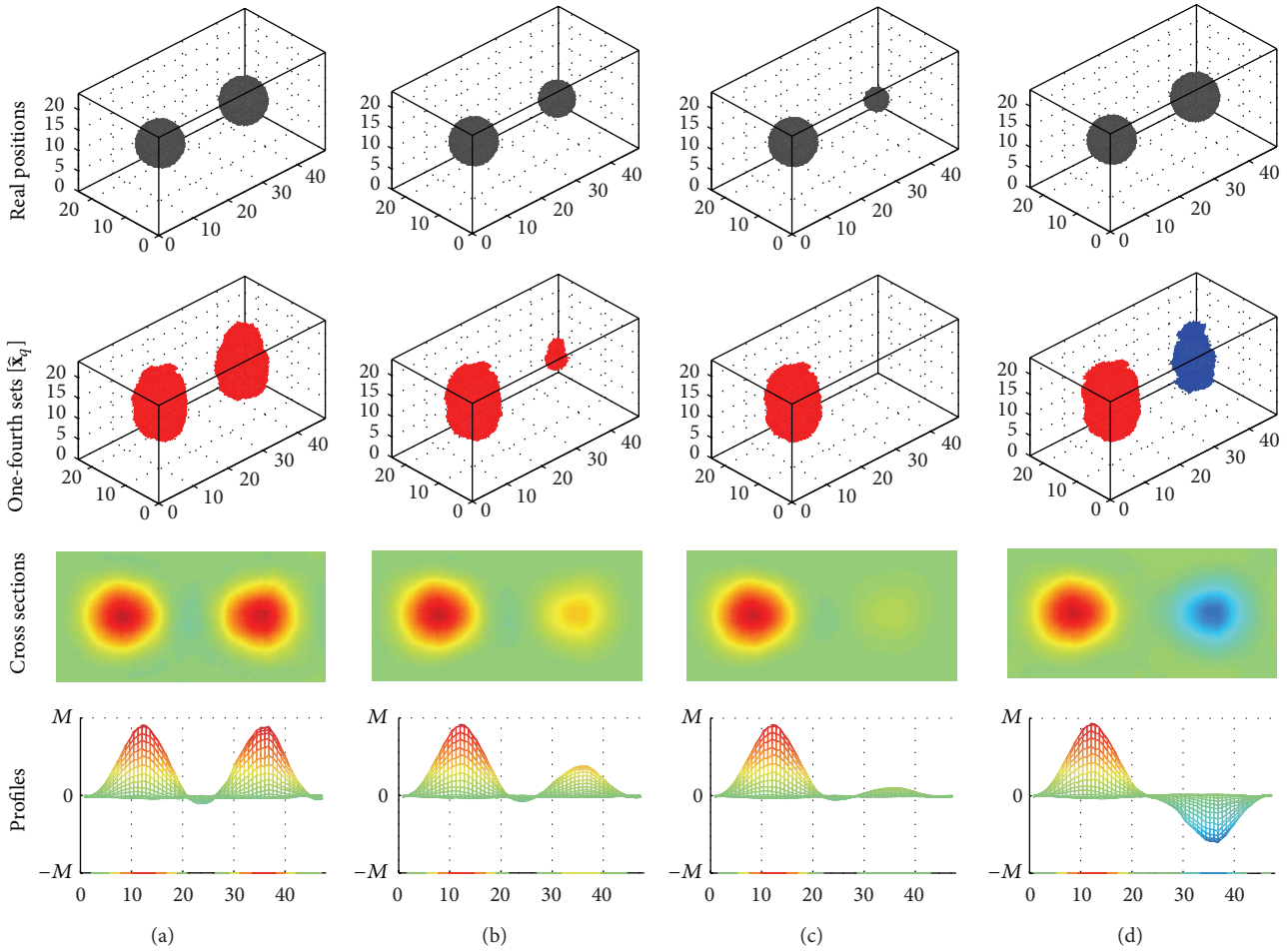

FIGURE 5: Two objects placed at (12, 12, 12) and (36, 12, 12). The radius of the left object was 5 mm. The radius of the right object was (a) 5 mm, (b) 3.75 mm, (c) 2.5 mm, and (d) 5 mm, respectively. The two objects had the same conductivity for (a)–(c) and a different conductivity for (d).

voltmeter. This allowed us to perform a calibration to remove the channel characteristics of the micro-EIT system.

As shown in Figure 7, the single object was clearly reconstructed at the expected location. We evaluated reconstructed images using five figures of merit. They tended to have similar results as the simulation except for the case of the right position. The magnitude of the reconstructed images gradually decreased as the location moved to the right. Figure 8 shows two reconstructed objects when the left object was smaller than the other. The left object with 216 mm^3 volume was reconstructed as one with 337.05 mm^3, whereas the right one with 1,000 mm^3 was reconstructed as 545.94 mm^3. The position dependent volume variation may be caused by the measurement system which used same ground for both current source and voltmeters. The common mode voltage can produce the gradient of voltage measurements. Also, there was a large artifact (overshoot) on the left side when positioning an object close to the current injection electrode. Artifacts around the objects were ringing effects of the reconstructed anomaly combined with current injection method. We observed small artifacts near the secondary electrodes, which were not observed in the numerical simulations. These may be caused by the highly conductive voltage sensing electrode array and secondary current injection electrodes used to produce the equipotential region.

5. Discussions and Conclusions

The new method for the micro-EIT system is focused on generating a uniform parallel current density inside the container when we apply the primary injection current in order to improve the image quality and achieve a high spatial resolution. The system is useful to measure the boundary voltage following the current flow because the equipotential lines are perpendicular to the current streamlines. The secondary current is used for finding a unique solution from the measurement data. It has advantages when we use dedicated current injection electrodes and a large number of separated voltage sensing electrodes. This configuration may

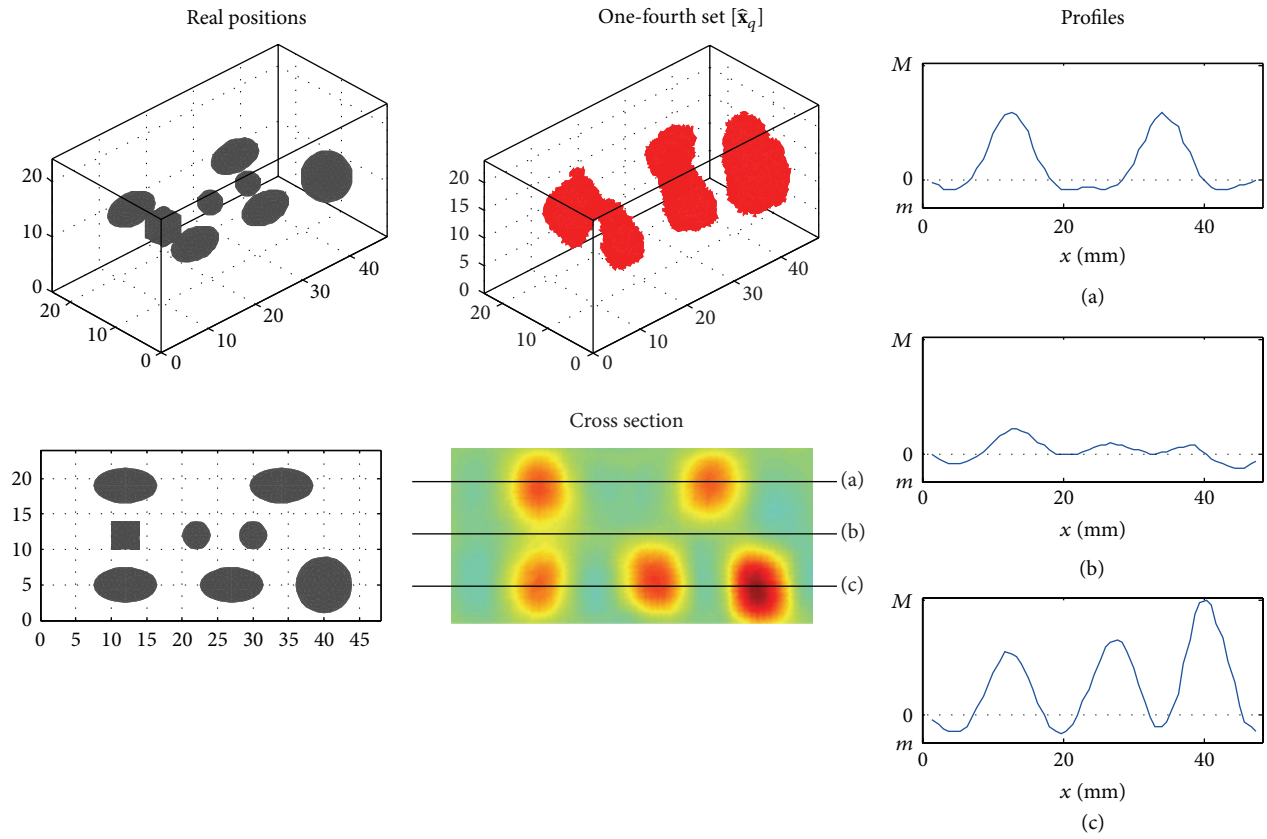

FIGURE 6: The reconstructed multiple objects from the modified Shepp-Logan model.

also provide better spatial resolution and simplified system design. The distance between two adjacent electrodes and the number of electrodes are limited by the system noise level. Since a container has a fixed boundary geometry and electrode configuration, the developed micro-EIT system is best suited for applying 3D GREIT algorithm. Therefore, we can generate the computational forward model as precisely as possible to obtain a training data set. In addition, one can create a suitable amount of synthetic training data and use it to construct the reconstruction matrix **R** before the 3D reconstruction of conductivity distributions. After obtaining the reconstruction matrix, one can create the reconstructed image by performing the simple matrix-vector multiplication of **R** and the boundary voltage data. This will be advantageous to detect fast physiological changes in tissue with a high temporal and spatial resolution. The spatial resolution is determined by the number and spacing of the voltage sensing electrodes.

We need to consider a few issues related to the optimal number of training data and the determination of the image voxel weighting matrix **W**. Adler et al. [20] discussed that the number of training sets was limited to the number of independent measurements. In order to generate conductivity values for all voxels, we needed more training targets than the number of voxel grid points to yield a sufficiently accurate spatial resolution for the reconstructed image. In this study, we used three-times more target positions than voxel grid points on the reconstructed images. The image weighting **W** may play an important role in deciding the error level of the voxels. The allowable error could be suppressed on the outside and inside of the desired target and alleviated on the transition zone, which is the boundary area near the target. We applied a uniform weight in this study; however, seeking the optimal weight **W** may result in improving the performance. In the numerical experiments, we used 1,410 boundary voltage values. From the observations regarding the five figures of merit, we infer that the strategy using the combined H-data and V-data may yield better images in the micro-EIT system. The differential voltage between the 15th electrode in each row and the ground was easily saturated in the phantom experiments. Therefore, we need to apply different gains for each voltmeter channel.

When the object was located on the right side near the ground electrode, there was a 50% underestimation regarding the original volume. This might stem from the common circuit ground for current source and voltmeter, the highly conductive voltage sensing electrode array, and secondary current injection electrode used to produce the equipotential region. This produced significant artifacts in the phantom experimental data. We did not consider the electrode effects and system characteristics in the numerical experiments. To diminish this effect, we may use a floating current injection method without employing a pair of secondary current injection electrodes and reduce the size

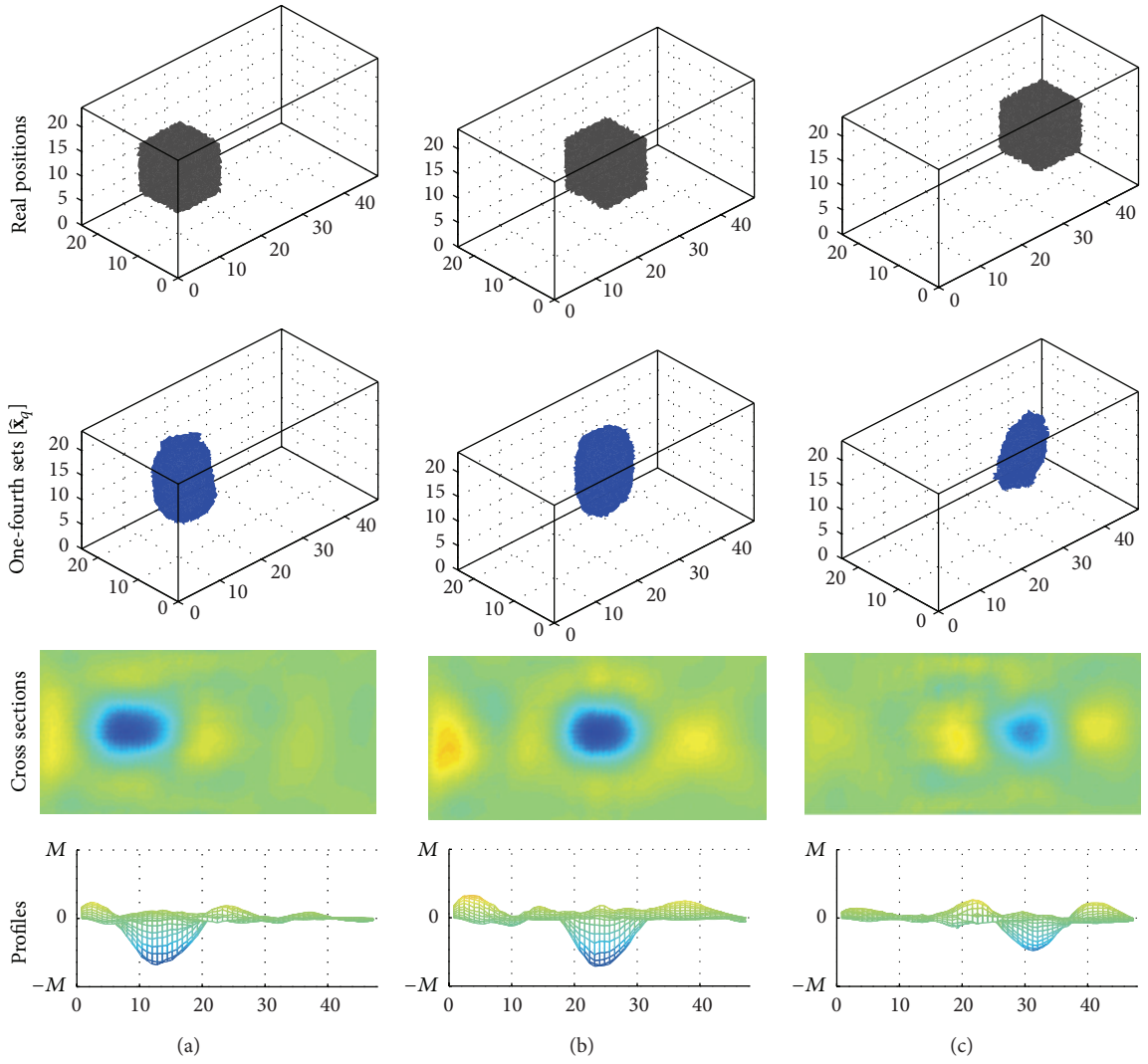

FIGURE 7: Carrot object placed at (a) (12, 12, 12), (b) (24, 12, 12), and (c) (36, 12, 12) in the saline container, respectively.

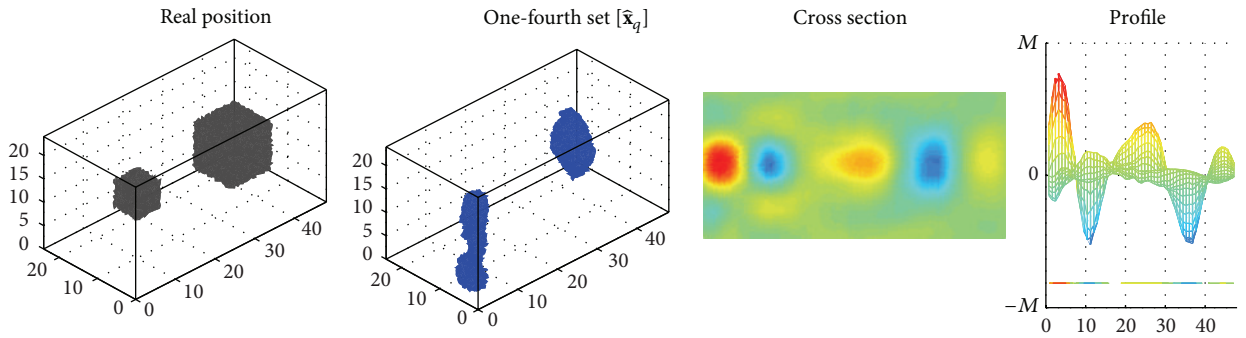

FIGURE 8: The two objects were placed at (12, 12, 12) and (36, 12, 12) at the same time. The edge length of the bigger object was 10 mm and that of the smaller object was 6 mm.

of the voltage sensing electrodes. Even though the phantom experiments did not produce enough performance, we verified that the three-dimensional GREIT using a well-trained reconstruction matrix was able to reconstruct micro-EIT conductivity images and found the practical consideration for the improvements of system.

When the object was placed near the sensing electrodes, the resolution was 5 mm^3 and position error was less than

2.54 mm. The SNR was 63 dB when using a biological object of $10 \times 10 \times 10\,\text{mm}^3$. Considering both simulation and experimental results, we may find the specification of the micro-EIT system to detect conductivity changes during tissue culture. Total volume of a container was 27,648 μL in the large scale model. It will be reduced below 256 μL under the reasonable amount for cell growth. Therefore, the size and distance of sensing electrodes will be smaller and closer. From the pilot test using the developed micro-EIT system, the contact impedance of sensing electrode was increased from 38 kΩ to 553 kΩ measured at 10 Hz when the diameter of electrode was reduced from 1 mm to 0.4 mm. Noise will be increased from 48 μV to 134 μV. We need to overcome the thermal noise due to the small size of electrodes. It can be studied more using the developed micro-EIT system. We might detect the continuous conductivity changes in the region when we reduced the size of container below 2 mm length including the same number of measuring electrodes.

By applying an optimal weighting matrix, we may expect further improvement in the image quality. In our subsequent work, their performance will be compared with regards to computation time and image quality under the same configurations. Several tissue experiments using the same method and a miniaturized container are in progress. This monitoring system can be applied to evaluate the quality of the *in vitro* grown cartilage tissue since the conductivity greatly depends on the extracellular matrix composition, structure, and functionality during the tissue formation process [23].

Conflict of Interests

The authors declare that there is no conflict of interests regarding the publication of this paper.

Acknowledgments

This work was supported by the National Research Foundation of Korea (NRF) Grant funded by the Korean government (MEST) (NRF-2009-0071225 and 2013R1A2A2A04016066) and a Grant of the Korean Health Technology R&D Project, Ministry of Health and Welfare, Republic of Korea (HI13C13590000).

References

[1] S. G. Priya, H. Jungvid, and A. Kumar, "Skin tissue engineering for tissue repair and regeneration," *Tissue Engineering B: Reviews*, vol. 14, no. 1, pp. 105–118, 2008.

[2] L. G. Griffith and G. Naughton, "Tissue engineering—current challenges and expanding opportunities," *Science*, vol. 295, no. 5557, pp. 1009–1014, 2002.

[3] M. Dezawa, I. Takahashi, M. Esaki, M. Takano, and H. Sawada, "Sciatic nerve regeneration in rats induced by transplantation of in vitro differentiated bone-marrow stromal cells," *European Journal of Neuroscience*, vol. 14, no. 11, pp. 1771–1776, 2001.

[4] I. M. Conboy and T. A. Rando, "Aging, stem cells and tissue regeneration: lessons from muscle," *Cell Cycle*, vol. 4, no. 3, pp. 407–410, 2005.

[5] F. Chen and Y. Jin, "Periodontal tissue engineering and regeneration: current approaches and expanding opportunities," *Tissue Engineering B: Reviews*, vol. 16, no. 2, pp. 219–255, 2010.

[6] D. A. Garzón-Alvarado, M. A. Velasco, and C. A. Narváez-Tovar, "Modeling porous scaffold microstructure by a reaction-diffusion system and its degradation by hydrolysis," *Computers in Biology and Medicine*, vol. 42, no. 2, pp. 147–155, 2012.

[7] T. H. Petersen, E. A. Calle, L. Zhao et al., "Tissue-engineered lungs for in vivo implantation," *Science*, vol. 329, no. 5991, pp. 538–541, 2010.

[8] J. J. Ballyns, J. P. Gleghorn, V. Niebrzydowski et al., "Image-guided tissue engineering of anatomically shaped implants via MRI and micro-CT using injection molding," *Tissue Engineering A*, vol. 14, no. 7, pp. 1195–1202, 2008.

[9] M. S. Judenhofer, H. F. Wehrl, D. F. Newport et al., "Simultaneous PET-MRI: a new approach for functional and morphological imaging," *Nature Medicine*, vol. 14, no. 4, pp. 459–465, 2008.

[10] I. Giaever and C. R. Keese, "Use of electric fields to monitor the dynamical aspect of cell behavior in tissue culture," *IEEE Transactions on Biomedical Engineering*, vol. 33, no. 2, pp. 242–247, 1986.

[11] D. A. McRae, M. A. Esrick, and S. C. Mueller, "Changes in the noninvasive, in vivo electrical impedance of three xenografts during the necrotic cell-response sequence," *International Journal of Radiation Oncology Biology Physics*, vol. 43, no. 4, pp. 849–857, 1999.

[12] D. Holder, *Electrical Impedance Tomography: Methods, History, and Applications*, IOP Publishing, 2005.

[13] H. Griffiths, M. G. Tucker, J. Sage, and W. G. Herrenden-Harker, "An electrical impedance tomography microscope," *Physiological Measurement*, vol. 17, no. 4, pp. A15–A24, 1996.

[14] T. York, L. Sun, C. Gregory, and J. Hatfield, "Silicon-based miniature sensor for electrical tomography," *Sensors and Actuators A: Physical*, vol. 110, no. 1–3, pp. 213–218, 2004.

[15] T. E. Oliphant, H. Liu, A. R. Hawkins, and S. M. Schultz, "Simple linear models of scanning impedance imaging for fast reconstruction of relative conductivity of biological samples," *IEEE Transactions on Biomedical Engineering*, vol. 53, no. 11, pp. 2323–2332, 2006.

[16] P. Linderholm, L. Marescot, M. H. Loke, and P. Renaud, "Cell culture imaging using microimpedance tomography," *IEEE Transactions on Biomedical Engineering*, vol. 55, no. 1, pp. 138–146, 2008.

[17] A. R. A. Rahman, J. Register, G. Vuppala, and S. Bhansali, "Cell culture monitoring by impedance mapping using a multi-electrode scanning impedance spectroscopy system (CellMap)," *Physiological Measurement*, vol. 29, no. 6, pp. S227–S239, 2008.

[18] E. Lee, J. K. Seo, E. J. Woo, and T. Zhang, "Mathematical framework for a new microscopic electrical impedance tomography system," *Inverse Problems*, vol. 27, no. 5, Article ID 055008, 2011.

[19] Q. Liu, T. I. Oh, H. Wi, E. J. Lee, J. K. Seo, and E. J. Woo, "Design of a microscopic electrical impedance tomography system using two current injections," *Physiological Measurement*, vol. 32, no. 9, pp. 1505–1516, 2011.

[20] A. Adler, J. H. Arnold, R. Bayford et al., "GREIT: a unified approach to 2D linear EIT reconstruction of lung images," *Physiological Measurement*, vol. 30, no. 6, pp. S35–S55, 2009.

[21] J. Kuen, E. J. Woo, and J. K. Seo, "Multi-frequency time-difference complex conductivity imaging of canine and human lungs using the KHU Mark1 EIT system," *Physiological Measurement*, vol. 30, no. 6, pp. S149–S164, 2009.

[22] S. C. Jun, J. Kuen, J. Lee, E. J. Woo, D. Holder, and J. K. Seo, "Frequency-difference EIT (fdEIT) using weighted difference and equivalent homogeneous admittivity: validation by simulation and tank experiment," *Physiological Measurement*, vol. 30, no. 10, pp. 1087–1099, 2009.

[23] L. Kock, C. C. van Donkelaar, and K. Ito, "Tissue engineering of functional articular cartilage: the current status," *Cell and Tissue Research*, vol. 347, no. 3, pp. 613–627, 2012.

Hindawi Publishing Corporation
Journal of Applied Mathematics
Volume 2014, Article ID 218373, 10 pages
http://dx.doi.org/10.1155/2014/218373

Research Article

Neuronal Ensemble Decoding Using a Dynamical Maximum Entropy Model

Duho Sin,[1] Jinsoo Kim,[1] Jee Hyun Choi,[2] and Sung-Phil Kim[3]

[1] *Department of Brain and Cognitive Engineering, Korea University, Seoul 136-713, Republic of Korea*
[2] *Center for Neural Science, Korea Institute of Science and Technology, Seoul 130-722, Republic of Korea*
[3] *School of Design and Human Engineering, Ulsan National Institute of Science and Technology, Ulsan 689-798, Republic of Korea*

Correspondence should be addressed to Sung-Phil Kim; spkim@unist.ac.kr

Received 28 March 2014; Accepted 27 May 2014; Published 9 July 2014

Academic Editor: Hang Joon Jo

Copyright © 2014 Duho Sin et al. This is an open access article distributed under the Creative Commons Attribution License, which permits unrestricted use, distribution, and reproduction in any medium, provided the original work is properly cited.

As advances in neurotechnology allow us to access the ensemble activity of multiple neurons simultaneously, many neurophysiologic studies have investigated how to decode neuronal ensemble activity. Neuronal ensemble activity from different brain regions exhibits a variety of characteristics, requiring substantially different decoding approaches. Among various models, a maximum entropy decoder is known to exploit not only individual firing activity but also interactions between neurons, extracting information more accurately for the cases with persistent neuronal activity and/or low-frequency firing activity. However, it does not consider temporal changes in neuronal states and therefore would be susceptible to poor performance for nonstationary neuronal information processing. To address this issue, we develop a novel decoder that extends a maximum entropy decoder to take time-varying neural information into account. This decoder blends a dynamical system model of neural networks into the maximum entropy model to better suit for nonstationary circumstances. From two simulation studies, we demonstrate that the proposed dynamic maximum entropy decoder could cope well with time-varying information, which the conventional maximum entropy decoder could not achieve. The results suggest that the proposed decoder may be able to infer neural information more effectively as it exploits dynamical properties of underlying neural networks.

1. Introduction

Ensemble data derived from neuronal population activities have been subject to numerous decoding attempts [1]. Traditional methods mainly focused on neural information of a single neuron averaged over multiple trials, consequently suffering from intertrial variations and neglecting ensemble information stemming from interactions between multiple neurons. Thus, decoding methods that directly tackle neuronal ensemble activity as a whole are more desirable in those terms [2].

To this end, an ensemble decoding method called the population vector (PV) model was proposed where the ensemble state was represented as a weighted sum of the preferred directions of individual neurons' firing rates [3]. Originally aimed for the analysis of primary motor cortical activity, the PV model was also utilized for the analysis of data from various regions such as primary visual cortex [1, 4]. The idea of the vector representation of neuronal ensemble activity was further extended in a form of the optimal linear estimator (OLE) [5].

Both PV and OLE, categorized as structural analysis methods for ensemble data, can be applied when covariate events lie in a single space such as the direction of movement. But in many real cases, where such a condition is not met, a Bayesian decoding method may provide a better decoding solution. Rather than simply merging the ensemble data structurally, a Bayesian method chooses the event with the maximum a posteriori probability. This recursive Bayesian decoding method has been proposed for neuronal ensemble decoding in various forms such as the point process [6], the Kalman filter, or the Particle filter [7, 8]. By considering the fact that neuronal ensemble data contain vital information regarding correlations between multiple neurons [9], different Bayesian decoding approaches utilize such correlations directly for probability distribution estimation [10] via

the statistical dynamics analysis [11–13], based on the maximum entropy principle. Being capable of extracting information from the data with a temporal resolution of millisecond [12], the maximum entropy decoding approach is known to be robust even to the neural data with a low firing rate [11, 14].

The maximum entropy decoding method directly draws upon the stability of neuronal states under certain condition and is well known for its simplicity and consistent performance. It is especially known to well represent collective behavior of neural networks. However, it does not take temporal patterns of neuronal ensemble activity into consideration. Therefore, we propose a novel maximum entropy decoder that can embrace information regarding temporal dynamics of neuronal ensemble activity and thus enhance decoding performance. Especially, our new model is expected to play a vital role in the decoding of neuronal ensemble signals in prefrontal regions of the brain where persistence firing activity with a low firing rate is often observed.

The paper is organized as follows. First we illustrate the basic concept of maximum entropy decoding for neuronal ensemble data and the computational models to implement this concept. Then, we describe an extended Ising decoder that has been recently proposed as an effective maximum entropy decoding method for various neuronal representations. Next, we propose a new decoder that incorporates temporal dynamics of neuronal ensemble into the maximum entropy decoding model. Simulation studies illustrating advantages of using the proposed model follow. Finally, we discuss advantages and limitations of the proposed model and possible future research directions.

2. Methods

2.1. Maximum Entropy Decoding. Let multivariate neuronal ensemble data R be observed in response to stimuli S. Our objective is to determine which stimulus $s \in S$ was applied by decoding a given neuronal data $r \in R$. One possible method would be to find $s \in S$ that maximizes the conditional probability of s given r:

$$\hat{s} = \arg\max_{s \in S} P(s \mid r). \tag{1}$$

Due to the difficulty of completely describing such a conditional probability, the Bayes Rule is applied to represent the conditional probability in terms of likelihood and prior,

$$\hat{s} = \arg\max_{s \in S} \frac{P(r \mid s) P(s)}{P(r)}. \tag{2}$$

In most cases, the likelihood of $P(r \mid s)$ describing a generative relationship between a specific stimulus and its consequential response can be determined. Also, since $P(r)$ is irrelevant to the inference of $s \in S$, the equation above can be reduced as follows:

$$\hat{s} = \arg\max_{s \in S} P(r \mid s) P(s). \tag{3}$$

When estimating $P(r \mid s)$, not only individual neuronal activity in response to a specific stimulus but also correlations among neurons should carry important information. By utilizing a measure that maximizes entropy, which can be applied with the information regarding neuronal correlations, we obtain a Bayesian model called the Ising model [14] and a method of decoding neuronal ensemble activity based on this model is called the Ising decoder [12]. The Ising decoder can be briefly described as follows.

Let us assume that the firing rate of the ith neuron at a given time instant is represented in a binary form: $r_i = +1$ when fired and $r_i = -1$ when silent. With a correlation between a specific stimulus s and the firing rate (Hz) of the ith neuron, denoted as $\{h_i\}$, together with $\{J_{ij}\}$ as the Lagrange multiplier and $\sum_{r \in R} P(r \mid s) = 1$ as the constraint, the probability that yields the maximum entropy is given by [12, 14]

$$P(r \mid s) = \frac{1}{\sum_{r \in R} e^{-H(r|s)}} e^{-H(r|s)}. \tag{4}$$

Here Hamiltonian H is defined by

$$H(r \mid s) = -\frac{1}{2} \sum_{i,j} J_{ij}(s) r_i r_j - \sum_i h_i(s) r_i. \tag{5}$$

The denominator in (4) will be henceforth referred to as a partition function denoted as Z.

In order to solve (4) with the Ising model, the partition function Z regarding s for given $\{J_{ij}, h_i\}$ must be calculated in advance. A direct approach, however, would require 2^N calculations for N neurons, rendering it intractable with a large number of neurons. Instead, one can use an approximation solution via the Markov chain Monte Carlo (MCMC) method [15, 16] or mean field approximation [17, 18]. In particular, mean field approximation of Z for given $\{J_{ij}, h_i\}$ can be expressed as [12]

$$\begin{aligned} \log Z = & \sum_i \log\left(2 \cosh\left(h_i + W_i\right)\right) \\ & - \sum_i W_i \langle r_i \rangle + \sum_{i<j} J_{ij} \langle r_i \rangle \langle r_j \rangle. \end{aligned} \tag{6}$$

Here, $\langle r_j \rangle$ indicates the mean firing rate of the jth neuron and $W_i = \sum_{i \neq j} J_{ij} \langle r_j \rangle$.

The next problem would be to find $\{J_{ij}, h_i\}$ that minimizes the Hamiltonian H in order to obtain a maximum entropy distribution. The Thouless-Anderson-Palmer method can be utilized to approximate computation [11, 12, 18, 19]. Using this method we can find J_{ij} that satisfies

$$\left(C^{-1}\right)_{ij} = -J_{ij} - 2J_{ij}^2 \langle r_i \rangle \langle r_j \rangle, \tag{7}$$

where $C_{ij} = \langle r_i r_j \rangle - \langle r_i \rangle \langle r_j \rangle$. Then, h_i can be computed by

$$h_i = \tanh^{-1} \langle r_i \rangle - \sum_i J_{ij} \langle r_j \rangle + \langle r_i \rangle \sum_j J_{ij}^2 \left(1 - \langle r_j \rangle^2\right). \tag{8}$$

2.2. Extended Ising Decoder. One of the biggest advantages of using the Ising decoder is its temporal resolution of one-thousandth of a second [12]. But there may be occasions

where a bigger bin size than 1 ms is required. In such cases, there would be multiple firings of a neuron within a single bin and thus resulting in information loss in the simple binary representation of firing activity (i.e., $\{-1, +1\}$). Hence, we should consider a system where a state of a neuron is represented in more diverse classes. Since the Ising model only takes binary states into consideration, a model with an extended flexibility is required; one of such models can be found in the Potts model.

The Potts model is a generalized version of the Ising model that embraces a state space of $\sum = \{1, 2, \ldots, q\}^V$, where an integer $q \geq 2$. Hamiltonian H for an arbitrary $\sigma \in \sum$ is defined as

$$H(\sigma) = -J \sum_{(i,j)\in E} \delta\left(\sigma_i, \sigma_j\right) - h \sum_{i\in V} \sigma_i. \tag{9}$$

Here, δ represents the kronecker delta function and σ_i is the firing state of a neuron i in the neuronal ensemble V. The subset of V, denoted as E, represents a set of neurons that are correlated with others. The Ising model is a special case of the Potts model with $q = 2$, $\sigma_i, \sigma_j \in \{-1, +1\}$, and $\delta(\sigma_i, \sigma_j) = (1/2)(1 + \sigma_i\sigma_j)$ [20]. We can generalize the equation even further to reflect differing levels of interaction depending on the class of state such as

$$H(\sigma) = -\frac{1}{2} \sum_{i,j\in V} \sum_{k,l=1}^{q} J_{ij}^{kl} m_{\sigma_i,k} m_{\sigma_j,l} - \sum_{i\in V} h_i \sigma_i, \tag{10}$$

where $m_{\sigma_i,r} = q\delta(\sigma_i r) - 1$ [21].

Representation of a neuronal state as a variable for the Potts model can be realized in multiple approaches: counting the total number of firings within a bin or measuring the ratio of a current firing rate with respect to a maximum firing rate for each neuron. The state space size would be equal to the maximum number of firings within a bin for the former, whereas the latter would yield an arbitrary size depending on a way of quantizing the firing rates.

In the same line with the Ising model, the Potts model requires approximation of the partition function. Unfortunately, it is not easy to provide a closed-form solution for the partition function in the Potts model. Instead, we utilize the MCMC method as follows [15, 16, 22].

Let s represent a Hamiltonian parameter pair (J, h) and let $H(\sigma; s)$ be $H(\sigma)$ conditioned on s; we would like to approximate $Z(s)$ via the MCMC method. Suppose that we know the information of $Z(s_0)$ for $s_0 = (0, 0)$ and we want to estimate $Z(s_1)$ from it. If we define $H(\sigma; s) = H(\sigma; s_0 + \lambda(s_1 - s_0))$, $Z(s_\lambda) = Z(s_0 + \lambda(s_1 - s_0))$, then

$$\log Z(s_1) = \log Z(s_0) + \int_0^1 \frac{d}{d\lambda} \log Z(s_\lambda)\, d\lambda. \tag{11}$$

Taking a closer look inside the integral term:

$$\begin{aligned} \frac{d}{d\lambda} \log Z(s_\lambda) &= \frac{1}{Z(s_\lambda)} \frac{d}{d\lambda} Z(s_\lambda) \\ &= \frac{1}{Z(s_\lambda)} \sum_{\sigma\in\Sigma} \frac{d}{d\lambda} e^{-H(\sigma;s_\lambda)} \\ &= \frac{1}{Z(s_\lambda)} \sum_{\sigma\in\Sigma} e^{-H(\sigma;s_\lambda)} \frac{d}{d\lambda} \left(-H(\sigma; s_\lambda)\right) \\ &= E\left(\frac{d}{d\lambda} \left(-H(\sigma; s_\lambda)\right)\right). \end{aligned} \tag{12}$$

We can apply the mean of Markov chain generated by a Gibbs sampler to obtain the expected value in (12). For a sufficiently large K, the integral is approximated by the trapezoidal rule as

$$\int_0^1 \frac{d}{d\lambda} \log Z(s_\lambda)\, d\lambda \approx \sum_{n=0}^{K} \frac{n}{K+1} E\left(\frac{d}{d\lambda} \left(-H(\sigma; s_{n/K})\right)\right). \tag{13}$$

Therefore,

$$Z(s_1) \approx Z(s_0) \exp\left(\sum_{n=0}^{K} \frac{n}{K+1} E\left(\frac{d}{d\lambda} \left(-H(\sigma; s_{n/K})\right)\right)\right). \tag{14}$$

The extended Ising decoder based on the Potts model will be henceforth referred to as the conventional maximum entropy decoder.

2.3. Dynamical Maximum Entropy Decoder. One of the neural network models exploiting statistical dynamics is the Hopfield network [23, 24]. It shows a distinct difference when compared to Perceptron [25, 26] models. Perceptron is aimed at physical systems and does not consider abstract population characteristics where the Hopfield model does. Moreover, while Perceptron is focused on synchronized systems, the Hopfield network can also be applied to more general dynamical systems.

In the Hopfield network, a state of each neuron is represented as $\sigma \in \{0, 1\}$, determined with a threshold θ and a synaptic connection strength J:

$$\sigma_i = \begin{cases} 1, & \text{if } \sum_j J_{ij}\sigma_j + h_i \geq \theta_i, \\ 0, & \text{if } \sum_j J_{ij}\sigma_j + h_i < \theta_i, \end{cases} \tag{15}$$

where i and j are index neurons and h represents an external input. The synaptic strength J is updated in a specific time range s as follows:

$$J_{ij} = \sum_s \left(2\sigma_i^s - 1\right)\left(2\sigma_j^s - 1\right). \tag{16}$$

In case of $i = j$, $J_{ij} = 0$.

The most important feature is that if we assume symmetry such that $J_{ij} = J_{ji}$, the Lyapunov function exists for this neural network. The Lyapunov function, also referred to as an energy function, is given by

$$L(\sigma) = -\frac{1}{2}\sum_{i,j} J_{ij}\sigma_i\sigma_j - \sum_i h_i\sigma_i. \tag{17}$$

The existence of the Lyapunov function is important because it analytically presents how the state of a system is likely to change. In such cases, the Lyapunov function is identical to Hamiltonian of the Ising model.

The Hopfield network has been generalized based on the Potts model [21]. In this case, along with various degrees of interactions depending on diverse neural states, the Lyapunov function becomes

$$L(\sigma) = -\frac{1}{2}\sum_{i,j\in V}\sum_{k,l=1}^{q} J_{ij}^{kl} m_{\sigma_i,k} m_{\sigma_j,l} - \sum_{i\in V} h_i\sigma_i, \tag{18}$$

where $m_{\sigma_i,r} = q\delta(\sigma_i r) - 1$. Note that Hamiltonian in the Potts model can be obtained from this Lyapunov function.

Now, we describe how to build a dynamical maximum entropy decoder. First, let us consider some basic aspects of a dynamical system. Let a dynamical system receiving an external input s be described by

$$f_s : \Sigma \longrightarrow \Sigma, \tag{19}$$

with a set of all possible neuronal states as Σ. We then make two basic assumptions on this dynamical system as follows.

Assumption 1. The dynamical system is assumed to approach a stable state over time with no input. Then, for every $s \in S$, $\sigma \in \Sigma$, and time $t \in Z^+$,

$$L\left(f_s^t(\sigma)\right) \le L(\sigma). \tag{20}$$

Assumption 2. Let $\Omega_s f \subseteq \Sigma$ be a pseudo-periodic set in response to an external input s. Then, we assume that

$$\left|\Omega_s f\right| < \infty, \qquad f_s^n(\sigma) \in \Omega_s f. \tag{21}$$

Here n is an integer and can be sufficiently small. We also assume that an external stimulus s is static during its stimulation period.

Next, we consider two cases when there is sufficient time for the system to be stabilized (Case 1) and when there is not (Case 2). For both cases, we need to estimate $\Omega_s f$ with the assumptions above, which allow us to conjecture that any σ_1 and σ_2 are close to each other if $\sigma_1 = w = \sigma_2$ for $w \in \Omega_s f$. Here w represents a pseudo-periodic discretized set belonging to $\Omega_s f$.

2.3.1. Case 1. In this case, we first define a probability that a state σ belongs to certain w:

$$P\left(\sigma = w \in \Omega_s f\right). \tag{22}$$

Using Hamiltonian based on the Lyapunov function, we can compute a probability that σ belongs to w as

$$P(\sigma = w) = \frac{P_w(\sigma)}{\sum_{w'} P_{w'}(\sigma)}. \tag{23}$$

The next step is to define a statistical state transition function. We represent every possible pair of states given a change of input from s to s' as $\widetilde{\Sigma}$; that is, $\langle\sigma_t, \sigma_{t+1}\rangle = \widetilde{\sigma} = \widetilde{\Sigma}$. Then, the transition function is defined as

$$\Phi_{w,w'}\left(w, w'\right) = \frac{1}{\left|\widetilde{\Sigma}\right|}\sum_{\widetilde{\sigma}\in\widetilde{\Sigma}} P\left(\sigma_t = w\right) P\left(\sigma_{t+1} = w'\right). \tag{24}$$

Decoding an input S_{t+1} with the knowledge of S_t from neuronal ensemble data is stated as the following problem:

$$\widehat{S_{t+1}} = \arg\max_{s\in S} P\left(S_{t+1} = s \mid \sigma_t, \sigma_{t+1}, S_t\right). \tag{25}$$

This problem can be solved using the transition function and probabilities described above:

$$\begin{aligned} &P\left(S_{t+1} = s \mid \sigma_t, \sigma_{t+1}, S_t\right) \\ &\quad = \sum_{w_{t+1}\in\Omega_s f} P\left(\sigma_{t+1} = w_{t+1}\right) \\ &\qquad \times \left(\sum_{w_t\in\Omega_s f} P\left(\sigma_t = w_t\right)\Phi_{S_{t+1},s}\left(w_t, w_{t+1}\right)\right). \end{aligned} \tag{26}$$

Note that we can also use a simplified version of this formula given by

$$\begin{aligned} &P\left(S_{t+1} = s \mid \sigma_t, \sigma_{t+1}\right) \\ &\quad = \sum_{w_{t+1}, w_t\in\Omega_s f} P\left(\sigma_t = w_t\right) P\left(\sigma_{t+1} = w_{t+1}\right)\Phi_s\left(w_t, w_{t+1}\right). \end{aligned} \tag{27}$$

2.3.2. Case 2. Let $\sum$ be a set of all possible neuronal ensemble states. Suppose there is a function on $\sum$ such as

$$\emptyset : \sum \times S \longrightarrow \sum. \tag{28}$$

$\emptyset$ can be seen as the restrictive function $f|_{\sum}$ of a dynamical system f and also as a reconstruction of f with respect to $\sum$. What this entails is the fact that $\overline{f(\sigma)} = \langle f^1(\sigma), f^2(\sigma), \ldots, f^{n+1}(\sigma)\rangle$ can be found if $\overline{s} \in \prod_{i=0}^{n} S_i$ is given for all $\sigma \in \sum$. Since solving the problem with every possible $\sigma \in \sum$ and $s \in S$ is difficult, we use a technique that limits the length of the sequence to N.

Rather than estimating $\Omega_s f$ as defined, we estimate the neural trajectory of a specific σ. For a small enough N, we substitute ω for $\overline{s} \in \prod_{i=0}^{n} S_i$, therefore acquiring the probability $P(\sigma = \omega)$ from (23). Now let $\Omega = \{\omega\}$, a temporary set that retains its elements but not further down the line. With this set, we redefine the function $\emptyset$ as

$$\emptyset : \Omega \times S \longrightarrow \Omega \tag{29}$$

and also in terms of Φ as

$$\emptyset\left(\Omega, s \in S\right) = \Phi_{s\in S}\left(\Omega, \Omega\right) \in [0,1], \tag{30}$$

such that the condition of $\sum_{\omega,\omega'\in\Omega}\Phi_s(\omega,\omega') = 1$ is satisfied. Hence, now our goal is to find a dynamical function Φ over time. The initial value of Φ can be assumed to follow the uniform distribution.

As time elapses, $\overline{\sigma} = \langle\sigma_1, \sigma_2, \ldots, \sigma_N\rangle$ and $\overline{s} = \omega$ turns into $\overline{\sigma'} = \langle\sigma_2, \ldots, \sigma_N, \sigma_{N+1}\rangle$ and $\overline{s'} = \omega'$. Then, we update Φ with the result of (26) as follows:

$$\frac{d}{dt}\Phi_s\left(\omega,\omega'\right) = \eta_1\left(\mathrm{val} - \Phi_s\left(\omega,\omega'\right)\right). \tag{31}$$

The "val" in above equation can be regarded as either 1 or 0. Once Φ_s is properly normalized, we accept and normalize the transformation with a probability η_2 if the updated $P(\sigma' = \omega')$ enhances the performance of (26). η_1 and η_2 introduced here are time-varying and converge to 0 when $t \to \infty$.

This method is partially in line with the simulated annealing technique. Hence, it is expected to approach to a right solution but, on the other hand, can consume longer computational time. The main characteristic of this method is that ω is not limited only to stable states. If not enough time is given to reach a stable state after each external input, it might be better to consider the temporary states generated during the process. The proposed method realizes such temporary states. Even the trajectory of state transition as a result of change in external input can be represented in ω. Although each ω does not necessarily represent the stable state of a neural network in such cases, it can be advantageous for the decoding system that involves temporal dynamics since it can represent the most likely state in response to the change.

2.4. Simulation Procedure. A synthetic neuronal ensemble data set was generated in order to test the new decoding method for both cases, "Case 1" and "Case 2," discussed above.

2.4.1. Case 1. A model capable of representing persistence activity of neurons is generally complex [27]; thus, for the sake of the simplicity of experiment, we generated neuronal ensemble data with fixed firing rates of sixteen neurons for each external stimulus, based on Poisson process. Stimuli were limited to two classes, S_1 and S_2, where two stable states existed for each. In short, for each stimulus, $S = \{S_1, S_2\}$, stable states $\Omega_{S_1} f = \{w_{1,1}, w_{1,2}\}$ and $\Omega_{S_2} f = \{w_{2,1}, w_{2,2}\}$ exist (see Figure 2(a)).

While four out of sixteen neurons represented the actual state, the rest were set to have random mean firing rates between 0 Hz to 10 Hz to represent irrelevant activity in the ensemble data. Those four state-representing neurons were divided into two pairs with neurons that were assigned the same mean firing rate. Thus, each state could be expressed as the following pairs: $w_{1,1} := (10, 10, 0, 0)$ Hz, $w_{1,2} := (0, 0, 10, 10)$ Hz, $w_{2,1} := (0, 0, 0, 0)$ Hz, and $w_{2,2} := (10, 10, 10, 10)$ Hz.

2.4.2. Case 2. In order to generate neuronal ensemble data for Case 2, we utilized the orientation tuning model [28] that represents a biological neural network model for directional coding [29, 30]. Similar to an excitatory-inhibitory neural network model, the model contains an ensemble of neurons that respond to the angular direction θ and delivers excitatory or inhibitory signals among neurons depending on the directional similarity. In our simulation, we defined a signal passed on from one population of direction θ to another population of θ' as

$$J_{\theta'\theta} = -J_0 + J_2\cos\left(\theta - \theta'\right). \tag{32}$$

Here, J_0 and J_2 as a balancing parameter were set as $J_0 = 0.14$ and $J_2 = 0.5$ for our simulation. The actual input that the neurons tuned to θ' received from an external input with an angle θ was given by

$$h^{\mathrm{ext}}_{\theta'\theta} = c\left(1 - \epsilon + \epsilon\cos\left(\theta - \theta'\right)\right), \tag{33}$$

where ϵ and c were parameters representing the degree of input focus and overall intensity of the input, respectively. The range of ϵ was given as $[0, 1/2]$; $\epsilon = 0$ indicated that every neuron received uniform input regardless of their inherent direction, and $\epsilon = 1/2$ indicated that less input was given if θ' was more distant from θ. Hence, a condition $|\theta' - \theta| = \pi$ left neurons of θ' unaffected. For this simulation, $\epsilon = 0.5$ and $c = 0.4$ were used (see Figure 1).

A temporal change of a neural network was expressed as a firing rate based on the neural network model. The firing rate U_i of the ith neuron was

$$\tau_i\frac{dU_i}{dt} = -U_i + S_i\left(\sum_i J_{ji}U_j\right). \tag{34}$$

Here, τ_i was a time constant representing a synaptic delay between neurons, J_{ji} was the synaptic strength between the ith and jth neurons, and S_i was a threshold function [31]. This part of the simulation utilized a total of $2^9 = 512$ neurons as well as a synaptic delay constant, $\tau = 10$ ms. A threshold function for the firing rate was defined with the scale of 10^2 Hz:

$$S(U) = \begin{cases} 0, & \text{if } U < 0, \\ U, & \text{if } 0 \le U \le 4, \\ 4, & \text{if } U > 4. \end{cases} \tag{35}$$

The number of neurons for each of eight directions was equal ($2^{9-3} = 64$) and the synaptic strength J and the external input h were identical to the setting of orientation tuning model of Case 1. The probability that neuronal connections between neurons exist was set below 0.5.

3. Results and Discussion

Performance of the decoders was assessed by means of "decoding error rate" and "decoding uncertainty" for the given dataset. Error rate calculated as a ratio of incorrectly

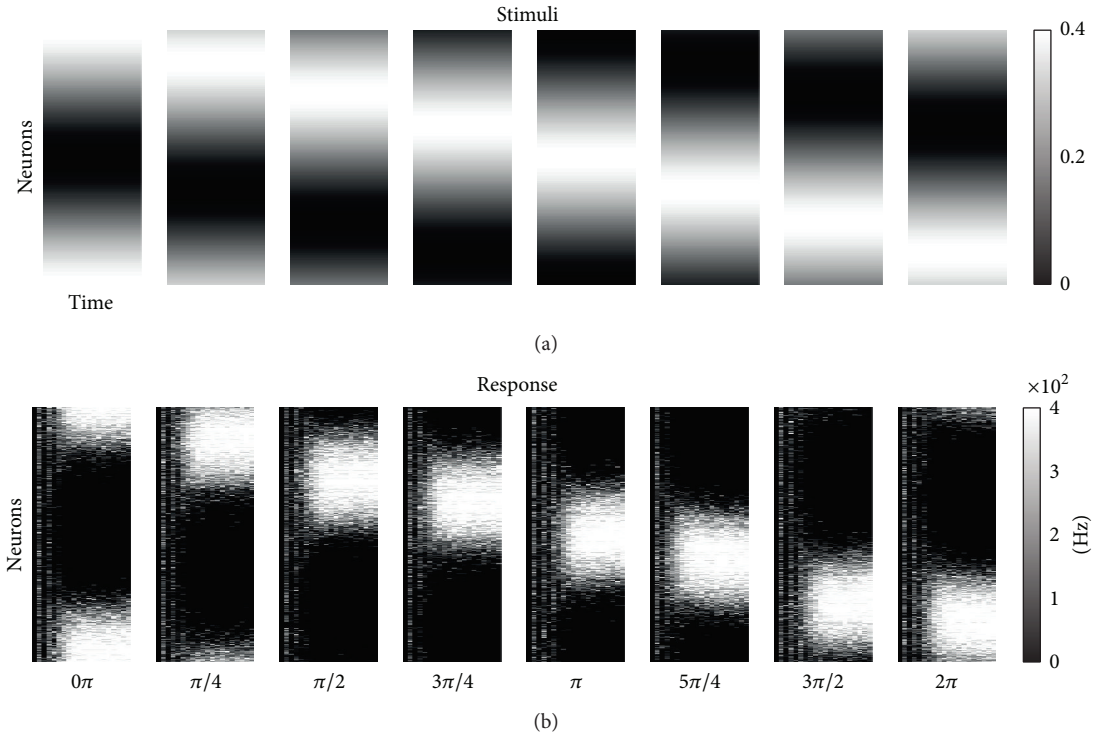

FIGURE 1: Simulated data generated from the orientation tuning model. For each of 8 directional stimuli provided to each neuron (a), simulated neuronal responses are generated (b). Horizontal axis for each box represents time-flow (for 200 ms, from left to right), and vertical axis represents single neurons. Magnitude of stimulation and neuronal response is represented by a greyscale colormap.

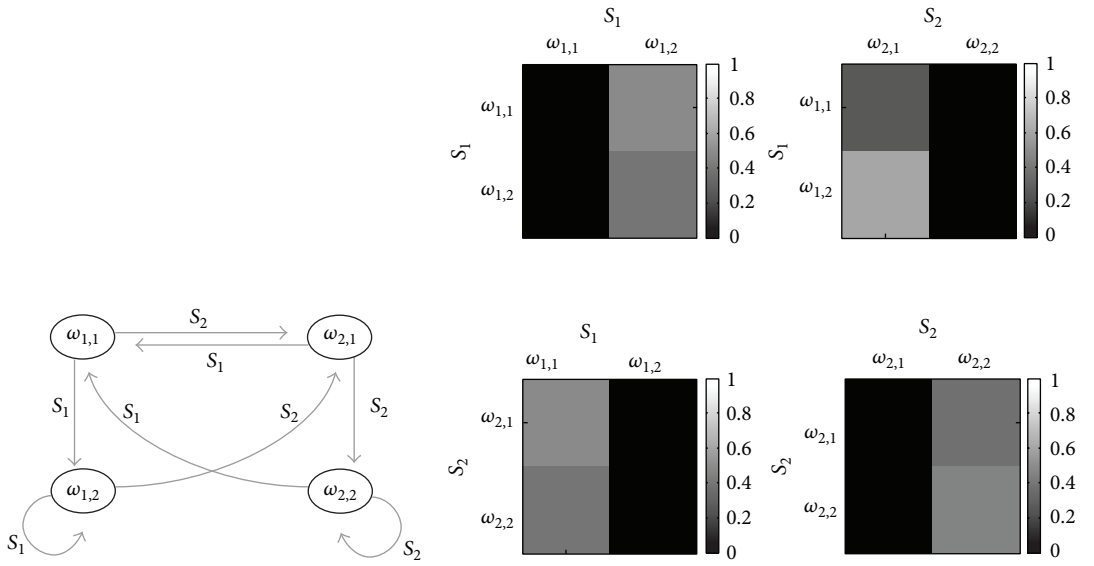

(a) State changes resulting from external stimuli

(b) An example of estimated $\Phi_{s,s'}(w, w')$

FIGURE 2: Ensemble state changes and its estimation. (a) Grey arrows represent change of states $w_{i,j} \in \Omega_{S_i} f$ for a specific stimulus S_k. (b) Estimated ensemble state transition of $\Phi_{s,s'}(w, w')$ for different external inputs. For each transition from S_i to S_j, the probability of state change from $w_{i,k}$ to $w_{j,l}$ is expressed in a greyscale mapping.

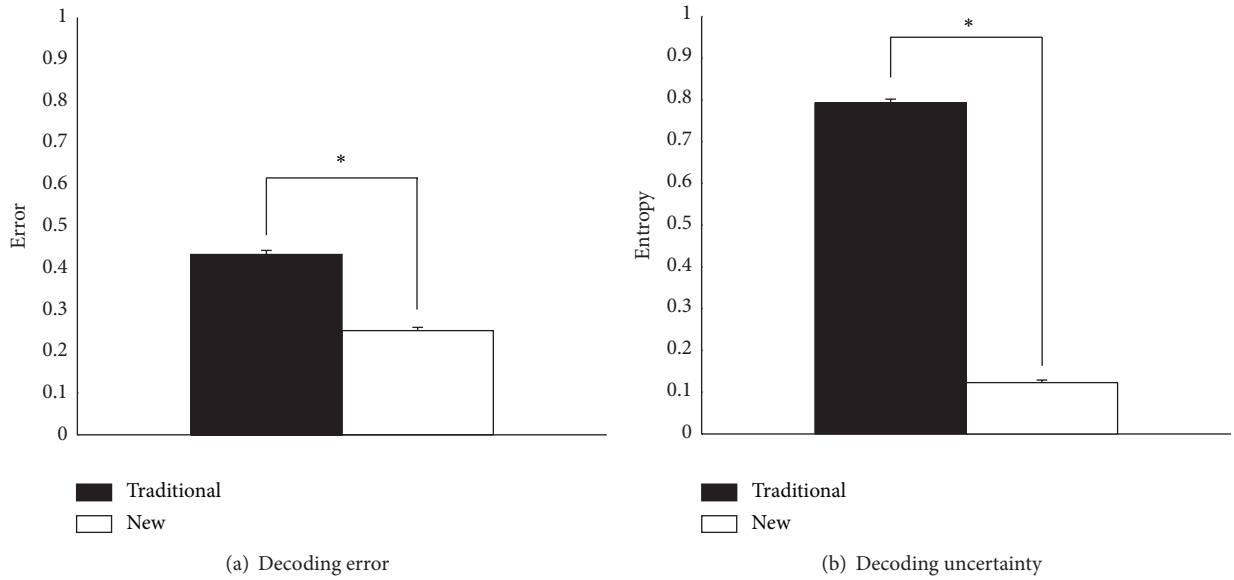

(a) Decoding error (b) Decoding uncertainty

FIGURE 3: (a) Decoding error rates and (b) uncertainty represented by entropy of decoding output using two decoding models from simulated neural data (see text). The maximum entropy is 1 bit in this case since there are two possible external events. In both categories, there is significant difference in error rates (t-test, $P < 0.00001$) between the dynamical maximum entropy decoder (new) and the traditional maximum entropy decoder (traditional).

classified samples to the total number of samples tested served as a direct measure of decoder performance. Decoding uncertainty was represented with the entropy of the normalized distribution of Bayesian probabilities for each class generated by the decoder. Small amount of entropy indicates less uncertainty of decoding performance, analogous to smaller variance of estimates of a model. Using these performance measures, we compared our proposed decoder (dynamical maximum entropy decoder) with the conventional decoder (the extended Ising decoder).

3.1. Case 1. The dynamical maximum entropy decoder estimated $\Phi_{s,s'}(w, w')$ as the first step of decoding. We examin ed whether this transition estimation was correctly represented by the decoder. Figure 2(b) demonstrates that the estimation results well represent state changes for a given external event (see Figure 2(a)). When there were more than two stable states for each event, the proposed method outperformed the conventional maximum entropy decoder in terms of both error rate and uncertainty (see Figure 3). The proposed decoder generated approximately 0.25 error rate and 0.12 bit of entropy which is a significant improvement over 0.45 error rate and 0.78 bit entropy by the conventional decoder. Superior performance of the dynamical maximum entropy decoder was based on its ability to alleviate signals from those neurons which were regarded as irrelevant to the event.

3.2. Case 2. The second study considered a case where the external stimulus changes before the system converges to a stable state. For each of 8 uniformly separated directions, the stimulus was changed after the first 200 ms and then lasted for another 200 ms period. The succeeding direction could either be different from or same as the former. A small number of neurons were randomly chosen out of 512 total neurons and were discretized within a bin size of 10 ms (see Figure 4).

For these data with temporal changes of stimuli, the proposed decoder was evidently superior compared to the conventional decoder in terms of error rates with 0.07-, 0.07-, 0.01-, and 0.11-point advantage for respective scenarios (see Figure 5(a)). However, decoding uncertainty was also significantly (difference range 0.3~0.8 bits; t-test, $P < 0.01$) higher in the proposed decoder than the conventional one in all scenarios (Figure 5(b)). This issue will be further discussed below.

3.3. Discussion. Decoding neuronal ensemble activity recorded from brain signals provides insights on how neural networks process information. Decoding models based on computational models for biological neural networks can provide these insights to deepen our understanding of neural network mechanisms. However, approaches directly using neural network models are not easily realized because it is challenging to know every synaptic strength between neurons and to obtain full information of all the neurons in a network. Therefore, the present study proposes an alternative approach to leveraging dynamical and collective behavior of an ensemble of neurons in response to various stimuli. From simple assumptions on the model, we blend neural dynamics into a decoder with which we are able to inspect the functions and roles of a neural network.

To the assessment of the performance of a decoder, the uncertainty of decoding outcome as well as the error rate is crucial. This uncertainty measures how robust the decision made by a decoder is regarding the information inferred from neuronal activity. Our proposed decoder exhibited a

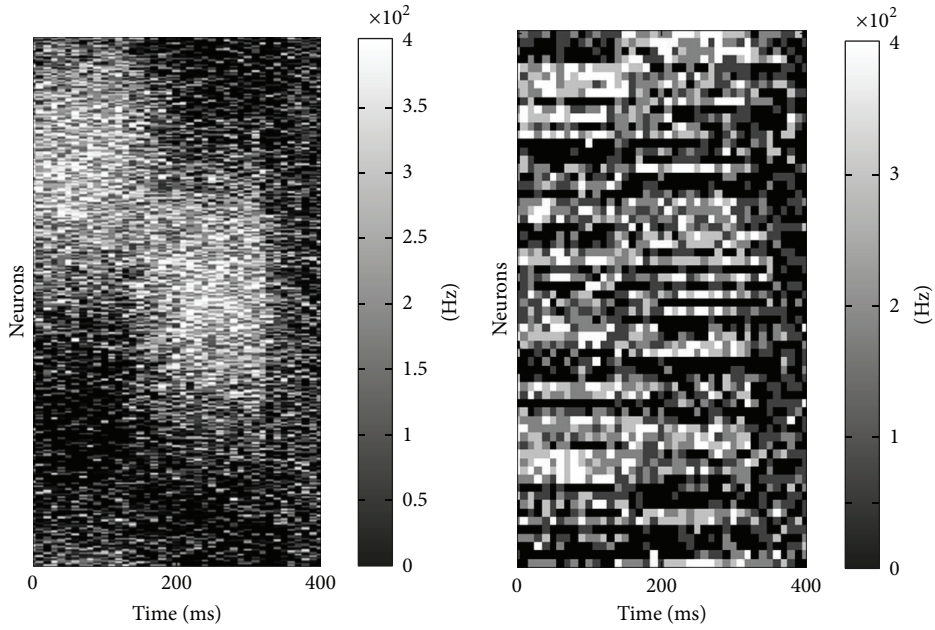

(a) Sampled simulation data (b) Discretized simulation data

FIGURE 4: Representation of sampled and discretized simulation data. 64 random neurons were sampled from virtual ensemble data with 512 neurons (a) and then discretized in a 10 ms resolution (100 Hz) (b). Stimulation direction was 0.5π for the first 120 ms and π for the next 240 ms.

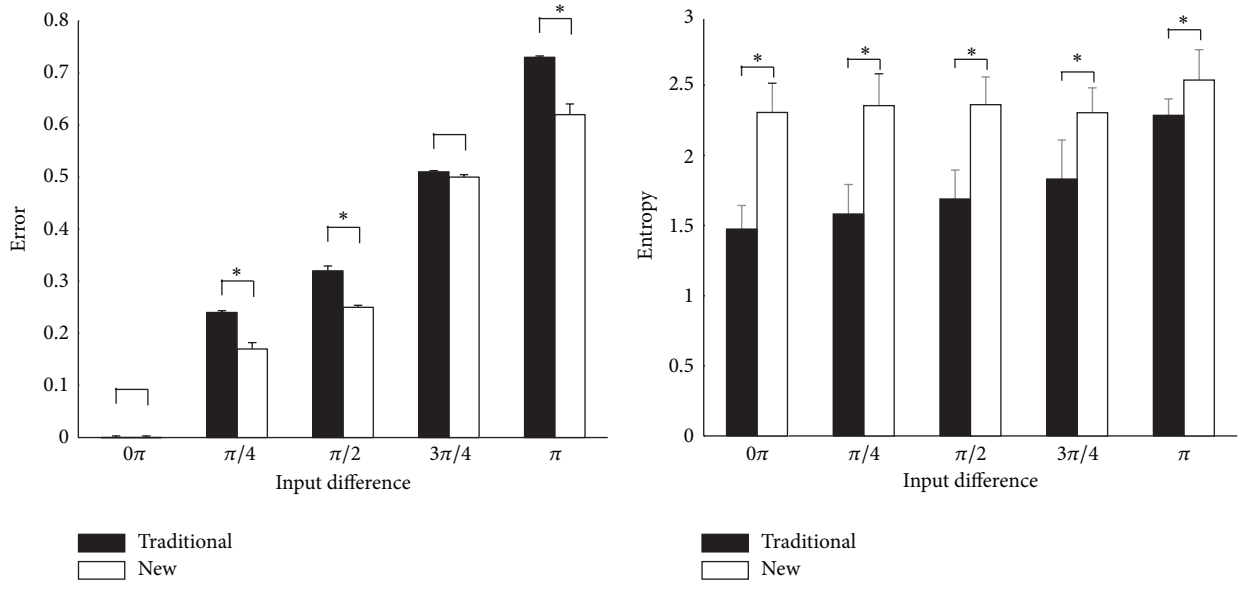

(a) Decoding error (b) Decoding uncertainty

FIGURE 5: A comparison of decoding error and uncertainty under various degrees of stimulus direction difference between the proposed (new) and the traditional maximum entropy decoders. (a) Both decoders demonstrate a similar trend of higher error rates for greater input difference. Except for the 0.75π condition, the proposed method yields significantly lower error rates (t-test, $P < 0.00001$). (b) A sensible increase of uncertainty is shown for both methods as the input difference grows. The proposed method contains greater uncertainty (t-test, $P < 0.01$) for all cases.

significantly low error rate and small uncertainty in the first case study (see Figure 3). However, it generated significantly larger uncertainty than the conventional maximum entropy decoder in the second case study despite its lower error rate (Figure 5). We speculate that such larger uncertainty may be due to model complexity in our decoder. More complex decoding procedure in our model includes uniformly distributed transition probabilities that may in turn equalize prior probabilities of individual stimuli, thus increasing uncertainty of a decoded stimulus. However, it may not be solely the result of model structure because the proposed decoder could also reduce uncertainty in the first case. Consequently, we suspect that increased uncertainty in the second case may indicate a particular outcome resulting from specific data properties, which need further investigation in the future.

Yet, we also recognize that there is plenty of room to improve in our model. In particular, more rigorous ways of obtaining information about neural dynamics may be necessary. For instance, our method to estimate stabilized states of a neuronal ensemble may be suboptimal to many different real data. Also, we need to apply our decoder to ensemble data from many different brain regions to generalize it further. Finally, continuous efforts to reduce computational loads in the proposed decoder will be required.

4. Conclusions

A number of methods have been continuously developed to decode neuronal ensemble activity. The design of decoding models draws upon the properties of a target brain region, a recording technique, neural signals, and the objectives of decoding. Among them, the maximum entropy decoding method takes into account correlations between neurons as well as firing rates of individual neurons. In particular, it produces good decoding performance when there exist marginal but clear interactions between neurons. However, the current maximum entropy decoder does not capture time-varying characteristics of neuronal ensemble activity, which often deliver essential information about underlying brain functions. Hence, the present study addresses this issue by developing a novel decoder that incorporates dynamical properties of a neuronal ensemble in the model while maintains the key functions of the maximum entropy decoder. We demonstrate that more information can be successfully decoded using the proposed decoder compared to the conventional maximum entropy decoder.

Conflict of Interests

The authors declare that there is no conflict of interests regarding the publication of this paper.

Acknowledgments

This work was partly supported by the Components and Materials Technology Development Program (10043826) funded by the Korean Ministry of Trade, Industry, and Energy (Jinsoo Kim, Sung-Phil Kim) and the Technological Innovation R&D program (S2087577) funded by the Small and Medium Business Administration of Korea (Sung-Phil Kim). Also, Jee Hyun Choi was being supported by the Global Frontier R&D Program funded by the National Research Foundation of Korea Grant (no. 2011-0031525) (Jee Hyun Choi).

References

[1] L. F. Abbott, "Decoding neuronal firing and modelling neural networks," *Quarterly Reviews of Biophysics*, vol. 27, no. 3, pp. 291–331, 1994.

[2] R. Quian Quiroga and S. Panzeri, "Extracting information from neuronal populations: Information theory and decoding approaches," *Nature Reviews Neuroscience*, vol. 10, no. 3, pp. 173–185, 2009.

[3] A. P. Georgopoulos, A. B. Schwartz, and R. E. Kettner, "Neuronal population coding on movement direction," *Science*, vol. 233, no. 4771, pp. 1416–1419, 1986.

[4] C. D. Gilbert and T. N. Wiesel, "The influence of contextual stimuli on the orientation selectivity of cells in primary visual cortex of the cat," *Vision Research*, vol. 30, no. 11, pp. 1689–1701, 1990.

[5] E. Salinas and L. F. Abbott, "Vector reconstruction from firing rates," *Journal of Computational Neuroscience*, vol. 1, no. 1-2, pp. 89–107, 1994.

[6] S. Koyama, U. T. Eden, E. N. Brown, and R. E. Kass, "Bayesian decoding of neural spike trains," *Annals of the Institute of Statistical Mathematics*, vol. 62, no. 1, pp. 37–59, 2010.

[7] S. Koyama and L. Paninski, "Efficient computation of the maximum a posteriori path and parameter estimation in integrate-and-fire and more general state-space models," *Journal of Computational Neuroscience*, vol. 29, no. 1-2, pp. 89–105, 2010.

[8] W. Q. Malik, W. Truccolo, E. N. Brown, and L. R. Hochberg, "Efficient decoding with steady-state kalman filter in neural interface systems," *IEEE Transactions on Neural Systems and Rehabilitation Engineering*, vol. 19, no. 1, pp. 25–34, 2011.

[9] S. Nirenberg and P. E. Latham, "Decoding neuronal spike trains: how important are correlations?" *Proceedings of the National Academy of Sciences of the United States of America*, vol. 100, no. 12, pp. 7348–7353, 2003.

[10] O. Marre, S. El Boustani, Y. Frégnac, and A. Destexhe, "Prediction of spatiotemporal patterns of neural activity from pairwise correlations," *Physical Review Letters*, vol. 102, no. 13, 2009.

[11] Y. Roudi, J. Tyrcha, and J. Hertz, "Ising model for neural data: model quality and approximate methods for extracting functional connectivity," *Physical Review E*, vol. 79, no. 5, Article ID 051915, 2009.

[12] M. T. Schaub and S. R. Schultz, "The Ising decoder: reading out the activity of large neural ensembles," *Journal of Computational Neuroscience*, vol. 32, no. 1, pp. 101–118, 2012.

[13] J. C. Vasquez, O. Marre, A. G. Palacios, M. J. Berry, and B. Cessac, "Gibbs distribution analysis of temporal correlations structure in retina ganglion cells," *Journal of Physiology—Paris*, vol. 106, no. 3-4, pp. 120–127, 2012.

[14] E. Schneidman, M. J. Berry II, R. Segev, and W. Bialek, "Weak pairwise correlations imply strongly correlated network states in a neural population," *Nature*, vol. 440, no. 7087, pp. 1007–1012, 2006.

[15] F. Huang and Y. Ogata, "Comparison of two methods for calculating the partition functions of various spatial statistical models," *Australian and New Zealand Journal of Statistics*, vol. 43, no. 1, pp. 47–65, 2001.

[16] Y. Ogata and M. Tanemura, "Likelihood analysis of spatial point patterns," *Journal of the Royal Statistical Society B: Methodological*, vol. 46, no. 3, pp. 496–518, 1984.

[17] H. J. Kappen and F. B. Rodríguez, "Efficient learning in boltzmann machines using linear response theory," *Neural Computation*, vol. 10, no. 5, pp. 1137–1156, 1998.

[18] T. Tanaka, "Mean-field theory of Boltzmann machine learning," *Physical Review E*, vol. 58, no. 2, pp. 2302–2310, 1998.

[19] D. J. Thouless, P. W. Anderson, and R. G. Palmer, "Solution of solvable model of a spin glass," *Philosophical Magazine*, vol. 35, no. 3, pp. 593–601, 1977.

[20] G. Grimmett, *Probability on Graphs: Random Processes on Graphs and Lattices*, Cambridge University Press, 2010.

[21] I. Kanter, "Potts-glass models of neural networks," *Physical Review A*, vol. 37, no. 7, pp. 2739–2742, 1988.

[22] Y. Ogata, "A Monte Carlo method for high-dimensional integration," *Numerische Mathematik*, vol. 55, no. 2, pp. 137–157, 1989.

[23] J. J. Hopfield, "Neural networks and physical systems with emergent collective computational abilities," *Proceedings of the National Academy of Sciences of the United States of America*, vol. 79, no. 8, pp. 2554–2558, 1982.

[24] J. J. Hopfield, "Neurons with graded response have collective computational properties like those of two-state neurons," *Proceedings of the National Academy of Sciences of the United States of America*, vol. 81, no. 10, pp. 3088–3092, 1984.

[25] M. L. Minsky and S. A. Papert, *Perceptrons*, The MIT Press, 1969.

[26] F. Rosenblatt, "The perceptron: a probabilistic model for information storage and organization in the brain," *Psychological Review*, vol. 65, no. 6, pp. 386–408, 1958.

[27] O. Barak and M. Tsodyks, "Persistent activity in neural networks with dynamic synapses," *PLoS Computational Biology*, vol. 3, no. 2, article e104, pp. 323–332, 2007.

[28] R. Ben-Yishai, R. L. Bar-Or, and H. Sompolinsky, "Theory of orientation tuning in visual cortex," *Proceedings of the National Academy of Sciences of the United States of America*, vol. 92, no. 9, pp. 3844–3848, 1995.

[29] P. C. Bressloff and J. D. Cowan, "A spherical model for orientation and spatial-frequency tuning in a cortical hypercolumn," *Philosophical Transactions of the Royal Society B: Biological Sciences*, vol. 358, no. 1438, pp. 1643–1667, 2003.

[30] S. Romani and M. Tsodyks, "Continuous attractors with morphed/correlated maps," *PLoS Computational Biology*, vol. 6, no. 8, Article ID e1000869, 2010.

[31] B. Ermentrout, "Neural networks as spatio-temporal pattern-forming systems," *Reports on Progress in Physics*, vol. 61, no. 4, pp. 353–430, 1998.

Hindawi Publishing Corporation
Journal of Applied Mathematics
Volume 2014, Article ID 248407, 14 pages
http://dx.doi.org/10.1155/2014/248407

Research Article

Modeling TB-HIV Syndemic and Treatment

Cristiana J. Silva and Delfim F. M. Torres

Center for Research and Development in Mathematics and Applications (CIDMA), Department of Mathematics, University of Aveiro, 3810-193 Aveiro, Portugal

Correspondence should be addressed to Delfim F. M. Torres; delfim@ua.pt

Received 27 March 2014; Accepted 3 June 2014; Published 8 July 2014

Academic Editor: Pedro Serranho

Copyright © 2014 C. J. Silva and D. F. M. Torres. This is an open access article distributed under the Creative Commons Attribution License, which permits unrestricted use, distribution, and reproduction in any medium, provided the original work is properly cited.

Tuberculosis (TB) and human immunodeficiency virus (HIV) can be considered a deadly human syndemic. In this paper, we formulate a model for TB and HIV transmission dynamics. The model considers both TB and acquired immune deficiency syndrome (AIDS) treatment for individuals with only one of the two infectious diseases or both. The basic reproduction number and equilibrium points are determined and stability is analyzed. Through simulations, we show that TB treatment for individuals with only TB infection reduces the number of individuals that become coinfected with TB and HIV/AIDS and reduces the diseases (TB and AIDS) induced deaths. Analogously, the treatment of individuals with only AIDS also reduces the number of coinfected individuals. Further, TB treatment for coinfected individuals in the active and latent stage of TB disease implies a decrease of the number of individuals that passes from HIV-positive to AIDS.

1. Introduction

Tuberculosis (TB) and human immunodeficiency virus/acquired immune deficiency syndrome (HIV/AIDS) are the leading causes of death from an infectious disease worldwide [1]. Individuals infected with HIV are more likely to develop TB disease because of their immunodeficiency, and HIV infection is the most powerful risk factor for progression from TB infection to disease [2]. This interaction justifies the fact that HIV and TB can be considered a deadly human *syndemic*, where syndemic refers to the convergence of two or more diseases that act synergistically to magnify the burden of disease [3].

Following UNAIDS global report on AIDS epidemic 2013 [4], globally, an estimated 35.3 million people were living with HIV in 2012, an increase from previous years as more people are receiving the life-saving antiretroviral therapy (ART). There were approximately 2.3 million new HIV infections globally, showing a 33% decline in the number of new infections with respect to 2001. At the same time, the number of AIDS deaths is also declining with around 1.6 million AIDS deaths in 2012, down from about 2.3 million in 2005. In 2012, 1.1 million of 8.6 million people who developed TB worldwide were HIV-positive. The number of people dying from HIV-associated TB has been falling since 2003. However, there were still 320 000 deaths from HIV-associated TB in 2012 and further efforts are needed to reduce this burden [1]. ART is a critical intervention for reducing the risk of TB morbidity and mortality among people living with HIV and, when combined with isoniazid preventive therapy, it can have a significant impact on TB prevention [1].

Collaborative TB/HIV activities (including HIV testing, ART therapy, and TB preventive measures) are crucial for the reduction of TB-HIV coinfected individuals. The World Health Organization (WHO) estimates that these collaborative activities prevented 1.3 million people from dying, from 2005 to 2012. However, significant challenges remain: the reduction of tuberculosis related deaths among people living with HIV has slowed in recent years; the ART therapy is not being delivered to TB-HIV coinfected patients in the majority of the countries with the largest number of TB/HIV patients; the pace of treatment scale-up for TB/HIV patients has slowed; less than half of notified TB patients were tested for HIV in 2012; and only a small fraction of TB/HIV-infected individuals received TB preventive therapy [4].

The study of the joint dynamics of TB and HIV presents formidable mathematical challenges due to the fact that the models of transmission are quite distinct [5]. Few mathematical models have been proposed for TB-HIV coinfection (see, e.g., [5–9]). Kirschner [7] developed a cellular model

for HIV-1 and TB coinfection inside a host. Roeger et al. [5] proposed a population model for TB-HIV/AIDS coinfection transmission dynamics, assuming that TB-infected individuals in the active stage of the disease are too ill to remain sexually active and therefore they are unable to transmit HIV. In this work, we assume that active TB-infected individuals are susceptible to HIV infection. Naresh and Tripathi [8] proposed a model for TB-HIV coinfection in a variable size population with only TB treatment. Here we consider TB and HIV treatment in different stages of the disease. Bhunu et al. [6] studied a TB-HIV coinfection model with both TB and HIV treatment. The authors did not take into account that an individual coinfected with TB and HIV can effectively recover from TB infection. We assume that TB can be cured, even in HIV-positive individuals [1]. Sharomi et al. [9] also considered these assumptions, subdividing the total population into 15 classes. It is our aim in this work to develop a model that balances two goals: simplicity and useful information.

The paper is organized as follows. Section 2 describes our model for TB-HIV syndemic with TB and HIV treatment. In Section 3, the positivity and boundedness of solutions of the model are proved and in Section 4 equilibrium points and respective stability are analyzed. Section 5 is devoted to numerical simulations and discussion of results.

2. TB-HIV/AIDS Model

The model subdivides the human population into 10 mutually exclusive compartments, namely, susceptible individuals (S), TB-latently infected individuals, who have no symptoms of TB disease and are not infectious (L_T), TB-infected individuals, who have active TB disease and are infectious (I_T), TB-recovered individuals (R_T), HIV-infected individuals with no clinical symptoms of AIDS (I_H), HIV-infected individuals with AIDS clinical symptoms (A), TB-latent individuals coinfected with HIV (pre-AIDS) (L_{TH}), HIV-infected individuals (pre-AIDS) coinfected with active TB disease (I_{TH}), TB-recovered individuals with HIV infection without AIDS symptoms (R_{TH}), and HIV-infected individuals with AIDS symptoms coinfected with TB (A_T). The total population at time t, denoted by $N(t)$, is given by

$$\begin{aligned} N(t) = {} & S(t) + L_T(t) + I_T(t) + R_T(t) + I_H(t) + A(t) \\ & + I_{TH}(t) + L_{TH}(t) + R_{TH}(t) + A_T(t). \end{aligned} \tag{1}$$

The susceptible population is increased by the recruitment of individuals (assumed susceptible) into the population, at a rate Λ. All individuals suffer from natural death, at a constant rate μ. Susceptible individuals acquire TB infection from individuals with active TB at a rate λ_T, given by

$$\lambda_T = \frac{\beta_1}{N}\left(I_T + I_{TH} + A_T\right), \tag{2}$$

where β_1 is the effective contact rate for TB infection. Similarly, susceptible individuals acquire HIV infection, following effective contact with people infected with HIV at a rate λ_H, given by

$$\lambda_H = \frac{\beta_2}{N}\left[I_H + I_{TH} + L_{TH} + R_{TH} + \eta\left(A + A_T\right)\right], \tag{3}$$

where β_2 is the effective contact rate for HIV transmission and the modification parameter $\eta \geqslant 1$ accounts for the relative infectiousness of individuals with AIDS symptoms, in comparison to those infected with HIV with no AIDS symptoms. Individuals with AIDS symptoms are more infectious than HIV-infected individuals (pre-AIDS) because they have a higher viral load and there is a positive correlation between viral load and infectiousness [14].

Individuals leave the latent TB class L_T by becoming infectious, at a rate k_1, or recovered, with a treatment rate τ_1. The treatment rate for active TB-infected individuals is τ_2. We assume that TB-recovered individuals R_T acquire partial immunity and the transmission rate for this class is given by $\beta_1'\lambda_T$ with $\beta_1' \leqslant 1$. Individuals with active TB disease suffer induced death at a rate d_T. We assume that individuals in the class R_T are susceptible to HIV infection at a rate λ_H. On the other hand, TB-active infected individuals I_T are susceptible to HIV infection, at a rate $\delta\lambda_H$, where the modification parameter $\delta \geqslant 1$ accounts for higher probability of individuals in class I_T to become HIV-positive.

HIV-infected individuals (with no AIDS symptoms) progress to the AIDS class A, at a rate ρ_1. HIV-infected individuals with AIDS symptoms are treated for HIV at the rate α_1 and suffer induced death at a rate d_A. Individuals in the class I_H are susceptible to TB infection at a rate $\psi\lambda_T$, where $\psi \geqslant 1$ is a modification parameter traducing the fact that HIV infection is a driver of TB epidemic [3].

HIV-infected individuals (pre-AIDS) coinfected with TB-disease, in the active stage I_{TH}, are treated for TB at the rate τ_3 and progress to the AIDS-TB coinfection class A_T at a rate ρ_2. Individuals in the class I_{TH} suffer TB induced death at a rate d_T. The anti-TB drugs can prevent or decrease the likelihood of TB infection progression to active TB disease in individuals in the class L_{TH} [13]. The treatment rate for individuals in this class is given by τ_4. However, individuals in the class L_{TH} are more likely to progress to active TB disease than individuals infected only with latent TB. In our model, this progression rate is given by k_2. Similarly, HIV infection makes individuals more susceptible to TB reinfection when compared with non-HIV-positive patients. The modification parameter associated with the TB reinfection rate, for individuals in the class R_{TH}, is given by β_2', where $\beta_2' \geqslant 1$. Individuals in this class progress to class A_T, at a rate ρ_3.

HIV-infected individuals (with AIDS symptoms), coinfected with TB, are treated for HIV, at a rate α_2. Individuals in the class A_T suffer from AIDS-TB coinfection induced death rate, at a rate d_{TA}.

The aforementioned assumptions result in the following system of differential equations that describes the transmission dynamics of TB and HIV disease:

$$\begin{aligned} \dot{S}(t) &= \Lambda - \lambda_T S(t) - \lambda_H S(t) - \mu S(t), \\ \dot{L}_T(t) &= \lambda_T S(t) + \beta_1'\lambda_T R_T(t) - \left(k_1 + \tau_1 + \mu\right) L_T(t), \\ \dot{I}_T(t) &= k_1 L_T(t) - \left(\tau_2 + d_T + \mu + \delta\lambda_H\right) I_T(t), \\ \dot{R}_T(t) &= \tau_1 L_T(t) + \tau_2 I_T(t) - \left(\beta_1'\lambda_T + \lambda_H + \mu\right) R_T(t), \end{aligned}$$

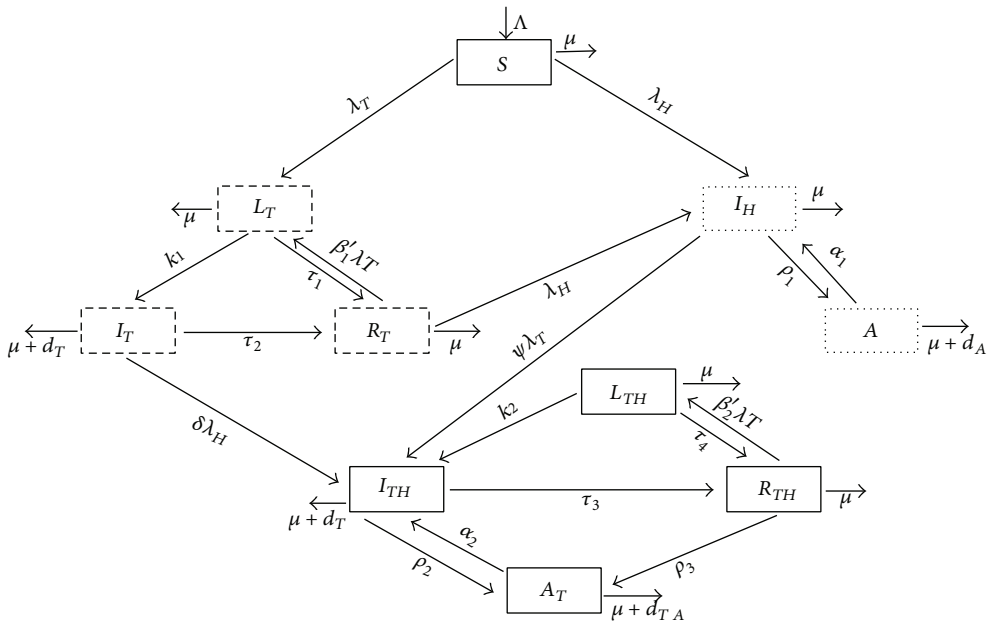

Figure 1: Model for TB-HIV/AIDS transmission with treatment.

$$\begin{aligned}
\dot{I}_H(t) &= \lambda_H S(t) - (\rho_1 + \psi\lambda_T + \mu) I_H(t) \\
&\quad + \alpha_1 A(t) + \lambda_H R_T(t), \\
\dot{A}(t) &= \rho_1 I_H(t) - \alpha_1 A(t) - (\mu + d_A) A(t), \\
\dot{L}_{TH}(t) &= \beta_2' \lambda_T R_{TH}(t) - (k_2 + \tau_4 + \mu) L_{TH}(t), \\
\dot{I}_{TH}(t) &= \delta\lambda_H I_T(t) + \psi\lambda_T I_H(t) + \alpha_2 A_T(t) \\
&\quad + k_2 L_{TH}(t) - (\tau_3 + \rho_2 + \mu + d_T) I_{TH}(t), \\
\dot{R}_{TH}(t) &= \tau_3 I_{TH}(t) + \tau_4 L_{TH}(t) - \left(\beta_2' \lambda_T + \rho_3 + \mu\right) R_{TH}, \\
\dot{A}_T(t) &= \rho_2 I_{TH}(t) + \rho_3 R_{TH} - (\alpha_2 + \mu + d_{TA}) A_T(t).
\end{aligned} \tag{4}$$

The model flow is described in Figure 1. The initial conditions of model (4) satisfy

$$\begin{aligned}
&S(0) = S_0 \geqslant 0, \qquad L_T(0) = L_{T0} \geqslant 0, \qquad I_T(0) = I_{T0} \geqslant 0, \\
&R_T(0) = R_{T0} \geqslant 0, \\
&I_H(0) = I_{H0} \geqslant 0, \qquad A(0) = A_0 \geqslant 0, \\
&L_{TH}(0) = L_{TH0} \geqslant 0, \\
&I_{TH}(0) = I_{TH0} \geqslant 0, \qquad R_{TH}(0) = R_{TH0} \geqslant 0, \\
&A_T(0) = A_{T0} \geqslant 0.
\end{aligned} \tag{5}$$

Note that if we consider the submodel of (4) with no HIV/AIDS disease, that is, $I_H = A = L_{TH} = I_{TH} = R_{TH} = A_T = 0$, then we obtain the TB model from [12]. On the other hand, if we consider the submodel with no TB, that is, $L_T = I_T = R_T = L_{TH} = I_{TH} = R_{TH} = A_T = 0$, then we obtain an HIV/AIDS model based on the models proposed in [6, 15].

3. Positivity and Boundedness of Solutions

Let $(S, L_T, I_T, R_T, I_H, A, L_{TH}, I_{TH}, R_{TH}, A_T) \in \mathbb{R}_+^{10}$ be any solution of (4) with initial conditions (5). Consider the biologically feasible region given by

$$\begin{aligned}
\Omega = \Bigg\{ &(S, L_T, I_T, R_T, I_H, A, L_{TH}, I_{TH}, R_{TH}, A_T) \\
&\in \mathbb{R}_+^{10} : 0 \leqslant N(t) \leqslant \frac{\Lambda}{\mu} \Bigg\}.
\end{aligned} \tag{6}$$

For the model system (4) to be epidemiologically meaningful, it is important to prove that all its state variables are nonnegative for all time $t > 0$. Suppose, for example, that at some $\bar{t} > 0$ the variable L_T becomes zero, that is, $L_T(\bar{t}) = 0$, while all other variables are positive. Then, from the L_T equation we have $dL_T(\bar{t})/dt > 0$. Thus, $L_T(t) \geqslant 0$ for all $t > 0$. Analogously, we can prove that all variables remain nonnegative for all time $t > 0$.

Adding all equations in model (4) gives

$$\begin{aligned}
\frac{dN}{dt}(t) &= \Lambda - \mu N(t) - d_T I_T(t) - d_A A(t) \\
&\quad - d_T I_{TH}(t) - d_{TA} A_T(t).
\end{aligned} \tag{7}$$

Since $N(t) \geqslant I_T(t) + A(t) + I_{TH}(t) + A_T(t)$, then

$$\Lambda - (\mu + d_T + d_A + d_{TA}) N(t) \leqslant \frac{dN}{dt}(t) \leqslant \Lambda - \mu N(t). \tag{8}$$

Therefore, we conclude that $N(t)$ is bounded for all $t > 0$ and every solution of system (4) with initial condition in Ω remains in Ω. This result is summarized below.

Lemma 1. *The region Ω is positively invariant for model (4) with nonnegative initial conditions in $\mathbb{R}^{10}_{+}$.*

4. Stability Analysis

Model (4) has four nonnegative equilibria, namely,

(i) the disease-free equilibrium (no disease):

$$\begin{aligned}\Sigma_0 &= \left(S_0, L_{T_0}, I_{T_0}, R_{T_0}, I_{H_0}, A_0, L_{TH_0}, I_{TH_0}, R_{TH_0}, A_{T_0}\right)\\ &= \left(\frac{\Lambda}{\mu}, 0, 0, 0, 0, 0, 0, 0, 0, 0\right),\end{aligned} \tag{9}$$

(ii) the HIV-AIDS free equilibrium:

$$\Sigma_T = \left(S^{\diamond}, L_T^{\diamond}, I_T^{\diamond}, R_T^{\diamond}, I_H^{\diamond}, A^{\diamond}, L_{TH}^{\diamond}, I_{TH}^{\diamond}, R_{TH}^{\diamond}, A_T^{\diamond}\right) \tag{10}$$

with $I_T^{\diamond} > 0$ and $I_H^{\diamond} = A^{\diamond} = L_{TH}^{\diamond} = I_{TH}^{\diamond} = R_{TH}^{\diamond} = A_T^{\diamond} = 0$ for $R_1 > 1$, where R_1 is the basic reproduction number of model (4) with $I_H = A = L_{TH} = I_{TH} = R_{TH} = A_T = 0$ (only TB model) that is given by

$$R_1 = \frac{\Lambda}{N\mu}\left(\frac{\beta_1}{d_T + \mu + \tau_2}\right)\left(\frac{k_1}{k_1 + \tau_1 + \mu}\right) \tag{11}$$

(see [12]),

(iii) the TB-free equilibrium:

$$\Sigma_H = \left(S^{\star}, L_T^{\star}, I_T^{\star}, R_T^{\star}, I_H^{\star}, A^{\star}, L_{TH}^{\star}, I_{TH}^{\star}, R_{TH}^{\star}, A_T^{\star}\right) \tag{12}$$

with $L_T^{\star} = I_T^{\star} = R_T^{\star} = L_{TH}^{\star} = I_{TH}^{\star} = R_{TH}^{\star} = A_T^{\star} = 0$ and

$$S^{\star} = \frac{\Lambda}{\mu R_2}, \tag{13}$$

$$I_H^{\star} = \left(R_2 - 1\right)\frac{\mu N_H\left(\alpha_1 + d_A + \mu\right)}{\beta_2\left(\alpha_1 + d_A + \mu + \eta\rho_1\right)}, \tag{14}$$

$$A^{\star} = \left(R_2 - 1\right)\frac{\rho_1\mu N_H}{\beta_2\left(\alpha_1 + d_A + \mu + \eta\rho_1\right)}, \tag{15}$$

for $R_2 > 1$, where R_2 is the basic reproduction number of model (4) with $L_T = I_T = R_T = L_{TH} = I_{TH} = R_{TH} = A_T = 0$ (only HIV-AIDS model); that is,

$$R_2 = \frac{\Lambda}{N\mu}\beta_2\left(\frac{\mu + \alpha_1 + d_A + \eta\rho_1}{\mu\alpha_1 + \left(\mu + \rho_1\right)\left(\mu + d_A\right)}\right), \tag{16}$$

(iv) the syndemic equilibrium:

$$\Sigma^{*} = \left(S^{*}, L_T^{*}, I_T^{*}, R_T^{*}, I_H^{*}, A^{*}, L_{TH}^{*}, I_{TH}^{*}, R_{TH}^{*}, A_T^{*}\right) \tag{17}$$

with $I_T^{*} > 0$, $I_H^{*} > 0$, $A^{*} > 0$, $L_{TH}^{*} > 0$, $I_{TH}^{*} > 0$, $R_{TH}^{*} > 0$, and $A_T^{*} > 0$, for $R_0 > 1$, where R_0 is the basic reproduction number of model (4); that is,

$$R_0 = \max\left\{R_1, R_2\right\}. \tag{18}$$

The details of the computation of the basic reproduction number R_0 are given in Appendix A.

The following theorem states the stability of the equilibrium points.

Theorem 2. *The disease-free equilibrium Σ_0 is locally asymptotically stable if $R_0 < 1$ and unstable if either $R_i > 1$ with $i = 1, 2$. The HIV-AIDS free equilibrium Σ_T is locally asymptotically stable if $R_1 > 1$, and the TB-free equilibrium Σ_H is locally asymptotically stable for R_2 near 1.*

Details of the proof of Theorem 2 are given in Appendix B.

Explicit expressions for the coinfection endemic equilibrium Σ^{*} are very difficult to compute analytically. In Section 5, we consider an example, with $R_0 > 1$, for which there exists a syndemic equilibrium, and analyze, numerically, the local asymptotical stability of the syndemic equilibrium Σ^{*}.

5. Numerical Analysis and Discussion

For numerical simulations, we consider the following initial conditions for system (4):

$$\begin{aligned}&\left(S(0), L_T(0), I_T(0), R_T(0), I_H(0), A(0),\right.\\ &\left.L_{TH}(0), I_{TH}(0), R_{TH}(0), A_T(0)\right)\\ &= \left(\frac{60N}{100}, \frac{14N}{100}, \frac{3N}{100}, 0, \frac{4N}{100}, \frac{N}{100}, \frac{12N}{100}, \frac{5N}{100}, 0, \frac{N}{100}\right)\end{aligned} \tag{19}$$

with $N = 50000$. The parameters of model (4) take the values of Table 1.

5.1. Equilibrium Points and Stability Analysis. In Table 2 we show the effect of the transmission coefficient β_1 on the state $I_T^{\diamond}$ of the HIV-free equilibrium Σ_T and on the basic reproduction number R_1. Table 3 shows the effect of the transmission coefficient β_2 on the states $I_H^{\star}$ and $A^{\star}$ of the TB-free equilibrium Σ_H and on the basic reproduction number R_2. We conclude that the equilibrium states $I_T^{\diamond}$ and $(I_H^{\star}, A^{\star})$ increase with the transmission coefficients β_1 and β_2, respectively.

In Figure 2 we considered different initial conditions in a neighborhood of the initial conditions given by (19) and $R_0 < 1$ ($R_1 < 1$ and $R_2 < 1$) to illustrate the stability of the disease-free equilibrium Σ_0 given by (9). In these numerical simulations we considered $\beta_1 = 2.7$ and $\beta_2 = 0.03$, corresponding to $R_1 = 0.62632$ and $R_2 = 0.55077$, while the rest of the parameters take the values in Table 1.

Figure 3 shows that, for $R_0 > 1$, the syndemic equilibrium Σ^{*} exists. We considered different initial conditions for the state variables of system (4) in a neighborhood of (19), $\beta_1 = 6$ and $\beta_2 = 0.1$, corresponding to $R_1 = 1.39239$ and $R_2 = 1.83593$, and the rest of the parameters take the values in

Table 1: Parameters of the TB-HIV/AIDS model (4).

Symbol	Value	References	Symbol	Value	References
Λ	714		τ_4	$1\ \text{yr}^{-1}$	
μ	$1/70\ \text{yr}^{-1}$		ρ_1	$0.1\ \text{yr}^{-1}$	[10, 11]
β_1	Variable		ρ_2	$0.25\ \text{yr}^{-1}$	
β_2	Variable		ρ_3	$0.125\ \text{yr}^{-1}$	
β_1'	0.9		α_1	$0.33\ \text{yr}^{-1}$	[6]
β_2'	1.1		α_2	$0.33\ \text{yr}^{-1}$	
k_1	1	[12]	ψ	1.07	
k_2	$1.3k_1$	[13]	d_T	$1/8\ \text{yr}^{-1}$	
τ_1	$1\ \text{yr}^{-1}$	[12]	d_A	$0.3\ \text{yr}^{-1}$	
τ_2	$2\ \text{yr}^{-1}$	[12]	d_{TA}	$0.33\ \text{yr}^{-1}$	
τ_3	$2\ \text{yr}^{-1}$		η	1.02	
δ	1.03				

Table 2: Effect of β_1 on $I_T^{\diamond}$ and R_1.

β_1	4.3	6	10	15	50
R_1	0.99788	1.39239	2.32065	3.48097	11.60326
$I_T^{\diamond}$	0.00397	903.93492	2206.57268	2870.72755	3804.50589

Table 3: Effect of β_2 on $I_H^{\star}$, $A^{\star}$, and R_2.

β_2	0.051	0.055	0.07	0.09	0.99
R_2	0.93669	1.01016	1.28566	1.65299	1.81829
$I_H^{\star}$	0.01708	135.73817	2516.54721	4472.84980	4930.48696
$A^{\star}$	0.00266	21.07182	390.59491	694.23361	765.26396

Table 1. We observe that the state variables converge to Σ^* when $t \to \infty$. In this case, Σ^* is given by

$$\begin{aligned}\Sigma^* &= \left(S^*, L_T^*, I_T^*, R_T^*, I_H^*, A^*, L_{TH}^*, I_{TH}^*, R_{TH}^*, A_T^*\right)\\ &= (4766.84, 2019.66, 943.06, 28621.89, 362.66, 56.29,\\ &\quad 31.39, 55.15, 495.68, 112.33)\,.\end{aligned} \tag{20}$$

5.2. Treatment Impact on TB-HIV/AIDS Coinfection. Consider $\beta_1 = 13$ and $\beta_2 = 0.06$, while the rest of the parameters take the values of Table 1. Figure 4 shows the impact of treating the individuals with active and latent TB on the number of individuals coinfected with TB-HIV/AIDS. The treatment of individuals with only TB, I_T and L_T, has a positive impact on the reduction of the number of individuals coinfected with TB-HIV/AIDS. Moreover, the number of individuals that suffered from disease (TB and AIDS) induced death is higher when individuals with TB-single infection are not treated. In this case, the total population at the end of 20 years is around 10509 and, in the case where individuals with only TB are treated, the total population at the end of 20 years is around 29758 individuals. In Figure 5, we assume that there are no disease induced deaths; that is, $d_T = d_A = d_{TA} = 0$. The impact of treating individuals with only TB on the reduction of the number of coinfected individuals is more evident.

Figure 6 illustrates the case where we compare the number of individuals coinfected with TB-HIV/AIDS when individuals with only AIDS symptoms A_T are or are not treated. We observe that treating this class of individuals is important for the reduction of the number of individuals that become coinfected, with special attention to the individuals that have AIDS symptoms and TB infection. In Figure 7, we considered that there are no disease induced deaths ($d_T = d_A = d_{TA} = 0$). It is crucial that TB-infected individuals (in the latent and active stage), which are also HIV-positive, take anti-TB drugs, since they can recover from TB. We analyze the impact of treating TB-HIV/AIDS coinfected individuals L_{TH}, I_{TH}, and A_T on the reduction of the number of individuals coinfection. If anti-TB drugs are supplied, then latent and active TB individuals with HIV can recover and pass to the class R_{TH} (the number of individuals in the class R_{TH} tends to zero when TB is not treated). In Figure 8, we observe that, after 7 years, the number of individuals infected with active TB and HIV, in the case without treatment, becomes lower than in the case with treatment. This is due to the fact that coinfection precipitates AIDS symptoms.

Appendices

A. Computation of R_0

The basic reproduction number represents the expected average number of new infections produced by a single infectious

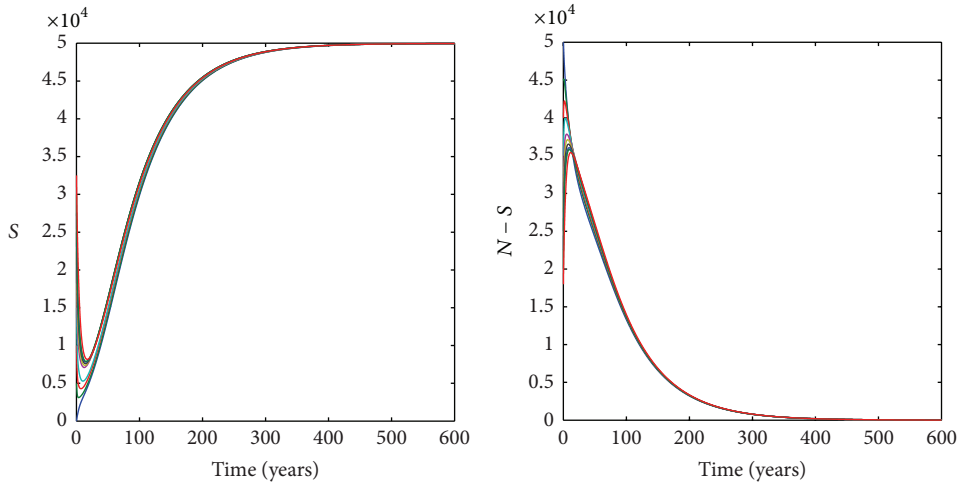

Figure 2: Stability of the disease-free equilibrium (9).

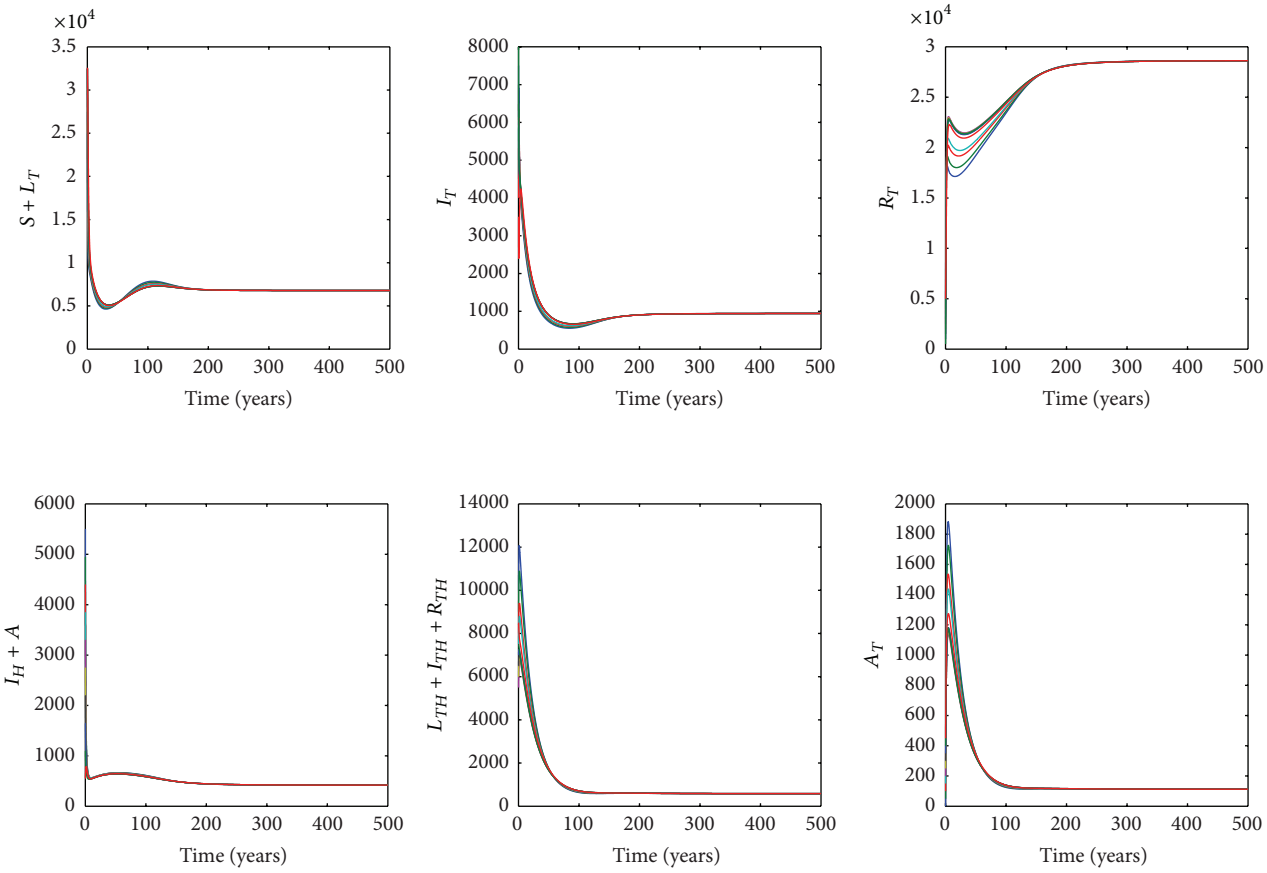

Figure 3: Stability of the syndemic equilibrium Σ^*.

individual when in contact with a completely susceptible population [16]. Following [16], the basic reproduction number R_0 is obtained as the spectral radius of the matrix $F \cdot V^{-1}$ at the disease-free equilibrium Σ_0, given by (9), with $F = [F_1 \quad F_2]$,

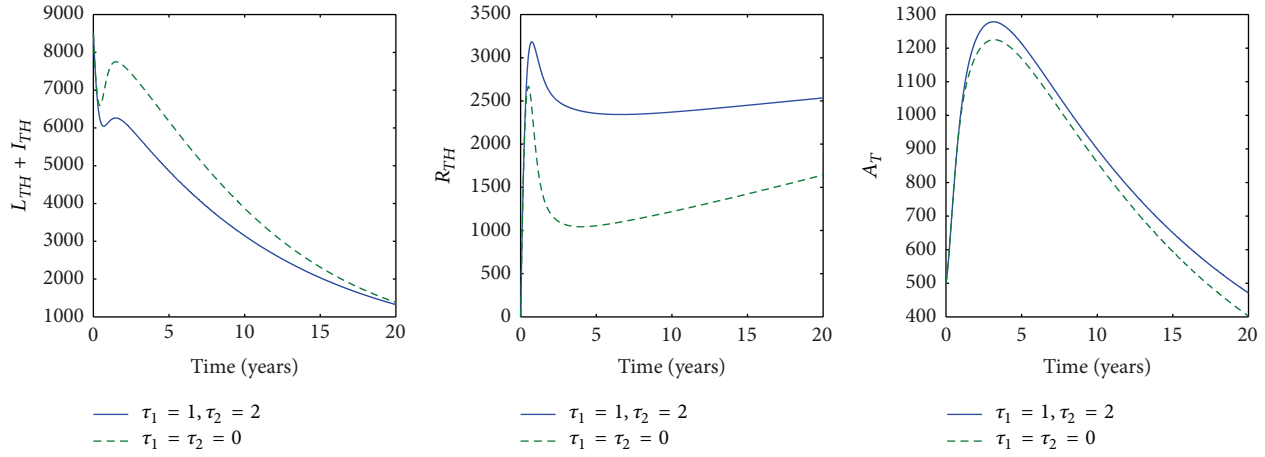

Figure 4: Impact of TB treatment on single-infected individuals with disease induced death.

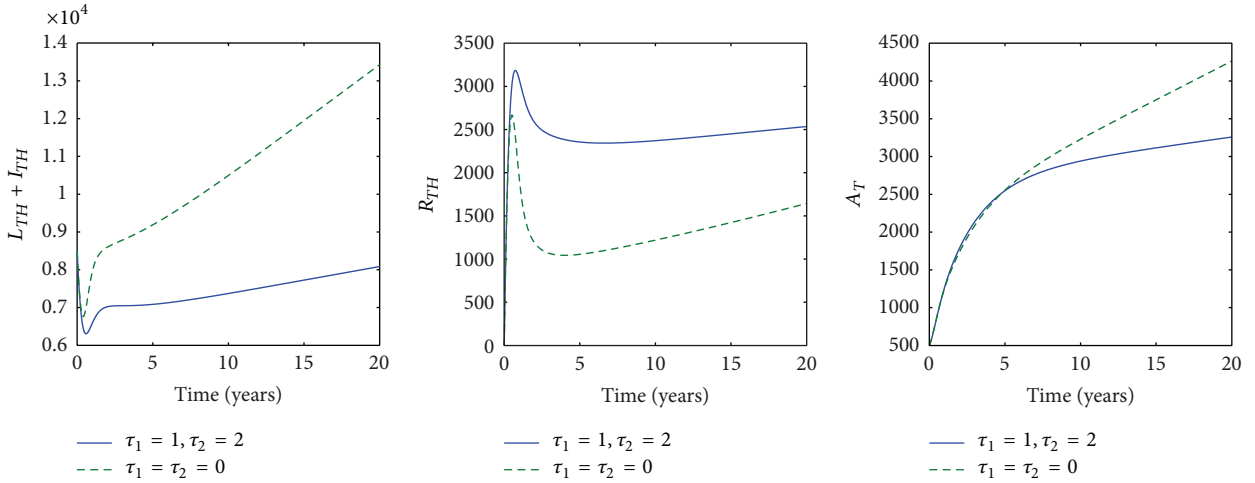

Figure 5: Impact of TB treatment on single-infected individuals with no disease induced death.

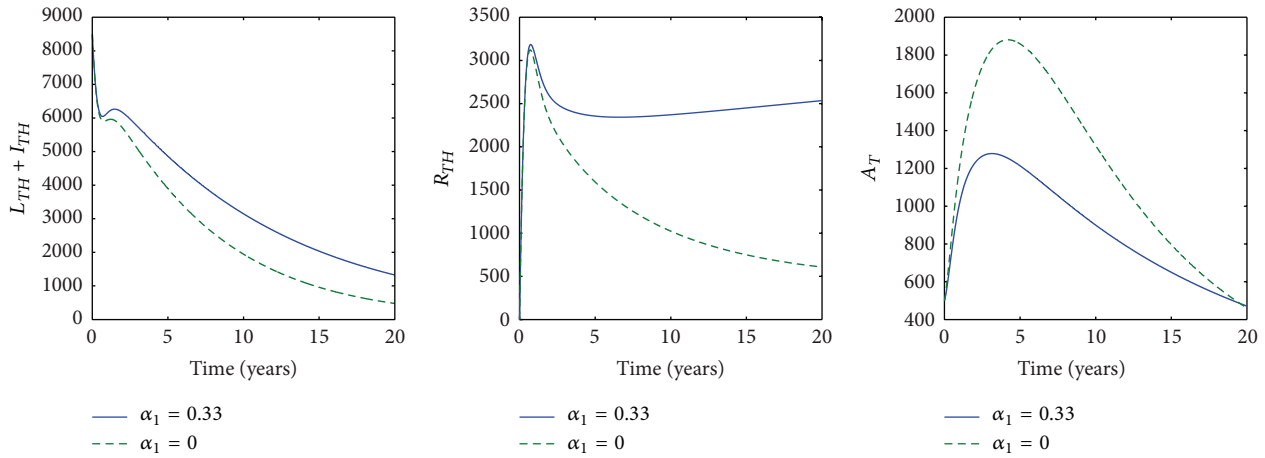

Figure 6: Impact of AIDS treatment on single-infected individuals with disease induced death.

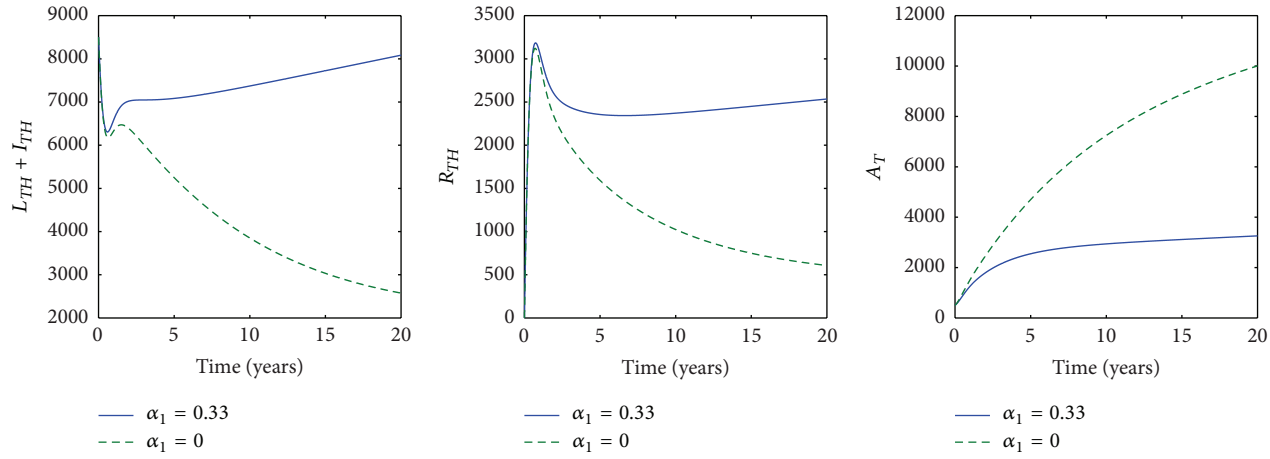

Figure 7: Impact of AIDS treatment on single-infected individuals with no disease induced death.

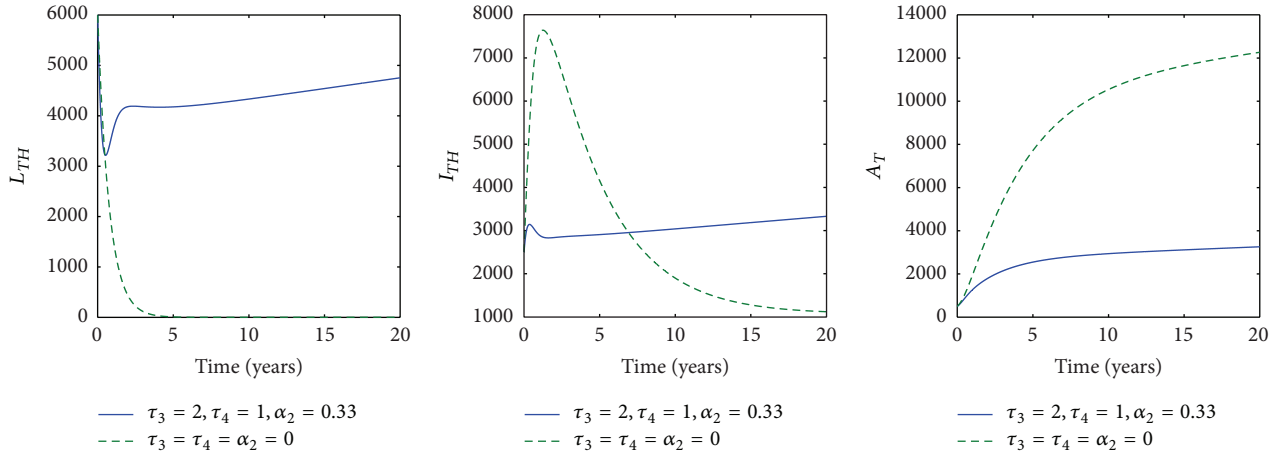

Figure 8: Impact of TB and AIDS treatment on coinfected individuals with no disease induced death.

$$F_1 = \begin{bmatrix} 0 & 0 & 0 & 0 & 0 \\ \lambda_T & 0 & \dfrac{\beta_1 S}{N} + \dfrac{\beta_1' \beta_1 R_T}{N} & \beta_1' \lambda_T & 0 \\ 0 & 0 & 0 & 0 & 0 \\ 0 & 0 & 0 & 0 & 0 \\ \lambda_H & 0 & 0 & \lambda_H & \dfrac{\beta_2 S}{N} + \dfrac{\beta_2 R_T}{N} \\ 0 & 0 & 0 & 0 & 0 \\ 0 & 0 & \dfrac{\beta_2' \beta_1 R_{TH}}{N} & 0 & 0 \\ 0 & 0 & \delta\lambda_H + \dfrac{\psi\beta_1 I_H}{N} & 0 & \dfrac{\delta\beta_2 I_T}{N} + \psi\lambda_T \\ 0 & 0 & 0 & 0 & 0 \\ 0 & 0 & 0 & 0 & 0 \end{bmatrix},$$

$$F_2 = \begin{bmatrix} 0 & 0 & 0 & 0 & 0 \\ 0 & 0 & \frac{\beta_1 S}{N} + \frac{\beta_1' \beta_1 R_T}{N} & 0 & \frac{\beta_1 S}{N} + \frac{\beta_1' \beta_1 R_T}{N} \\ 0 & 0 & 0 & 0 & 0 \\ 0 & 0 & 0 & 0 & 0 \\ \frac{\beta_2 \eta S}{N} + \frac{\beta_2 \eta R_T}{N} & \frac{\beta_2 S}{N} + \frac{\beta_2 R_T}{N} & \frac{\beta_2 S}{N} + \frac{\beta_2 R_T}{N} & \frac{\beta_2 S}{N} + \frac{\beta_2 R_T}{N} & \frac{\beta_2 S \eta}{N} + \frac{R_T \beta_2 \eta}{N} \\ 0 & 0 & 0 & 0 & 0 \\ 0 & 0 & \frac{\beta_2' \beta 1 R_{TH}}{N} & \beta_2' \lambda_T & \frac{\beta_2' \beta_1 R_{TH}}{N} \\ \frac{\delta \beta_2 \eta I_T}{N} & \frac{\delta \beta_2 I_T}{N} & \frac{\delta \beta_2 I_T}{N} + \frac{\psi \beta_1 I_H}{N} & \frac{\delta \beta_2 I_T}{N} & \frac{\delta \beta_2 \eta I_T}{N} + \frac{\psi \beta_1 I_H}{N} \\ 0 & 0 & 0 & 0 & 0 \\ 0 & 0 & 0 & 0 & 0 \end{bmatrix}, \tag{A.1}$$

and $V = [V_1 \quad V_2]$ with

$$V_1 = \begin{bmatrix} \lambda_T + \lambda_H + \mu & 0 & \frac{\beta_1 S}{N} & 0 & \frac{\beta_2 S}{N} \\ 0 & k_1 \tau_1 + \mu & 0 & 0 & 0 \\ 0 & -k_1 & \tau_2 + \delta \lambda_H + \mu + d_T & 0 & \frac{\delta \beta_2 I_T}{N} \\ 0 & -\tau_1 & -\tau_2 + \frac{\beta_1' \beta_1 R_T}{N} & \beta_1' \lambda_T + \lambda_H + \mu & \frac{\beta_2 R_T}{N} \\ 0 & 0 & \frac{\psi \beta_1 I_H}{N} & 0 & \rho_1 + \psi \lambda_T + \mu \\ 0 & 0 & 0 & 0 & -\rho_1 \\ 0 & 0 & 0 & 0 & 0 \\ 0 & 0 & 0 & 0 & 0 \\ 0 & 0 & \frac{\beta_2' \beta_1 R_{TH}}{N} & 0 & 0 \\ 0 & 0 & 0 & 0 & 0 \end{bmatrix},$$

$$V_2 = \begin{bmatrix} \frac{\beta_2 \eta S}{N} & \frac{\beta_2 S}{N} & \frac{\beta_1 S}{N} + \frac{\beta_2 S}{N} & \frac{\beta_2 S}{N} & \frac{\beta_1 S}{N} + \frac{\beta_2 S \eta}{N} \\ 0 & 0 & 0 & 0 & 0 \\ \frac{\delta \beta_2 \eta I_T}{N} & \frac{\delta \beta_2 I_T}{N} & \frac{\delta \beta_2 I_T}{N} & \frac{\delta \beta_2 I_T}{N} & \frac{\delta \beta_2 \eta I_T}{N} \\ \frac{\beta_2 \eta R_T}{N} & \frac{\beta_2 R_T}{N} & \left(\frac{\beta_1' \beta_1}{N} + \frac{\beta_2}{N} \right) R_T & \frac{\beta_2 R_T}{N} & \left(\frac{\beta_1' \beta_1}{N} + \frac{\beta_2 \eta}{N} \right) R_T \\ -\alpha_1 & 0 & \frac{\psi \beta_1 I_H}{N} & 0 & \frac{\psi \beta_1 I_H}{N} \\ \alpha_1 + \mu + d_A & 0 & 0 & 0 & 0 \\ 0 & k_2 + \tau_4 + \mu & 0 & 0 & 0 \\ 0 & -k_2 & \rho_2 + \tau_3 + \mu + d_T & 0 & -\alpha_2 \\ 0 & -\tau_4 & -\tau_3 + \frac{\beta_2' \beta_1 R_{TH}}{N} & \beta_2' \lambda_T + \rho_3 + \mu & \frac{\beta_2' \beta_1 R_{TH}}{N} \\ 0 & 0 & -\rho_2 & -\rho_3 & \alpha_2 + d_{TA} + \mu \end{bmatrix}. \tag{A.2}$$

The dominant eigenvalues of the matrix $F \cdot V^{-1}$ are

$$R_1 = \frac{\Lambda}{N\mu}\left(\frac{\beta_1}{d_T+\mu+\tau_2}\right)\left(\frac{k_1}{k_1+\tau_1+\mu}\right),$$
$$R_2 = \frac{\Lambda}{N\mu}\beta_2\left(\frac{\mu+\alpha_1+d_A+\eta\rho_1}{\mu\alpha_1+(\mu+\rho_1)(\mu+d_A)}\right). \tag{A.3}$$

Thus, the basic reproduction number R_0 of model (4) is given by

$$R_0 = \max\{R_1, R_2\}. \tag{A.4}$$

Note that R_1 is the basic reproduction number of model (4) with $I_T = A = L_{TH} = I_{TH} = R_{TH} = A_T = 0$ (only TB model), and R_2 is the basic reproduction number of model (4) with $L_T = I_T = R_T = L_{TH} = I_{TH} = R_{TH} = A_T = 0$ (only HIV-AIDS model).

B. Proof of Theorem 2

In this Appendix, we provide details of the proof of Theorem 2.

Local Asymptotical Stability of the Disease-Free Equilibrium Σ_0. Following Theorem 2 of [16], the disease-free equilibrium, Σ_0, is locally asymptotically stable if all the eigenvalues of the Jacobian matrix of the system (4), here denoted by $M_T(\Sigma_0)$, computed at the disease-free equilibrium Σ_0, given by (9), have negative real parts.

The Jacobian matrix of the system (4) at disease-free equilibrium Σ_0 is given by

$$M_T(\Sigma_0) = \left[M_{T1}(\Sigma_0) \;\; M_{T_2}(\Sigma_0)\right] \tag{B.1}$$

with

$$M_{T1}(\Sigma_0) = \begin{bmatrix} -\mu & 0 & -\frac{\beta_1\Lambda}{\mu N} & 0 & -\frac{\beta_2\Lambda}{\mu N} \\ 0 & -d_1 & \frac{\beta_1\Lambda}{\mu N} & 0 & 0 \\ 0 & k_1 & -d_2 & 0 & 0 \\ 0 & \tau_1 & \tau_2 & -\mu & 0 \\ 0 & 0 & 0 & 0 & \frac{\beta_2\Lambda}{\mu N} - d_3 \\ 0 & 0 & 0 & 0 & \rho_1 \\ 0 & 0 & 0 & 0 & 0 \\ 0 & 0 & 0 & 0 & 0 \\ 0 & 0 & 0 & 0 & 0 \\ 0 & 0 & 0 & 0 & 0 \end{bmatrix},$$

$$M_{T2}(\Sigma_0) = \begin{bmatrix} -\frac{\beta_2\eta\Lambda}{\mu N} & -\frac{\beta_2\Lambda}{\mu N} & -\frac{\beta_1\Lambda}{\mu N} - \frac{\beta_2\Lambda}{\mu N} & -\frac{\beta_2\Lambda}{\mu N} & -\frac{\beta_1\Lambda}{\mu N} - \frac{\beta_2\eta\Lambda}{\mu N} \\ 0 & 0 & \frac{\beta_1\Lambda}{\mu N} & 0 & \frac{\beta_1\Lambda}{\mu N} \\ 0 & 0 & 0 & 0 & 0 \\ 0 & 0 & 0 & 0 & 0 \\ \frac{\beta_2\eta\Lambda}{\mu N} + \alpha_1 & \frac{\beta_2\Lambda}{\mu N} & \frac{\beta_2\Lambda}{\mu N} & \frac{\beta_2\Lambda}{\mu N} & \frac{\beta_2\eta\Lambda}{\mu N} \\ -d_4 & 0 & 0 & 0 & 0 \\ 0 & -d_5 & 0 & 0 & 0 \\ 0 & k_2 & -d_6 & 0 & \alpha_2 \\ 0 & \tau_4 & \tau_3 & -d_7 & 0 \\ 0 & 0 & \rho_2 & \rho_3 & -d_8 \end{bmatrix}, \tag{B.2}$$

where $d_1 = k_1 + \tau_1 + \mu$; $d_2 = \tau_2 + \mu + d_T$; $d_3 = \rho_1 + \mu$; $d_4 = \alpha_1 + \mu + d_A$; $d_5 = k_2 + \mu + \tau_4$; $d_6 = \rho_2 + \tau_3 + \mu + d_T$; $d_7 = \rho_3 + \mu$; $d_8 = \alpha_2 + d_{TA} + \mu$. One has

$$\begin{aligned}
&\operatorname{trace}\left[M_T\left(\Sigma_0\right)\right] \\
&\quad = -2\mu - \left(d_1 + d_2 + d_3 + d_4 + d_5 + d_6 + d_7 + d_8\right) < 0, \\
&\det\left[M_T\left(\Sigma_0\right)\right] \\
&\quad = \frac{1}{N^2}\left(d_5\left(d_6 d_7 + d_T\left(\alpha_2 + \mu\right)d_7 + \alpha_2\mu d_6 + d_T d_{TA} d_7\right)\right. \\
&\qquad \times \left(N\mu\left(\alpha_1\mu + \left(\mu + \rho_1\right)\left(\mu + d_A\right)\right)\right. \\
&\qquad\quad \left.\left. - \beta_2\Lambda\left(\alpha_1 + \mu + d_A + \rho_1\eta\right)\right)\right. \\
&\qquad \left. \times \left(N\mu\left(d_T + \mu + \tau_2\right)\left(k_1 + \tau_1 + \mu\right) - k_1\beta_1\Lambda\right) > 0\right.
\end{aligned} \tag{B.3}$$

for

$$\begin{aligned}
R_1 &= \frac{\Lambda}{N\mu}\left(\frac{\beta_1}{d_T + \mu + \tau_2}\right)\left(\frac{k_1}{k_1 + \tau_1 + \mu}\right) < 1, \\
R_2 &= \frac{\Lambda}{N\mu}\beta_2\left(\frac{\mu + \alpha_1 + d_A + \eta\rho_1}{\mu\alpha_1 + \left(\mu + \rho_1\right)\left(\mu + d_A\right)}\right) < 1.
\end{aligned} \tag{B.4}$$

We have just proved that the disease-free equilibrium Σ_0 of model (4) is locally asymptotically stable if $R_0 < 1$ and unstable if either $R_i > 1$, $i = 1, 2$.

Global Asymptotical Stability of the Disease-Free Equilibrium Σ_0. For convenience, let us rewrite the model system (4) as

$$\begin{aligned}
\frac{dX}{dt} &= F\left(X, Z\right), \\
\frac{dZ}{dt} &= G\left(X, Z\right), \qquad G\left(X, 0\right) = 0,
\end{aligned} \tag{B.5}$$

where $X = (S, R_T)$ and $Z = (L_T, I_T, I_H, A, L_{TH}, I_{TH}, R_{TH}, A_T)$, with $X \in \mathbb{R}_+^2$ denoting (its components) the number of uninfected individuals and $Z \in \mathbb{R}_+^8$ denoting (its components) the number of infected individuals including the latent and infectious.

The disease-free equilibrium is denoted by

$$E_0 = \left(X_0, 0\right), \quad \text{where } X_0 = \left(\frac{\Lambda}{\mu}, 0\right). \tag{B.6}$$

Following [6], if

(H1) E_0 is globally asymptotically stable for $dX/dt = F(X, 0)$,

(H2) $\widehat{G}(X, Z) \geqslant 0$ for $(X, Z) \in \Omega$, where $G(X, Z) = AZ - \widehat{G}(X, Z)$, $A = D_Z G(E_0, 0)$ is a Metzler matrix, and Ω is given by (6),

then the fixed point $E_0 = (X_0, 0)$ is a globally asymptotically stable equilibrium of system (B.5). We have

$$\begin{aligned}
\frac{dX}{dt} = F\left(X, Z\right) &= \begin{bmatrix} \Lambda - \lambda_T S - \lambda_H S - \mu S \\ \tau_1 L_T + \tau_2 I_T - \left(\beta_1'\lambda_T + \lambda_H + \mu\right)R_T \end{bmatrix}, \\
F\left(X, 0\right) &= \begin{bmatrix} \Lambda - \mu S \\ -\mu R_T \end{bmatrix}, \\
\frac{dZ}{dt} &= G\left(X, Z\right) \\
&= \begin{bmatrix} \lambda_T S + \beta_1'\lambda_T R_T - \left(k_1 + \tau_1 + \mu\right)L_T \\ k_1 L_T - \left(\tau_2 + d_T + \mu + \delta\lambda_H\right)I_T \\ \lambda_H S - \left(\rho_1 + \psi\lambda_T + \mu\right)I_H + \alpha_1 A + \lambda_H R_T \\ \rho_1 I_H - \alpha_1 A - \left(\mu + d_A\right)A \\ \beta_2'\lambda_T R_{TH} - \left(k_2 + \tau_4 + \mu\right)L_{TH} \\ \delta\lambda_H I_T + \psi\lambda_T I_H + \alpha_2 A_T + k_2 L_{TH} - \left(\tau_3 + \rho_2 + \mu + d_T\right)I_{TH} \\ \tau_3 I_{TH} + \tau_4 L_{TH} - \left(\beta_2'\lambda_T + \rho_3 + \mu\right)R_{TH} \\ \rho_2 I_{TH} + \rho_3 R_{TH} - \left(\alpha_2 + \mu + d_{TA}\right)A_T \end{bmatrix},
\end{aligned} \tag{B.7}$$

and $G(X, 0) = 0$. Thus,

$$\begin{aligned}
\frac{dX}{dt} &= F\left(X, 0\right) = \begin{bmatrix} \Lambda - \mu S \\ -\mu R_T \end{bmatrix}, \\
A &= D_Z G\left(X_0, 0\right) = \begin{bmatrix} D_1 & D_2 \end{bmatrix}
\end{aligned} \tag{B.8}$$

with

$$D_1 = \begin{bmatrix} -k_1 - \tau_1 - \mu & \frac{\beta_1 \Lambda}{\mu N} & 0 & 0 \\ k_1 & -\tau_2 - \mu - d_T & 0 & 0 \\ 0 & 0 & \frac{\beta_2 \Lambda}{\mu N} - \rho_1 - \mu & \frac{\beta_2 \eta \Lambda}{\mu N} + \alpha_1 \\ 0 & 0 & \rho_1 & -\alpha_1 - \mu - d_A \\ 0 & 0 & 0 & 0 \\ 0 & 0 & 0 & 0 \\ 0 & 0 & 0 & 0 \\ 0 & 0 & 0 & 0 \end{bmatrix},$$

$$D_2 = \begin{bmatrix} 0 & \frac{\beta_1 \Lambda}{\mu N} & 0 & \frac{\beta_1 \Lambda}{\mu N} \\ 0 & 0 & 0 & 0 \\ \frac{\beta_2 \Lambda}{\mu N} & \frac{\beta_2 \Lambda}{\mu N} & \frac{\beta_2 \Lambda}{\mu N} & \frac{\beta_2 \eta \Lambda}{\mu N} \\ 0 & 0 & 0 & 0 \\ -k_2 - \tau_4 - \mu & 0 & 0 & 0 \\ k_2 & -\rho_2 - \tau_3 - \mu - d_T & 0 & \alpha_2 \\ \tau_4 & \tau_3 & -\rho_3 - \mu & 0 \\ 0 & \rho_2 & \rho_3 & -\alpha_2 - d_{TA} - \mu \end{bmatrix},$$

$$\widehat{G}(X, Z) = \begin{bmatrix} \lambda_T \left(\frac{\Lambda}{\mu} - S - \beta_1' R_T \right) \\ -\delta \lambda_H I_T \\ \lambda_H \left(\frac{\Lambda}{\mu} - S - R_T - \psi I_H \right) \\ 0 \\ -\beta_2' \lambda_T R_{TH} \\ -\left(\delta \lambda_H I_T + \psi \lambda_T I_H \right) \\ \beta_2' \lambda_T R_{TH} \\ 0 \end{bmatrix}. \tag{B.9}$$

From (B.9) the condition (H2) is not satisfied, since $\widehat{G}(X, Z) \geqslant 0$ is not true. Therefore, the disease-free equilibrium E_0 may not be globally asymptotically stable. Following [17], the backward bifurcation occurs at $R_0 = 1$ and the double endemic equilibria can be supported for $R_c < R_0 < 1$, where R_c is a positive constant.

Existence and Stability of HIV-AIDS Free Equilibrium Σ_T. The expressions for $S^\diamond$, $L_T^\diamond$, $I_T^\diamond$, and $R_T^\diamond$ are obtained if we consider a submodel of (4) for which $I_H = A = L_{TH} = I_{TH} = R_{TH} = A_T = 0$ and the total population N is given by $N_T = S + L_T + I_T + R_T$. The basic reproduction number of this submodel is given by R_1 (11). The existence, uniqueness, and local asymptotic stability of Σ_T are proven in [12, Theorem 1].

Existence and Stability of TB-Free Equilibrium Σ_H. To prove the existence of Σ_T, consider the submodel of (4) for which $L_T = I_T = R_T = L_{TH} = I_{TH} = R_{TH} = A_T = 0$ and the total population N_H is given by $N_H = S + I_H + A$. The equations of this submodel are

$$\begin{aligned} \dot{S}(t) &= \Lambda - \lambda_H S(t) - \mu S(t), \\ \dot{I}_H(t) &= \lambda_H S(t) - (\rho_1 + \mu) I_H(t) + \alpha_1 A(t), \\ \dot{A}(t) &= \rho_1 I_H(t) - \alpha_1 A(t) - (\mu + d_A) A, \end{aligned} \tag{B.10}$$

where $\lambda_H = \beta_2((I_H + \eta A)/N_H)$. Setting the right-hand sides of submodel (B.10) to zero, we obtain the endemic equilibrium $\Sigma_H^\star = (S^\star, I_H^\star, A^\star)$ given by

$$S^\star = \frac{\Lambda}{\mu R_2},$$

$$I_H^\star = (R_2 - 1)\frac{\mu N_H(\alpha_1 + d_A + \mu)}{\beta_2(\alpha_1 + d_A + \mu + \eta\rho_1)},$$
$$A^\star = (R_2 - 1)\frac{\rho_1 \mu N_H}{\beta_2(\alpha_1 + d_A + \mu + \eta\rho_1)}, \tag{B.11}$$

where $I_H^\star > 0$ and $A^\star > 0$, whenever $R_2 > 1$.

In what follows we prove the local asymptotic stability of the endemic equilibrium $\Sigma_H^\star$, using the center manifold theory [18], as described in [19, Theorem 4.1] (see also [16]), considering ART treatment. The basic reproduction number of this submodel R_2 is given by (16). Choose bifurcation parameter, β^*, by solving for β_2 from $R_2 = 1$:

$$\beta^* = \frac{\mu\alpha_1 + (\mu + \rho_1)(\mu + d_A)}{\alpha + d_A + \mu + \eta\rho}. \tag{B.12}$$

Submodel (B.10) has a disease-free equilibrium given by $\Sigma_{H0}^* = (x_{10}, x_{20}, x_{30}) = (\Lambda/\mu, 0, 0)$.

The Jacobian of the system (B.10), evaluated at Σ_{H0}^* and with $\beta_2 = \beta^*$, is given by

$$J(\Sigma_{H0}^*) = \begin{bmatrix} -\mu & -\beta_2 & -\beta_2\eta \\ 0 & \beta_2 - \rho - \mu & \beta_2\eta + \alpha \\ 0 & \rho & -\alpha - d_A - \mu \end{bmatrix}. \tag{B.13}$$

The eigenvalues of the linearized system (B.13) are

$$\lambda_1 = 0, \qquad \lambda_2 = -\mu,$$
$$\lambda_3 = -\left(\eta\rho\left(2\mu^2 + \rho + d_A + \alpha\right) + d_A(2\alpha + 2\mu + d_A) + \rho\alpha + (\mu + \alpha)^2\right)(\alpha + d_A + \mu + \eta\rho)^{-1}. \tag{B.14}$$

We observe that there is a simple eigenvalue with zero real part and the other two eigenvalues have negative real part. Thus, the system (B.10), with $\beta_2 = \beta^*$, has a hyperbolic equilibrium point and the center manifold theory [18] can be used to analyze the dynamics of submodel (B.10) near $\beta_2 = \beta^*$.

The Jacobian $J(\Sigma_{H0}^*)$ at $\beta_2 = \beta^*$ has a right eigenvector (associated with the zero eigenvalue) given by $w = [w_1, w_2, w_3]^T$, where

$$w_1 = -\frac{(\mu\alpha_1 + (\mu + \rho_1)(\mu + d_A))w_3}{\rho_1\mu},$$
$$w_2 = \frac{(\alpha_1 + d_A + \mu)w_3}{\rho_1}, \tag{B.15}$$
$$w_3 = w_3 > 0.$$

Further, $J(\Sigma_{H0}^*)$ for $\beta_2 = \beta^*$ has a left eigenvector $v = [v_1, v_2, v_3]$ (associated with the zero eigenvalue), where

$$v_1 = 0,$$
$$v_2 = \frac{v_3(\alpha_1 + d_A + \mu + \eta\rho_1)}{\alpha_1 + \eta\rho_1 + \mu\eta}, \tag{B.16}$$
$$v_3 = v_3 > 0.$$

To apply Theorem 4.1 in [19] it is convenient to let f_k represent the right-hand side of the kth equation of the system (B.10) and let x_k be the state variable whose derivative is given by the kth equation for $k = 1, 2, 3$. The local stability near the bifurcation point $\beta_2 = \beta^*$ is then determined by the signs of two associated constants, denoted by a and b, defined (respectively) by

$$a = \sum_{k,i,j=1}^{3} v_k w_i w_j \frac{\partial^2 f_k}{\partial x_i \partial x_j}(0,0),$$
$$b = \sum_{k,i=1}^{3} v_k w_i \frac{\partial^2 f_k}{\partial x_i \partial \phi}(0,0) \tag{B.17}$$

with $\phi = \beta_2 - \beta^*$.

For the system (B.10), the associated partial derivatives at the disease-free equilibrium Σ_{H0} are given by

$$\frac{\partial^2 f_1}{\partial x_2^2} = \frac{2\beta^*\mu}{\Lambda}, \qquad \frac{\partial^2 f_1}{\partial x_2 \partial x_3} = \frac{\beta^*\mu(1+\eta)}{\Lambda},$$
$$\frac{\partial^2 f_1}{\partial x_3^2} = \frac{2\beta^*\mu\eta}{\Lambda}, \qquad \frac{\partial^2 f_2}{\partial x_2^2} = \frac{-2\beta^*\mu}{\Lambda}, \tag{B.18}$$
$$\frac{\partial^2 f_2}{\partial x_2 \partial x_3} = \frac{-\beta^*\mu(1+\eta)}{\Lambda}, \qquad \frac{\partial^2 f_2}{\partial x_3^2} = \frac{-2\beta^*\mu\eta}{\Lambda}.$$

It follows from the above expressions that

$$a = -v_3 w_3^2 \beta^* \mu (k_1 + \mu + \eta\rho_1) \times \left(2k_1^2 + 4\mu k_1 + 2\mu^2 + \rho_1(\alpha_1 + \eta(\alpha_1 + \mu + 2\rho_1) + d_A(1+\eta) + \mu)\right) \times \left(\rho_1^2 \Lambda(\alpha_1 + \eta\rho_1 + \mu\eta)\right)^{-1} < 0 \tag{B.19}$$

with $k_1 = \alpha_1 + d_A$.

For the sign of b, it can be shown that the associated nonvanishing partial derivatives are

$$\frac{\partial^2 f_1}{\partial x_2 \partial \beta^*} = -1, \qquad \frac{\partial^2 f_1}{\partial x_3 \partial \beta^*} = -\eta,$$
$$\frac{\partial^2 f_2}{\partial x_2 \partial \beta^*} = 1, \qquad \frac{\partial^2 f_2}{\partial x_3 \partial \beta^*} = \eta. \tag{B.20}$$

It also follows from the above expressions that

$$b = \frac{v_3 w_3 (k_1 + \mu + \eta\rho_1)(k_1 + \mu)}{(\alpha_1 + \eta\rho_1 + \mu\eta)\rho_1} + \frac{\eta v_3 w_3 (k_1 + \mu + \eta\rho_1)}{\alpha_1 + \eta\rho_1 + \mu\eta} > 0. \tag{B.21}$$

Thus, $a < 0$ and $b > 0$. Using Theorem 4.1 of [19], the endemic equilibrium $\Sigma_H^\star$ is locally asymptotically stable for R_2 near 1.

Conflict of Interests

The authors declare that there is no conflict of interests regarding the publication of this paper.

Acknowledgments

This work was supported by Portuguese funds through the Center for Research and Development in Mathematics and Applications (CIDMA, University of Aveiro) and *The Portuguese Foundation for Science and Technology* (FCT—Fundação para a Ciência e a Tecnologia), within Project PEst-OE/MAT/UI4106/2014. Silva was also supported by FCT through the Postdoc Fellowship SFRH/BPD/72061/2010 and Torres by the FCT Project PTDC/EEI-AUT/1450/2012, cofinanced by FEDER under POFC-QREN with COMPETE Reference FCOMP-01-0124-FEDER-028894.

References

[1] WHO, *Global Tuberculosis Report*, World Health Organization, Geneva, Switzerland, 2013.

[2] H. Getahun, C. Gunneberg, R. Granich, and P. Nunn, "HIV infection-associated tuberculosis: the epidemiology and the response," *Clinical Infectious Diseases*, vol. 50, supplement 3, pp. S201–S207, 2010.

[3] C. Kwan and J. D. Ernst, "HIV and tuberculosis: a deadly human syndemic," *Clinical Microbiology Reviews*, vol. 24, no. 2, pp. 351–376, 2011.

[4] UNAIDS, *Global Report: UNAIDS Report on the Global AIDS Epidemic 2013*, World Health Organization, Geneva, Switzerland, 2013.

[5] L. W. Roeger, Z. Feng, and C. Castillo-Chavez, "Modeling TB and HIV co-infections," *Mathematical Biosciences and Engineering (MBE)*, vol. 6, no. 4, pp. 815–837, 2009.

[6] C. P. Bhunu, W. Garira, and Z. Mukandavire, "Modeling HIV/AIDS and tuberculosis coinfection," *Bulletin of Mathematical Biology*, vol. 71, no. 7, pp. 1745–1780, 2009.

[7] D. Kirschner, "Dynamics of co-infection with *M. tuberculosis* and HIV-1," *Theoretical Population Biology*, vol. 55, no. 1, pp. 94–109, 1999.

[8] R. Naresh and A. Tripathi, "Modelling and analysis of HIV-TB co-infection in a variable size population," *Mathematical Modelling and Analysis*, vol. 10, no. 3, pp. 275–286, 2005.

[9] O. Sharomi, C. N. Podder, A. B. Gumel, and B. Song, "Mathematical analysis of the transmission dynamics of HIV/TB coinfection in the presence of treatment," *Mathematical Biosciences and Engineering*, vol. 5, no. 1, pp. 145–174, 2008.

[10] http://en.wikipedia.org/wiki/HIV_disease_progression_rates.

[11] http://hivinsite.ucsf.edu/InSite?page=kb-03-01-04.

[12] C. Castillo-Chavez and Z. Feng, "To treat or not to treat: the case of tuberculosis," *Journal of Mathematical Biology*, vol. 35, no. 6, pp. 629–656, 1997.

[13] http://www.usaid.gov/news-information/fact-sheets/twin-epidemics-hiv-and-tb-co-infection.

[14] D. P. Wilson, M. G. Law, A. E. Grulich, D. A. Cooper, and J. M. Kaldor, "Relation between HIV viral load and infectiousness: a model-based analysis," *The Lancet*, vol. 372, no. 9635, pp. 314–320, 2008.

[15] J. M. Hyman, J. Li, and E. Ann Stanley, "The differential infectivity and staged progression models for the transmission of HIV," *Mathematical Biosciences*, vol. 155, no. 2, pp. 77–109, 1999.

[16] P. van den Driessche and J. Watmough, "Reproduction numbers and sub-threshold endemic equilibria for compartmental models of disease transmission," *Mathematical Biosciences*, vol. 180, pp. 29–48, 2002.

[17] Z. Feng, C. Castillo-Chavez, and A. F. Capurro, "A model for tuberculosis with exogenous reinfection," *Theoretical Population Biology*, vol. 57, no. 3, pp. 235–247, 2000.

[18] J. Carr, *Applications of Centre Manifold Theory*, Springer, New York, NY, USA, 1981.

[19] C. Castillo-Chavez and B. Song, "Dynamical models of tuberculosis and their applications," *Mathematical Biosciences and Engineering (MBE)*, vol. 1, no. 2, pp. 361–404, 2004.

Hindawi Publishing Corporation
Journal of Applied Mathematics
Volume 2014, Article ID 285367, 11 pages
http://dx.doi.org/10.1155/2014/285367

Research Article

Regularization of DT-MRI Using 3D Median Filtering Methods

Soondong Kwon,[1] Dongyoun Kim,[1] Bongsoo Han,[2] and Kiwoon Kwon[3]

[1] *Department of Biomedical Engineering, Yonsei University, Wonju 220-710, Republic of Korea*
[2] *Department of Radiological Science, Yonsei University, Wonju 220-710, Republic of Korea*
[3] *Department of Mathematics, Dongguk University, Seoul 100-715, Republic of Korea*

Correspondence should be addressed to Kiwoon Kwon; kwkwon@dongguk.edu

Received 21 March 2014; Accepted 7 May 2014; Published 7 July 2014

Academic Editor: Chang-Hwan Im

Copyright © 2014 Soondong Kwon et al. This is an open access article distributed under the Creative Commons Attribution License, which permits unrestricted use, distribution, and reproduction in any medium, provided the original work is properly cited.

DT-MRI (diffusion tensor magnetic resonance imaging) tractography is a method to determine the architecture of axonal fibers in the central nervous system by computing the direction of the principal eigenvectors obtained from tensor matrix, which is different from the conventional isotropic MRI. Tractography based on DT-MRI is known to need many computations and is highly sensitive to noise. Hence, adequate regularization methods, such as image processing techniques, are in demand. Among many regularization methods we are interested in the median filtering method. In this paper, we extended two-dimensional median filters already developed to three-dimensional median filters. We compared four median filtering methods which are two-dimensional simple median method (SM2D), two-dimensional successive Fermat method (SF2D), three-dimensional simple median method (SM3D), and three-dimensional successive Fermat method (SF3D). Three kinds of synthetic data with different altitude angles from axial slices and one kind of human data from MR scanner are considered for numerical implementation by the four filtering methods.

1. Introduction

DT-MRI tractography is a method of noninvasively tracing neuronal fiber bundles. DT-MRI measures anisotropy per pixel and provides the directional information of eigenvectors relevant for fiber tractography. Since DT-MRI data which eigenvectors are computed from usually contain noise, the calculated principal eigenvector direction assumed to be the fiber direction may be different from the real direction in the voxel. As the propagation becomes longer, these differences in the voxels, how small it is, make the whole computed fiber direction deviate far away from the real fiber direction [1]. Since *in vivo* field maps are usually corrupted by noise, the tractography problem turns out to be a mathematically "ill-posed" problem which means that the tracking results are very sensitive to perturbations by noise. The mathematical attempt to stabilize the solution is known as regularization [2].

Many approaches have been attempted to stabilize the noise problem. The approaches are to stabilize six or more diffusion weighted tensors. Since a diffusion-weighted image is a scalar image, there are many conventional image processing techniques [3–5]. The diffusion weighted images make one diffusion tensor for each voxel using Stejskal-Tanner formula. There are conflicting opinions for using more than six diffusion-weighed images to make a diffusion tensor for each voxel [6–9]. Diffusion tensor regularization shows different aspects than conventional scalar image regularization [10, 11]. In fiber tractography, the information about PEV (principal eigenvector) and FA (fractional anisotropy) from the diffusion tensor for each voxel is required. PEV and FA are stabilized using many assumptions or facts including low curvature, small total variation, and orthogonality of eigenpairs [12–15].

Among many regularization techniques we are interested in the median filtering of diffusion tensor data [16–18]. It is known that the median filtering for anisotropic tensor data preserves the good property of denoising and structure-preserving, which is well known for median filtering of isotropic data [18]. In addition, Kwon et al. devised a successive Fermat filtering for tensor data [19]. Tensor-valued median filter is computed using minimization problem such

as gradient descent method or Newton type method in general. Unlike the conventional minimization algorithm, more simple methods, simple median (SM) and successive Fermat (SF) methods, are suggested in [18, 19], respectively. In the papers, only one slice filtering method, that is to say, two-dimensional method for three-dimensional tensor, is considered. In this regard, we call these two-dimensional methods SM2D and SF2D, respectively. But the real DT-MR tensor data are composed of numerous axial, coronal, or sagittal slices. In this paper, we extend SM2D and SF2D to three-dimensional methods SM3D and SF3D, respectively, finding median tensor from $3 \times 3 \times 3$ neighbor tensors. That is to say, the SF3D/SM3D median tensor is the Fermat/simple median of the three SF2D/SM2D medians from the three consecutive slices.

This paper is organized as follows. Section 2 describes the three-dimensional extension (SM3D and SF3D) of the two-dimensional median algorithms (SM2D and SF2D). In Section 3, we generate the synthetic data and describe MR data for numerical simulations of DT-MR tractography. And we also explained the error measures to test the numerical experiment. In Section 4, a performance characterization of the four-median filtering is presented. Section 5 is devoted to concluding remarks.

2. 3D Median Filtering Methods

In this section, we describe general median filtering and explain briefly SM2D and SF2D. We also extend the two-dimensional methods to the three-dimensional methods: SM3D and SF3D. In this paper, we use the following Frobenius norm as a matrix norm of a matrix $A = \{a_{jk}\}_{j,k=1,\dots,3}$:

$$\|A\| = \sqrt{\sum_{j,k=1}^{3} a_{jk}^2}. \tag{1}$$

Let B be an admissible set of matrices and let $S = \{A_1, \dots, A_n\}$ be any set of n matrices. Then the median A_{Median} of the set S is defined as

$$A_{\text{Median}} = \underset{X \in B}{\operatorname{argmin}} \; E_S(X), \quad E_S(X) = \sum_{i=1}^{n} \|X - A_i\|. \tag{2}$$

In general median filtering method, B is chosen as the set of symmetric positive-definite 3×3 matrices. The neighboring set S can be chosen arbitrarily in general, but we specify just two neighboring sets S_2 and S_3 for two-dimensional and three-dimensional cases. That is to say, in two-dimensional methods, S_2 has chosen nine neighboring matrices in each axial (or sagital or coronal) slice as in Figure 1(a) and, in three-dimensional cases, S_3 has chosen 27 neighboring matrices which is 9 matrices for every consecutive three axial slices as in Figure 1(b). After the median filtering, A_{Median}, replaces A_5 in two-dimensional methods and A_{14} in three-dimensional methods as in Figure 1, the Frobenius norm matrix median filter A_{Median} defined in (2) preserves the following properties [16–18].

(1) If all matrices in S are symmetric, scalar-valued, and positive-definite, then A_{Median} is also symmetric, scalar-valued, and positive-definite, respectively.

(2) If A_{Median} is Frobenius matrix median of S, kA_{Median} and $B_\theta A_{\text{Median}}$ are Frobenius matrix median of kS and $B_\theta S$, respectively, where k is a given positive constant and B_θ is a matrix rotating all vectors in three dimensions by angle θ for some given orientation.

2.1. Simple Median Filtering Methods (SM2D and SM3D). The SM2D method is to find a simple approximation A_{SM2D} of the median A_{Median} as in the following equation:

$$A_{\text{SM2D}} = \underset{X \in S_2}{\operatorname{argmin}} \; E_{S_2}. \tag{3}$$

It is well known that A_{Median} is contained in the convex hull of the set neighboring set S_2, whereas A_{SM2D} is a member of S_2, which is one of the nine vertices A_i, $i = 1, 2, \dots, 9$, of the convex hull. We extend the SM filter to three dimensions. While the two-dimensional SM filter uses a 3×3 mask for filtering, we propose three-dimensional SM (SM3D) filtering using a $3 \times 3 \times 3$ sized mask that covers above $(n-1)$th slice and below $(n+1)$th slice in addition to the current nth slice, 9 tensors for each. Consequently, the neighboring matrix set S_3 is defined as $\{A_1, A_2, A_3, \dots, A_{27}\}$ as in Figure 1(b). More explicitly, SM3D is to find the solution of the following minimization problem:

$$A_{\text{SM3D}} = \underset{X \in S_3}{\operatorname{argmin}} \; E_{S_3}(X), \tag{4}$$

and SM3D filtering returns better results than SM2D filtering, because it uses all the three-dimensional neighboring tensor matrices; however, it is more computationally intensive. The SM3D method is explained in Figure 1.

2.2. Successive Fermat Median Filtering Methods (SF2D and SF3D). Fermat median filtering algorithm proposed by Kwon et al. [19] is extended to three dimensions. Fermat median filtering method is based on the Fermat-Torricelli problem, which is raised by Pierre de Fermat in 1643 to Evangelista Torricelli:

> *"Given three points in the two-dimensional plane, find the point having the minimal sum of distances to these three points."*

The above problem is the same as the minimizing solution of (2) for three two-dimensional vectors, since any three points in Euclidean space form a two-dimensional hyperplane in the Euclidean space. Several solutions and generalizations are given in [20–22]. The algorithm to find Fermat point is obtained by the following properties (see Figure 2).

(1) If one of the three angles in the triangle is greater than or equal to 120°, the Fermat point is the vertex at that angle (Figure 2(a)).

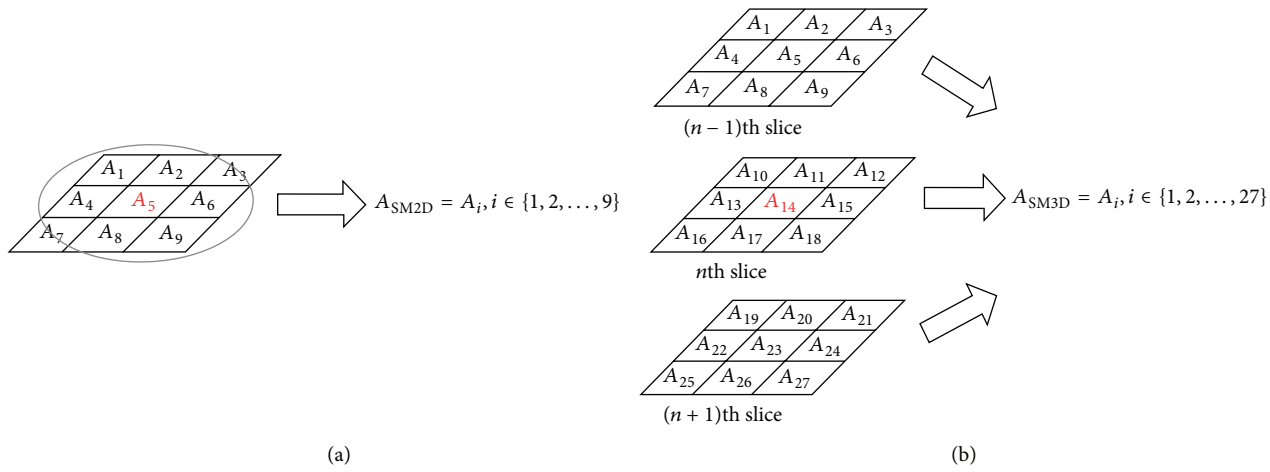

Figure 1: Computations of (a) SM2D and (b) SM3D medians.

(2) If all the three angles in the triangle are less than 120°, the Fermat point is the intersection of the two straight lines joining any vertex of the triangle and its symmetrical point. The symmetrical point of A_1, for example, is computed as follows: the symmetrical point (A_1') of a point (A_1) of the triangle ($\Delta A_1 A_2 A_3$) is chosen by making equilateral triangle ($\Delta A_1' A_2 A_3$) at the outside of the triangle but contacting the opposite side ($\overline{A_2 A_3}$) of the point (A_1) (Figure 2(b)).

We call the algorithm to find Fermat point for three tensors using the above properties, Fermat algorithm. Then, SF2D is a method to find the approximation of A_{Median} for neighboring set S_2 by using Fermat algorithms successively as follows:

$$A_{\text{SF2D}} = \underset{X \in B}{\operatorname{argmin}}\, E_{\text{SF}}(X), \quad \text{SF} = \{\text{SF}_1, \text{SF}_2, \text{SF}_3\},$$
$$\text{SF}_i = \underset{X \in B}{\operatorname{argmin}}\, E_{F_i}(X), \tag{5}$$
$$F_i = \{A_{3(i-1)+1}, A_{3(i-1)+2}, A_{3(i-1)+2}\}, \quad i = 1, 2, 3.$$

For the illustration of (5), see Figure 3(a). The error between A_{Median} and A_{SF2D} is analyzed in [19].

To define a three-dimensional SF3D, we divided 27 points in S_3 into three groups with nine tensors in three consecutive slices. A tensor computed by SF3D is the Fermat point of the three tensors which are SF2D solutions for each slice. Let us assume that A_{14} in S_3 is contained in nth axial slice. The SF3D method is depicted in Figure 2(b) and mathematically it is formulated as follows:

$$A_{\text{SF3D}} = \underset{X \in B}{\operatorname{argmin}}\, E_{\text{SF}}(X),$$
$$\text{SF} = \left\{\text{SF}^{n-1}, \text{SF}^{n}, \text{SF}^{n+1}\right\},$$
$$\text{SF}^m = \underset{X \in B}{\operatorname{argmin}}\, E_{F^m}(X), \quad m = n-1, n, n+1, \tag{6}$$
$$F^m = \{A_{9(m-n+1)+i}\}_{i=1,2,\ldots,9}.$$

See Figure 3(b) for the illustration of SF3D.

3. Numerical Experiments

To evaluate the four filtering methods, we prepared three kinds of synthetic data depending on the angle deviating from each axial slice and human data from the MR scanner. These data are three-dimensional.

The flowchart of our numerical experiment is given in Figure 4. Given synthetic or human data, diffusion tensor is computed. In order to compare the filtering methods with respect to noise level, we added Gaussian noise with mean 0 and standard deviation $\sigma = 0.001$, 0.01, and 0.1 to the original data. The noisy images were reconstructed using the four methods: SM2D, SM3D, SF2D, and SF3D. The eigenvalues (λ_1, λ_2, λ_3) and eigenvectors were calculated by using the power method [23]. Fractional anisotropy (FA) of the tensor A for each voxel is given in relation to the three eigenvalues by

$$\text{FA}(A) = \frac{\sqrt{3(\lambda_1 - m)^2 + (\lambda_2 - m)^2 + (\lambda_3 - m)^2}}{\sqrt{2\left(\lambda_1^2 + \lambda_2^2 + \lambda_3^2\right)}}, \tag{7}$$
$$m = \frac{\lambda_1 + \lambda_2 + \lambda_3}{3}.$$

The fiber tracking was based on the fiber assignment continuous tracking (FACT) algorithm and a brute-force reconstruction approach [24]. Following the analysis in [1, 24], the fiber tracking was started at the center of an every voxel with FA value greater than 0.3, and terminated at the voxel with an FA less than 0.3 and a tract turning-angle less than 70° in our numerical implementation. Computing FA value, FACT algorithm, and brute-force approach are done using DTI-Studio (CMRM, Johns Hopkins Medical Institute, USA).

3.1. Error Measures. Error measures used in the analysis of numerical examples are also given in this section. Let us define the followings:

N : The number of voxels

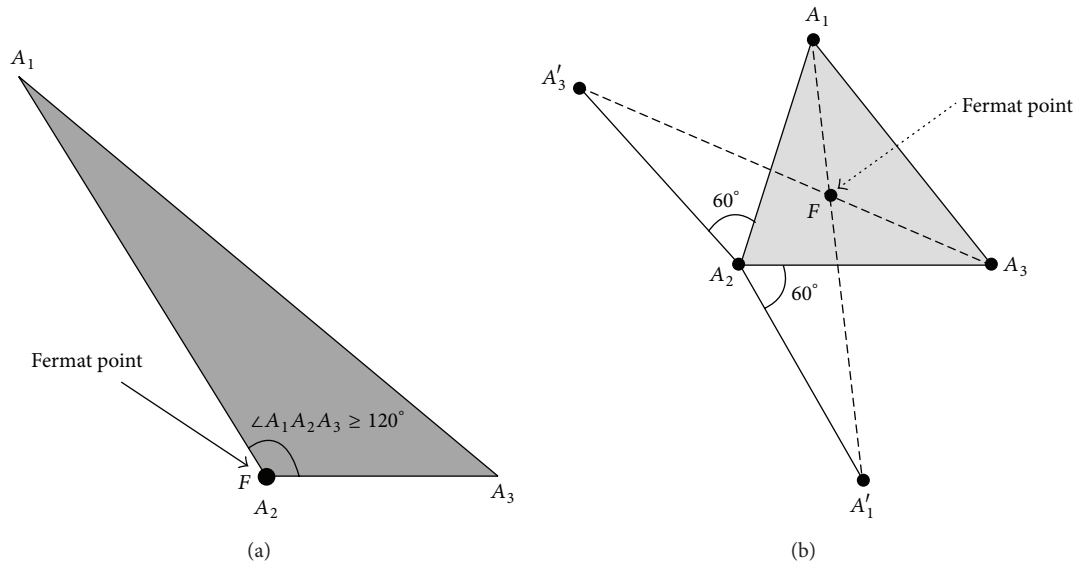

FIGURE 2: Computing Fermat point F (a) when one of the three angles is greater than 120° and (b) when all the three angles are less than 120°. In the latter case, the Fermat point is the intersection of the two straight lines $\overline{A_1A'_1}$ and $\overline{A_3A'_3}$.

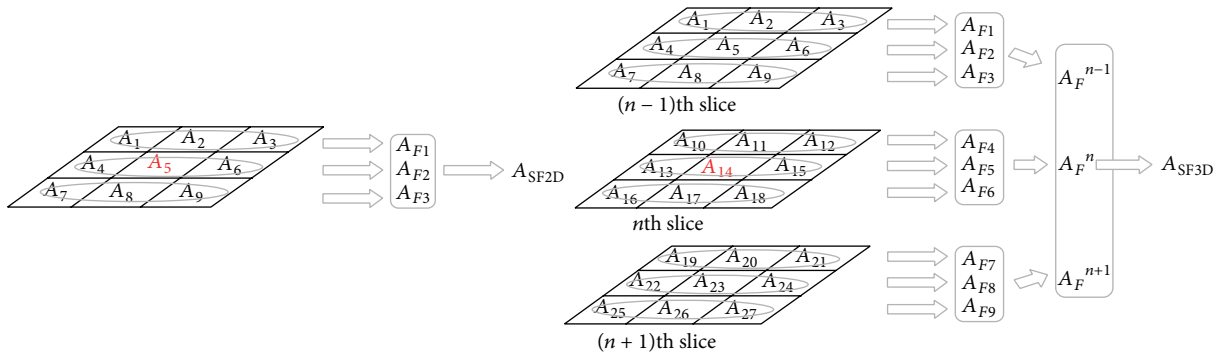

FIGURE 3: Computations of (a) SF2D and (b) SF3D medians.

$A = \{A_n\}_{n=1,\ldots,N}$: The set of original neighboring tensors

A^σ: The set of tensors disturbed by Gaussian noise with mean 0 and variance σ^2

X: The set of tensors whose error from original tensor set A should be computed.

In this paper, X can be reconstructed tensor sets using one of the four filtering method or A^σ. The error measures used in this paper are the average angular error (AAE) and the average fractional anisotropy (AFA) defined as follows:

$$\begin{aligned} \mathrm{AAE}(X:A) &= \frac{1}{N}\sum_{n=1}^{N}\cos^{-1}\left(\mathrm{PEV}(X_n)\cdot\mathrm{PEV}(A_n)\right), \\ \mathrm{FA}(X:A) &= \frac{1}{N}\sum_{n=1}^{N}\left|\mathrm{FA}(X_n)-\mathrm{FA}(A_n)\right|. \end{aligned} \tag{8}$$

3.2. Synthetic Data Generation. The tensor data for each voxel was constructed using the following diagonalization with a diagonal matrix having three eigenvalues (1, 0.2, 0.2) and an orthogonal matrix parameterized by azimuth angle θ and altitude angle φ as follows:

$$\begin{aligned} A_{\theta,\varphi} &= T^t_{\theta,\varphi}\begin{pmatrix}1&0&0\\0&0.2&0\\0&0&0.2\end{pmatrix}T_{\theta,\varphi}, \\ T_{\theta,\varphi} &= \begin{pmatrix}\cos\phi\cos\theta & \cos\phi\sin\theta & \sin\phi\\ \sin\phi\cos\theta & \sin\phi\sin\theta & -\cos\phi\\ \sin\theta & -\cos\theta & 0\end{pmatrix}. \end{aligned} \tag{9}$$

We designed PEV, the first eigenvector, of $A_{\theta,\phi}$ to have azimuth angle θ and altitude angle ϕ, since the first, second, and third row of $T_{\theta,\phi}$ corresponds to the corresponding eigenvector for the first, second, and third diagonal elements,

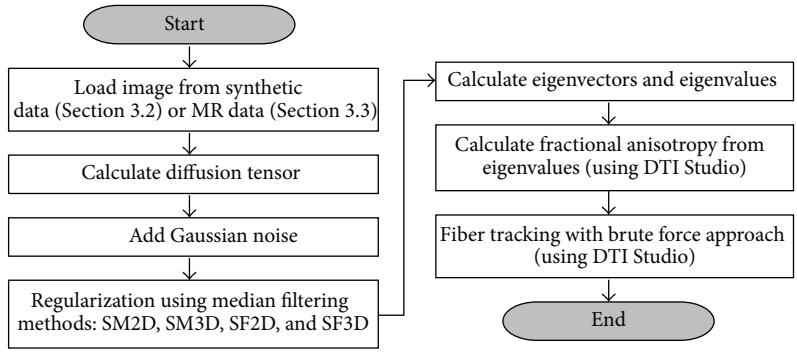

Figure 4: Flowchart of the fiber tractography loaded from synthetic data (Section 3.2) or DTI data (Section 3.3).

respectively. The second and third row of $T_{\theta,\phi}$ is chosen to make $T_{\theta,\phi}$ orthogonal matrix.

The number of voxels for the synthesized data was chosen $128 \times 128 \times 3$ just to verify the efficiency of the filtering in the middle slice for three consecutive slices. The generalization to more slices is not so difficult. Let (i_x, i_y) be the position of the voxel in the xy-plane.

We have considered three kinds of synthetic data, with different altitude angles $\phi = 30^\circ, 45^\circ, 60^\circ$. We set azimuth angle $\theta = 45^\circ$ and make synthetic data zero matrices except 19 continuous diagonal lines as follows:

$$A_I = \begin{cases} A_{\pi/4,\pi/6} = \begin{pmatrix} 0.500 & 0.300 & 0.245 \\ 0.300 & 0.500 & 0.245 \\ 0.245 & 0.245 & 0.400 \end{pmatrix}, \\ \qquad i_y - 10 < i_x < i_y + 10, \\ O, \quad \text{otherwise}, \end{cases} \tag{10}$$

$$A_{II} = \begin{cases} A_{\pi/4,\pi/4} = \begin{pmatrix} 0.400 & 0.200 & 0.283 \\ 0.200 & 0.400 & 0.283 \\ 0.283 & 0.283 & 0.600 \end{pmatrix}, \\ \qquad i_y - 10 < i_x < i_y + 10, \\ O, \quad \text{otherwise}, \end{cases} \tag{11}$$

$$A_{III} = \begin{cases} A_{\pi/4,\pi/3} = \begin{pmatrix} 0.500 & 0.300 & 0.245 \\ 0.300 & 0.500 & 0.245 \\ 0.245 & 0.400 & 0.400 \end{pmatrix}, \\ \qquad i_y - 10 < i_x < i_y + 10, \\ O, \quad \text{otherwise}, \end{cases} \tag{12}$$

where O is the zero matrix.

The synthesized data and their projection to xy- and yz-plane are depicted in Figure 5.

3.3. Human Data from MR Scanner. The whole procedure obtaining fiber tracts for DT-MR images from the MR scanner data is as follows. The single-shot spin echo is used in the image acquisition and data preprocessing from MR scanner. Echo planar imaging (SE-EPI) pulse sequence with two diffusion sensitizing gradients placed on both sides of the 180° refocusing pulse. Fifty contiguous DT-MR images were obtained at 1.5 T Philips Gyroscan MR scanner with the following imaging parameters: field of view = 224 × 224 mm^2, slice thickness = 3 mm, acquisition matrix = 96, reconstruction matrix = 128, TR = 10,000 ms, TE = 76 ms, b factor = 1000 s/mm^2, the number of diffusion sensitizing gradients = 6.

To correct subject head motion and the image distortion due to eddy current, every DTI 3D volume image was realigned to b_0 image in FSL (Analysis Group, FMRIB, Oxford, UK). The diffusion tensor was calculated from the 7- volume images (six diffusion weighted images and one image with $b = 0$). To assess the effects of median filtering on the regularization of the noise in DT-MRI tractography, a noisy data was generated by adding the Gaussian noise with 0 mean and 0.0001 standard deviation to the original human DTI data. Fiber tracking for the original data and noisy data with no filtering, SM3D, SF3D, SM2D and SF2D was performed using the DTI-Studio (CMRM, Johns Hopkins Medical Institute, USA). To select the corticospinal tract (CST), a ROI (Region Of Interest) was drawn on the known anatomical CST area in the pons as shown in Figure 6 and the fibers passing through the ROI were considered as the CST.

4. Numerical Results and Discussion

The numerical results about the three synthetic data in Section 3.2, are given in Figures 7, 8, and 9. Gaussian noise with 0 mean and various standard deviations σ = 0.1, 0.01, 0.001 are added to the synthesized data A_{II} in (11). And we compared the performance of the four median filtering regularization algorithms (SM2D, SF2D, SM3D, and SF3D) with respect to AAE and AFA errors in Figure 7. As shown in the figure, three-dimensional filters are superior to two-dimensional filters and SF3D/SF2D is superior to SM3D/SM2D. It is remarkable that SF2D is superior to SM3D in the figure. This shows that the simple median is not so close the median point, whereas the successive median point is much close to the median point even in two-dimension. The xy-plane projection as in Figure 5(a) of the original data A_{II}, the disturbed image with Gaussian noise having 0 mean and standard deviation 0.01, and reconstructed images by the four methods are pictured in Figure 8. The reconstructed image in Figure 8(c) from SM2D is slightly improved from

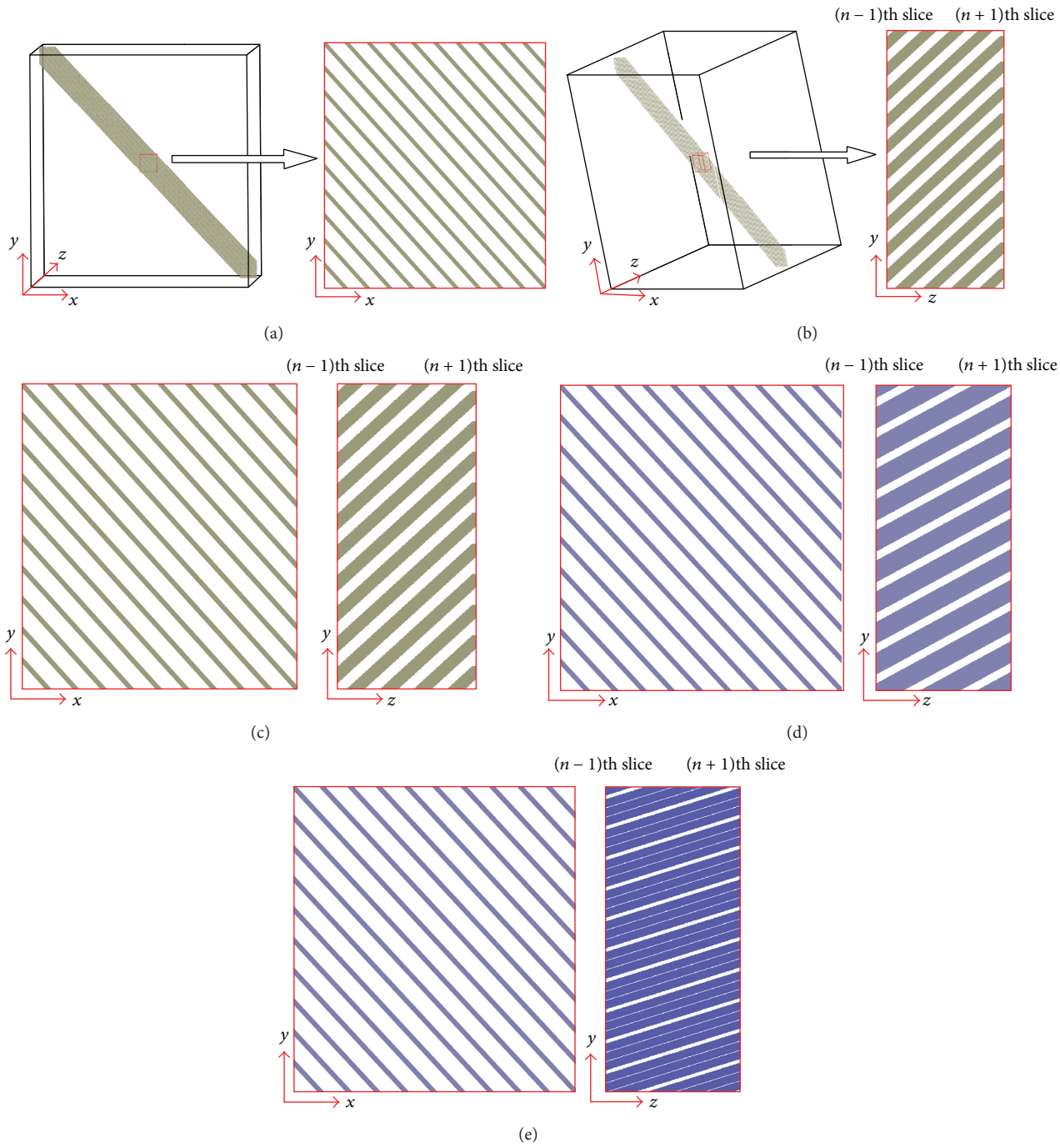

FIGURE 5: Synthesized data A_I, A_{II}, and A_{III} given in (10), (11), and (12): (a) three-dimensional representation of A_I and its projection to xy-plane, (b) another three-dimensional representation of A_I and its projection to yz-plane, and resulting two-dimensional representation of the synthetic data (c) A_I, (d) A_{II}, and (e) A_{III}.

the disturbed image in Figure 8(b), but still many distorted and broken lines are observed. The distortion and breakage of lines from the original image Figure 8(a) is more improved in Figure 8(d) (SF2D) or Figure 8(e) (SM3D) than the image from Figure 8(b) (SM2D). However, most improved image is found in Figure 8(f), the reconstructed image using SF3D.

In Section 3.2, we considered three kinds of synthetic data A_I, A_{II}, A_{III} with different altitude angles $\phi = 30^\circ, 45^\circ, 60^\circ$. In Figure 9, the reconstructed image using the four methods are compared for the three kinds of synthetic data. In the x-axis label, the altitude angle in degree of the three synthetic data is considered. Added Gaussin noise in the disturbed image has zero mean and $\sigma = 0.01$. The two-dimensional filters show no change of errors with respect to altitude angle. However, three-dimensional filters decreased when altitude angle increases: this phenomenon is observed not

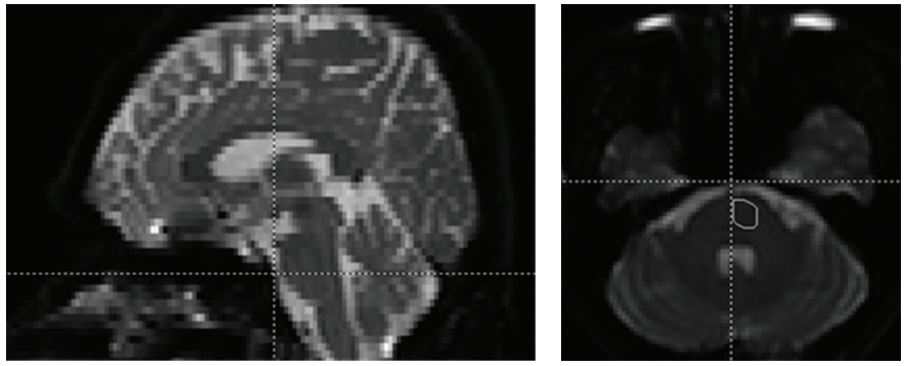

(a) (b)

FIGURE 6: MRI data for the pons in the (a) sagittal and (b) axial planes. The rectangle in (b) was chosen as ROI to select the corticospinal tract (CST).

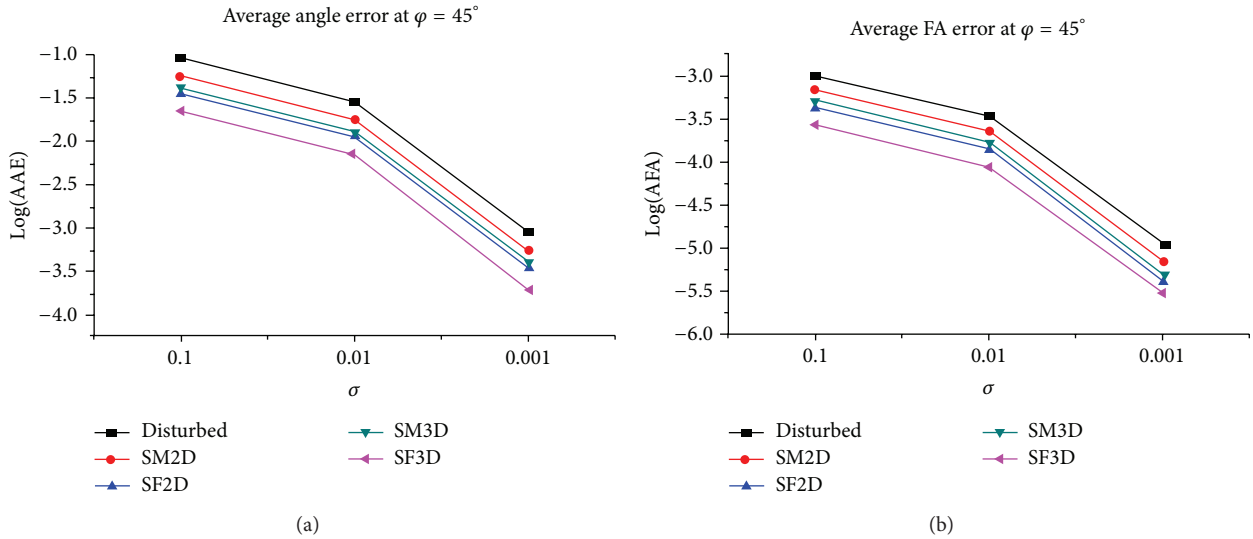

FIGURE 7: Errors with respect to $\sigma = 0.1$, 0.01, and 0.001 when we recover the synthetic data A_{II} using the four median filtering methods: (a) Log (AAE) error and (b) Log (AFA) error.

so outstandingly for SM3D, but very remarkably for SF3D. The increase of altitude angle means that fiber tract strays out of xy-plane and propagates in the direction close to the z-axis. Due to this fact, three dimensional filters shows more sensitive to the altitude angle whereas two-dimensional filters shows no change of the errors with respect to the altitude angle.

In Figures 10, 11, and 12, the reconstruction for human data is considered. Gaussian noise with 0 mean and 0.0001 standard deviation are added. As shown in Figure 10, SF methods show better results than SM methods and three-dimensional methods are better than two-dimensional methods. It is remarkable that SF2D make smaller error than SM3D as in Figure 7. In Figures 11(a)–11(c) show the CSTs from the original DTI data and Figures 11(d)–11(f), 11(h) and 11(i) from noisy ones ($\sigma = 0.0001$) with no median filtering, SM3D and SF3D, SM2D and SF2D, respectively. And the green rectangular regions in Figures 11(b) and 11(h) were magnified and arranged on the left and the right in Figure 11(g), respectively. The images in the bottom left corners in Figure 11 show the CSTs in the axial planes represented by the horizontal line in Figure 11(a). Not knowing the true CST, we couldn't tell which one among Figures 11(a)–11(c) was closest to the true CSTs. Therefore, Figures 11(a)–11(c) were used as the standards to assess the effect of the median filtering in the CST fiber tracking from noisy data: the CSTs in Figures 11(d)–11(f) were compared with Figures 11(a)–11(c), respectively. In case of no filtering, the number of fibers in the CST in Figure 11(d) is considerably decreased, while the CST in Figure 11(d) shows a similar shape to the one in Figure 11(a). For the SM3D filtering, the CST in Figure 11(e) shows distinct differences in the region enclosed by the blue circles: In the axial image, the fiber tracts indicated by two yellow arrows in Figure 11(b) disappear in Figure 11(e). For the SF3D filtering, although the CSTs in Figures 11(c) and 11(f) show a few differences, they are similar in shape and the fiber tracts in

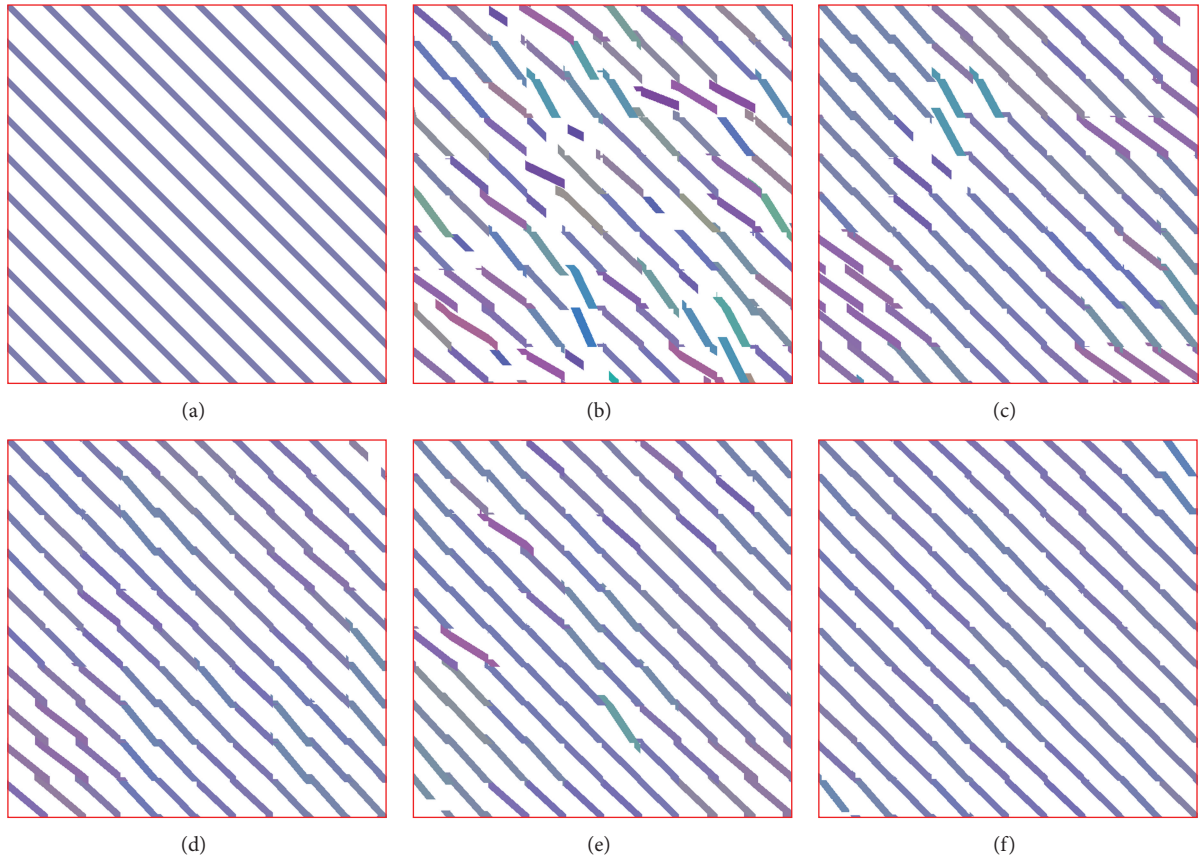

FIGURE 8: Filtering of synthetic data A_{II} corrupted with Gaussian noise having zero mean and $\sigma = 0.01$: (a) the original image, (b) the disturbed image, and the reconstructed images using (c) SM2D, (d) SF2D, (e) SM3D, and (f) SF3D.

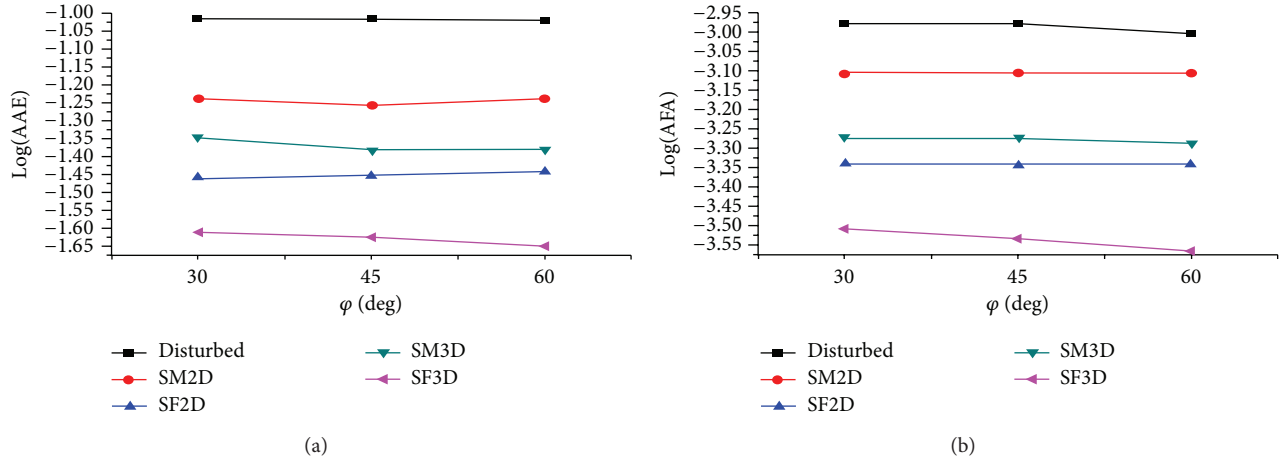

FIGURE 9: Errors with respect to A_I, A_{II}, and A_{III} with $\varphi = 30^\circ, 45^\circ, 60^\circ$, respectively, when we recover the synthetic data with Gaussian noise having mean 0 and $\sigma = 0.01$ using the four median filtering methods: (a) Log (AAE) error and (b) Log (AFA) error.

the axial images show little difference. In comparison with 2-dimensional filters, SF3D Figure 11(f) is closer to Figure 11(c) than SF2D Figure 11(i). On the other hand, SM2D Figure 11(h) appears to be closer to Figure 11(b) than SM3D Figure 11(e), however, as one can see in Figure 11(g), the fibers in SM2D (right) show complicate fiber connections by comparison with the left image, which was not realistic and caused from the poor regularization of the noise in the region. Therefore, the SF3D filter shows best regularization of the noise in CST tracking.

The calculation time average and standard deviation for the four methods are graphed in Figure 12. Intel Pentium with

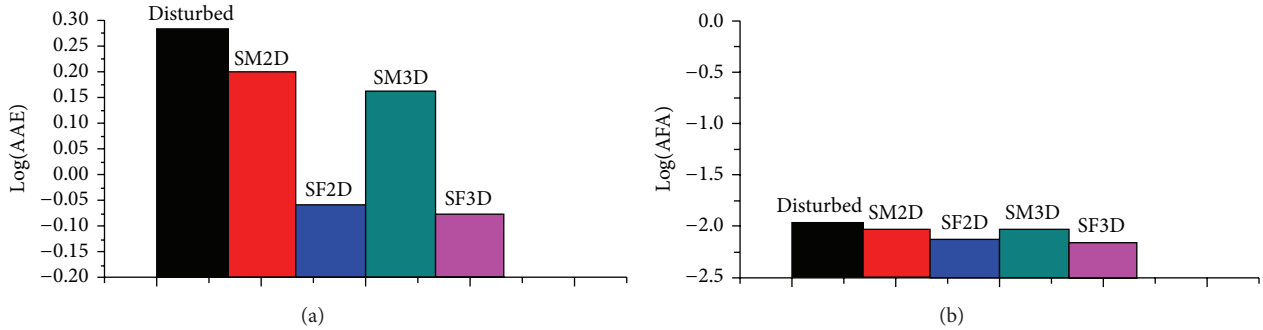

FIGURE 10: Errors when we recover human data from MR scanner corrupted with Gaussian noise having zero mean and $\sigma = 0.0001$ by using the four median filtering methods: (a) Log (AAE) error and (b) Log (AFA) error.

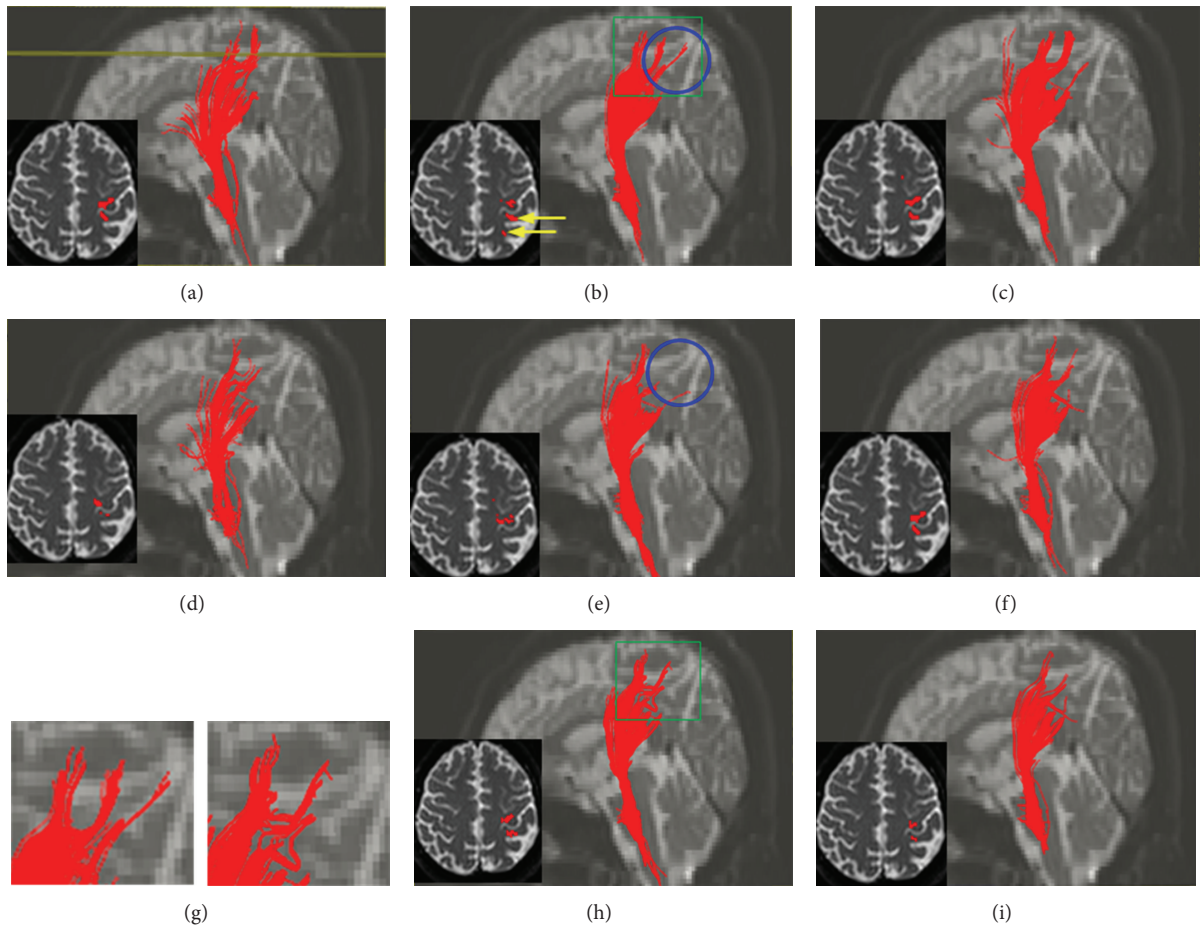

FIGURE 11: CSTs passing through the pons of a human subject: corticospinal tracts obtained from the original data with (a) no filter, (b) SM3D, and (c) SF3D and the CSTs obtained from the disturbed data ($\sigma = 0.0001$) with (d) no filter, (e) SM3D, (f) SF3D, (h) SM2D, and (i) SF2D. The images in the bottom left corners show the CSTs in the axial planes represented by the horizontal line in (a). And the left figure and the right one in (g) are magnified images of the green rectangular regions in (b) and (h), respectively.

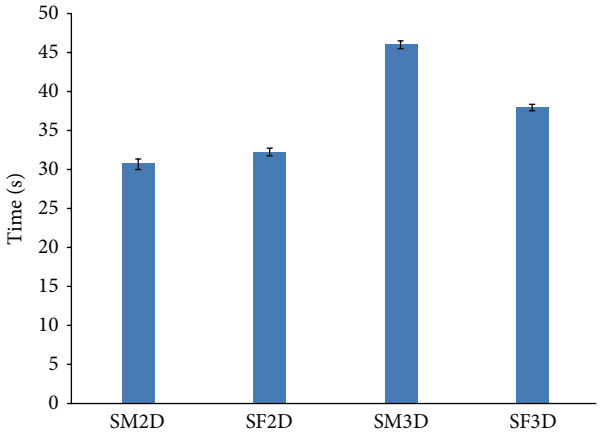

Figure 12: Computation time for the four methods to reconstruct the DT-MR data: the blue solid bar and small vertical bar at the top end of the blue bar represent the average and the standard deviation of computational times for the four methods, respectively, after testing the four median filters five times for each.

3 GHz CPU and 2 GB RAM was used for the simulation. The difference of calculation times for SM2D and SF2D is not so remarkable, as we know how exactly SF2D recover fiber tracts than SM2D from Figures 7 and 11. And the difference of computation times between SF2D and SF3D is not so outstanding, since we also know the efficiency of SF3D from previous figures. That is to say, even though SF3D needs a little more computation time than SF2D, SF3D recover DT-MR image far better than SF2D. However, SM3D needs too much time than the other three methods and recovering error is larger than SF2D and slightly better than SM2D.

5. Conclusion

In this study, we developed three-dimensional median filters SM3D and SF3D, extending previously developed SM2D and SF2D in [19]. We implemented three kinds of synthetic data with different altitude angle deviating from the axial slices and one human data form MR scanner. As altitude angle increase from the xy-plane we observed that three dimensional median filters more efficient than two-dimensional filters. For all four synthetic and human data, the four median filters (SM2D, SF2D, SM3D, and SF3D) have same tendency with respect to AAE and AFA errors: three-dimensional filters show superior results to corresponding two-dimensional median filters and SF filters show better reconstruction than SM filters. With respect to computation time, SF2D or SF3D filters need not so much time compared to SM2D filter but SM3D filter needs far more computation time than the other three filters. Therefore, SF3D is proved to be the most efficient median filters and is supposed to be one of powerful regularization methods.

Conflict of Interests

The authors declare that there is no conflict of interests regarding the publication of this paper.

Acknowledgments

This research was supported by the Leading Foreign Research Institute Recruitment Program through the National Research Foundation of Korea (NRF) funded by the Ministry of Science, ICT & Future Planning (2010-00757), and by Basic Science Research Program through the National Research Foundation of Korea (NRF) funded by the Ministry of Education (NRF-2013R1A1A2010624).

References

[1] S. Mori and P. C. M. van Zijl, "Fiber tracking: principles and strategies—a technical review," *NMR in Biomedicine*, vol. 15, no. 7-8, pp. 468–480, 2002.

[2] R. Bammer, B. Acar, and M. E. Moseley, "In vivo MR tractography using diffusion imaging," *European Journal of Radiology*, vol. 45, no. 3, pp. 223–234, 2003.

[3] G. J. M. Parker, J. A. Schnabel, R. Symms, D. J. Werring, and G. J. Barker, "Nonlinear smoothing for reduction of systematic and random errors in diffusion tensor imaging," *Journal of Magnetic Resonance Imaging*, vol. 11, pp. 702–710, 2000.

[4] P. Perona and J. Malik, "Scale-space and edge detection using anisotropic diffusion," *IEEE Transactions on Pattern Analysis and Machine Intelligence*, vol. 12, no. 7, pp. 629–639, 1990.

[5] B. Vemuri, Y. Chen, M. Rao, T. McGraw, Z. Wang, and T. Mareci, "Fiber tract mapping from diffusion tensor MRI," in *IEEE Workshop on Variational and Level Set Methods in Computer Vision*, IEEE, 2001.

[6] S. Skare, M. Hedehus, M. E. Moseley, and T.-Q. Li, "Condition number as a measure of noise performance of diffusion tensor data acquisition schemes with MRI," *Journal of Magnetic Resonance*, vol. 147, no. 2, pp. 340–352, 2000.

[7] K. M. Hasan, D. L. Parker, and A. L. Alexander, "Comparison of gradient encoding schemes for diffusion-tensor MRI," *Journal of Magnetic Resonance Imaging*, vol. 13, no. 5, pp. 769–780, 2001.

[8] D. K. Jones, "The effect of gradient sampling schemes on measures derived from diffusion tensor MRI: a monte carlo study," *Magnetic Resonance in Medicine*, vol. 51, no. 4, pp. 807–815, 2004.

[9] T. Zhu, X. Liu, M. D. Gaugh et al., "Evaluation of measurement uncertainties in human diffusion tensor imaging (DTI)-derived parameters and optimization of clinical DTI protocols with a wild bootstrap analysis," *Journal of Magnetic Resonance Imaging*, vol. 29, no. 2, pp. 422–435, 2009.

[10] C. F. Westin, S. E. Maier, B. Khidhir, P. Everett, F. A. Jolesz, and R. Kikinis, "Image processing for diffusion tensor magnetic resonance imaging," in *Medical Image Computing and Computer-Assisted Intervention*, vol. 2208, pp. 441–452, 1999.

[11] K. Hahn, S. Prigarin, and B. Putz, "Edge preserving regularization and tracking for diffusion tensor imaging," in *Medical Image Computing and Computer-Assisted Intervention*, vol. 2208 of *Lecture Notes in Computer Science*, pp. 195–203, 2001.

[12] P. J. Basser and S. Pajevic, "Statistical artifacts in diffusion tensor MRI(DT-MRI) caused by background noise," *Magnetic Resonance in Medicine*, vol. 44, pp. 41–50, 2000.

[13] C. Poupon, C. A. Clark, V. Frouin et al., "Regularization of diffusion-based direction maps for the tracking of brain white matter fascicles," *NeuroImage*, vol. 12, no. 2, pp. 184–195, 2000.

[14] D. Tschumperle and R. Deriche, "Regularization of orthonormal vector sets using coupled PDE's," in *Proceedings of the IEEE Workshop on Variational and Level Set Methods*, IEEE, 2001.

[15] O. Coulon, D. C. Alexander, and S. Arridge, "Diffusion tensor magnetic resonance image regularization," *Medical Image Analysis*, vol. 8, no. 1, pp. 47–67, 2004.

[16] M. Welk, C. Feddern, B. Burgeth, and J. Weickert, "Median filtering of tensor-valued images," in *Pattern Recognition*, Lecture Notes in Computer Science, Springer, Berlin, Germany, 2003.

[17] M. Welk, C. Feddern, B. Burgeth, and J. Weickert, "Tensor median filtering and M-smoothing," in *Visualization and Processing of Tensor Fields*, Springer, Berlin, Germany, 2006.

[18] M. Welk, J. Weickert, F. Becker, C. Schnörr, C. Feddern, and B. Burgeth, "Median and related local filters for tensor-valued images," *Signal Processing*, vol. 87, no. 2, pp. 291–308, 2007.

[19] K. Kwon, D. Kim, S. Kim et al., "Regularization of DT-MR images using a successive Fermat median filtering method," *Physics in Medicine and Biology*, vol. 53, no. 10, pp. 2523–2536, 2008.

[20] A. Bogomolny, "The Fermat Point and Generalizations," http://www.cut-the-knot.org/Generalization/fermat_point point.shtm.

[21] L. Dalla, "A note on the Fermat-Torricelli point of a d-simplex," *Journal of Geometry*, vol. 70, no. 1-2, pp. 38–43, 2001.

[22] R. Honsberger, *Mathematical Gems: The Dolciani Mathematical Expositions*, The Mathematical Association of America, 1973.

[23] N. S. Mendelsohn, "An iterative method for the solution of linear equations based on the power method for proper vectors," *Mathematical Tables and Other Aids to Computation*, vol. 11, pp. 88–91, 1957.

[24] H. Huang, J. Zhang, P. C. M. van Zijl, and S. Mori, "Analysis of noise effects on DTI-based tractography using the brute-force and multi-ROI approach," *Magnetic Resonance in Medicine*, vol. 52, no. 3, pp. 559–565, 2004.

Hindawi Publishing Corporation
Journal of Applied Mathematics
Volume 2014, Article ID 658719, 15 pages
http://dx.doi.org/10.1155/2014/658719

Research Article

A Constitutive Model for the Annulus of Human Intervertebral Disc: Implications for Developing a Degeneration Model and Its Influence on Lumbar Spine Functioning

J. Cegoñino,[1] V. Moramarco,[2] A. Calvo-Echenique,[1] C. Pappalettere,[2] and A. Pérez del Palomar[1]

[1] *Biomaterials Group, Mechanical Engineering Department, Aragón Institute of Engineering Research (I3A), University of Zaragoza, C/Mariano Esquillor s/n, 50018 Zaragoza, Spain*
[2] *Department of Mechanical, Mathematics and Management (DMMM), Politecnico di Bari, Viale Japigia 182, 70126 Bari, Italy*

Correspondence should be addressed to A. Pérez del Palomar; amaya@unizar.es

Received 19 December 2013; Revised 29 April 2014; Accepted 14 May 2014; Published 12 June 2014

Academic Editor: Kiwoon Kwon

Copyright © 2014 J. Cegoñino et al. This is an open access article distributed under the Creative Commons Attribution License, which permits unrestricted use, distribution, and reproduction in any medium, provided the original work is properly cited.

The study of the mechanical properties of the annulus fibrosus of the intervertebral discs is significant to the study on the diseases of lumbar intervertebral discs in terms of both theoretical modelling and clinical application value. The annulus fibrosus tissue of the human intervertebral disc (IVD) has a very distinctive structure and behaviour. It consists of a solid porous matrix, saturated with water, which mainly contains proteoglycan and collagen fibres network. In this work a mathematical model for a fibred reinforced material including the osmotic pressure contribution was developed. This behaviour was implemented in a finite element (FE) model and numerical characterization and validation, based on experimental results, were carried out for the normal annulus tissue. The characterization of the model for a degenerated annulus was performed, and this was capable of reproducing the increase of stiffness and the reduction of its nonlinear material response and of its hydrophilic nature. Finally, this model was used to reproduce the degeneration of the L4L5 disc in a complete finite element lumbar spine model proving that a single level degeneration modifies the motion patterns and the loading of the segments above and below the degenerated disc.

1. Introduction

The annulus fibrosus (AF) of the human intervertebral disc (IVD) presents a complex structure. Located on the radial periphery of the IVD, the AF is believed to experience a combination of compressive, tensile, and shear stresses during weight-bearing and intervertebral joint motions [1, 2]. For these reasons, its structure combines a highly orientated fibres network with a multiphasic behaviour [3–5]. Furthermore, the presence of osmotic forces, due to the hydrophilic nature of the proteoglycans aggregates (PGs) [1, 2], ensures that the fibre network of the tissue works under tensile prestress and that the fluid inside the tissue is under pressure. This is essential for the correct functioning of the tissue since the fluid typically resists compression and fibres resist tension [6].

In the last years several analytical and numerical models have been developed to simulate the AF tissue behaviour. Some of them, like those proposed by Simon and coworkers [7], implemented its poroelastic behaviour and swelling. Others authors, like Lai et al. [8] and Sun et al. [9], or Frijns et al. [10] and van Loon et al. [11], developed multiphasic mixture models that permit a good modelling of poromechanics of the tissue. All these models, nevertheless, neglected the mechanical behaviour of the extracellular matrix related to collagen network. In this regard, others authors [12, 13], who considered that the fibres network implies a linear viscoelastic response, did not consider the high nonlinearity behaviour of the fibres, though.

Furthermore, in spite of the fact that AF tissue is subjected to several changes during life [1, 14–16], there are not many models to simulate the effects of degeneration. Some of them [17] simply removed some elements from the annulus. Others, like Rohlmann et al. [18], Polikeit et al. [19], and Natarajan et al. [20], showed the influence of geometrical, mechanical, or poromechanical parameters on disc behaviour but did not show clearly how the mechanical properties change with degeneration. More recently, Schmidt et al. [21] developed a poroelastic finite element model of the lumbar spine to investigate spinal response during physiological activities. In any case, nobody of the aforementioned authors has directly validated the influence of these changes on AF tissue behaviour.

On the other hand, the degenerative disc disease seems to be related to the modification of the biomechanical functioning of the spine. Abnormal mechanical loads and/or motion patterns have been related to risk of injury to the spine [22, 23]. Despite numerous studies on the mechanics of the degenerated disc, there is limited data on how this condition affects the adjacent caudal and cephalic segments or the lumbar spine stability contributing to the progression of disc degeneration [1, 4, 14, 15, 18, 20, 24–28]. The results of these studies vary considerably. Similarly to Kirkaldy-Willis and Farfan [29], some authors report instability during the early stages of degeneration [30, 31] while others rather show the opposite [32, 33]. These partial contradictive results are probably enforced by the relative small number of specimens. Recently, Kettler et al. [34] analyze the influence of the degree of disc degeneration on the flexibility of lumbar spine segments based on the data from a large *in vitro* database. There are several studies that numerically analyze the degeneration of the adjacent levels after lumbar fusion [35, 36] but not much has been done to computationally reproduce the influence of a single-level lumbar degenerative disc disease on the behaviour of the adjacent segments except from the work of Ruberte et al. [37].

In this work a constitutive model to describe the mechanical behaviour of the normal and degenerated AF tissue of human IVD has been developed. The complete mathematical formulation is presented with particular focusing on the PGs behaviour modelling. Then, complete characterization and validation of the osmotic and elastic response for a normal and degenerated AF have been carried out [4, 38–40]. Afterwards, a complete finite element model of the lumbar spine was analyzed inferring the mechanical consequences on the overall behaviour of the spine taking into account some degree of degeneration at a single-level.

2. Methods

The annulus fibrosus (AF) of human IVD presents a very particular structure. It consists of a solid porous matrix, saturated with water, which mainly contains proteoglycans and collagen fibres. To simulate its behaviour a 3D osmo-hyperelastic model reinforced with two families of fibres was constructed and implemented. Several validation tests were performed in order to validate the accuracy of this model and its ability of reproducing some of the consequences of degeneration.

2.1. Constitutive Modeling of the Annulus Fibrosus. The strain energy density function (1), initially presented by Eberlein et al. [17] to characterize fiber reinforced materials extensively used for biological tissues, was modified to introduce the contribution of the osmotic pressure. This term takes into account the effect of the electric charged proteoglycans and it can be coupled with biphasic formulation.

As widely known, the Helmholtz free energy function Ψ can be divided into different components corresponding to the ground substance, the fibres network, and the material compressibility (see Nomenclature for notation). In this case it can be written as

$$\begin{aligned}\Psi\left(\mathbf{C},\mathbf{A_1},\mathbf{A_2}\right) &= \Psi_{\text{gs}}\left(\mathbf{C}\right) + \Psi_f\left(\mathbf{C},\mathbf{A_1},\mathbf{A_2}\right) + \Psi_{\text{vol}}\left(J\right)\\ &= C_{10}\left(\bar{I}_1 - 3\right) + C_{20}\left(\bar{I}_1 - 3\right)^2\\ &\quad + \frac{K_1}{2K_2}\left\{\exp\left[K_2\left(\bar{I}_4^* - 1\right)^2\right] - 1\right\}\\ &\quad + \frac{K_1}{2K_2}\left\{\exp\left[K_2\left(\bar{I}_6^* - 1\right)^2\right] - 1\right\}\\ &\quad + \frac{1}{D}(J-1)^2.\end{aligned} \tag{1}$$

Accordingly, the 2nd Piola-Kirchhoff stress tensor $\mathbf{S}$ is

$$\mathbf{S} = 2\frac{\partial\Psi}{\partial\mathbf{C}} = \mathbf{S}_{\text{gs}} + \mathbf{S}_f + \mathbf{S}_{\text{vol}}, \tag{2}$$

where the contribution of each part can be expressed as

$$\begin{aligned}\mathbf{S}_{\text{gs}} &= 2\frac{\partial\Psi_{\text{gs}}}{\partial\mathbf{C}} = 2\frac{\partial}{\partial\mathbf{C}}\left(C_{10}\left(\bar{I}_1 - 3\right) + C_{20}\left(\bar{I}_1 - 3\right)^2\right)\\ &= 2J^{2/3}\mathbb{P} : C_{10}\mathbf{I} + 4J^{2/3}\mathbb{P} : C_{20}\mathbf{I}\end{aligned} \tag{3}$$

$$\begin{aligned}\mathbf{S}_f &= 2\frac{\partial\Psi_f}{\partial\mathbf{C}} = 2\frac{\partial}{\partial\mathbf{C}}\sum_{n=1}^{2}\frac{K_1}{2K_2}\left\{\exp\left[K_2\left(\bar{I}_n^* - 1\right)^2\right] - 1\right\}\\ &= 2J^{2/3}\mathbb{P} : \sum_{n=1}^{2} 2K_1\left\{\exp\left[K_2\left(\bar{I}_n^* - 1\right)^2\right]\left(\bar{I}_n^* - 1\right)\mathbf{A}_n\right\},\end{aligned} \tag{4}$$

$$\mathbf{S}_{\text{vol}} = 2\frac{\partial \Psi_{\text{vol}}}{\partial \mathbf{C}} = \frac{2}{D} J\left(J-1\right)\mathbf{C}^{-1} - J\left(\Delta\Pi + \mu_f\right)\mathbf{C}^{-1}. \quad (5)$$

It can be seen that in (5), the term relative to the material compressibility has been modified to incorporate the osmotic pressure contribution. Thus, in agreement with Wilson et al. [13, 40], the water chemical potential μ_f can be defined as

$$\mu_f = p - \Delta\Pi \quad (6)$$

while the osmotic pressure gradient $\Delta\Pi$ is calculated by means of the external and internal osmotic pressure:

$$\Delta\Pi = \Pi_{\text{int}} - \Pi_{\text{ext}}. \quad (7)$$

Both external and internal osmotic pressures depend on the external and internal osmotic coefficients, respectively, and on the external salt concentration, while the internal osmotic pressure depends also on the fixed charged density that is related to the proteoglycans content,

$$\Pi_{\text{ext}} = 2\phi_{\text{ext}} RT c_{\text{ext}}, \quad (8)$$

$$\Pi_{\text{int}} = \phi_{\text{int}} RT \sqrt{c_F^2 + 4c_{\text{ext}}^2}. \quad (9)$$

Furthermore in (9), the fixed charged density c_F associated with the affinity to water is calculated as:

$$c_F = c_{F,0}\left(\frac{n_{f,0}}{n_{f,0} - 1 + J}\right). \quad (10)$$

Finally, it can be considered that the hydraulic permeability k of the ground substance matrix also decreases as the tissue is compressed. It can be assumed to be dependent on porosity changes in the following way [41]; therefore,

$$k = k_0\left(\frac{n}{n_0}\right)^m, \quad (11)$$

where m is a positive coefficient equal to 15.

2.2. Material and Testing Simulations for Healthy Annulus Fibrosus Tissue. To characterize and validate the model presented in the previous section, we reproduced *in silico* some *in vitro* experimental results available in the literature for healthy samples of annulus.

2.2.1. Osmotic Swelling Behaviour. To point out the principal effects of the osmotic swelling on the behaviour of soft hydrated tissues, the most common validation test to assess the contribution of electrochemical effects to the response of the tissue is a pure swelling test.

A 1D simplified numerical model was run in ABAQUS 6.11 (Figure 1(a)). The constitutive equations were implemented in a user defined UMAT subroutine. A specimen of tissue ($h = 0.5$ mm), equilibrated in a NaCl solution with a salt concentration of c_{ext}, was placed inside an impermeable confined compression chamber (Figure 1(b)). After an equilibrium phase, at $t = 0$ the external salt concentration was changed to c^* (Figure 1(c)) and, at $t = t^*$, the external salt concentration was returned to c_{ext}. To simulate the swelling effect, only the axial displacements were allowed for all nodes while free flux condition ($p = 0$ bar) was assumed only at the lower nodes. See Table 1 for material properties.

2.2.2. Characterization of the Normal IVD Annulus Tissue. To characterize the solid matrix AF behaviour, the polynomial strain energy function shown before was used. The values of the elastic constants (C_{10}, C_{20}, D, K_1, and K_2) were determined using the stress-strain response under a traction axial load for a specimen with two families of fibres, placed at $\pm 30^\circ$ [42]. The theoretical model behaviour was fitted to experimental data presented by Ebara et al. [38] using MatLab v.7.1. It can be observed (Figure 2) how the resultant curve can be considered a good average fit of experimental data of the whole annulus [17, 43, 44]. These constants are summarized in Table 2. Here, we have to point out that each part of the disc could have been considered with different mechanical properties but we were interested in the overall behaviour of the annulus.

To validate the global behaviour of the proposed model two different compression tests were performed in order to compare our results with previous data in the literature [4, 39]. A 3D finite element (FE) mesh was created (Figure 3(a)). The chosen geometry was in agreement with that proposed by Wilson et al. [13]. Each family of fibres was placed radially with an angle orientation ϕ of $\pm 30^\circ$ with respect to the xz-plane [39, 42] (Figure 3(b)). In both tests the displacements for the lower nodes were restricted in the z-direction while for lateral perimetric nodes the radial displacements were confined. In the first test, a zero pore pressure condition was imposed at the top while the remaining surfaces were assumed to be impermeable. In this case, the loading protocol implied that the mesh was axially compressed by 5% strain followed by a relaxation period (Figure 3(c)). The second test was conducted following the guidelines proposed by Iatridis et al. [4]. In this case, free flux condition ($p = 0$ bar) was assumed on the bottom surface. Initially a compression strain of 10% (velocity strain ratio $0.001\,\text{s}^{-1}$) was applied on top followed by 2500 s of relaxation at fixed displacement. Then, this loading cycle was repeated three times adding a 5% of deformation strain at each increment (Figure 3(d)).

2.3. Material and Testing Simulations for Degenerated Annulus Fibrosus Tissue. Several experimental studies have shown how degeneration process produces serious changes on AF tissue behaviour [14, 15, 24, 28]. Particularly, Iatridis et al. [4] showed that the residual stress at the equilibrium point under a compression strain of 20% for the degenerated (grade IV) AF tissue was nearly twice in comparison with the normal AF tissue. Therefore, the same test procedure made for normal tissue was done for the degenerated one.

Some authors [4, 15, 27] agree with relating the reduction of proteoglycans content to disc degeneration. In our simulations, this phenomenon was taken into account reducing the tissue initial fixed charge density $c_{F,0}$. Furthermore, AF tissue permeability k_0 has also shown a decrease with degeneration process [4] that also was considered into this model.

For sure, also the elastic behaviour of the AF would be subjected to changes [4, 14, 24]. In particular, an increase of the stiffness has been addressed [4, 24]. However, it has been seen that annulus fibrosus stiffening is not due to the reduction of water content which slightly changes with

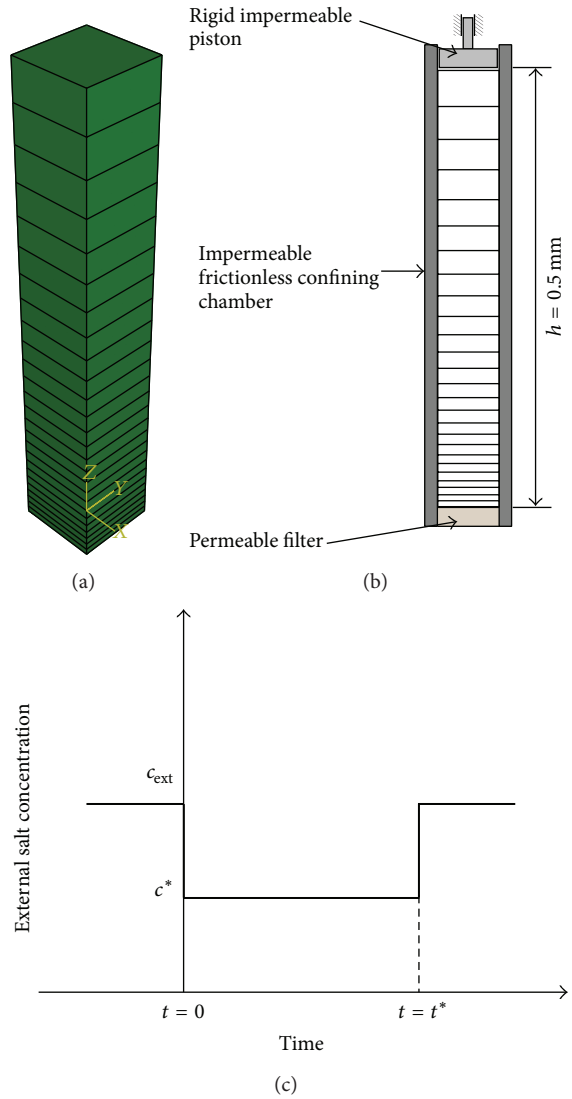

Figure 1: Finite element model (24 poroelastic three-dimensional elements of ABAQUS, C3D8P) for the free-swelling test (a), applied boundary conditions (b), and external salt concentration history (c).

Table 1: Material properties of the reference case [40].

Material parameters	Input value	Description
$c_{F,0}$ [meq/mm^3]	2.0×10^{-4}	Initial fix charge density
c_{ext} [mmol/mm^3]	1.5×10^{-4}	Initial external salt concentration
c^* [mmol/mm^3]	1.0×10^{-4}	External salt concentration at $t = 0$
k_0 [m^4/Ns]	1.0×10^{-15}	Initial permeability
$n_{f,0}$	0.75	Initial fluid fraction

degeneration [15]. Furthermore, other experimental works [45] have shown that this stiffening is not related either to fibres behaviour. Therefore, one reasonable assumption would be to suppose that this increase could be related to the ground substance material behaviour. To simulate this phenomenon the value of the elastic constant C_{10} was modified in order to reproduce a stress increase of 100% for a compression strain of −0.20 at equilibrium [4] (see Table 2).

To validate these assumptions the same test procedure as for healthy AF was done for the degenerated one following Iatridis et al. [4] simulating a Grade IV degeneration.

2.4. FE Simulation of the Complete Lumbar Spine. A complete finite element of the lumbar spine (see [43] for model details) was used. This model is composed of the lumbosacral segment (L1-S1) including the five intervertebral discs and

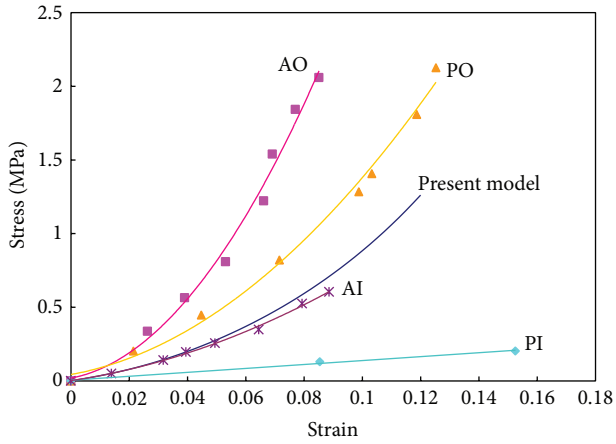

Figure 2: Comparison between experimental data, measured by Ebara et al. [38], and the response of the present model under a traction axial load (AO = anterior outer annulus; PO = posterior outer annulus; AI = anterior inner annulus; PI = posterior inner annulus).

the most important ligaments. The validation of this model with experimental data of the literature is presented [46]. The degeneration of the AF of the L4L5 disc as in the previous section was simulated and the movement and tensional response of the overall spine were compared with those of the healthy one during flexion-extension loading (see Figure 4).

The mechanical properties of the different tissues involved are summarized in Tables 3 and 4. It can be seen that degeneration of L4L5 disc has been considered by modifying the permeability, the void ratio, and the stiffness of the annulus fibrosus as in previous section.

3. Results

3.1. Healthy Annulus Fibrosus. Regarding the free swelling test, an excellent agreement between these calculations and those presented by Wilson et al. [40] for human cartilage was achieved (Figure 5). It can be seen that our simulations are almost equal to the mechanoelectrochemical model of Wilson et al. [40]. Only a slight difference can be appreciated in the swelling part of the test, since the shrinking part perfectly fits.

For the complete validation set described in Section 2.2.2, two different simulations were performed. In the first, a relaxation test, the stress-time behaviour, was compared with experimental results presented by Schroeder et al. [39]. The trends of the numerical and experimental curves showed a very good agreement (Figure 6(a)). It can be noted how the numerical curve is almost completely falling within the experimental interval found by Schroeder et al. [39]. The differences between numerical and experimental results could be related to the permeability value not measured in the experimental set-up and the neglecting of the intrinsic viscoelasticity of the matrix and collagen fibres in our numerical model.

Table 2: Material properties used for the normal and degenerated AF [4, 15, 17, 26, 39, 43, 44, 47].

	Normal	Degenerated
Biphasic material parameters		
$c_{F,0}$ [meq/mm^3]	1.8×10^{-4}	0.9×10^{-4}
k_0 [m^4/Ns]	1.924×10^{-16}	1.5×10^{-16}
$n_{f,0}$	0.75	0.7
e (void ratio)	3.0	2.33
Elastic material parameters		
C_{10} [MPa]	0.1	0.45
C_{20} [MPa]	2.5	
D [MPa^{-1}]	4.8	
K_1 [MPa]	1.8	
K_2	11.0	

The second test, which implies a cycled loading to the sample, was conducted following the guidelines proposed by Iatridis et al. [4]. In this test, the normalized stress-time behaviour of the material was recorded. The comparison between the experimental results, reported by Iatridis et al. [4], and our calculations are shown in Figure 7(b). In general a good agreement can be found. Furthermore, if we consider the ratio between the pick and the valley of each cycle, it can be noted that it is quite perfect for the second cycle (exp. 4.07, FE 4.11) while the maximal difference was found for the last cycle (exp. 2.55, FE 3.13).

3.2. Degenerated Annulus Fibrosus. Using the same constitutive equations for healthy AF but taking into account some modifications of different constants as mentioned in Section 2.3, the same experimental test performed by Iatridis et al. [4] was numerically reproduced. The equilibrium elastic stress-stretch responses of a normal and degenerated model are shown in Figure 8. The numerical results showed a good fit with experimental data, and these prove the matrix stiffening with degeneration.

Subsequently, the stress-strain curves in traction for normal and degenerated cases are plotted in Figure 9. The results showed an increase of the elastic modulus (+91%) in the first part of the curve but no important changes are observed in the second part (+7%). These results were in agreement with the experimental ones found by Guerin and Elliott [24], who obtained an increase of +124% and −0.8%, respectively.

3.3. Finite Element Simulation of Healthy and Degenerated Lumbar Spine. First of all the finite element model of the healthy lumbar spine [43] was validated using data from the literature. The degree of rotation of the different segments was compared with Guan et al. [46]. It can be seen in Figure 10 how this model mimics the behaviour of the healthy spine both under flexion and extension moments. The relative rotation between each pair of vertebrae is plotted and compared with the experimental results obtained from the literature. It can be seen that the response of the numerical simulation fits within the dispersion limits of the experimental protocol.

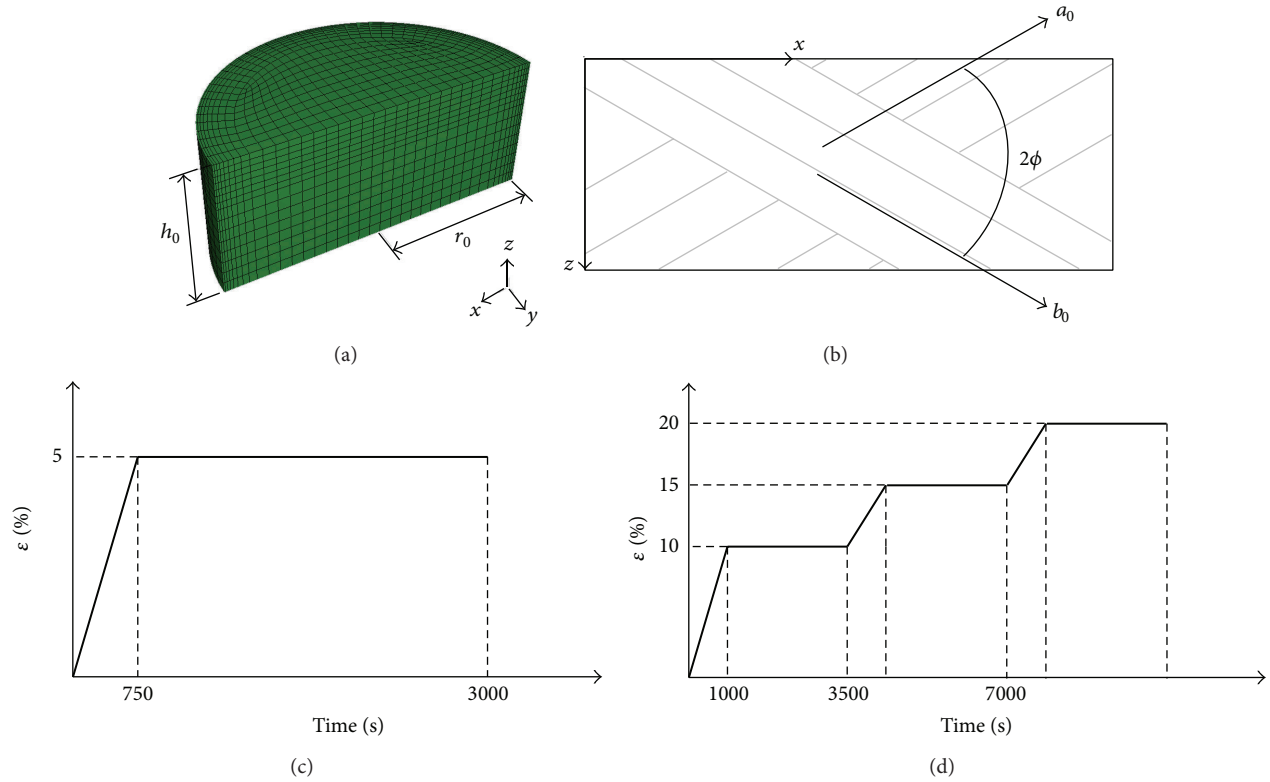

Figure 3: (a) 3D finite element model mesh (16800 hexaedrical porous elements C3D8P). $r_0 = 1.5$ mm $h_0 = 1.281$ mm. (b) Fibres direction in the x-z plane. (c) Mesh axially compressed by 5% strain followed by a relaxation period. (d) Compression strain of 10% followed by 2500 s of relaxation, loading cycle repeated three times adding a 5% of deformation at each increment.

Now the influence of the degeneration of the disc at the L4L5 level is analyzed. First of all, the movement of the spine when the D45 disc is degenerated is compared with the healthy spine shown before. The comparison between both models is presented in Figure 11. It can be seen that the effect of degeneration is not only located at the damaged level L45 since the adjacent levels are also modified with respect to the healthy scenario. It can be appreciated that with degeneration the pair L4L5 gets stiffer and the degree of rotation is smaller in both flexion and extension. This effect also extends to the adjacent levels (L3L4 and L5S1) but the loss of rotation is less pronounced.

Moreover, the stresses in the discs can also be analyzed to prove the influence of the degeneration of one disc on the overall behaviour of the spine. In Figure 12 the maximum and minimum principal stresses are plotted at the levels affected by the degeneration of D45. The remaining discs, D12 and D23, are not shown because these are not affected by the degenerated D45. The stresses are shown for the posterior and anterior part of each disc taking into account both the flexion and extension moment. It can be seen that the stresses are not very different in any case, but it is interesting to highlight that the stresses are more similar in D45 disc between healthy and degenerated situation than in D34 and D51 which are only influenced by degeneration in L4L5 level.

4. Discussion

The goal of this work was to construct a suitable constitutive model to characterize the mechanical behaviour of normal and degenerated annulus fibrosus of the IVD. This model takes into account the biphasic nature and also the clear preferential orientation of the collagen fibres in the annulus. The phenomenon of swelling, indeed, is really important for a correct simulation of the stress-strain behaviour of cartilage as it has evidently shown in previous numerical [7, 40] and experimental works [39, 47, 51]. Furthermore, it plays an important role in the stress relaxation, in fluid regulation and therefore in tissue permeability. Here, the model for fibred reinforced materials, originally proposed by Holzapfel [52], was modified to incorporate the swelling contribution due to the PGs being coupled with the biphasic formulation.

Due to the hydrophilic behaviour of cartilage, an increase of PG's concentration (e.g., due to a compression of the tissue) produces an influx of fluid into the cartilage. This implies an increase of the internal pressure giving the tissue more capacity to absorb loads. To simulate this effect, the component of the 2nd Piola-Kirchhoff stress tensor related to the material compressibility was modified introducing the osmotic gradient pressure. This term considers the tissue fixed charge density as a function of the volume variation [26, 40].

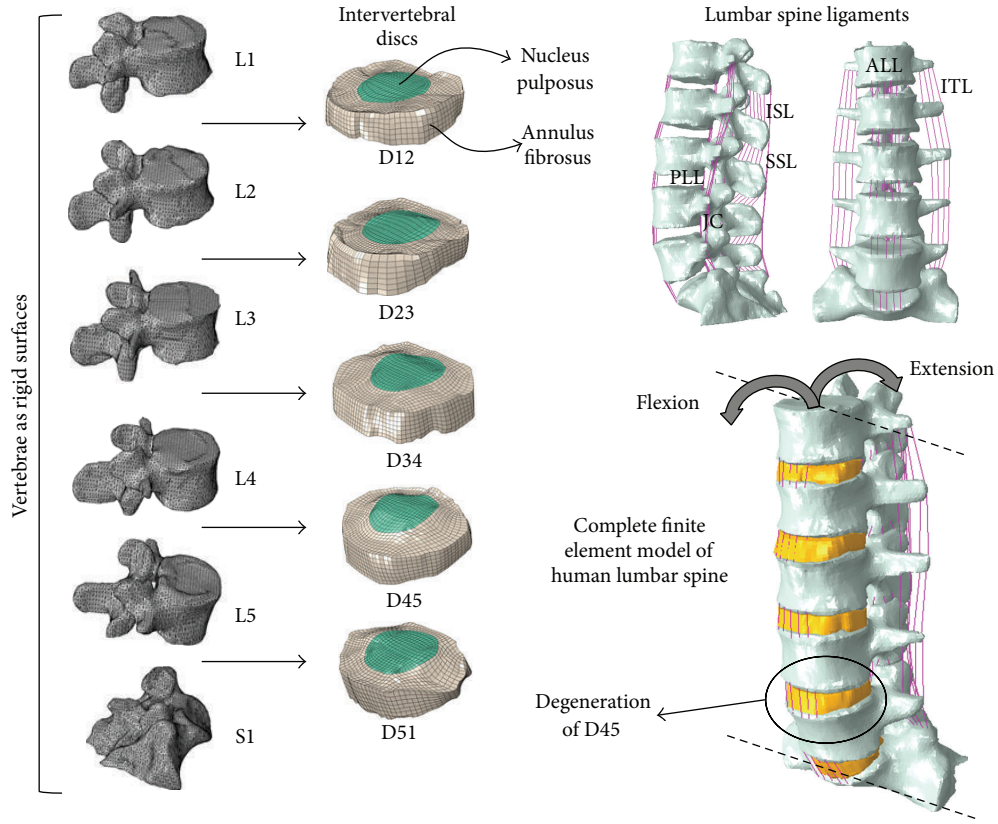

Figure 4: Finite element model of the lumbar spine from a previous publication of the authors, Moramarco et al. [43].

Table 3: Material properties, geometrical parameters, and elements number of the lumbosacral spine ligaments [42, 48–50].

Ligament	E_1 (MPa)	E_2	ϵ_{12}	Number of elements	Area (mm^2)
ALL	7.8	20.0	0.12	5	32.4
PLL	1.0	2.0	0.11	5	5.2
LF	1.5	1.9	0.062	3	84.2
ITL	10.0	59	0.18	4	1.8
SSL	3.0	5.0	0.20	3	25.2
Ligament	Spine level	Area (mm^2)	Poisson's ratio ν	Number of elements	Stiffness k (N/mm)
JC	L1-L2	43.8	0.4	6	42.5 ± 0.8
	L2-L3				33.9 ± 19.2
	L3-L4				32.3 ± 3.3
	L4-L5				30.6 ± 1.5
	L5-S1				29.9 ± 22.0
ISL	L1-L2	35.1	0.4	6	10.0 ± 5.2
	L2-L3				9.6 ± 4.8
	L3-L4				18.1 ± 15.9
	L4-L5				8.7 ± 6.5
	L5-S1				16.3 ± 15.0

Finally, a strain dependent permeability function was implemented in the model. A power-low function of the porosity rate change was chosen relating the actual and the initial permeability [53]. The equivalence between this function and an exponential one [54] was demonstrated by Riches et al. [41].

To validate the behaviour of the poromechanical part of the model a 1D free swelling test was reproduced *in silico*. Because of the lack of data regarding the AF tissue free swelling behaviour, human cartilage tissue behaviour was simulated and compared with previous results found in the literature. Since this tissue did not present a fibred structure,

Table 4: Material properties and element types of the finite element model.

Component	Element type	Number of elements	Material constants	Notes
Bone	R3D3	73016		Rigid body
Nucleus	C3D8	10106	$C_1 = 0.16$ MPa $D = 0.024$ MPa $^{-1}$ $c_{F,0} = 1.810^{-4}$ meq/mm^3 $k_0 = 1.92410^{-16}$ m^4/Ns $n_{f,0} = 0.8$ $e = 4.8$	Porohyperelastic NeoHookean [44]
Annulus	C3D8	19421	see Table 2	Porohyperelastic Fibre reinforced material ($\alpha = \pm 30^\circ$) [17]
Ligaments	T3D2	180	see Table 1	Tension only truss
Posterior processes contact	GAP	30		

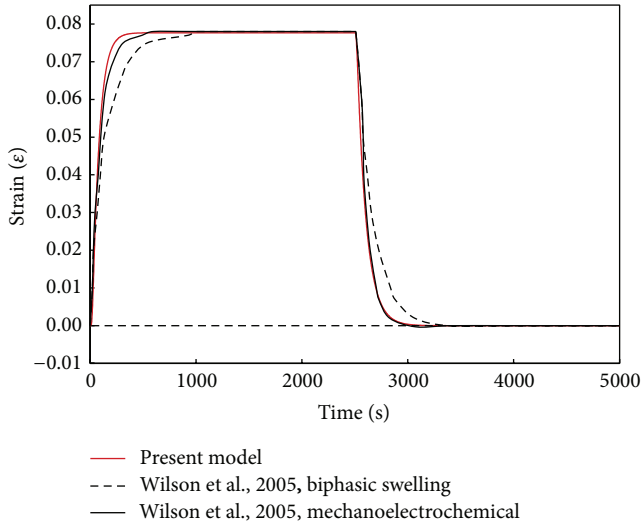

Figure 5: Evolution of the strain during 1D swelling test. Comparison with Wilson et al. [40].

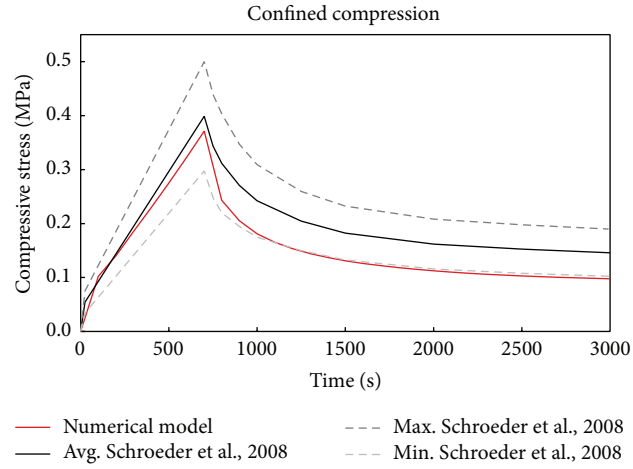

Figure 6: Comparison between experimental data reported by Schroeder et al. [39] and the present numerical model for a confined compression test.

no fibres were considered in the model in agreement with Wilson et al. [40]. The response of the model showed an excellent agreement with these authors [40].

Once the model was validated for free swelling, different tests were performed to guarantee the accuracy of the results. The material constants of the annulus fibrosus related to the fluid and ionic contribution ($k_0, n_0, c_{F,0}$) were obtained from the literature [4, 26, 40, 47]. On the other hand, we were not interested in detecting differences across the zones of the annulus (anterior, posterior, inner, or outer). Therefore, only one set of elastic constant values (C_{10}, C_{20}, D, K_1, and K_2) was fitted to the experimental data by Ebara et al. [38] representing a good average behaviour for the whole annulus. This assumption was fully demonstrated in a previous work [43].

First, the experimental confined compression test proposed by Schroeder et al. [39] for the healthy AF tissue was reproduced *in silico*. The FE model showed a good agreement

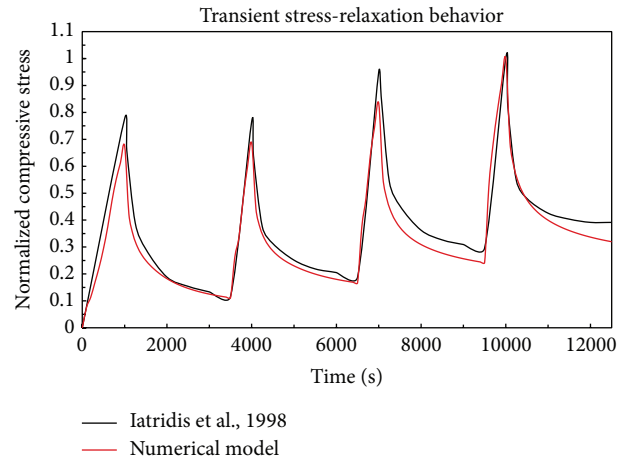

Figure 7: Comparison between experimental data reported by Iatridis et al. [4] and the present numerical model for a confined compression test.

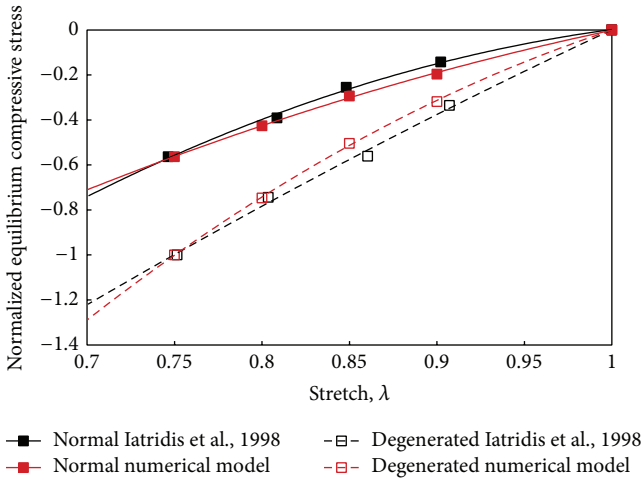

FIGURE 8: Comparison between experimental data reported by Iatridis et al. [4] and the present numerical model for normalized stress-stretch at equilibrium.

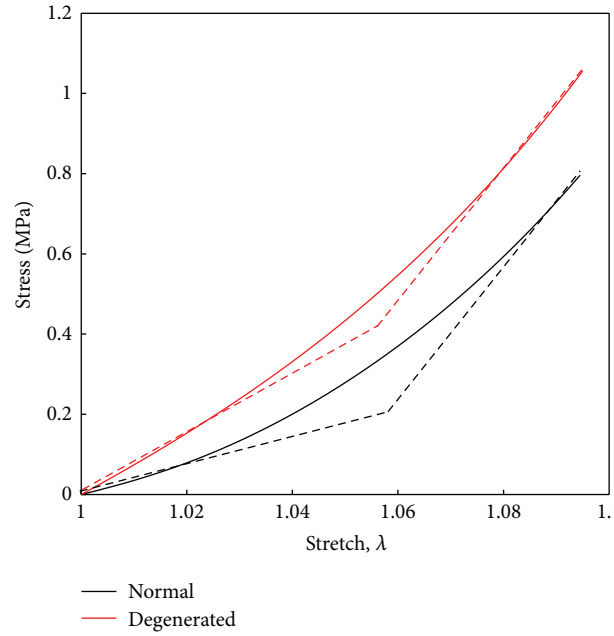

FIGURE 9: Comparison between normal and degenerated behaviour in traction.

with the experimental results. The numerical curve, in fact, fills within the experimental curves range. Furthermore this first analysis showed that our model was capable of predicting values of stresses equivalent to those measured experimentally. However, the found value of stress at the end of the relaxation period was rather different in comparison with the average value reported in the literature. Many explanations could be made for this behaviour. For example the PGs content, or equivalently the fixed charge density, strongly influences the material response [9, 25, 55]. Also the distribution and orientation of the fibres direction could influence the behaviour of the tissue [39, 52].

Then, a transient response behaviour analysis as proposed by Iatridis and coworkers [4] was carried out. Since the experimental curve presented by Iatridis et al. [4] is only related to a specific specimen and not to an average curve; the value of force was normalised and compared. This procedure, furthermore, is in agreement with that proposed by DiSilvestro and Suh [56] and Wilson et al. [13]. From the other hand, the results obtained with the experimental result proposed by Schroeder and coworkers [39] are adequate to guarantee the goodness of found internal stress values. The results showed a good accordance with experimental data. In particular the model showed the ability to recover the value of the stress with the same velocity of experimental data.

In Section 4 a criterion to define a degenerated AF tissue behaviour was defined. In particular the experimental evidences of Iatridis et al. [4] were used to modify the constant values of the model. In Figure 8 the normalised value of the stress was compared between experimental and numerical results for normal and degenerated AF tissue. It can be noted how the proposed procedure was able to reproduce the effects of degeneration: increase of stiffness and reduction of nonlinearity of the behaviour. Iatridis et al. [4] mentioned that the increase in the elastic modulus with degeneration is likely related to an increase in tissue density resulting from the loss of water content. However, the reduction in nonlinearity behaviour with degeneration could suggest a diminished compaction effect of the degenerate tissues at large deformations which could be related to structural changes in matrix. Besides, the effect of the increase of the ground substance elastic modulus was analysed under a pure axial tensile load. The obtained results are also in agreement with the experimental behaviour showed by Guerrin et al. [24]. Experimental results, in fact, showed an increase of the elastic modulus in the toe part, before fibres act, but when the fibres act there is no additional stiffening.

Finally, the constitutive model that has been presented here has been applied to a complete finite element model of the lumbar spine and degeneration of one disc has been provoked by modifying its mechanical properties. In this analysis it has been obtained that the degeneration of one level affects the biomechanics of the adjacent levels; in particular a decrease of the range of motion in flexion/extension has been seen. These results are in agreement with Kettler et al. [34] who analyzed 203 lumbar spine segments obtaining that the range of motion decreased with degeneration. This same result was radiographically shown by Mimura et al. [33] for flexion/extension moments. Regarding the stress distributions in the discs, there is no much data to compare. As mentioned in the introduction, only the work of Ruberte et al. [37] analyzed the influence of single-level lumbar degenerative disc disease on the behaviour of the adjacent levels using the finite element model. However, the conclusions of their study are opposite to what we have obtained here and other experimental results [30, 31]. They obtained that as degeneration progresses the stiffness increased but was significantly less than the healthy model; however it seems that the clinical evidence proves our results. With respect to the stresses distribution, our results showed that there is a

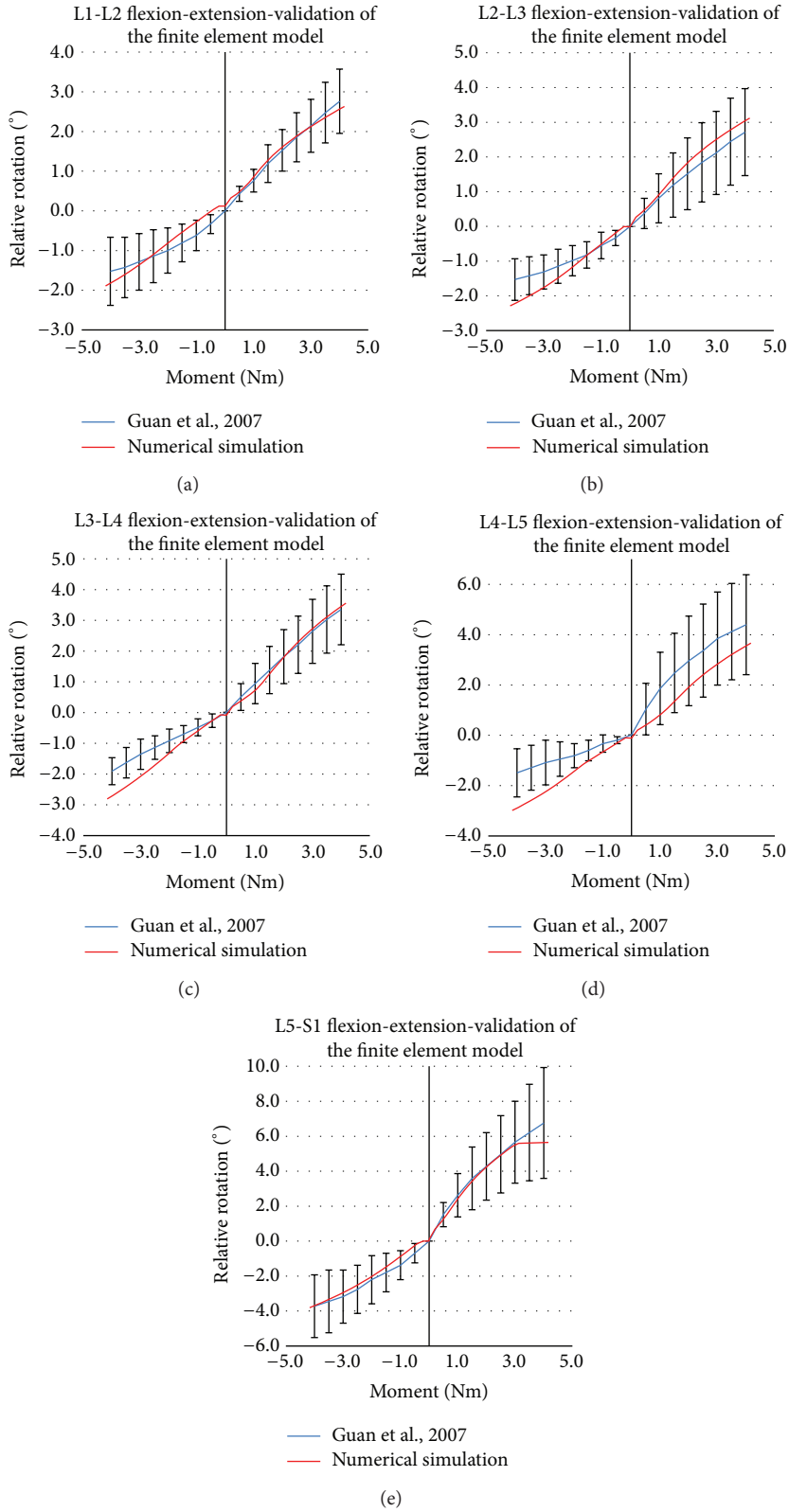

Figure 10: Relative rotation of each pair of vertebrae both in flexion and extension. Comparison between numerical simulation and experimental measures of Guan et al. [46].

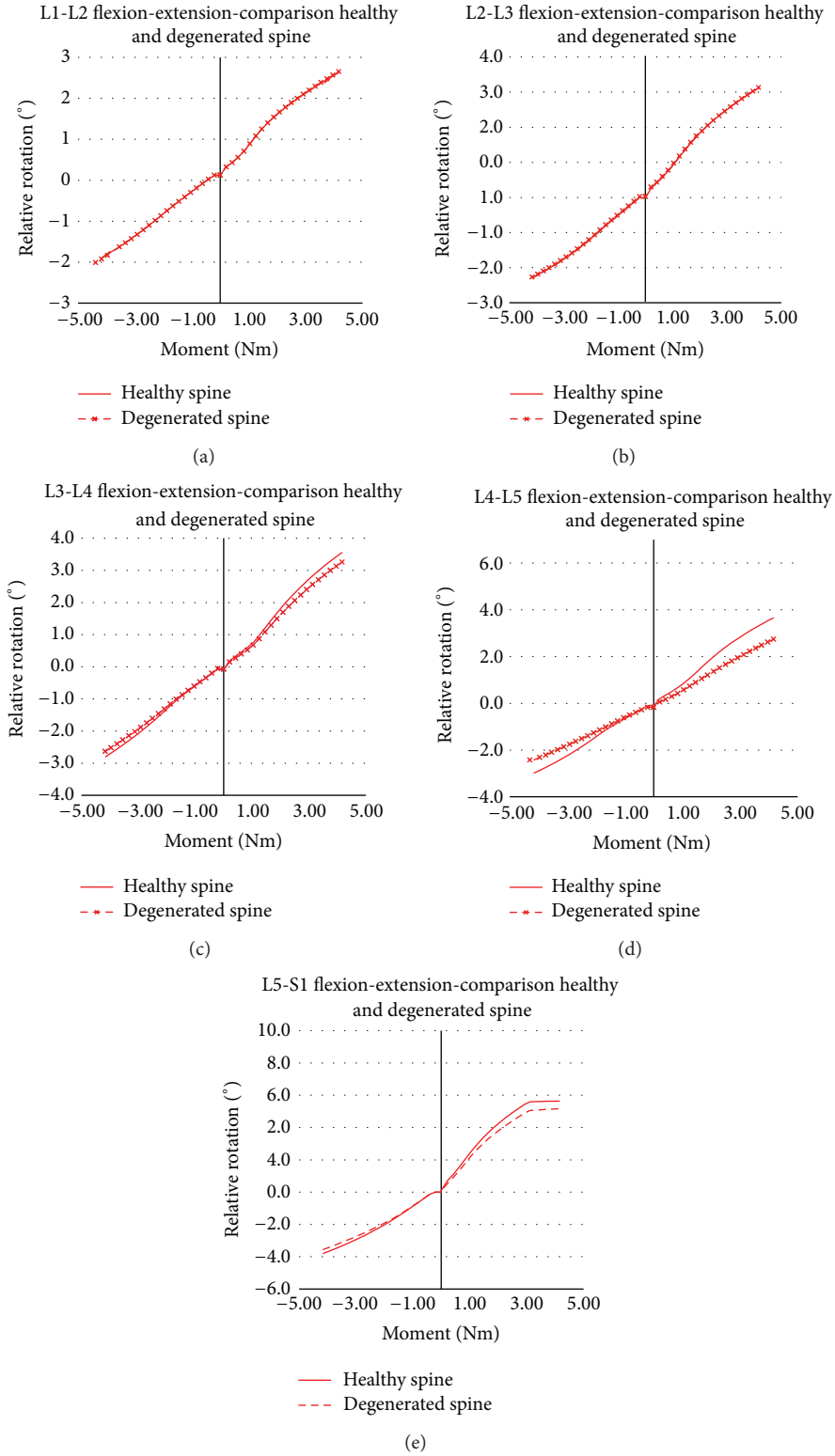

Figure 11: Relative rotation of each pair of vertebrae. Comparison between healthy spine (continuous line) and damaged spine (dashed line) in which D45 disc has been degenerated.

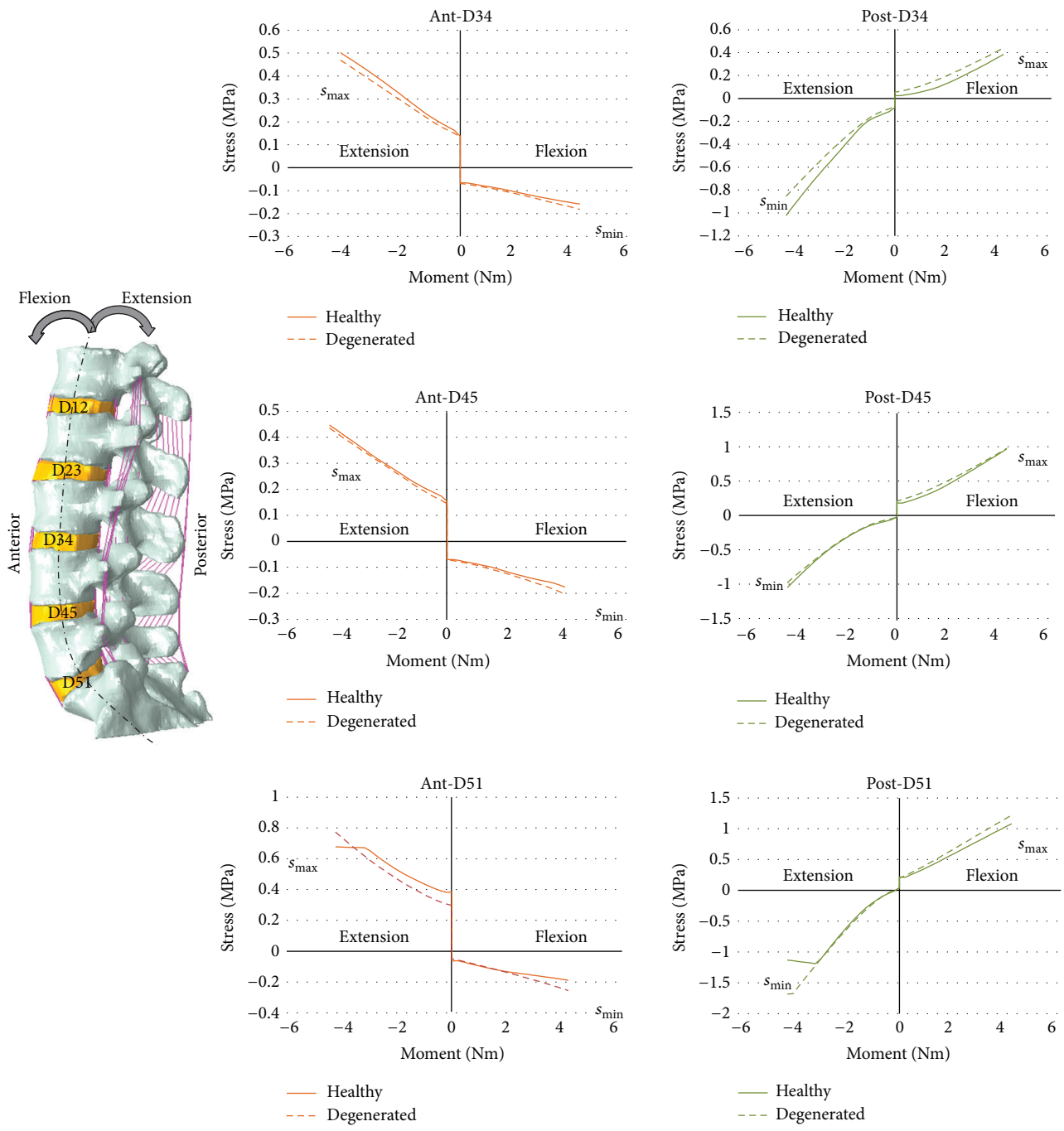

FIGURE 12: Maximum and minimum principal stresses in the anterior and posterior part of D34, D45, and D51 discs. Plots in continuous line correspond to the healthy spine, and plots in dashed lines correspond to the degenerated model.

slight modification on the adjacent levels when one single level is degenerated. However, this data cannot be transferred to the clinical evidence because it is not quantitatively known to what extent loading changes involve degenerative changes.

5. Assumptions and Limitations

The numerical model for the degeneration of the annulus fibrosus has several limitations. First, only the swelling effect has been introduced to describe its behaviour. There are more effects related to the electrochemical nature of cartilage that will be taken into account in further developments. As shown in Figure 6, the viscoelastic nature of the solid matrix can affect the overall response of the tissue and it should be included to improve this model. Numerical predictions have been compared with experimental results; however, there is a lack of data in the literature about the poromechanics of the healthy or degenerated AF and therefore more experimental

data would be required to better guarantee our results. On the other hand, the stiffening of the annulus fibrosus has been reproduced by modifying the mechanical behaviour of the matrix. It is known that with degeneration, collagen fibers are reoriented and broken. This contribution should be introduced in future works.

With respect to the lumbar spine finite element model there are also limitations and underlying assumptions. The most important one is that the same finite element model has been used for healthy and damaged spine. It is known that the height of the discs is modified with degeneration and also the internal structure of the disc but here only the mechanical properties of the degenerated disc have been modified. Notwithstanding the fact that the height of the discs can modify the biomechanical response of the spine, it has been seen [57] that when the disc height is reduced, flexibility of the motion segment decreased. Therefore, this effect would contribute in the same direction to the results that have been obtained here.

6. Conclusions

In conclusion, the developed model is capable of simulating the poromechanical behaviour of normal and degenerated AF tissue with a good approximation. The most important feature of this model is related to the coupling between a strongly fibred matrix and its intrinsic affinity to water regulated by its ionic nature. On the other hand, the degeneration of cartilage is a very complex process that has been here simplified for AF tissue with accurate predictions.

Moreover, the present study provides a qualitative analysis of the influence of single level disc degeneration on the mechanics of the adjacent segments under flexion/extension moments. It has been seen that degeneration modified the degree of motion and loading of both the degenerated disc and adjacent levels. These changes could increase the risk of progression of degeneration to the nearest segments of the spine.

Nomenclature

Ψ: Helmholtz free energy function
Ψ_{gs}: Ground substance Helmholtz free energy function
Ψ_f: Fibres behaviour Helmholtz free energy function
Ψ_{vol}: Material compressibility Helmholtz free energy function
$\mathbf{C}$: Right Cauchy-Green tensor
$\overline{\mathbf{C}}$: Modified right Cauchy-Green tensor
J: Relative volume change $\det \mathbf{C}^{1/2}$
$\mathbf{A}_n$: Structural tensor of the fibre direction
$\mathbf{a}_n$: Fiber direction
$\mathbf{S}$: 2nd Piola-Kirchhoff stress tensor
$\mathbf{S}_{gs}$: Ground substance 2nd Piola-Kirchhoff stress tensor
$\mathbf{S}_f$: Fibres behaviour 2nd Piola-Kirchhoff stress tensor
$\mathbf{S}_{vol}$: Material compressibility 2nd Piola-Kirchhoff stress tensor
$\mathbb{P}$: Project tensor
$\mathbb{I}$: Fourth-order unite tensor
C_{ij}: Ground substance material constants
K_n: Collagen fibres behaviour constants
D: Tissue incompressibility modulus
$\overline{I}_1$: First invariant $\mathrm{tr}\,\overline{\mathbf{C}}$
$\overline{I}_n^*$: Fibres invariants $\mathbf{a}_n^0 \cdot \overline{\mathbf{C}}\mathbf{a}_n^0$
μ_f: Water chemical potential
p: Fluid pressure
$\Delta\Pi$: Osmotic pressure gradient
Π_{ext}: External osmotic pressure
Π_{int}: Internal osmotic pressure
R: Universal gas constant
T: Absolute temperature
ϕ_{int}: Internal osmotic coefficient
ϕ_{ext}: External osmotic coefficient
c_{ext}: External salt concentration
c_F: Fixed charge density
$c_{F,0}$: Initial fixed charge density
$n_{f,0}$: Initial fluid fraction
k: Permeability
k_0: Initial permeability
n: Porosity
n_0: Initial porosity
m: Positive coefficient.

Conflict of Interests

There is not any financial and personal relationship with other people or organisations that could inappropriately influence this work.

Acknowledgment

The support of the Spanish Ministry of Economy and Competitiveness through DPI 2011-23148 project is highly appreciated.

References

[1] M. A. Adams and P. J. Roughley, "What is intervertebral disc degeneration, and what causes it?" *Spine*, vol. 31, no. 18, pp. 2151–2161, 2006.

[2] J. P. Urban, A. Maroudas, M. T. Bayliss, and J. Dillon, "Swelling pressures of proteoglycans at the concentrations found in cartilaginous tissues," *Biorheology*, vol. 16, no. 6, pp. 447–464, 1979.

[3] J. O. Galante, "Tensile properties of the human lumbar annulus fibrosus," *Acta Orthopaedica Scandinavica*, supplement 100, pp. 1–91, 1967.

[4] J. C. Iatridis, L. A. Setton, R. J. Foster, B. A. Rawlins, M. Weidenbaum, and V. C. Mow, "Degeneration affects the anisotropic and nonlinear behaviors of human anulus fibrosus in compression," *Journal of Biomechanics*, vol. 31, no. 6, pp. 535–544, 1998.

[5] A. Shirazi-Adl, "On the fibre composite material models of disc annulusâĂŤcomparison of predicted stresses," *Journal of Biomechanics*, vol. 22, no. 4, pp. 357–365, 1989.

[6] V. C. Mow, W. Zhu, and A. Ratclife, "Structure and function of articular cartilage and meniscus," in *Basic Orthopaedic Biomechanics*, V. C. Mow and W. C. Hayes, Eds., pp. 43–198, Raven Press, New York, NY, USA, 1991.

[7] B. R. Simon, J. P. Liable, D. Pflaster, Y. Yuan, and M. H. Krag, "A poroelastic finite element formulation including transport and swelling in soft tissue structures," *Journal of Biomechanical Engineering*, vol. 118, no. 1, pp. 1–9, 1996.

[8] W. M. Lai, J. S. Hou, and V. C. Mow, "A triphasic theory for the swelling and deformation behaviors of articular cartilage," *Journal of Biomechanical Engineering*, vol. 113, no. 3, pp. 245–258, 1991.

[9] D. N. Sun, W. Y. Gu, X. E. Guo, W. M. Lai, and V. C. Mow, "A mixed finite element formulation of triphasic mechano-electrochemical theory for charged, hydrated biological soft tissues," *International Journal for Numerical Methods in Engineering*, vol. 45, no. 10, pp. 1375–1402, 1999.

[10] A. J. H. Frijns, J. M. Huyghe, and J. D. Janssen, "A validation of the quadriphasic mixture theory for intervertebral disc tissue," *International Journal of Engineering Science*, vol. 35, no. 15, pp. 1419–1429, 1997.

[11] R. van Loon, J. M. Huyghe, M. W. Wijlaars, and F. P. T. Baaijens, "3D FE implementation of an incompressible quadriphasic mixture model," *International Journal for Numerical Methods in Engineering*, vol. 57, no. 9, pp. 1243–1258, 2003.

[12] L. P. Li and W. Herzog, "Strain-rate dependence of cartilage stiffness in unconfined compression: the role of fibril reinforcement versus tissue volume change in fluid pressurization," *Journal of Biomechanics*, vol. 37, no. 3, pp. 375–382, 2004.

[13] W. Wilson, C. C. van Donkelaar, B. van Rietbergen, and R. Huiskes, "A fibril-reinforced poroviscoelastic swelling model for articular cartilage," *Journal of Biomechanics*, vol. 38, no. 6, pp. 1195–1204, 2005.

[14] E. R. Acaroglu, J. C. Iatridis, L. A. Setton, R. J. Foster, V. C. Mow, and M. Weidenbaum, "Degeneration and aging affect the tensile behavior of human lumbar anulus fibrosus," *Spine*, vol. 20, no. 24, pp. 2690–2701, 1995.

[15] J. Antoniou, T. Steffen, F. Nelson et al., "The human lumbar intervertebral disc: evidence for changes in the biosynthesis and denaturation of the extracellular matrix with growth, maturation, ageing, and degeneration," *Journal of Clinical Investigation*, vol. 98, no. 4, pp. 996–1003, 1996.

[16] W. Y. Gu, X. G. Mao, R. J. Foster, M. Weidenbaum, V. C. Mow, and B. A. Rawlins, "The anisotropic hydraulic permeability of human lumbar anulus fibrosus: influence of age, degeneration, direction, and water content," *Spine*, vol. 24, no. 23, pp. 2449–2455, 1999.

[17] R. Eberlein, G. A. Holzapfel, and C. A. J. Schulze-Bauer, "An anisotropic model for annulus tissue and enhanced finite element analyses of intact lumbar disc bodies," *Computer Methods in Biomechanics and Biomedical Engineering*, vol. 4, no. 3, pp. 209–229, 2001.

[18] A. Rohlmann, T. Zander, H. Schmidt, H. Wilke, and G. Bergmann, "Analysis of the influence of disc degeneration on the mechanical behaviour of a lumbar motion segment using the finite element method," *Journal of Biomechanics*, vol. 39, no. 13, pp. 2484–2490, 2006.

[19] A. Polikeit, P. Nolte, and S. J. Ferguson, "Simulated influence of osteoporosis and disc degeneration on the load transfer in a lumbar functional spinal unit," *Journal of Biomechanics*, vol. 37, no. 7, pp. 1061–1069, 2004.

[20] R. N. Natarajan, J. R. Williams, S. A. Lavender, and G. B. J. Andersson, "Poro-elastic finite element model to predict the failure progression in a lumbar disc due to cyclic loading," *Computers and Structures*, vol. 85, no. 11âĂŞ14, pp. 1142–1151, 2007.

[21] H. Schmidt, A. Shirazi-Adl, F. Galbusera, and H. J. Wilke, "Response analysis of the lumbar spine during regular daily activitiesâĂŤa finite element analysis," *Journal of Biomechanics*, vol. 43, no. 10, pp. 1849–1856, 2010.

[22] M. A. Adams, B. J. C. Freeman, H. P. Morrison, I. W. Nelson, and P. Dolan, "Mechanical initiation of intervertebral disc degeneration," *Spine*, vol. 25, no. 13, pp. 1625–1636, 2000.

[23] I. A. Stokes and J. C. Iatridis, "Mechanical conditions that accelerate intervertebral disc degeneration: overload versus immobilization," *Spine*, vol. 29, no. 23, pp. 2724–2732, 2004.

[24] H. A. L. Guerin and D. M. Elliott, "Degeneration affects the fiber reorientation of human annulus fibrosus under tensile load," *Journal of Biomechanics*, vol. 39, no. 8, pp. 1410–1418, 2006.

[25] W. Johannessen and D. M. Elliott, "Effects of degeneration on the biphasic material properties of human nucleus pulposus in confined compression," *Spine*, vol. 30, no. 24, pp. E724–E729, 2005.

[26] R. N. Natarajan, J. R. Williams, and G. B. J. Andersson, "Recent advances in analytical modeling of lumbar disc degeneration," *Spine*, vol. 29, no. 23, pp. 2733–2741, 2004.

[27] K. Singh, K. Masuda, E. J. M. Thonar, H. S. An, and G. Cs-Szabo, "Age-related changes in the extracellular matrix of nucleus pulposus and anulus fibrosus of human intervertebral disc," *Spine*, vol. 34, no. 1, pp. 10–16, 2009.

[28] S. Umehara, S. Tadano, K. Abumi, K. Katagiri, K. Kaneda, and T. Ukai, "Effects of degeneration on the elastic modulus distribution in the lumbar intervertebral disc," *Spine*, vol. 21, no. 7, pp. 811–820, 1996.

[29] H. J. Kirkaldy-Willis and H. F. Farfan, "Instability of the lumbar spine," *Clinical Orthopaedics and Related Research*, vol. 165, pp. 110–123, 1982.

[30] A. Fujiwara, T. H. Lim, H. S. An, C. H. Jeon, G. B. Andersson, and V. M. Haughton, "The effect of disc degeneration and facet joint osteoarthritis on the segmental flexibility of the lumbar spine," *Spine*, vol. 25, no. 23, pp. 3036–3044, 2000.

[31] N. Tanaka, H. S. An, T. H. Lim, A. Fujiwara, C. H. Jeon, and V. M. Haughton, "The relationship between disc degeneration and flexibility of the lumbar spine," *Spine Journal*, vol. 1, no. 1, pp. 47–56, 2001.

[32] M. Krismer, C. Haid, H. Behensky, P. Kapfinger, F. Landauer, and F. Rachbauer, "Motion in lumbar functional spine units during side bending and axial rotation moments depending on the degree of degeneration," *Spine*, vol. 25, no. 16, pp. 2020–2027, 2000.

[33] M. Mimura, M. M. Panjabi, T. R. Oxland, J. J. Crisco, I. Yamamoto, and A. Vasavada, "Disc degeneration affects the multidirectional flexibility of the lumbar spine," *Spine*, vol. 19, no. 12, pp. 1371–1380, 1994.

[34] A. Kettler, F. Rohlmann, C. Ring, C. Mack, and H. J. Wilke, "Do early stages of lumbar intervertebral disc degeneration really cause instability? Evaluation of an in vitro database," *European Spine Journal*, vol. 20, no. 4, pp. 578–584, 2011.

[35] S. Tang and B. J. Rebholz, "Does anterior lumbar interbody fusion promote adjacent degeneration in degenerative disc disease? A finite element study," *Journal of Orthopaedic Science*, vol. 16, no. 2, pp. 221–228, 2011.

[36] J. Z. Yan, G. X. Qiu, Z. H. Wu, X. S. Wang, and Z. J. Xing, "Finite element analysis in adjacent segment degeneration after lumbar fusion," *International Journal of Medical Robotics and Computer Assisted Surgery*, vol. 7, no. 1, pp. 96–100, 2011.

[37] L. M. Ruberte, R. N. Natarajan, and G. B. Andersson, "Influence of single-level lumbar degenerative disc disease on the behavior of the adjacent segmentsâĂŤa finite element model study," *Journal of Biomechanics*, vol. 42, no. 3, pp. 341–348, 2009.

[38] S. Ebara, J. C. Iatridis, L. A. Setton, R. J. Foster, V. C. Mow, and M. Weidenbaum, "Tensile properties of nondegenerate human lumbar anulus fibrosus," *Spine*, vol. 21, no. 4, pp. 452–461, 1996.

[39] Y. Schroeder, D. M. Elliott, W. Wilson, F. P. T. Baaijens, and J. M. Huyghe, "Experimental and model determination of human intervertebral disc osmoviscoelasticity," *Journal of Orthopaedic Research*, vol. 26, no. 8, pp. 1141–1146, 2008.

[40] W. Wilson, C. C. van Donkelaar, and J. M. Huyghe, "A comparison between mechano-electrochemical and biphasic swelling theories for soft hydrated tissues," *Journal of Biomechanical Engineering*, vol. 127, no. 1, pp. 158–165, 2005.

[41] P. E. Riches, N. Dhillon, J. Lotz, A. W. Woods, and D. S. McNally, "The internal mechanics of the intervertebral disc under cyclic loading," *Journal of Biomechanics*, vol. 35, no. 9, pp. 1263–1271, 2002.

[42] V. K. Goel, T. Monroe, L. G. Gilbertson, and P. Brinckmann, "Interlaminar shear stresses and laminae separation in a disc," *Spine*, vol. 20, pp. 243–246, 1995.

[43] V. Moramarco, V. P. del Palomar, C. Pappalettere, and M. DoblarÃĺ, "An accurate validation of a computational model of a human lumbosacral segment," *Journal of Biomechanics*, vol. 43, no. 2, pp. 334–342, 2010.

[44] A. P. del Palomar, B. Calvo, and M. DoblarÃĺ, "An accurate finite element model of the cervical spine under quasi-static loading," *Journal of Biomechanics*, vol. 41, no. 3, pp. 523–531, 2008.

[45] G. A. Holzapfel, C. A. J. Schulze-Bauer, G. Feigl, and P. Regitnig, "Single lamellar mechanics of the human lumbar anulus fibrosus," *Biomechanics and Modeling in Mechanobiology*, vol. 3, no. 3, pp. 125–140, 2005.

[46] Y. Guan, N. Yoganandan, J. Moore et al., "Moment-rotation responses of the human lumbosacral spinal column," *Journal of Biomechanics*, vol. 40, no. 9, pp. 1975–1980, 2007.

[47] Y. Schroeder, W. Wilson, J. M. R. J. Huyghe, and F. P. T. Baaijens, "Osmoviscoelastic finite element model of the intervertebral disc," *European Spine Journal*, vol. 15, no. 3, pp. 361–371, 2006.

[48] J. Chazal, A. Tanguy, M. Bourges et al., "Biomechanical properties of spinal ligaments and a histological study of the supraspinal ligament in traction," *Journal of Biomechanics*, vol. 18, no. 3, pp. 167–176, 1985.

[49] K. Goto, N. Tajima, E. Chosa et al., "Effects of lumbar spinal fusion on the other lumbar intervertebral levels (three-dimensional finite element analysis)," *Journal of Orthopaedic Science*, vol. 8, no. 4, pp. 577–584, 2003.

[50] F. A. Pintar, N. Yoganandan, T. Myers, A. Elhagediab, and A. Sances Jr., "Biomechanical properties of human lumbar spine ligaments," *Journal of Biomechanics*, vol. 25, no. 11, pp. 1351–1356, 1992.

[51] N. O. Chahine, F. H. Chen, C. T. Hung, and G. A. Ateshian, "Direct measurement of osmotic pressure of glycosaminoglycan solutions by membrane osmometry at room temperature," *Biophysical Journal*, vol. 89, no. 3, pp. 1543–1550, 2005.

[52] G. A. Holzapfel, *Nonlinear Solid Mechanics*, Wiley, New York, NY, USA, 2000.

[53] A. Koponen, M. Kataja, and J. Timonen, "Permeability and effective porosity of porous media," *Physical Review E*, vol. 56, pp. 3319–3325, 1997.

[54] M. Argoubi and A. Shirazi-Adl, "Poroelastic creep response analysis of a lumbar motion segment in compression," *Journal of Biomechanics*, vol. 29, no. 10, pp. 1331–1339, 1996.

[55] J. C. Iatridis, J. P. Laible, and M. H. Krag, "Influence of fixed charge density magnitude and distribution on the intervertebral disc: applications of a poroelastic and chemical electric (PEACE) model," *Journal of Biomechanical Engineering*, vol. 125, no. 1, pp. 12–24, 2003.

[56] M. R. DiSilvestro and J.-K. F. Suh, "A cross-validation of the biphasic poroviscoelastic model of articular cartilage in unconfined compression, indentation, and confined compression," *Journal of Biomechanics*, vol. 34, no. 4, pp. 519–525, 2001.

[57] R. N. Natarajan and G. B. J. Andersson, "The influence of lumbar disc height and cross-sectional area on the mechanical response of the disc to physiologic loading," *Spine*, vol. 24, no. 18, pp. 1873–1881, 1999.

Hindawi Publishing Corporation
Journal of Applied Mathematics
Volume 2014, Article ID 261347, 10 pages
http://dx.doi.org/10.1155/2014/261347

Research Article

Removal of Muscle Artifacts from Single-Channel EEG Based on Ensemble Empirical Mode Decomposition and Multiset Canonical Correlation Analysis

Xun Chen,[1,2] Chen He,[2] and Hu Peng[1]

[1] *Department of Biomedical Engineering, School of Medical Engineering, Hefei University of Technology, Hefei, Anhui 230009, China*
[2] *Department of Electrical and Computer Engineering, University of British Columbia, Vancouver, BC, Canada V6T 1Z4*

Correspondence should be addressed to Hu Peng; hpeng@hfut.edu.cn

Received 27 March 2014; Revised 25 May 2014; Accepted 25 May 2014; Published 12 June 2014

Academic Editor: Chang-Hwan Im

Copyright © 2014 Xun Chen et al. This is an open access article distributed under the Creative Commons Attribution License, which permits unrestricted use, distribution, and reproduction in any medium, provided the original work is properly cited.

Electroencephalogram (EEG) recordings are often contaminated with muscle artifacts. This disturbing muscular activity strongly affects the visual analysis of EEG and impairs the results of EEG signal processing such as brain connectivity analysis. If multichannel EEG recordings are available, then there exist a considerable range of methods which can remove or to some extent suppress the distorting effect of such artifacts. Yet to our knowledge, there is no existing means to remove muscle artifacts from single-channel EEG recordings. Moreover, considering the recently increasing need for biomedical signal processing in ambulatory situations, it is crucially important to develop single-channel techniques. In this work, we propose a simple, yet effective method to achieve the muscle artifact removal from single-channel EEG, by combining ensemble empirical mode decomposition (EEMD) with multiset canonical correlation analysis (MCCA). We demonstrate the performance of the proposed method through numerical simulations and application to real EEG recordings contaminated with muscle artifacts. The proposed method can successfully remove muscle artifacts without altering the recorded underlying EEG activity. It is a promising tool for real-world biomedical signal processing applications.

1. Introduction

The electroencephalogram (EEG) is frequently contaminated by various physiological activities of noninterest, such as electrocardiogram (ECG), electrooculogram (EOG), and electromyogram (EMG). These artifacts reduce the quality of the signal and blur features of interest. While ECG and EOG artifacts can be effectively removed by using adaptive filters and blind source separation (BSS) techniques [1], the perturbation induced by muscular activity (e.g., biting, chewing, and frowning) is particularly difficult to correct as recently reviewed in [2]. The main reason lies in the fact that EMG artifacts have higher amplitude (compared with the EEG signal), wide spectral distribution, and variable topographical distribution [2]. These muscle artifacts obscure EEG signals and make the interpretation of the EEG complicated or even unfeasible [3].

Low-pass filters are commonly employed to remove muscle artifacts. However, since the frequency spectrum of muscle artifacts significantly overlaps with that of brain signals, these filters not only suppress muscle artifacts but also interesting brain signals [4]. Recently, as one of the most popular BSS techniques, independent component analysis (ICA) has been extensively explored for this purpose [5–7]. ICA utilizes higher-order statistics and aims to separate the EEG recordings into statistically independent components (ICs). Clean EEG data can then be reconstructed by removing artifacts-related ICs from the raw EEG data. However, in some studies muscle artifacts seriously contaminate most ICs and crosstalk of brain and muscle activity can be observed [8, 9]. One possible reason is that ICA only exploits the spatial structure of source signals and the marginal distribution of the observations. Thus, it is suitable when source signals are temporally independent [10]. However, the artifacts typically

have certain temporal structure which can be exploited for better source separation.

Second order blind identification (SOBI) takes temporal structure into consideration and simultaneously diagonalizes several covariance matrices at different time lags [10]. It has been shown that SOBI improved the performance significantly over ICA [11]. Yet, SOBI only considers stationary sources and it may suffer when there exist nonstationary ones, such as transient muscular activities [12]. More recently, a canonical correlation analysis (CCA) method has been proposed as a more suitable BSS approach for separating EMG artifacts from EEG [13]. Due to the broad frequency spectrum of the EMG artifacts, they resemble temporal white noise and thus have lower autocorrelation compared to EEG signals. The method exploits this characteristic for EMG removal and has been shown to outperform ICA on simulated data. Later, the result has been again documented by Gao et al. [14]. One possible reason for CCAs superior performance over ICA is due to the fact that muscle artifacts involve the movement of a group of muscles, which do not have a stereotyped topography [14]. Therefore, ICA does not function correctly here. Lately, a novel multiple time-lag CCA-based method was proposed to further improve the performance for removing muscular artifact in EEG [15]. However, it did not provide enough quantitative and comparative results based on either simulated or real data.

In recent years, biomedical signal measurement and processing are increasingly being deployed in ambulatory situations, particularly in healthcare applications. It is a trend to transit healthcare systems from hospital-centric toward ambulation-based, where minimal instrumentation and low computational complexity are required. The emerging wearable and portable wireless EEG system is a representative [16–18]. To reduce the complexity, quite a few ambulatory systems operate using only one single EEG channel, for example, [17, 18], in which case it is crucial to suppress muscle artifacts to extract as much valuable information as possible. However, almost all current methods for muscle artifact removal so far have been designed to handle multichannel/multidimensional datasets and will fail to isolate muscle activity in the current situation where only single-channel (unidimensional) EEG recordings are available.

In this study, we therefore propose a simple yet effective method to achieve the muscle artifact removal from single-channel EEG. Actually, it is a two-step modeling strategy. In the first step, unidimensional EEG is decomposed into multidimensional datasets. To implement this step, empirical mode decomposition (EMD) is a suitable option. EMD is a single-channel technique that decomposes nonstationary and nonlinear time series into a finite number of intrinsic mode functions (IMFs) [19]. Compared with other decomposition methods (e.g., wavelet transform), EMD is completely data-driven, meaning that it decomposes a signal in a natural way without requiring prior knowledge [20]. It has been shown to be efficient in many biomedical applications, for example, removing motion artifacts from functional near-infrared spectroscopy (fNIRS) data [21] and eliminating eye blink artifacts from EEG recordings [22]. However, the original EMD algorithm is highly sensitive to noise and may cause mode mixing. Recently, a noise assisted version of EMD, called ensemble EMD (EEMD), was proposed and has been demonstrated to be more robust in real-life applications [23]. In the second step, multiset canonical correlation analysis (MCCA) [24] is utilized as a BSS technique instead of the conventional CCA to the multidimensional datasets obtained from the first step. The advantage of MCCA over CCA will be discussed. The separation of muscle and brain activity components can then be achieved due to the relative low autocorrelation of muscle artifacts in comparison with brain activity. We denote the method as EEMD-MCCA by exploring the combination of EEMD and MCCA. The main contribution of the proposed method is to solve the practical muscle artifact removal problem from single-channel EEG, especially at the time when ambulatory healthcare is drawing continuously increasing attention.

We will examine the performance of the proposed EEMD-MCCA method on both synthetic and real datasets. We first validate it on simulated data by quantitative measures. We then apply it to real EEG recordings contaminated with muscle artifacts. We note that while EEMD-MCCA is proposed to remove muscle activity for the single-channel EEG case, it is generally applicable when one dataset contains relatively fewer channels (e.g., two or three) by first applying EEMD to each channel and then utilizing MCCA to the integrated signals after decomposition.

2. Materials and Methods

2.1. Methods. In this section, we first briefly introduce the techniques employed in this paper. Then we describe the new proposed EEMD-MCCA method.

Notations. Scalars are denoted by lowercase italic letters $(a, b, \ldots)$, vectors by lowercase boldface letters $(\mathbf{a}, \mathbf{b}, \ldots)$, matrices by boldface capitals $(\mathbf{A}, \mathbf{B}, \ldots)$, and the number of rows and columns by italic capitals $(T, N, \ldots)$. Matrix or vector transposition is denoted by an uppercase superscript T (e.g., $\mathbf{X}^T$, $\mathbf{v}^T$). The symbol $\mathbf{x}$ (with size $1 \times T$) is used to represent the original single-channel signal. It can be also expressed like this $\mathbf{x} = [\mathbf{x}(1), \mathbf{x}(2), \ldots, \mathbf{x}(T)]$, where $\mathbf{x}(t)$ $(t = 1, 2, \ldots, T)$ is the value of the signal at the time point t.

2.1.1. Ensemble Empirical Mode Decomposition. EMD is a single-channel decomposition method for nonstationary and nonlinear signals [19]. EMD decomposes a signal into a finite number of IMFs, which represent fast to slow oscillations. An IMF is a function that satisfies two following conditions [19]: (1) the number of extrema and the number of zero crossings must either be equal or differ at most by one; and (2) at any point, the mean value of the envelope defined by the local maxima and the envelope defined by the local minima are zero. To obtain an IMF from the original signal $\mathbf{x}$, a sifting process is performed [19]. First, all extrema of the original signal $\mathbf{x}$ need to be identified. All local maximum points are connected by a cubic spline line as the upper envelope $\mathbf{e}_u$.

Repeat the procedure for local minimum points to form the lower envelope $\mathbf{e}_l$. Their mean $\mathbf{a}_1$ is calculated as

$$\mathbf{a}_1 = \frac{\mathbf{e}_u + \mathbf{e}_l}{2}. \tag{1}$$

The difference between the signal and the mean is defined as the first component $\mathbf{h}_1$ as follows:

$$\mathbf{h}_1 = \mathbf{x} - \mathbf{a}_1. \tag{2}$$

In the second sifting process, $\mathbf{h}_1$ is treated as the signal, and we can have

$$\mathbf{h}_{11} = \mathbf{h}_1 - \mathbf{a}_{11}. \tag{3}$$

Subsequently, we can repeat this sifting procedure k times until $\mathbf{h}_{1k}$ is an IMF, with

$$\mathbf{h}_{1k} = \mathbf{h}_{1(k-1)} - \mathbf{a}_{1k}. \tag{4}$$

Therefore the first IMF component derived from the original signal is designated as

$$\mathbf{c}_1 = \mathbf{h}_{1k}. \tag{5}$$

A criterion for stopping the sifting process to have an IMF has been established by limiting the size of the standard deviation (SD), calculated from the two consecutive sifting sequences as follows:

$$\mathrm{SD} = \sum_{t=1}^{T} \left\{ \frac{\left[\mathbf{h}_{1(k-1)}(t) - \mathbf{h}_{1k}(t)\right]^2}{\mathbf{h}_{1(k-1)}^2(t)} \right\}. \tag{6}$$

A typical value for SD can be set between 0.2 and 0.3 [19].

To extract the 2nd IMF component, we remove c_1 from the original signal x to have

$$\mathbf{r}_1 = \mathbf{x} - \mathbf{c}_1. \tag{7}$$

The residual r_1 is treated as a new signal and the same sifting process is applied to obtain the 2nd IMF component c_2 and the residual

$$\mathbf{r}_2 = \mathbf{r}_1 - \mathbf{c}_2. \tag{8}$$

This procedure can be repeated on the subsequent residuals $\mathbf{r}_j$'s until the final residual $\mathbf{r}_J$ no longer contains any oscillation information:

$$\mathbf{r}_j = \mathbf{r}_{j-1} - \mathbf{c}_j. \tag{9}$$

By summing up (7), (8), and (9), we can obtain

$$\mathbf{x} = \sum_{j=1}^{J} \mathbf{c}_j + \mathbf{r}_J. \tag{10}$$

Thus, we decompose the original signal $\mathbf{x}$ into J empirical modes $\mathbf{c}_i$'s and a residue $\mathbf{r}_J$.

However, the original EMD algorithm is highly sensitive to noise. Recently, Wu and Huang introduced a new noise-assisted data analysis method, called EEMD [23]. The method defines the true IMF components as the mean of an ensemble of trials. Each trial consists of the signal plus an additive independent identically distributed white noise of the same standard deviation. In this case, although each individual trial may produce noisy results, it is canceled out in the ensemble mean of sufficient trials since the noise in each trial is assumed independently.

2.1.2. Canonical Correlation Analysis. Two zero-mean data sets are stored in two matrices, $\mathbf{X}_1$ with size $P_1 \times T$ and $\mathbf{X}_2$ with size $P_2 \times T$, where T means the number of observations and P_1 and P_2 indicate the numbers of variables in corresponding matrices. Conventional CCA is to find linear combinations of both $\mathbf{X}_1$ and $\mathbf{X}_2$ variables which have maximum correlation coefficient with each other [25]. This leads to the following objective function with constraints:

$$\begin{aligned} &\max_{\mathbf{v}_1,\mathbf{v}_2} \quad \left(\mathbf{v}_1^T \mathbf{X}_1 \mathbf{X}_2^T \mathbf{v}_2\right)^2 \\ &\text{s.t.} \quad \mathbf{v}_1^T \mathbf{X}_1 \mathbf{X}_1^T \mathbf{v}_1 = 1, \qquad \mathbf{v}_2^T \mathbf{X}_2 \mathbf{X}_2^T \mathbf{v}_2 = 1, \end{aligned} \tag{11}$$

where $\mathbf{v}_i$'s $(i = 1, 2)$ are the weight vectors.

The solutions to this problem are the largest eigenvectors of the matrices $(\mathbf{X}_1\mathbf{X}_1^T)^{-1}\mathbf{X}_1\mathbf{X}_2^T(\mathbf{X}_2\mathbf{X}_2^T)^{-1}\mathbf{X}_2\mathbf{X}_1^T$ and $(\mathbf{X}_2\mathbf{X}_2^T)^{-1}\mathbf{X}_2\mathbf{X}_1^T(\mathbf{X}_1\mathbf{X}_1^T)^{-1}\mathbf{X}_1\mathbf{X}_2^T$, respectively. The subsequent weights are the eigenvectors of the same matrix in the order of decreasing eigenvalues. The canonical variates $\mathbf{U}_i$ $(i = 1, 2)$ can be calculated directly from the original matrices $\mathbf{X}_i$'s as $\mathbf{U}_i = \mathbf{V}_i^T \mathbf{X}_i$. The corresponding rows between $\mathbf{U}_1$ and $\mathbf{U}_2$ are highly correlated, while the rows within each individual $\mathbf{U}_i$ are uncorrelated with each other. The detailed derivation can be referred to [26].

Due to the aforementioned property, conventional CCA has been further extended to solve the BSS problem by assuming source components to be maximally autocorrelated and mutually uncorrelated in a functional magnetic resonance imaging (fMRI) study [27]. In the setting, let $\mathbf{X}_1$ be the observed data matrix $\mathbf{X}$ with P mixtures and T samples, and let $\mathbf{X}_2$ be a temporally delayed version of the original data matrix $\mathbf{X}_2(t) = \mathbf{X}(t-\tau)$. Thus, CCA can separate the recorded data into the self-correlated and mutually uncorrelated sources. As a potential alternative for the most widely used ICA method, CCA has been previously examined against a number of ICA algorithms using multichannel or single-channel recordings. The CCA-based methods were shown to outperform the ICA-based techniques for EEG/fNIRS artifact removal [13, 14, 21] and also demonstrated to be more computationally efficient when having similar qualitative results for EEG/fMRI source separation [27, 28] due to the usage of second-order statistics.

2.1.3. Multiset Canonical Correlation Analysis. MCCA extends the theory of CCA to more than two data sets to identify canonical variates that summarize the correlation structure among multiple random vectors by linear transformations. Unlike CCA where correlation between two canonical variates is maximized, MCCA aims to optimize an objective function of the correlation matrix of the canonical variates from multiple random vectors in order to make the canonical variates achieve the maximum overall correlation [24]. Suppose we have M data sets $\mathbf{X}_m$ $(m = 1, 2, \ldots, M)$ with size $P \times T$. The aim of MCCA is to extract source components which are uncorrelated within each individual data set $\mathbf{X}_m$ and meanwhile correlated well across the M data sets. Analogously, it is straightforward to

Input: the single-channel EEG signal $\mathbf{x}$ with size $1 \times T$.
Output: the reconstructed EEG signal $\widehat{\mathbf{x}}$ after muscle artifact removal.
The First Step:
(1) **for** $i = 1 : I$ **do**
(2) Add independent identically distributed white noise to the single-channel EEG $\mathbf{x}$;
(3) Apply EMD to the above noisy signal and derive a set of IMFs by (1)–(10), denoted as $\mathbf{F}_i$;
(4) **end for**
(5) Obtain an ensemble of IMF sets $\mathbf{F}_i$'s;
(6) Calculate a set of averaged IMFs as the final decomposition, that is $\mathbf{X} = \sum_{i=1}^{I} F_i/I$;
The Second Step:
(7) M temporally delayed versions of the matrix $\mathbf{X}$ are generated according to (12), that is $\mathbf{X}_m$, $m = 1, 2, \ldots, M$;
(8) Apply MCCA to the M data sets and extract the underlying sources $\widehat{\mathbf{S}}$ in $\mathbf{X}$;
(9) Set the sources $\widehat{\mathbf{S}}$ corresponding to muscle artifacts (with low autocorrelation) to zero;
(10) Return the cleaned multichannel signals $\widehat{\mathbf{X}}$ by passing the source matrix through the mixing matrix $\mathbf{A}$;
(11) Reconstruct the single-channel EEG signal $\widehat{\mathbf{x}}$ by summing the recovered IMFs in the matrix $\widehat{\mathbf{X}}$.

Algorithm 1: The EEMD-MCCA Algorithm.

extend MCCA to handle the BSS problem under the similar assumption by letting

$$\mathbf{X}_m(t) = \mathbf{X}(t - (m-1)\tau), \quad m = 1, 2, \ldots, M. \tag{12}$$

To demonstrate the advantage of MCCA over CCA, we will briefly discuss the source separability conditions. For more details, one can refer to [24]. When $M = 2$, the following condition must be satisfied to successfully recover the P underlying sources by CCA:

$$\left|r_{1,2}^{(k)}\right| \neq \left|r_{1,2}^{(l)}\right|, \quad (1 \leq k < l \leq P), \tag{13}$$

where $|r_{1,2}^{(k)}|$ represents the correlation coefficient between the kth source from the 1st data set and the kth source from the 2nd data set. When $M > 2$, the following requirement must be met to successfully recover the P underlying sources from each of M data sets correspondingly by MCCA:

$$\begin{aligned} &\forall m \in 1, 2, \ldots, M, \quad \exists\, n \neq m, \text{ such that} \\ &\left|r_{m,n}^{(k)}\right| \neq \left|r_{m,n}^{(l)}\right|, \quad 1 \leq k < l \leq P, \end{aligned} \tag{14}$$

where $|r_{m,n}^{(k)}|$ represents the correlation coefficient between the kth source from the mth data set and the kth source from the nth data set.

It is important to note that condition (14) is more relaxed than (13), especially for our discussed BSS problem. More specifically, if two underlying sources have the same autocorrelation regarding to the time delay τ, condition (13) will not be met so that these two sources cannot be recovered successfully by CCA. However, as long as these two sources have different autocorrelations for one of the possible time delays $m\tau$ ($m = 1, 2, \ldots, M$), they can be extracted completely by MCCA according to (14). The difference between (14) and (13) suggests that solving the BSS problem on a larger group of data sets is easier than doing that on a smaller group of datasets.

2.1.4. The Proposed EEMD-MCCA. To deal with the muscle artifact removal problem in single-channel EEG, we propose taking advantage of both EEMD and MCCA by exploring their combination and denote the proposed method as EEMD-MCCA. In fact, it is a two-step modeling strategy.

In the first step, EEMD is employed to decompose the single-channel EEG signal $\mathbf{x}$ and derive a set of averaged IMFs. All the IMF components and the final residual are placed into a matrix $\mathbf{X}$. The size of $\mathbf{X}$ is $N \times T$, where $N = J + 1$. Regarding the ensemble number I, it is found that the performance of the technique becomes fairly consistent when using ten or more ensembles in our application. This is a proper number in practice considering the computational cost. The noise standard deviation has been suggested empirically to 0.2 times the standard deviation of the original signal [23].

In the second step, (12) is first used to generate M temporally delayed versions of the matrix $\mathbf{X}$. Then MCCA is applied to the M data sets and the underlying sources $\widehat{\mathbf{S}}$ in $\mathbf{X}$ are extracted and ordered in terms of autocorrelation from high to low. The sources with low autocorrelation correspond to muscle artifacts and can be removed by setting the corresponding row of the matrix $\widehat{\mathbf{S}}$ to be zero. The source matrix is then passed through the mixing matrix $\mathbf{A}$ to return the cleaned multichannel signals $\widehat{\mathbf{X}}$ which are now, ideally, free of artifacts. The artifact-free single-channel recording $\widehat{\mathbf{x}}$ can be determined by summing the recovered IMFs in the matrix $\widehat{\mathbf{X}}$. Regarding the parameter M, we will discuss more in the simulation part. After these two steps, the muscle activity can almost be removed from single-channel EEG. The specific implementation procedure is shown in Algorithm 1.

2.2. Data Description

2.2.1. Synthetic Data. To demonstrate the performance of the proposed EEMD-MCCA method, in this section we will generate synthetic single-channel EEG with real-life muscle

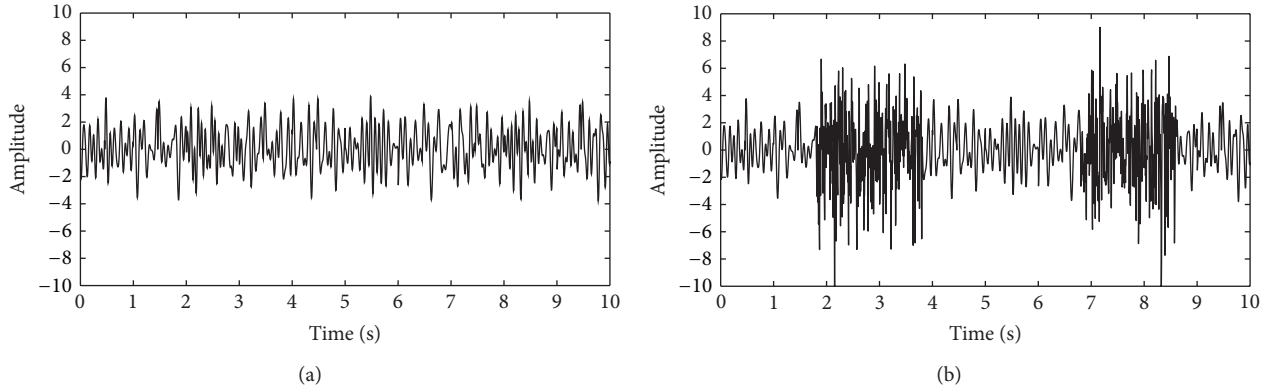

Figure 1: (a) The original EEG data. (b) The contaminated EEG data by muscle activity.

artifacts. Further, we employ some measures to test the performance since the ground truth is known.

Conventionally, the "ground truth" EEG signals without muscle artifacts were selected according to the visual inspection of experienced neurophysiologists. However, not only it is difficult to obtain clean EEG signals, but also there is no guarantee that the signals are completely free of muscle activity solely relying on visual inspection. Thus, in this study, we tend to use synthetic EEG data. A single-channel EEG series can be generated according to the phase-resetting theory [29, 30]. Similar to Mäkinen et al. [29], we generated our simulated data by summing 4 such sinusoids with frequencies chosen randomly from range 4–20 Hz. The sampling frequency was 250 Hz. Ten trials of EEG were generated and each trial was 1 second long. Then a 10-second series $\mathbf{x}_{\mathrm{EEG}}$ could be formed by concatenating the 10 trials, containing mainly theta, alpha, and beta activity. It should be noted that while each trial included 4 distinct frequencies, the frequencies chosen in different trials were also independent, which means that there was rich frequency information in the 10-second series.

To simulate real-life situations, obtaining pure muscle activity is quite necessary. It is insufficient to select muscle artifacts directly from the EEG as they contain both muscle and brain activity. To remove EEG activity and acquire muscle activity, ICA was utilized to decompose a real EEG data set with 21 channels. A neurophysiologist labeled the eye blink artifacts, eye movement artifacts, and muscle artifacts from all the decomposed ICs by inspecting some features such as the power spectral density and topography. It is important to note that a large number of ICs contained both EMG and ongoing EEG activity. Nevertheless, there existed one component containing pure EMG activity, denoted by $\mathbf{x}_{\mathrm{EMG}}$. Since we focus on single-channel issues, it is unnecessary to reconstruct the component with the corresponding field distribution.

The EMG activity was superimposed on the EEG signal as follows:

$$\mathbf{x} = \mathbf{x}_{\mathrm{EEG}} + \varepsilon \cdot \mathbf{x}_{\mathrm{EMG}}, \tag{15}$$

where ε represents the contribution of muscle activity. Figure 1 shows the original EEG signal $\mathbf{x}_{\mathrm{EEG}}$ and the EEG containing muscle artifacts $\mathbf{x}$ ($\varepsilon = 1.5$). The signal-to-noise ratio (SNR) can then be adjusted by changing the parameter ε:

$$\mathrm{SNR} = \frac{\mathrm{RMS}\left(\mathbf{x}_{\mathrm{EEG}}\right)}{\mathrm{RMS}\left(\varepsilon \cdot \mathbf{x}_{\mathrm{EMG}}\right)}, \tag{16}$$

where the root mean squared (RMS) value is defined as

$$\mathrm{RMS}\left(\mathbf{x}\right) = \sqrt{\frac{1}{T}\mathbf{x}\mathbf{x}^{T}}. \tag{17}$$

The relative root-mean-squared error (RRMSE) is used as an evaluation measure to the effect of muscle artifact removal, which is defined as follows:

$$\mathrm{RRMSE} = \frac{\mathrm{RMS}\left(\mathbf{x}_{\mathrm{EEG}} - \widehat{\mathbf{x}}\right)}{\mathrm{RMS}\left(\mathbf{x}_{\mathrm{EEG}}\right)}, \tag{18}$$

where $\widehat{\mathbf{x}}$ is the estimated EEG signal after muscle artifact removal. To further measure the capability of the proposed method for preserving the original EEG signal, correlation coefficients between the two waveforms $\mathbf{x}_{\mathrm{EEG}}$ and $\widehat{\mathbf{x}}$ are also calculated. Hence, in this work, RRMSE and correlation coefficient (CC) serve as the main criteria for measuring the performance of muscle artifact removal.

2.2.2. Real Data. In the real data study, two datasets were employed to demonstrate the effect of the proposed method. One dataset was collected by us from eight health subjects during their stable cycling on an exercise bicycle. The study was approved by the University of British Columbia Ethics Board, and all subjects gave written, informed consent prior to participating. The EEG data were collected using an EEG cap (Quick-Cap, Compumedics, Texas, USA) with 9 electrodes based on the International 10–20 system, referenced to linked mastoids. The EEG data were sampled at 1000 Hz using SynAmps2 amplifiers (NeuroScan, Compumedics, Texas, USA). Data were later processed by a band-pass filter between 1~70 Hz. EEG recordings during exercise are easily contaminated with muscle artifacts and those artifacts can largely complicate the subsequent EEG signal processing such as brain connectivity analysis. Figure 2 displays one 10-second scalp EEG segment. All channels were

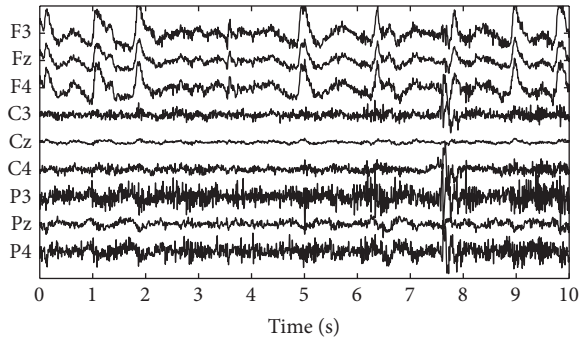

Figure 2: The original 10-second scalp EEG recordings during cycling.

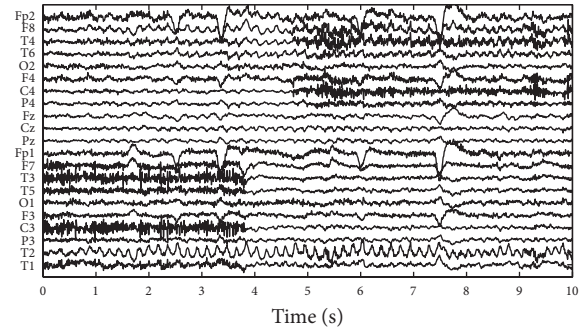

Figure 3: The original ictal 10-second scalp EEG recordings.

more or less contaminated with muscle activity during the 10 seconds.

The other dataset is the public ictal EEG from the BioSource database established by Sabine Van Huffel (http://www.esat.kuleuven.be/stadius/members/biomed/biosource.htm). Ictal EEG is often severely contaminated with muscle artifacts, which make the determination and localization of the ictal onset complicated. Figure 3 shows the 10-second scalp EEG recordings with 21 channels from a long-term Epilepsy Monitoring Unit (OSG EEG recorders, Rumst, Belgium). Electrodes were placed according to the International 10–20 system with additional sphenoidal electrodes. The sampling frequency was 250 Hz. The EEG was digitally filtered by a band-pass filter between 0.3~35 Hz. A notch filter was applied to suppress the 50 Hz power-line interference. The seizure EEG was contaminated with muscle artifacts and eye blinks. Muscle artifacts can be observed between 0 s and 3.9 s on channels F7, T3, T5, C3, and T1 and between 5 s and 10 s on channels F8, T4, F4, C4, and P4.

Although the EEG recordings here are not based on single-channel, we can still apply the proposed EEMD-MCCA method to each channel individually and demonstrate its effectiveness for removing muscle artifacts from different regions in the brain.

3. Results and Discussion

3.1. The Synthetic Data Case. We applied the proposed EEMD-MCCA method to the synthetic single-channel data $\mathbf{x}$ according to the procedure of Algorithm 1. As mentioned in Section 2.1.4, we tested the reliability of the method with different M and SNR values in terms of RRMSE and CC as shown in Figure 4. Note that the number of data sets M was chosen from 2 to 20 (i.e., $M = 2, 3, 4, \ldots, 20$). When $M = 2$, it means that CCA was used. When $M > 2$, MCCA was employed. The parameter τ in (12) can be chosen empirically as it may highly depend on the data structure. In this simulation study, we found that similar results could be obtained by examining a set of τ values. One possible reason is that by applying MCCA to multiple time-delayed data sets it is sufficient to fully exploit the temporal structure of the original data set no matter what value τ is. Among the values, $\tau = 10$ provided slightly better performance and was chosen here.

It can be seen from Figure 4 that MCCA can consistently achieve better performance than CCA, which is in accord with the theoretical analysis in Section 2.1.3. Another interesting observation is that when $M \geq 3$ the performance becomes quite stable. This suggests that $M = 3$ is a proper number of data sets in practical applications. To further demonstrate the practicability of the method, we tested the time cost when $M = 2$ and $M = 3$, which were 2.61 seconds and 2.73 seconds averaged over 100 independent runs separately. The implementation was done in MATLAB (MathWorks Inc., Novi, MI, USA) and run under Microsoft Windows 8 x64 OS on the computer with Dual Intel(R) Core(TM) i-3427U 1.80 GHz CPU and 8.00 GB RAM. Considering the improved performance, the slightly increased time cost is well acceptable for removing artifacts from 10-second EEG data, especially for a number of ambulatory systems in which fast clean information and direct feedback are essentially important.

To see some details of the method, we also present the stepwise results in Figure 5. The IMF components extracted by EEMD were shown in Figure 5(a) from high to low frequencies. After applying MCCA, the uncorrelated sources were ordered in terms of their autocorrelations as displayed in Figure 5(b). The muscle activity was present in the last two components with lowest autocorrelations in the MCCA decomposition. Excluding the muscle artifact components in the reconstruction led to the cleaned EEG shown in Figure 5(c). To further illustrate the performance, an amplified version including both recovered and original EEG signals was present in Figure 5(d), from which we can see that the proposed method highly preserved the original brain activity.

In addition, we also implemented low-pass filter and ICA-based methods for a performance comparison study in terms of RRMSE and CC at various SNR values. Butterworth filter of order 8 was employed with three different cutoff frequencies equal to 10, 30, and 50 Hz. ICA was applied to the same IMF components extracted by EEMD as our proposed method did. It is termed EEMD-ICA. The joint approximate diagonalization of eigenmatrices (JADE) algorithm was adopted here for ICA implementation [31]. Muscle artifact components, after applying EEMD-ICA, had to be selected according to visual inspection. The cleaned signal was reconstructed by

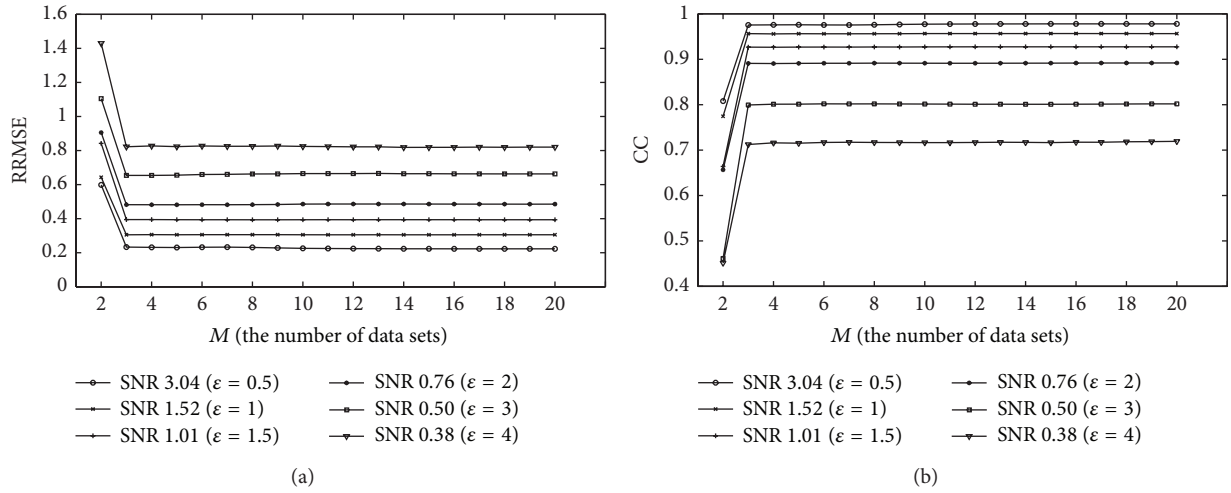

FIGURE 4: The performance measure in different M and SNR values: (a) RRMSE and (b) CC.

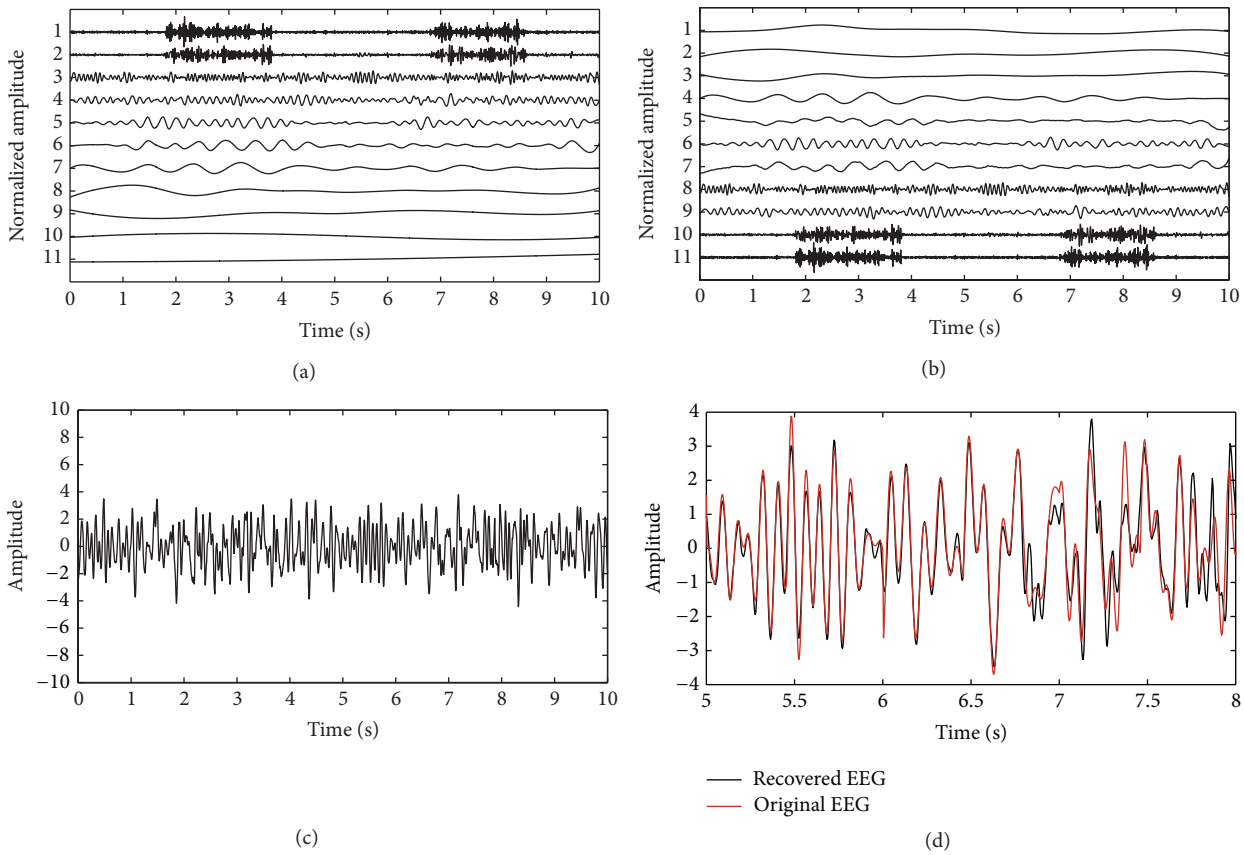

FIGURE 5: The stepwise results of the proposed method: (a) the IMF components after applying EEMD to the single-channel EEG $\mathbf{x}$ ($\varepsilon = 1.5$); (b) the canonical variates after using MCCA ($M = 3$); (c) the reconstructed EEG signal $\hat{\mathbf{x}}$ after muscle artifact removal; (d) the amplified version of $\hat{\mathbf{x}}$ compared with the original EEG $\mathbf{x}_{\text{EEG}}$.

excluding the components related to the artifact. The results are shown in Figure 6, from which we can see that EEMD-MCCA has consistently better performance than the low-pass filters. The possible reason is due to the fact that the low-pass filters were insufficient to remove all artifacts without altering the underlying brain activity since the frequency spectrum of the muscle artifacts overlaps with that of the brain signal [13]. Another concern for the low-pass filters is the nonlinear phase-frequency response characteristic in practice, which will lead to signal distortion. It should be noted that we did

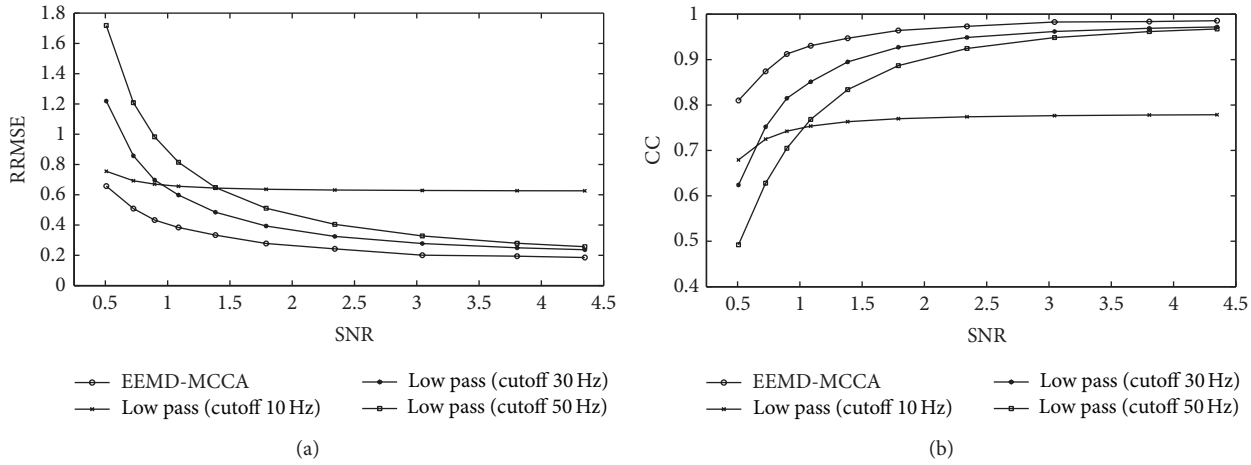

Figure 6: The performance comparisons between EEMD-MCCA and low-pass filters at various SNR values in terms of two criteria: (a) RRMSE and (b) CC.

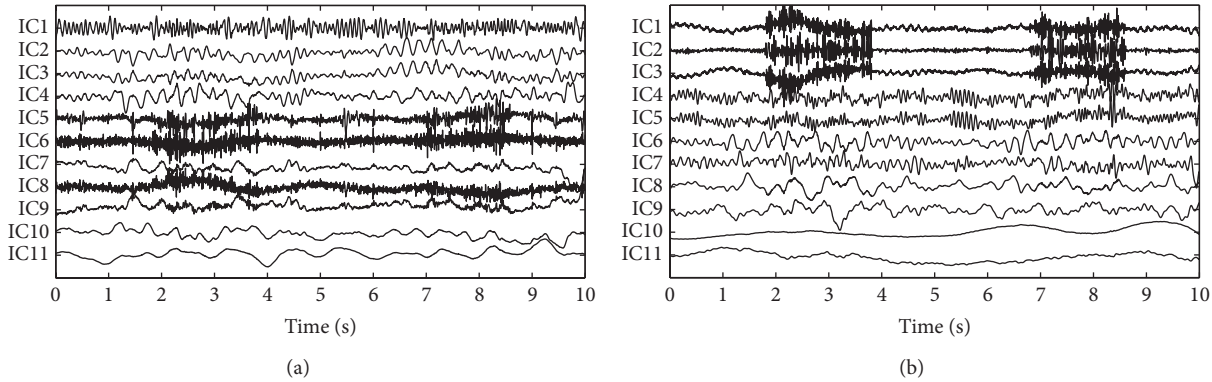

Figure 7: The components decomposed by using EEMD-ICA to the synthetic data at two different SNR values: (a) SCICA at $\varepsilon = 0.4$ (SNR = 3.80) and (b) SCICA at $\varepsilon = 2$ (SNR = 0.76).

not present the results of EEMD-ICA in Figure 6, because it was not capable of separating the muscle artifact from the EEG signal. Two examples of its decomposition are shown in Figure 7. We can easily observe that the EMG and EEG components were mixed together (e.g., IC9 in Figure 7(a) and IC1 in Figure 7(b)). It is quite difficult to determine which components should be excluded since we did not want to remove any brain activity.

3.2. The Real Data Case. In this case study, we applied the proposed EEMD-MCCA method to each individual channel of the EEG recordings as shown in Figures 2 and 3. We found that it was fairly easy to distinguish the muscle artifact components from the ones related to the brain activity. When processing each single-channel EEG recordings, muscle activity was almost present in the last several components in the MCCA decomposition. Excluding those components in the reconstruction of the EEG resulted in the cleaned EEG as shown in Figures 8 and 9. It can be seen that muscle artifacts have been sufficiently removed. In particular, for the ictal EEG, the ictal activity on the T2, F8, T4, and T6 electrodes was perfectly preserved. The ictal activity on F8 and T4, which originally was blurred by muscle artifacts, becomes visible by using the proposed EEMD-MCCA method. It should also be noted that there exist some obvious EOG artifacts in both real datasets, while their removal is beyond the scope of this paper. However, these EOG artifacts can help demonstrate the superior performance of our proposed method due to the fact that they were preserved with little distortion.

4. Conclusions

In this paper, we proposed a simple yet effective EEMD-MCCA method to realize muscle artifact removal from single-channel EEG. We illustrated the performances of the proposed method using both synthetic data and real-life data. We observed that the method is able to remove muscle activity effectively and efficiently and meanwhile preserve the brain activity very well. It is worth noting that while EEMD-MCCA is proposed to remove muscle activity for the single-channel EEG case, it is generally applicable when one dataset contains relatively fewer channels (e.g., two or three). The proposed method is a promising single-channel technique

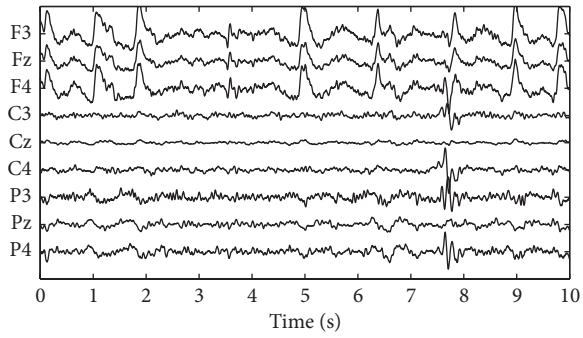

Figure 8: Reconstructed EEG signals after muscle artifact removal.

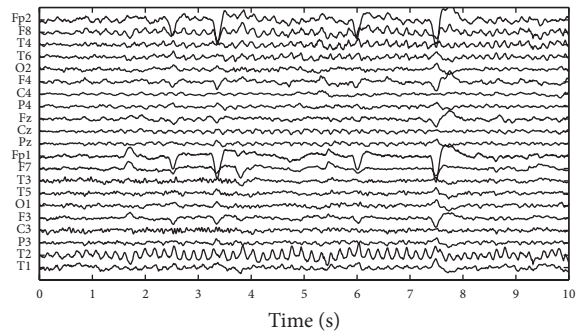

Figure 9: Reconstructed ictal EEG signals after muscle artifact removal.

under the current situation that ambulatory healthcare systems are increasingly emerging.

Conflict of Interests

The authors declare that there is no conflict of interests regarding the publication of this paper.

Acknowledgment

The work is supported by the National Natural Science Foundation of China (no. 61172037).

References

[1] S. Y. Shao, K. Q. Shen, C. J. Ong, E. P. V. Wilder-Smith, and X. P. Li, "Automatic EEG artifact removal: a weighted support vector machine approach with error correction," *IEEE Transactions on Biomedical Engineering*, vol. 56, no. 2, pp. 336–344, 2009.

[2] B. W. McMenamin, A. J. Shackman, L. L. Greischar, and R. J. Davidson, "Electromyogenic artifacts and electroencephalographic inferences revisited," *NeuroImage*, vol. 54, no. 1, pp. 4–9, 2011.

[3] S. S. Spencer, P. Williamson, S. Bridgers, R. Mattson, and D. Cicchetti, "Reliability and accuracy of localization by scalp ictal EEG," *Neurology*, vol. 35, no. 11, pp. 1567–1575, 1985.

[4] I. I. Goncharova, D. McFarland, T. Vaughan, and J. Wolpaw, "EMG contamination of EEG: spectral and topographical characteristics," *Clinical Neurophysiology*, vol. 114, no. 9, pp. 1580–1593, 2003.

[5] R. Vigario, J. Sarela, V. Jousmaki, M. Hamalainen, and E. Oja, "Independent component approach to the analysis of EEG and MEG recordings," *IEEE Transactions on Biomedical Engineering*, vol. 47, no. 5, pp. 589–593, 2000.

[6] N. P. Castellanos and V. A. Makarov, "Recovering EEG brain signals: artifact suppression with wavelet enhanced independent component analysis," *Journal of Neuroscience Methods*, vol. 158, no. 2, pp. 300–312, 2006.

[7] M. Crespo-Garcia, M. Atienza, and J. L. Cantero, "Muscle artifact removal from human sleep EEG by using independent component analysis," *Annals of Biomedical Engineering*, vol. 36, no. 3, pp. 467–475, 2008.

[8] H. Nam, T. G. Yim, S. K. Han, J. B. Oh, and S. K. Lee, "Independent component analysis of ictal EEG in medial temporal lobe epilepsy," *Epilepsia*, vol. 43, no. 2, pp. 160–164, 2002.

[9] E. Urrestarazu, J. Iriarte, M. Alegre, M. Valencia, C. Viteri, and J. Artieda, "Independent component analysis removing artifacts in ictal recordings," *Epilepsia*, vol. 45, no. 9, pp. 1071–1078, 2004.

[10] A. Belouchrani, K. Abed-Meraim, J. F. Cardoso, and E. Moulines, "A blind source separation technique using second-order statistics," *IEEE Transactions on Signal Processing*, vol. 45, no. 2, pp. 434–444, 1997.

[11] A. Ziehe, K. R. Müller, G. Nolte, B. M. Mackert, and G. Curio, "Artifact reduction in magnetoneurography based on time-delayed second-order correlations," *IEEE Transactions on Biomedical Engineering*, vol. 47, no. 1, pp. 75–87, 2000.

[12] S. Choi, A. Cichocki, and A. Beloucharni, "Second order nonstationary source separation," *Journal of VLSI Signal Processing Systems for Signal, Image and Video Technology*, vol. 32, no. 1-2, pp. 93–104, 2002.

[13] W. D. Clercq, A. Vergult, B. Vanrumste, W. van Paesschen, and S. van Huel, "Canonical correlation analysis applied to remove muscle artifacts from the electroencephalogram," *IEEE Transactions on Biomedical Engineering*, vol. 53, no. 12, pp. 2583–2587, 2006.

[14] J. Gao, C. Zheng, and P. Wang, "Online removal of muscle artifact from electroencephalogram signals based on canonical correlation analysis," *Clinical EEG and Neuroscience*, vol. 41, no. 1, pp. 53–59, 2010.

[15] K. Shen, K. Yu, A. Bandla, Y. Sun, N. Thakor, and X. Li, "Multiple time-lag canonical correlation analysis for removing muscular artifacts in EEG," in *Proceedings of the IEEE 35th Annual International Conference of Engineering in Medicine and Biology Society (EMBC '13)*, pp. 6792–6795, Osaka, Japan, July 2013.

[16] X. Chen and Z. J. Wang, "Design and implementation of a wearable, wireless EEG recording system," in *Proceedings of the 5th International Conference on Bioinformatics and Biomedical Engineering (ICBBE '11)*, pp. 1–4, Wuhan, China, May 2011.

[17] S. D. Ridwan, R. Thompson, B. T. Jap, S. Lal, and P. Fischer, "Single channel wireless EEG: proposed application in train drivers," in *Proceedings of the 3rd International Conference on Broadband Communications, Information Technology and Biomedical Applications*, pp. 58–63, Gauteng, South Africa, November 2008.

[18] B. Koley and D. Dey, "An ensemble system for automatic sleep stage classification using single channel EEG signal," *Computers in Biology and Medicine*, vol. 42, no. 12, pp. 1186–1195, 2012.

[19] N. E. Huang, Z. Shen, S. R. Long et al., "The empirical mode decomposition and the Hilbert spectrum for nonlinear and

non-stationary time series analysis," *Proceedings of the Royal Society of London A*, vol. 454, no. 1971, pp. 903–995, 1998.

[20] B. Mijović, M. de Vos, I. Gligorijević, J. Taelman, and S. van Huffel, "Source separation from single-channel recordings by combining empirical-mode decomposition and independent component analysis," *IEEE Transactions on Biomedical Engineering*, vol. 57, no. 9, pp. 2188–2196, 2010.

[21] K. T. Sweeney, S. F. McLoone, and T. E. Ward, "The use of ensemble empirical mode decomposition with canonical correlation analysis as a novel artifact removal technique," *IEEE Transactions on Biomedical Engineering*, vol. 60, no. 1, pp. 97–105, 2013.

[22] H. Zeng, A. Song, R. Yan, and H. Qin, "EOG artifact correction from EEG recording using stationary subspace analysis and empirical mode decomposition," *Sensors*, vol. 13, no. 11, pp. 14839–14859, 2013.

[23] Z. Wu and N. E. Huang, "Ensemble empirical mode decomposition: a noise-assisted data analysis method," *Advances in Adaptive Data Analysis*, vol. 1, no. 1, pp. 1–41, 2009.

[24] Y. Li, T. Adali, W. Wang, and V. Calhoun, "Joint blind source separation by multiset canonical correlation analysis," *IEEE Transactions on Signal Processing*, vol. 57, no. 10, pp. 3918–3929, 2009.

[25] H. Hotelling, "Relations between two sets of variates," *Biometrika*, vol. 28, pp. 321–377, 1936.

[26] X. Chen, A. Liu, Z. J. Wang, and H. Peng, "Corticomuscular activity modeling by combining partial least squares and canonical correlation analysis," *Journal of Applied Mathematics*, vol. 2013, Article ID 401976, 11 pages, 2013.

[27] O. Friman, M. Borga, P. Lundberg, and H. Knutsson, "Exploratory fMRI analysis by autocorrelation maximization," *NeuroImage*, vol. 16, no. 2, pp. 454–464, 2002.

[28] M. Borga and H. Knutsson, "A canonical correlation approach to blind source separation," Tech. Rep. LiU-IMT-EX-0062, Linkoping University, Linkoping, Sweden, 2001.

[29] V. Mäkinen, H. Tiitinen, and P. May, "Auditory event-related responses are generated independently of ongoing brain activity," *NeuroImage*, vol. 24, no. 4, pp. 961–968, 2005.

[30] N. Yeung, R. Bogacz, C. B. Holroyd, S. Nieuwenhuis, and J. D. Cohen, "Theta phase resetting and the error-related negativity," *Psychophysiology*, vol. 44, no. 1, pp. 39–49, 2007.

[31] J. F. Cardoso, "High-order contrasts for independent component analysis," *Neural Computation*, vol. 11, no. 1, pp. 157–192, 1999.

Hindawi Publishing Corporation
Journal of Applied Mathematics
Volume 2014, Article ID 528071, 7 pages
http://dx.doi.org/10.1155/2014/528071

Research Article

Enhanced Template Matching Using Dynamic Positional Warping for Identification of Specific Patterns in Electroencephalogram

Won-Du Chang and Chang-Hwan Im

Department of Biomedical Engineering, Hanyang University, 222 Wangsimni-ro, Seongdong-gu 133-791, Republic of Korea

Correspondence should be addressed to Chang-Hwan Im; ich@hanyang.ac.kr

Received 25 March 2014; Accepted 4 April 2014; Published 27 April 2014

Academic Editor: Kiwoon Kwon

Copyright © 2014 W.-D. Chang and C.-H. Im. This is an open access article distributed under the Creative Commons Attribution License, which permits unrestricted use, distribution, and reproduction in any medium, provided the original work is properly cited.

Template matching is an approach for signal pattern recognition, often used for biomedical signals including electroencephalogram (EEG). Since EEG is often severely contaminated by various physiological or pathological artifacts, identification and rejection of these artifacts with improved template matching algorithms would enhance the overall quality of EEG signals. In this paper, we propose a novel approach to improve the accuracy of conventional template matching methods by adopting the dynamic positional warping (DPW) technique, developed recently for handwriting pattern analysis. To validate the feasibility and superiority of the proposed method, eye-blink artifacts in the EEG signals were detected, and the results were then compared to those from conventional methods. DPW was found to outperform the conventional methods in terms of artifact detection accuracy, demonstrating the power of DPW in identifying specific one-dimensional data patterns.

1. Introduction

Template matching has been one of the most popular approaches in pattern recognition over the past few decades [1–4]. This technique is designed to match parts of a signal (or image) to a predefined template signal (or image) in order to quantify similarity of shapes among test and template signals. Thanks to its applicability in detecting various kinds of patterns, successful applications in a variety of different research fields have been reported. Such fields include eye-region detection [5, 6], human authentication [7], stock change categorization [8], handwriting recognition [9], signature verification [10], and electroencephalogram (EEG) artifact detection [11–13].

Pattern-detection studies on EEG signals have been conducted for the purpose of identifying pathologically driven EEG patterns or EEG artifacts [11, 12, 14–16]. However, there is still a need for better identification of eye-blink and motion artifacts, so that they can be rejected nearly perfectly in hopes of obtaining more reliable EEG analyses results. Precise automatic identification of artifacts is of great necessity in applications requiring online EEG processing or long-term EEG monitoring. Aside from the need for better artifact detection, there is also a need for better detection of abnormal EEG patterns associated with various brain disorders in order to achieve improved diagnostic decisions or better lesion localization [17, 18].

Dynamic time warping (DTW), a technique for enhanced template matching, has been widely studied in speech recognition [19, 20] and is gradually being applied in other ways, such as shape-boundary matching [21], facial recognition [22], signature verification [23], and EEG pattern detection [12]. DTW is a method that has been applied to achieve more accurate quantification of differences between template and test-signal subpatterns, through optimal matching of corresponding points. Instead of assuming uniform distributions among corresponding points between template and test subpatterns, DTW finds the best corresponding points by warping the template pattern at the time axis. Recent studies have shown higher accuracies for template matching with DTW than for conventional template matching methods that assume uniform distributions among corresponding points [24–26].

Dynamic positional warping (DPW) is a modification of DTW that was developed to improve accuracy in distance quantification [27]. It was originally developed for the accurate matching of contour data with two-dimensional shapes and frequently used for signature verification. By allowing for the signal to be warped on the ordinate axis in addition to the time axis, DPW can more accurately identify corresponding points than can conventional DTW.

The main goal of this study was to investigate whether DPW could be extended to one-dimensional pattern recognition problems. To approach this aim, we applied DPW for the detection of eye-blink artifact patterns in frontal EEG data acquired from 24 healthy subjects. The detection accuracy of DPW was then compared to those of the conventional template matching methods.

2. Materials and Methods

2.1. Experimental Data and Preprocessing. In this study, eye-blink artifacts in continuous EEG signals were selected as the target patterns to be detected. The reason for this is that, while eye-blink artifacts were regarded as representative artifacts contaminating EEG signals, it was difficult to accurately identify them due to high variability among events or individuals. EEG data were recorded from 24 healthy participants using a multichannel EEG recording system (ActiveTwo AD-box, BioSemi, The Netherlands) at a sampling rate of 2,048 Hz, while the participants performed spot-the-difference puzzles for 25 seconds. Two slightly different images were presented on the left and right halves of a display, and the participants were asked to find the differences between two images for 15 seconds. The task was repeated five times for each participant. A particular frontal channel Fp2 in the international 10–20 system was used for the eye-blink artifact detection. To verify eye-blink detection accuracy, it was necessary to use a ground-truth dataset indicating the presence of an eye-blink artifact. For this aim, time ranges of eye-blink artifacts were marked by two experienced researchers based on visual inspection of EEG data.

Before the primary analyses, EEG data were high-pass filtered with a 0.1 Hz cutoff frequency, downsampled to a 64 Hz sampling rate in order to reduce the computation cost, and median-filtered with a five-point width in order to smooth the data. The width of the median filter was determined empirically.

2.2. Procedure for Template Matching. In order to evaluate and compare different distance metrics, a typical template matching protocol was implemented. The template matching protocol was designed to be as simple as possible so as to exclude any potential influence from any confounding factors. Figure 1 illustrates the schematic diagram of our study protocol.

The core parts of this process include distance calculation between templates and test patterns (denoted by Step 1 in Figure 1) and an overall similarity decision based on a predetermined threshold (denoted by Step 3 in Figure 1). Both of these steps are common among studies using template matching approaches [11, 12, 28]. In the current study, test patterns were extracted from the continuous test EEG data using a fixed-size sliding window, and the distances between the template and test EEG signals were evaluated at every time point (the number of sliding windows was denoted by N). The size of the sliding window was set to be the same as the length of the template as this was an assumption indispensable for applying linear template matching such as correlation and root-mean-square error. The decision step was only applied for the local minima of the distance array, and equal widths were assumed for the detected pattern and template. When ranges of adjacent detected patterns overlapped with one another, the detected pattern ranges were merged into a single range in order to avoid duplicate detection.

Template signals were randomly selected by a computer as in [4], so as to eliminate any possible bias toward the use of a specific method. When used by experts, manual template selection has the potential for achievement of higher performance outcomes [11, 12] compared to random selection; however, manual selection processes are highly dependent on experts' subjective decisions and can lead to biased results.

Approaches for better use of training data involve construction of a single template by averaging patterns in a single cluster or selection of best-fit templates for each cluster. Unfortunately, however, these methods do not generally show high performance when template widths and shapes have large variances. In this study, we adopted a normalization method [29], considering large variances of template widths and shapes due to random selection of templates. There are two advantages for normalization approach compared to the conventional approaches: (1) effects of improper template selection can be minimized by distance-averaging; (2) variations in template width and shape do not need to be considered. Normalized distance (denoted by D_j) between the jth test pattern and templates can be calculated by

$$D_j = \frac{\left(\sum_{i=1}^{n} d_{ij}\right)}{n \cdot \sigma}, \tag{1}$$

where d_{ij} is distance between the ith template and the jth test pattern, n is the number of templates, and σ is a normalization factor, given as

$$\sigma = \frac{\left(\sum_{i=1}^{n} \sum_{j=i+1}^{n} d_{ij}\right)}{\{n \cdot (n-1)/2\}}. \tag{2}$$

The test pattern T_j is accepted if D_j is a local minimum and if this local minimum is lower than a predefined threshold. This overall process was repeated 20 times in order to achieve an unbiased comparison.

2.3. Traditional Distance Metrics. Because it is generally assumed that target-pattern shapes are unchanging, Euclidean distance and correlation-coefficients have been most commonly used for template matching applications [4, 30]. Three traditional distance metrics are investigated in this study, which are root-mean-square error (RMSE) based on Euclidean distances (with linear matching), correlation coefficient, and Kurtosis. Kurtosis was considered in this study because it is widely used in biomedical data analysis

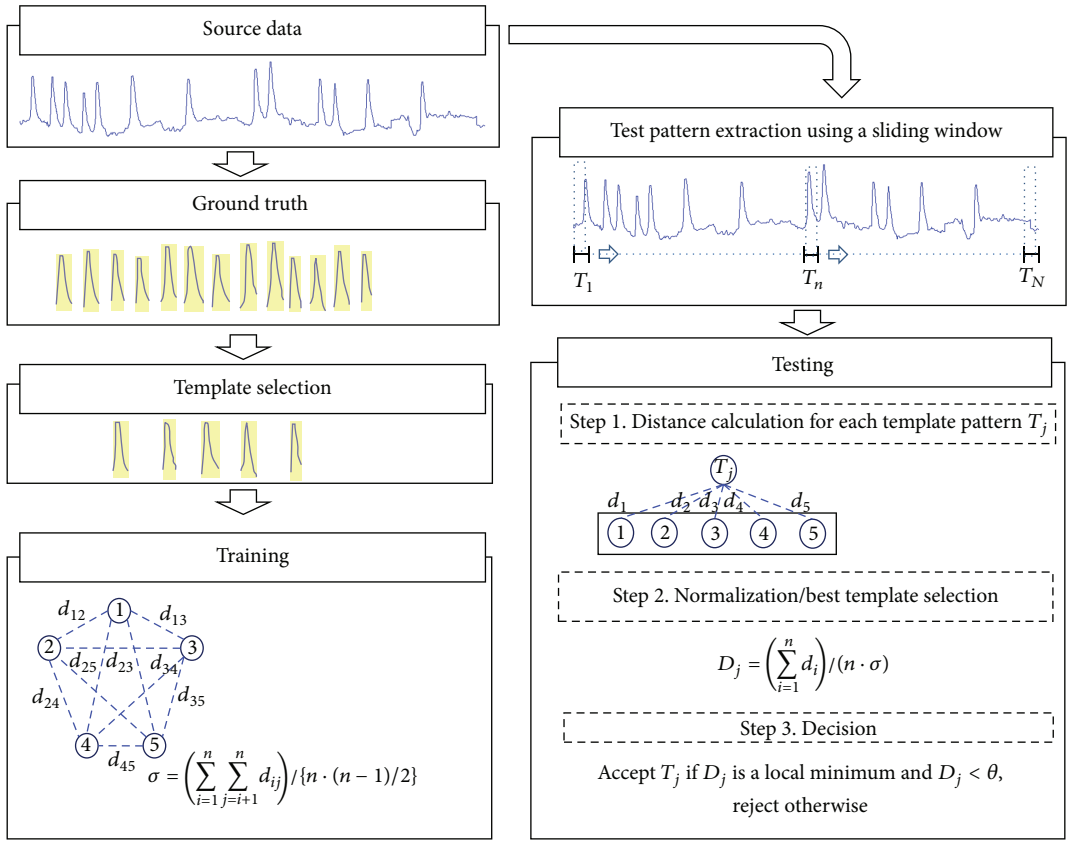

FIGURE 1: Schematic diagram of our study protocol for $n = 5$ templates. After selecting templates from the ground-truth dataset, the average distance among the templates is calculated for normalization (during the "Training" phase). During the "Testing" phase, distances between templates and test patterns within test-signal sliding windows are calculated.

[31, 32]. Between two signals A and B, with L_A and L_B as the respective signal lengths, distances for each metric are defined as follows.

Root-mean-square error:

$$d_{\text{rmse}} = \sqrt{\frac{1}{L}\cdot\sum_{k=1}^{L}\{A(k)-B(k)\}^2}. \tag{3}$$

Correlation:

$$d_{\text{corr}} = \frac{\sum_{k=1}^{L}\left\{A(k)-\overline{A}\right\}\cdot\left\{B(k)-\overline{B}\right\}}{\sqrt{\sum_{k=1}^{L}\left\{A(k)-\overline{A}\right\}^2}\cdot\sqrt{\sum_{k=1}^{L}\{B(k)-B\}^2}}. \tag{4}$$

Kurtosis:

$$d_{\text{ku}} = \left|\frac{\sum_{k=1}^{L_A}\left\{A(k)-\overline{A}\right\}^4}{L_A\cdot{\sigma_A}^4} - \frac{\sum_{k=1}^{L_B}\left\{B(k)-\overline{B}\right\}^4}{L_B\cdot{\sigma_B}^4}\right|, \tag{5}$$

where $A(k)$ and $B(k)$ denote kth data in signals A and B, respectively. Note that RMSE and correlation are calculable only for identical signal lengths. Thus, a common variable L was used to represent the signal length in (3) and (4).

2.4. Dynamic Time Warping. In spite of various modifications of DTW in previous decades, original kernel models for calculating distance are still being widely used in many applications. In this study, we adopted a common implementation of DTW [19] and empirically determined parameters for slope constraints. The DTW distance between two signals is defined as

$$d_{\text{dtw}} = \tau\left(L_A, L_B\right), \tag{6}$$

where L_A and L_B are respective template and test pattern lengths, and $\tau(i, j)$ is the distance between two subsignals $\{A(k) \mid 1 \le k \le i\}$ and $\{B(k) \mid 1 \le k \le j\}$, defined as

$$\begin{aligned}\tau(i,j) = {} & \left|\{A(i)-A(1)\}-\{B(j)-B(1)\}\right| \\ & + \min_{c}\left\{\tau\left(i-C_A(c), j-C_B(c)\right)\right\},\end{aligned} \tag{7}$$

where $\tau(1, 1) = 0$, and $C_A(c)$ and $C_B(c)$ are cth slope constraints on pattern axes, which limit the number of skipping (jumping) data points. $C_{AB}(c)$ denotes the cth pair of the slope constraints on template and test pattern axes and can be written as

$$C_{AB} = \{(1,m),(m,1) \mid 1 \le m \le M\}, \tag{8}$$

where M is the maximum branch length of slope constraints. Note that the values at the starting points of the two patterns are adjusted to be overlapped.

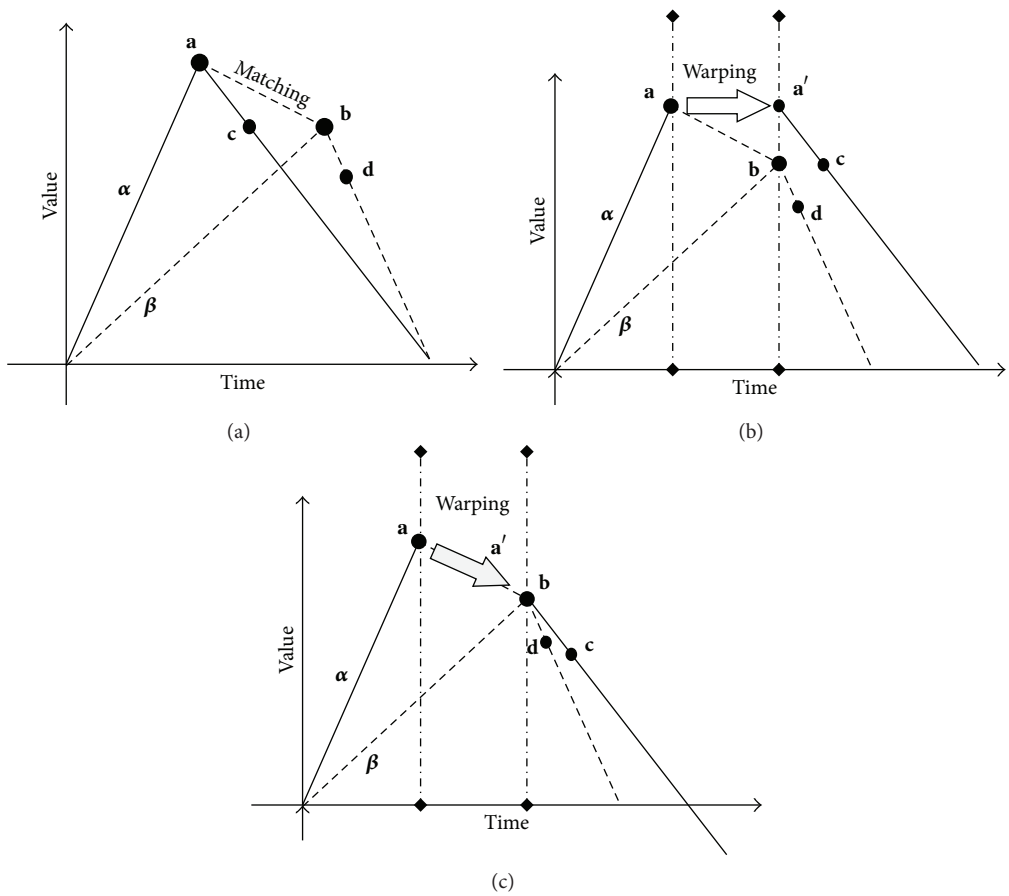

Figure 2: Schematic illustrations for elucidating dynamic time warping and positional warping for one-dimensional data matching: (a) two signals $\boldsymbol{\alpha}$ (solid line) and $\boldsymbol{\beta}$ (dashed line) are compared and considered a pair of corresponding points. (b) Time warping in DTW: **a** is warped to $\mathbf{a}'$ by time shifting. (c) Positional and time warping in DPW: **a** is warped to $\mathbf{a}'$ to be overlapped onto **b**.

2.5. Dynamic Positional Warping (DPW). DPW was originally proposed for accurate quantification of differences between two-dimensional data such as an object's contour or handwritten characters, by searching similar subsequences recursively [27]. When employed for one-dimensional data, the DPW distance between time series signals A and B can be written as follows:

$$d_{\mathrm{dtw}} = \tau\left(L_A, L_B\right), \tag{9}$$

$$\tau\left(i,j\right) = \left|\left\{A\left(i\right) - A\left(i_{\mathrm{prev}}\right)\right\} - \left\{B\left(j\right) - B\left(j_{\mathrm{prev}}\right)\right\}\right| + \omega\left(i,j\right), \tag{10}$$

$$i_{\mathrm{prev}} = i - C_A\left(c_{\min}\left(i,j\right)\right), \tag{11}$$

$$j_{\mathrm{prev}} = j - C_B\left(c_{\min}\left(i,j\right)\right), \tag{12}$$

$$c_{\min}\left(i,j\right) = \arg\min_{c}\left\{\varphi\left(i - C_A\left(c\right), j - C_B\left(c\right)\right)\right\}, \tag{13}$$

$$\omega\left(i,j\right) = \min_{c}\left\{\varphi\left(i - C_A\left(c\right), j - C_B\left(c\right)\right)\right\}, \tag{14}$$

where most notations are the same as those used in the original DTW equations ((6) and (7)). In these equations, i_{prev} and j_{prev} represent preceding corresponding points that minimize $\tau(i, j)$. As shown in (9) and (10), the forms of the equations are the same as those of conventional DTW equations, except with regard to distance calculation between two points. Note that $A(i_{\mathrm{prev}})$ and $B(j_{\mathrm{prev}})$ are substituted for $A(1)$ and $B(1)$, respectively, in (10).

Figure 2 compares the mechanisms of DPW and DTW in one-dimensional data-matching applications. When two signals are compared and points **a** and **b** are matched as a corresponding pair (Figure 2(a)), DTW shifts a subsequence that begins with **a** on the time axis such that the shifted point is moved to the same time index as the subsequence starting with **b** (Figure 2(b)). This process, denoted as time warping, allows for distance calculation between points **c** and **d** by placing them closely on time axis. In the case of DPW, upon matching **a** and **b**, the subsequence starting from **a** is warped so that **a** is overlapped onto **b**. Please note this subsequence warping costs the distance (on the axis of ordinate) between the two points **a** and **b**, while the warping cost on the time axis is free (refer to [27] for more detailed description on the original DPW method).

3. Results and Discussion

Receiver operating characteristic (ROC) curves were used to compare pattern-detection performances among the various template matching approaches introduced in Section 2. To evaluate ROC curves, recall rates were evaluated with respect

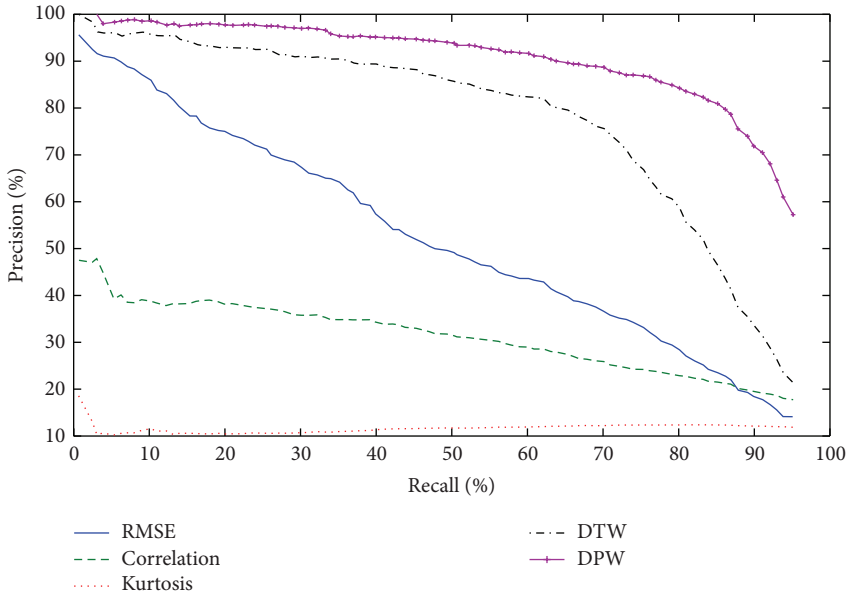

Figure 3: ROC curves of five different methods.

to fixed precision rates for each iteration of each participant. Then, for each precision rate, recall rates were averaged across all the iterations and participants. Figure 3 shows ROC curves illustrating detection accuracies for five different methods. DPW showed the highest accuracy among all methods investigated, with an accuracy of 82% for equal precision and recall rates. DPW accuracy was 10% higher than that for conventional DTW (where accuracy rating was 72%) and even higher than those for conventional distance metrics (RMSE: 49%, correlation: 34%, and Kurtosis: 11%). These results demonstrate that positional warping, as has been used for two-dimensional pattern recognition problems, might be also effective in one-dimensional pattern recognition problems.

The extremely low accuracies of RMSE and correlation may be surprising, considering that both distance metrics are so commonly used for template matching applications. The poor performances found for both metrics are thought to partly originate from high target-pattern shape variations. It is also possible that these poor performances were the result of the chosen task being more difficult than typical tasks. Since the templates in the current task were selected randomly from ground-truth datasets, there may have been many templates with irregular shapes. Despite these difficult conditions, the proposed DPW approach showed much higher detection accuracy than the DTW approach, suggesting that DPW might be used as a new and powerful method for extracting specific signal patterns for EEG applications.

Table 1 summarizes the best detection accuracies among 20 iterations, evaluated for each participant. Accuracy was calculated as the percentage of precision or recall for equal precision and recall values in ROC curves. When ROC curves were evaluated for each participant and best accuracies were selected among the 20 iteration results, the conventional methods based on correlation coefficients or RMSEs yielded better accuracies than the results shown in Figure 3. Nevertheless, DPW still outperformed the other metrics, ranking the highest for 22 of 24 participants. The averaged detection accuracy for DPW (96.10%) was 3.62% higher than that for DTW (92.38%).

In addition, the influence of the number of templates on detection accuracy was investigated. The detection accuracy was evaluated by increasing the number of templates and then averaging across all iterations and participants (Table 2). The results show a weak influence of the number of templates on detection accuracy. Except for correlation, accuracy did not change significantly as the number of templates increased. Instead, the standard deviations of DTW and DPW decreased significantly, demonstrating the possibility for more stable pattern detection by the use of sufficient numbers of templates in DTW and DPW.

4. Conclusion

In this paper, we investigated whether DPW, originally developed for two-dimensional pattern recognition, could be successfully employed for one-dimensional pattern recognition. To validate our alternative hypothesis that DPW is effective for one-dimensional data analysis, DPW was applied to the problem of EEG eye-blink artifact detection. DPW outperformed conventional template matching methods including DTW, demonstrating that this positional warping method, which warps signals on both ordinate and abscissa axes, is also effective in one-dimensional pattern recognition. This study suggests the possibility of applying DPW to many other types of signal patterns and applications. We are also planning to combine DPW with other methodologies in our future studies.

Conflict of Interests

The authors declare that there is no conflict of interests regarding the publication of this paper.

Table 1: Best accuracies (%) evaluated for each participant among results from 20 iterations. Best accuracy values for each participant are in bold font.

Subject ID	Correlation	RMSE	Kurtosis	DTW	DPW
1	86.96	61.32	22.86	94.97	**98.55**
2	84.25	90.67	39.46	97.60	**98.28**
3	49.19	60.83	15.98	77.42	**85.27**
4	69.02	84.38	15.77	93.65	**95.41**
5	49.28	73.69	18.45	83.50	**92.39**
6	26.67	84.44	13.33	90.00	**91.55**
7	80.72	92.80	30.95	94.64	**98.66**
8	88.19	92.86	48.00	98.01	**100.00**
9	62.96	98.77	31.34	98.77	**99.38**
10	71.83	71.33	17.94	93.57	**95.11**
11	40.00	86.67	20.71	91.55	**100.00**
12	61.32	91.74	13.24	93.28	**99.26**
13	57.48	41.88	15.10	79.21	**96.56**
14	60.83	78.89	30.19	91.43	**97.14**
15	63.89	76.07	15.01	94.36	**98.65**
16	80.63	94.18	34.05	96.84	**98.95**
17	60.87	54.01	22.79	**84.28**	80.82
18	40.30	86.38	24.00	97.37	**98.72**
19	65.01	72.08	18.37	89.81	**94.95**
20	17.59	76.67	17.69	93.33	**94.94**
21	79.20	91.67	22.13	92.51	**97.94**
22	63.11	41.63	25.10	91.88	**96.70**
23	65.55	90.23	23.08	**100.00**	98.08
24	40.99	97.53	20.71	**99.17**	**99.17**
Average	61.08	78.78	23.18	92.38	**96.10**

Table 2: Artifact detection accuracies (%) with respect to the number of templates, for equal precision and recall.

Number of templates	Correlation	RMSE	Kurtosis	DTW	DPW
1	49.54 ± 22.45	61.65 ± 28.42	9.65 ± 5.63	77.58 ± 22.44	83.94 ± 23.52
2	34.37 ± 27.54	62.55 ± 25.51	11.74 ± 11.01	68.29 ± 29.59	78.23 ± 30.35
3	28.42 ± 25.93	61.60 ± 25.08	10.20 ± 7.21	76.38 ± 20.47	86.06 ± 17.06
4	27.31 ± 24.58	60.42 ± 25.52	9.88 ± 7.49	75.51 ± 20.07	85.79 ± 16.36
5	23.84 ± 22.28	59.77 ± 24.72	10.77 ± 8.15	74.64 ± 19.79	85.92 ± 16.24
6	24.89 ± 21.47	58.90 ± 25.72	10.47 ± 8.35	77.49 ± 17.44	86.63 ± 15.41
7	25.76 ± 22.91	58.44 ± 25.09	10.37 ± 8.14	76.09 ± 17.64	86.42 ± 15.74
8	25.35 ± 22.23	58.59 ± 25.25	10.85 ± 8.74	76.80 ± 17.32	86.87 ± 14.60
9	24.56 ± 20.88	59.65 ± 24.45	11.08 ± 8.90	77.92 ± 15.12	87.13 ± 14.16
10	24.17 ± 19.33	59.49 ± 25.37	10.69 ± 9.17	78.68 ± 15.35	86.54 ± 15.25

Acknowledgments

This work was supported in part by the IT R&D program of MSIP/KEIT (KI10045461, Development of Cultural Contents Evaluation Technology Based on Real-Time Biosignal of Multiple Subjects), in part by the IT R&D program of MOTIE/MISP/KEIT (10045452, Development of Multimodal Brain-Machine Interface System Based on User Intent Recognition), and in part by the National Research Foundation of Korea (NRF) funded by the Ministry of Science, ICT and Future Planning (NRF-2012R1A2A2A03045395).

References

[1] A. Goshtasby, "Template matching in rotated images," *IEEE Transactions on Pattern Analysis and Machine Intelligence*, vol. 7, no. 3, pp. 338–344, 1985.

[2] J. Frank, S. Mannor, J. Pineau, and D. Precup, "Time series analysis using geometric template matching," *IEEE Transactions on Pattern Analysis and Machine Intelligence*, vol. 35, no. 3, pp. 740–754, 2013.

[3] S. Omachi and M. Omachi, "Fast template matching with polynomials," *IEEE Transactions on Image Processing*, vol. 16, no. 8, pp. 2139–2149, 2007.

[4] J.-H. Chen, C.-S. Chen, and Y.-S. Chen, "Fast algorithm for robust template matching with M-estimators," *IEEE Transactions on Signal Processing*, vol. 51, no. 1, pp. 230–243, 2003.

[5] K. Peng, L. Chen, S. Ruan, and G. Kukharev, "A robust algorithm for eye detection on gray intensity face without spectacles," *Journal of Computer Science & Technology*, vol. 5, no. 3, pp. 127–132, 2005.

[6] R. Wagner and H. L. Galiana, "Evaluation of three template matching algorithms for registering images of the eye," *IEEE Transactions on Biomedical Engineering*, vol. 39, no. 12, pp. 1313–1319, 1992.

[7] Z. Lin and L. S. Davis, "Shape-based human detection and segmentation via hierarchical part-template matching," *IEEE Transactions on Pattern Analysis and Machine Intelligence*, vol. 32, no. 4, pp. 604–618, 2010.

[8] T.-C. Fu, F.-L. Chung, R. Luk, and C.-M. Ng, "Stock time series pattern matching: template-based vs. rule-based approaches," *Engineering Applications of Artificial Intelligence*, vol. 20, no. 3, pp. 347–364, 2007.

[9] S. D. Connell and A. K. Jain, "Template-based online character recognition," *Pattern Recognition*, vol. 34, no. 1, pp. 1–14, 2001.

[10] M. Faundez-Zanuy, "On-line signature recognition based on VQ-DTW," *Pattern Recognition*, vol. 40, no. 3, pp. 981–992, 2007.

[11] Y. Li, Z. Ma, W. Lu, and Y. Li, "Automatic removal of the eye blink artifact from EEG using an ICA-based template matching approach," *Physiological Measurement*, vol. 27, no. 4, pp. 425–436, 2006.

[12] A. Aarabi, K. Kazemi, R. Grebe, H. A. Moghaddam, and F. Wallois, "Detection of EEG transients in neonates and older children using a system based on dynamic time-warping template matching and spatial dipole clustering," *NeuroImage*, vol. 48, no. 1, pp. 50–62, 2009.

[13] E. Olejarczyk, A. Jozwik, W. Zmyslowski et al., "Automatic detection and analysis of the EEG sharp wave-slow wave patterns evoked by fluorinated inhalation anesthetics," *Clinical Neurophysiology*, vol. 123, no. 8, pp. 1512–1522, 2012.

[14] H. Nolan, R. Whelan, and R. B. Reilly, "FASTER: fully automated statistical thresholding for EEG artifact rejection," *Journal of Neuroscience Methods*, vol. 192, no. 1, pp. 152–162, 2010.

[15] A. Delorme, T. Sejnowski, and S. Makeig, "Enhanced detection of artifacts in EEG data using higher-order statistics and independent component analysis," *NeuroImage*, vol. 34, no. 4, pp. 1443–1449, 2007.

[16] T. A. Camilleri, K. P. Camilleri, and S. G. Fabri, "Automatic detection of spindles and K-complexes in sleep EEG using switching multiple models," *Biomedical Signal Processing and Control*, vol. 10, pp. 117–127, 2014.

[17] G. Wang, G. Worrell, L. Yang, C. Wilke, and B. He, "Interictal spike analysis of high-density eeg in patients with partial epilepsy," *Clinical Neurophysiology*, vol. 122, no. 6, pp. 1098–1105, 2011.

[18] M. S. Aldrich, E. A. Garofalo, and I. Drury, "Epileptiform abnormalities during sleep in Rett syndrome," *Electroencephalography and Clinical Neurophysiology*, vol. 75, no. 5, pp. 365–370, 1990.

[19] L. Rabiner and B. H. Juang, *Fundamentals of Speech Recognition*, Prentice Hall, New York, NY, USA, 1993.

[20] C. Myers, L. R. Rabiner, and A. E. Rosenberg, "Fully automated statistical thresholding for EEG artifact rejection," *IEEE Transactions on Acoustics, Speech, and Signal Processing*, 1980.

[21] N. Alajlan, I. El Rube, M. S. Kamel, and G. Freeman, "Shape retrieval using triangle-area representation and dynamic space warping," *Pattern Recognition*, vol. 40, no. 7, pp. 1911–1920, 2007.

[22] H. Sahbi and N. Boujemaa, "Robust face recognition using dynamic space warping," in *Biometric Authentication*, M. Tistarelli, J. Bigun, and A. K. Jain, Eds., vol. 2359 of *Lecture Notes in Computer Science*, pp. 121–132, Springer, 2002.

[23] H. Feng and C. C. Wah, "Online signature verification using a new extreme points warping technique," *Pattern Recognition Letters*, vol. 24, no. 16, pp. 2943–2951, 2003.

[24] Y.-S. Jeong, M. K. Jeong, and O. A. Omitaomu, "Weighted dynamic time warping for time series classification," *Pattern Recognition*, vol. 44, no. 9, pp. 2231–2240, 2011.

[25] B. S. Raghavendra, D. Bera, A. S. Bopardikar, and R. Narayanan, "Cardiac arrhythmia detection using dynamic time warping of ECG beats in e-healthcare systems," in *Proceedings of the IEEE International Symposium on a World of Wireless, Mobile and Multimedia Networks (WoWMoM '11)*, pp. 1–6, June 2011.

[26] M. Parizeau and R. Plamondon, "Comparative analysis of regional correlation, dynamic time warping, and skeletal tree matching for signature verification," *IEEE Transactions on Pattern Analysis and Machine Intelligence*, vol. 12, no. 7, pp. 710–716, 1990.

[27] W.-D. Chang and J. Shin, "Dynamic positional warping: dynamic time warping for online handwriting," *International Journal of Pattern Recognition and Artificial Intelligence*, vol. 23, no. 5, pp. 967–986, 2009.

[28] H.-C. Huang and B. H. Jansen, "EEG waveform analysis by means of dynamic time-warping," *International Journal of Bio-Medical Computing*, vol. 17, no. 2, pp. 135–144, 1985.

[29] W.-D. C. W. D. Chang and J. S. J. Shin, "DPW approach for random forgery problem in online handwritten signature verification," in *Proceedings of the 4th International Conference on Networked Computing and Advanced Information Management (NCM '08)*, vol. 1, pp. 347–352, September 2008.

[30] S. Kim and J. McNames, "Automatic spike detection based on adaptive template matching for extracellular neural recordings," *Journal of Neuroscience Methods*, vol. 165, no. 2, pp. 165–174, 2007.

[31] T. Akiyama, M. Osada, M. Isowa et al., "High kurtosis of intracranial electroencephalogram as a marker of ictogenicity in pediatric epilepsy surgery," *Clinical Neurophysiology*, vol. 123, no. 1, pp. 93–99, 2012.

[32] L. Canuet, R. Ishii, M. Iwase et al., "MEG-SAM kurtosis analysis in the localization of the epileptogenic tuber in tuberous sclerosis: a case report," *International Congress Series*, vol. 1300, pp. 653–656, 2007.